

SEARCH FOR HEAVY RESONANCE DECAYS INTO SEMILEPTONIC FINAL
STATES IN PROTON-PROTON COLLISIONS AT $\sqrt{s} = 13$ TEV WITH THE ATLAS
DETECTOR

By

Julia Rose Hinds

A DISSERTATION

Submitted to
Michigan State University
in partial fulfillment of the requirements
for the degree of

Physics — Doctor of Philosophy

2025

PUBLIC ABSTRACT

SEARCH FOR HEAVY RESONANCE DECAYS INTO SEMILEPTONIC FINAL STATES IN PROTON-PROTON COLLISIONS AT $\sqrt{s} = 13$ TEV WITH THE ATLAS DETECTOR

By

Julia Rose Hinds

This dissertation presents a search for heavy resonances decaying to pairs of Standard Model bosons in semileptonic final states, where one vector boson (W or Z) decays leptonically and the other boson (W, Z, or Higgs) decays hadronically. The analysis uses the full Run 2 proton-proton collision dataset collected by the ATLAS detector at CERN between 2015-2018 at a center-of-mass energy of $\sqrt{s} = 13$ TeV, corresponding to an integrated luminosity of 140 fb^{-1} . The search targets localized excesses in the invariant mass distributions of diboson candidates, interpreted in the context of several Beyond Standard Model theories, including the Heavy Vector Triplet (HVT) framework and warped extra dimension models. These historically separate searches for $X \rightarrow VV$ and $X \rightarrow VH$ has been unified into a single, harmonized semileptonic analysis with reoptimized event selection. This work contributes to the development of common selection criteria, reoptimization of a lepton channel, and the evaluation of $t\bar{t}$ modeling uncertainties. Also the implementation of the UFO jet definition led to improved reconstruction of large-radius jets. All of these developments result in an overall improvement in sensitivity of at least 20% over previous ATLAS searches in the same channels and dataset. Notably, this analysis sets the first ATLAS upper limits on the vector boson fusion production of heavy resonances decaying to VH final states, with 95% confidence-level upper limits placed on the production cross-section times branching ratio for spin-1 and spin-0 resonances in the mass range of 220 GeV to 5 TeV. Additionally, performance studies of top-quark and W-boson jet taggers are conducted using semilep-

tonic $t\bar{t}$ events, yielding scale factors to correct mismodeling between data and Monte Carlo simulation.

Copyright by
JULIA ROSE HINDS
2025

ACKNOWLEDGMENTS

As I sit here reflecting on my entire life, I am so thankful for so many people. While this dissertation may be a cumulation of the work I've help contribute to over the past 6 years, my growth as a scientist, friend, and person, is due to everyone who has impacted my life. It would be impossible to list every single person - but I will do my best.

Firstly, to the best advisor, Dan Hayden: thank you. I simply do not know how to even begin to describe how incredibly grateful I am to have you as my mentor. Imposter syndrome is real and I fear I suffer greatly from it; but in our conversations, I have never once felt unintelligent for asking questions (even when I ask the same questions, repeatedly, because it didn't quite stick the first time). Your intelligence and ability to distill complex problems have continually inspired me to think more deeply and critically. I am a better scientist because of your thoughtful guidance and unwavering support.

Thank you to my committee members, Wade Fisher, Andreas von Manteuffel, Artemis Spyrou, and Danny Caballero, for your guidance and support over these past few years. I thank and appreciate your time and investment in me, as well as for reading this document!

Thank you to Robert Les, the MSU postdoc whom I've had the great pleasure to working with. Your technical skills and expertise have continually challenged and pushed me forward in my growth as a physicist. I'm grateful to have had the opportunity to learn from you. I would also like to thank all of the MSU postdocs for their collaboration, support, and camaraderie, both in our work together and during my visits to CERN. It was a pleasure to learn from you, share experiences, and build friendships along the way. CERN beers will forever hold a special place in my heart.

Thank you to the entire MSU ATLAS group for the welcoming environment and collabo-

rative spirit. Additionally, thank you to everyone in both of the groups I've had the pleasure of working with at CERN: the JetETmiss Group and the VV+VH Semileptonic Group. The work presented in this dissertation is the result of our collective efforts.

To my family, I love you all so much. To my amazing parents, Carl Hinds and Alexis Hinds, thank you for always believing in me, and pushing me to be the best version of myself. Dad, thank you for helping me develop a love of science early on in life. I thank you for nourishing my inquisitive younger self when I was asking you a million questions about everything. Thank you for always answering the phone when I called, even when it was just to ramble about all the interesting things I learned during my physics courses. I guess I've finally satiated the "how does the world work" questions I've always asked you! Mom, thank you for being my best friend and role model in life. From dropping me off my freshman year of college, to my current daily rants about the job market - I am forever humbled by your love and support. Thank you for helping me become the person I am today, words cannot express my gratitude for everything you do for me. Thank you to my brother, Ryan Hinds, for keeping me humble and being a great big brother. Thank you to my bonus parents, Melissa Hinds and Marvin Robbins, for loving and supporting me. To my extended family, thank you as well for all of your love and support.

Thank you to both of my undergraduate research mentors from Appalachian State University, Nicholas Shaw and Anthony Calami. You each played a pivotal role in my growth, and gave me the confidence I needed to trust in my abilities. Your guidance, patience, and belief in my potential have made a lasting impact, and I am truly grateful to have had the opportunity to learn from and work alongside you both. I would also like to extend my thanks to Dean Hidas, for being my mentor at Brookhaven National Lab, and teaching me how to code (which I now do everyday!). I am so thankful for all of my wonderful

undergraduate mentors, I would not be here without your belief in me.

Graduate School is not for the faint of heart, and I'm so lucky to have found phenomenal, lasting friendships here. Hannah Berg and Josh Wylie, thank you both for being my first friends at MSU, and the best roommates. We weathered a pandemic, and even worse - subject exams - together. I truly would be lost without you both. Carissa Myers, thank you for being my other-physicist-half. We dragged each other through the trenches (both with classes and graduate organizations), and you have helped make me a better person. Thank you to all my friends - Emily Rowland, Jeremiah Rowland, Bob Klaes, Jamie Kimble, Renee Maring, Brandon Barker, Daniel Lay, Austin Schleusner, David Greene, Kelly Anderson, Brandon Henke, Kelsey Bees - and everyone else (this is a very long list I'm sorry). Thank you for being my community.

To my friends I've collected before starting graduate school, Mel Bogert, Nicole Vetti, Anita Dziedzic, and Sam Sullivan - thank you for grounding me, for reminding me of who I am outside of research, and for being a constant source of laughter, encouragement, and perspective. Your unwavering support, even from afar, has meant more than I can express.

James - my fiancé, my person, my love - thank you for being the calm in the storm. Thank you for loving me through the craziness, and cheers to the start of a new chapter in our lives - one filled with hope, possibility, and everything the future has in store.

Finally, it wouldn't be my dissertation if I didn't include something about running! A lifelong goal of mine is to run a marathon (26.2 miles/ 42.195 km) in every US State. Since starting at Michigan State University in Fall 2019, I spent over 1000 hours running, completed 13 marathons in 8 states and 2 other countries, with a total of 4500 miles (equivalent to: running 200 marathons, 16% of the Earth's circumference, and approximately the distance to run latitudinally across the continental US and back). I've now completed a total of 21

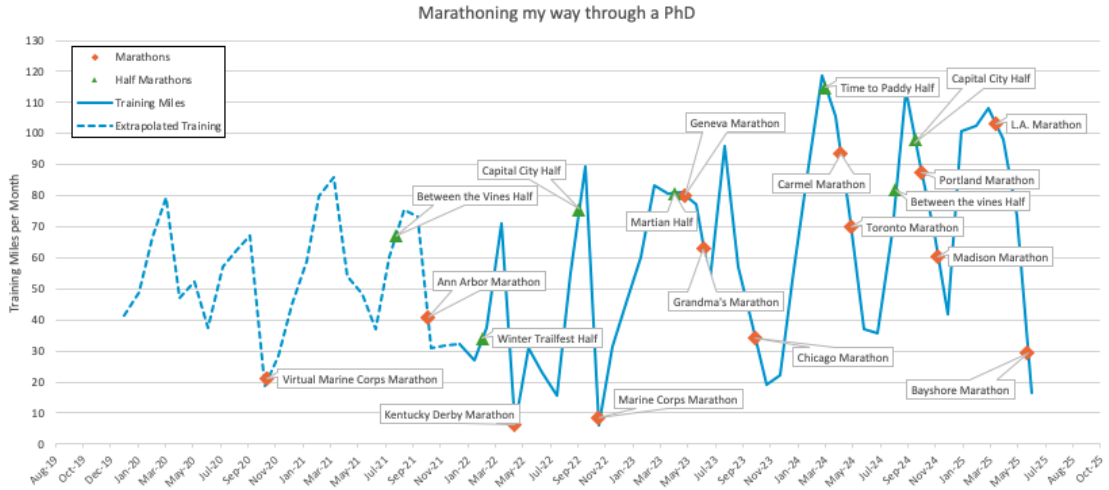


Figure 1: Running miles ran per month during my graduate school time (Aug. 2019 to Jul. 2025). Marathons (orange) and half-marathons (green) are shown. I started using Strava in 2022 so running statistics before that has been extrapolated. Only one virtual race occurring early on due to the COVID Pandemic (shout out to Hannah Berg for biking the race alongside me so I could complete it!).

marathons, 3 ultramarathons, and 16/50 States (and 4 countries). Shout out to my amazing fiancé, James, for crunching the number for me and creating Figure 1!

TABLE OF CONTENTS

Chapter 1. Introduction	1
Chapter 2. Theoretical Framework	4
2.1 The Standard Model of Particle Physics	4
2.1.1 Quantum Field Theory	8
2.1.2 Quantum Electrodynamics	14
2.1.3 Quantum Chromodynamics	15
2.1.4 Electroweak Theory	16
2.1.4.1 Electroweak Unification	17
2.1.4.2 Electroweak Symmetry Breaking and the Higgs Mechanism	18
2.2 Beyond SM Physics	20
2.2.1 Heavy Gauge Bosons	21
2.2.2 Extra Dimension Models	24
Chapter 3. Experimental Apparatus	27
3.1 CERN and the Large Hadron Collider	27
3.2 ATLAS Detector	31
3.3 Coordinate System	33
3.4 Magnet System	33
3.5 Tracking	35
3.5.1 Pixel Detector	36
3.5.2 Semiconductor Tracker (SCT)	37
3.5.3 Transition Radiation Tracker (TRT)	37
3.6 Calorimeters	38
3.6.1 Electromagnetic Calorimeters	41
3.6.2 Hadronic Calorimeters	42
3.7 Muon Spectrometer	43
3.8 Trigger and Data Acquisition	45
Chapter 4. Event Generation, Simulation, and Reconstruction	47
4.1 Event Generation	47
4.2 Event Simulation	49
4.3 Reconstruction	52
4.3.1 Pile-Up	52
4.3.2 Tracks and Vertices	53
4.3.3 Electrons and Photons	54
4.3.4 Muons	56
4.3.5 Jets	58
4.3.5.1 Particle Flow	61
4.3.5.2 Track-CaloClusters	62
4.3.5.3 Unified Flow Objects	62
4.3.6 Missing Transverse Energy	64

4.4	Data Sets and Formats	65
Chapter 5.	$t\bar{t}$ Jet-Tagging Scale Factors	67
5.1	Introduction	67
5.1.1	Jet Substructure Variables	68
5.2	Taggers	73
5.2.1	Truth Information	74
5.2.2	Top Taggers	74
5.2.3	W Taggers	74
5.3	Scale Factor Determination	75
5.3.1	Strategy	75
5.3.2	Systematic Uncertainties	77
5.3.3	Event Selection	79
5.3.4	Results	80
5.3.4.1	Kinematic Variables	81
5.3.4.2	Tagger Performance	88
5.3.4.3	Signal Efficiency and Scale Factors	93
5.4	Summary	98
Chapter 6.	Search for heavy resonances decaying into two SM bosons in semi-leptonic final states	99
6.1	Analysis Overview	99
6.2	Analysis Strategy	101
6.3	Signal Models, Backgrounds, and Data	104
6.3.1	Signal Models	104
6.3.2	Backgrounds	107
6.3.3	Data Samples	108
6.4	Object Selection	109
6.4.1	Large-R Jets	110
6.4.2	Small-R Jets	110
6.4.3	Electrons	111
6.4.4	Muons	111
6.4.5	Missing Transverse Energy	112
6.4.6	Tracks	112
6.4.7	Variable-Radius Track-Jet	113
6.4.8	Flavor Tagging	113
6.4.9	Vector-Boson Tagging	114
6.4.10	Overlap-Removal	114
6.5	Event Selection	117
6.5.1	Preselection	118
6.5.2	Jet Requirements	118
6.5.2.1	Resolved Regime	118
6.5.2.2	Merged Regime	119
6.5.3	Lepton Requirements	119
6.5.3.1	0-Lepton Optimization and Selection	120

6.5.3.2	1-Lepton Selection	126
6.5.3.3	2-Lepton Selection	127
6.5.4	Multi-Class Classifier (MCT)	128
6.6	Systematic Uncertainty	128
6.6.1	Experimental Uncertainties	129
6.6.2	Modeling Uncertainties	131
6.6.2.1	$t\bar{t}$ and single-top Modeling	132
6.6.2.2	V + jets Modeling	151
6.6.2.3	Minor Background	151
6.7	Statistical Interpretation	151
6.7.1	Binned Maximum Likelihood Fit	152
6.7.2	Test Statistic	153
6.8	Results	155
6.8.1	Pre-Fit Validation	156
6.8.2	Post-Fit Validation	164
6.8.2.1	Control Regions	164
6.8.2.2	Signal Regions	167
6.8.3	Systematic Constraints	172
6.8.4	Exclusion Limits	176
6.8.4.1	HVT $W' \rightarrow WZ$	176
6.8.4.2	HVT $W' \rightarrow WH$	177
6.8.4.3	HVT $Z' \rightarrow WW$	178
6.8.4.4	HVT $Z' \rightarrow ZH$	179
6.8.4.5	HVT $VV+VH$ Combination	180
6.8.4.6	$G_{KK} \rightarrow WW + ZZ$	181
6.8.4.7	$R \rightarrow WW + ZZ$	182
6.8.4.8	Summary	183
6.8.5	Comparison of the limits	184
6.9	Summary	186
Chapter 7. Conclusion		188
BIBLIOGRAPHY		190
APPENDIX A. $t\bar{t}$ SF tables		204
APPENDIX B. Previous Cuts for $VV+VH$		207
APPENDIX C. Data/MC Plots		209
C.0.1	Modelling in 1-lepton Control regions	209
C.0.2	Modelling in 2-lepton Control regions	210
C.0.3	Post-Fit Validation in Control Regions for 1-Lepton and 2-Lepton Channels	219
C.0.4	Post-Fit Validation in Signal Regions for 1-Lepton and 2-Lepton Channels	223

C.0.4.1	HVT $W^{\prime} \rightarrow WZ$	224
C.0.5	More Systematic Constraints	228

Chapter 1. Introduction

Reflecting on introductory chemistry courses from high school or college, one might recall studying the Periodic Table of Elements and learning that matter consists fundamentally of molecules and atoms, which themselves can be further broken down into distinct elemental substances. The realization that the visible universe is composed of these fundamentally “invisible” elements prompts a deeper question: what constitutes the elements themselves? The discipline of particle physics addresses precisely this question by investigating the fundamental constituents of matter. Within particle physics, the term particle refers explicitly to “a minute quantity or fragment,” [1] denoting the most elementary units of matter. Taking helium as a representative example, this element can be broken down into protons, neutrons, and electrons, with protons and neutrons further divisible into more fundamental constituents, namely quarks and gluons.

At first glance, these concepts might seem abstract; however, empirical evidence has firmly established their validity. In the late 19th century, J.J. Thomson experimentally demonstrated the existence of electrons through his work with cathode rays [2]. Subsequent pioneering experiments by Ernest Rutherford and James Chadwick led to the discoveries of the proton [3] and neutron [4], respectively. Later, in the mid-20th century, experimental results [5] revealed that protons and neutrons themselves are composite particles composed of even more fundamental constituents, known as quarks and gluons. Collectively, these experimental breakthroughs have significantly advanced the field of particle physics, transforming it from purely theoretical conjectures to empirically validated scientific knowledge. Such experiments have both confirmed theoretical predictions and simultaneously guided theorists toward refining and enhancing their models, fostering a dynamic interplay between

theory and experiment.

Today, the Standard Model (SM) [6] provides the most comprehensive and accurate description of the known universe at its smallest and most fundamental scales. To an unfamiliar audience, the SM might superficially resemble a “Periodic Table” of subatomic particles; however, in practice, it represents a sophisticated mathematical framework integrating three fundamental interactions: the electromagnetic force, governing phenomena such as light and interactions among charged particles; the weak nuclear force, which mediates processes including radioactive decay; and the strong nuclear force, responsible for binding protons and neutrons within atomic nuclei. The most recent significant advancement within this theoretical framework was the 2012 experimental discovery of the Higgs boson, responsible for the mass generation mechanism of fundamental particles, achieved by the ATLAS [7] and CMS [8] experiments at CERN.

However, the narrative of particle physics does not conclude with the SM; rather, it serves as the starting point for deeper exploration. While the SM has described the outcomes of major experiments with remarkable precision and accuracy, it remains inadequate for fully addressing several critical phenomena. Notable unresolved issues include the observed matter-antimatter asymmetry of the universe, the fundamental nature and composition of dark matter and dark energy, and the inability of the SM to reconcile or incorporate gravity, particularly the significant discrepancy in its relative strength compared to other fundamental forces. Therefore, it would be imprecise to characterize the SM as incorrect; rather, it is more accurately considered incomplete. Extensions or modifications to the SM intended to address these gaps are collectively termed Beyond the Standard Model (BSM) physics. This dissertation presents the methodology and results of a BSM search performed using data collected by the ATLAS experiment, derived from proton-proton collisions at the Large

Hadron Collider (LHC) at a center-of-mass energy of 13 TeV.

Chapter 2. Theoretical Framework

To understand physics is to try to understand how the world works. That elusive goal is attempted in this section, where first the Standard Model of Particle Physics is introduced, which gives the current understanding of the observed world at its smallest, most fundamental scale, followed by the BSM, which attempts to probe in areas that are not currently understood and represented by the SM.

2.1 The Standard Model of Particle Physics

The Standard Model [9] was developed in the mid 20th century, and describes the forces and interactions between the smallest building blocks of nature (as we currently know it). These fundamental building blocks are referred to as elementary particles, and can be separated into two groups based on their spin ¹: fermions (half-interger-spin particles) and bosons (interger-spin particles). They can also be categorized by their interactions with the known forces: electromagnetic, weak, and strong. Gravity is currently not described by the SM due to the incompatibility between general relativity and quantum mechanics. Fermions can be further classified into two categories: quarks and leptons. Quarks are the fundamental constituents of hadrons, interacting through the strong nuclear force described by Quantum Chromodynamics (QCD) via the exchange of gluons. They form baryons (such as protons and neutrons, made up of three quarks) and mesons (such as pions, composed of a quark-antiquark pair), with their interactions mediated by the color charge, a unique property carried only by quarks. Leptons, unlike quarks, do not carry color charge and therefore do

¹Spin is an intrinsic form of angular momentum carried by elementary particles, independent of their physical size or spatial extent.

not participate in the strong nuclear force. They include the electron e , muon μ , tau τ , and their corresponding neutrinos (electron neutrino ν_e , muon neutrino ν_μ , tau neutrino ν_τ), each existing as free particles that interact through the electromagnetic and weak forces, making them essential components of atomic structure and particle interactions. Bosons are classified based on their intrinsic spin, which can either be a scalar (spin-0) or a vector (spin-1) depending on their quantum properties. Scalar bosons, like the Higgs boson, have no intrinsic directional properties and are described by a single value at each point in space (they do not carry any angular momentum). In contrast, vector bosons, such as the photon, W, and Z bosons, have spin-1, giving them a directional component that allows them to mediate forces with a well-defined orientation in space. This distinction significantly affects how these particles interact with matter and influence the structure of the quantum fields they represent. Figure 2.1 gives an overview of the all of the SM particles.

Standard Model of Elementary Particles

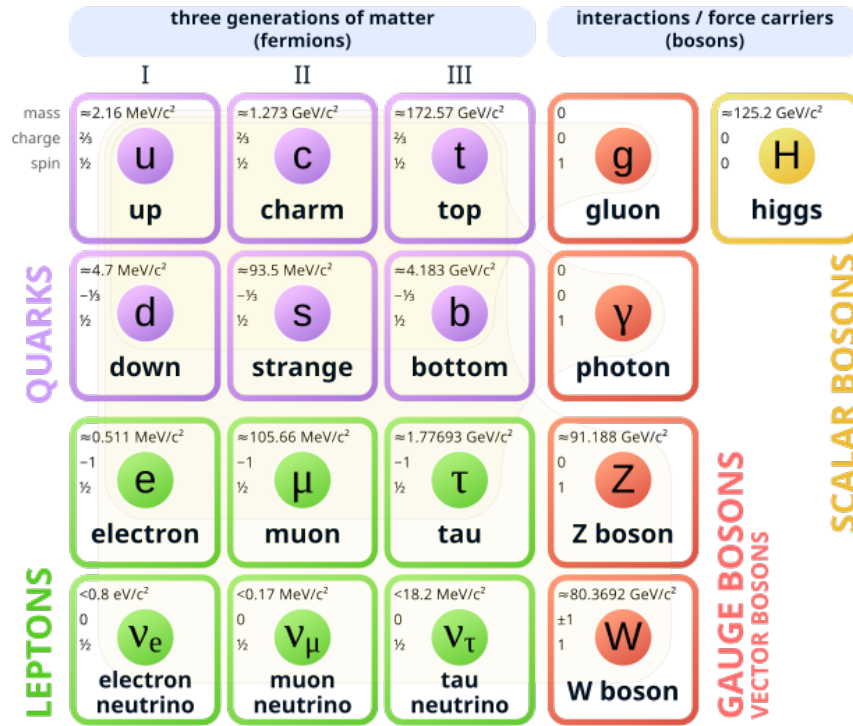


Figure 2.1: Diagram of the SM, containing six quarks and six leptons in three generations, four vector bosons, and one scalar boson. [10]

Fermions possess half-integer spin, obey Fermi-Dirac statistics [11], and function as the building blocks of matter. The SM contains 12 spin-1/2 particles organized into three generations, with each generation differing only by their mass (except for neutrinos, which are assumed massless by the SM). Each generation contains:

- one electrically charged lepton (e^- , μ^- , τ^-)
- one neutral lepton, or neutrino, (ν_e , ν_μ , ν_τ)
- one up-type quark (u , c , t)
- one down-type quark (d , s , b)

Additionally, for fermions, each matter particle has an antimatter counterpart, resulting in 6 antileptons and 6 anti-quarks (for example, the anti-matter counterpart of the up quark, u , is denoted as \bar{u}). These antimatter particles have properties which are similar to their particle counterparts, but oftentimes opposite sign quantum numbers.

Quarks, governed by the strong force, do not exist freely in nature but are instead confined within composite particles. They are most commonly observed as quark-antiquark pairs, known as mesons, or as bound states of three quarks (or three antiquarks), known as baryons. The formation of baryons is only possible due to the presence of the color charge. Without it, the total wavefunction of the three constituent quarks would be antisymmetric under exchange, and any attempt to place two identical fermions in the same quantum state would result in a wavefunction amplitude of zero. This is a direct consequence of the Pauli Exclusion Principle [12], which asserts that no two fermions can simultaneously occupy the same quantum state. The color degree of freedom resolves this by allowing the quarks to differ in color, thereby enabling the construction of an overall antisymmetric wavefunction and allowing baryons to exist as physically realizable states.

Scalar and vector particles have integer spin, adhere to Bose-Einstein statistics [13], and serve as force mediators. In the SM, each fundamental force is mediated by bosons. The electromagnetic force, which affects charged particles, is mediated by the photon. Photons are massless and enable phenomena such as electricity, magnetism, and light. The weak force, responsible for processes like beta decay in nuclear reactions, is mediated by the W^\pm and Z^0 bosons. These particles are much heavier than protons or neutrons and are responsible for the weak interactions that change the flavor of quarks and influence the decay of particles. The strong force, which binds quarks together inside baryons and mesons, is mediated by the gluons. Gluons are massless and carry the “color charge” associated with the strong

interaction. They act to keep quarks confined within hadrons and govern the strong force between quarks. While gravity in the SM is not accounted for by any known mediator boson, theoretical physics suggests the existence of a graviton, which would be a massless particle that mediates the gravitational force. However, this particle has not yet been observed. Unlike fermions, a boson's wavefunction is symmetric, allowing multiple identical bosons to occupy the same quantum state. Among these, vector bosons are typically known as gauge bosons. Notably, the Higgs boson is the only scalar boson in the SM, and will be discussed further in Subsection 2.1.4.2.

2.1.1 Quantum Field Theory

Quantum field theory (QFT) [14, 15, 16, 17] is a mathematical formalism used to describe our current understanding of the physics of particles, by combining classical field theory, relativity, and quantum mechanics; where here particles are quantized excitations of quantum fields that permeate all spacetime. The evolution of quantum fields is expressed using Lagrangian mechanics and Hamilton's principle of least action. The Lagrangian, L , contains the kinetic energy of a system, T , minus the potential energy, V , and is time-dependent. However, in QFT, it is more appropriate to use field variables (ϕ_i) that are a function of a spacetime 4-vector, $\phi_i(x^\mu)$. This transformation of variables transitions the Lagrangian into the Lagrangian Density: $L(q_i, \dot{q}_i, t) \rightarrow \mathcal{L}(x^\mu, \phi_i, \delta_\mu \phi_i)$ (which is often just referred to as the Lagrangian for simplicity). If the Lagrangian only contains kinetic terms with no interaction components, or potentials, it is considered a free-field Lagrangian. This formalism can then be applied to different types of fields which correspond to particles of various spins, such as a scalar field ϕ (spin-0), a vector field A (spin-1), or the spinor fields ψ (spin-1/2). Examples of the corresponding particles to these fields are the Higgs boson for the scalar field, gauge

bosons for the vector field, and fermions for the spinor fields, and their Lagrangian densities are

$$L_0 = \frac{1}{2}\partial_\mu\phi\partial^\mu\phi - \frac{1}{2}m^2\phi^2, \quad (2.1)$$

$$L_1 = -\frac{1}{4}F_{\mu\nu}F^{\mu\nu} + \frac{1}{2}m^2A^\mu A_\mu, \quad (2.2)$$

$$L_{\frac{1}{2}} = i\bar{\psi}\gamma^\mu\partial_\mu\psi - m\bar{\psi}\psi, \quad (2.3)$$

where $F_{\mu\nu} = \partial_\mu A_\nu - \partial_\nu A_\mu$ represents the field strength tensor and γ^μ represent the Dirac matrices. Hamilton's principle of least action, S , model the dynamics of the fields

$$S(q_i) = \int L(q_i, \dot{q}_i, t) dt \quad (2.4)$$

where q_i is the generalized spatial coordinates, and \dot{q}_i is its time derivative. When S evolves such that the action is minimized, $\delta S = 0$, the resulting Euler-Lagrange equation of motion

$$\frac{d}{dt} \left(\frac{\delta L}{\delta \dot{q}_i} \right) = \frac{\delta L}{\delta q_i} \quad (2.5)$$

is achieved. For each of the free-fields described above, this results in equations of motion. For scalar fields, the Klein-Gordon equation,

$$\partial_\mu\partial^\mu\phi + m^2\phi = 0 \quad (2.6)$$

The Proca equation for vector fields,

$$\partial_\mu F^{\mu\nu} + m^2 A^\nu = 0 \quad (2.7)$$

which for massless fields, such as photons, simplifies to the Maxwell equation $\partial_\mu F^{\mu\nu} = 0$.

Last but not least, the Dirac equation for spinor fields,

$$i\gamma^{mu}\partial_{mu}\psi - m\psi = 0 \quad (2.8)$$

Moreover, describing the entire SM into one compact Lagrangian ² is possible with Yang-Mills theory [18]:

$$L_{\text{SM}} = -\frac{1}{4}G_{\mu\nu}^a G^{\mu\nu a} - \frac{1}{4}W_{\mu\nu}^a W^{\mu\nu a} - \frac{1}{4}B_{\mu\nu} B^{\mu\nu} + |D_\mu\phi|^2 + \bar{\psi}D_\mu\psi - V(\phi) + \lambda\bar{\psi}\psi\phi \quad (2.9)$$

Where each term describes part of the SM described above. The $G_{\mu\nu}^a G^{\mu\nu a}$, $W_{\mu\nu}^a W^{\mu\nu a}$, and $B_{\mu\nu} B^{\mu\nu}$ components describe the strong, weak, and electromagnetic forces, respectively. The $|D_\mu\phi|^2$ component describes the Higgs kinetic terms, where D_μ refers to the gauge covariant derivative and ϕ is the complex Higgs scalar field. Similarly, the $\bar{\psi}D_\mu\psi$ component describes the Higgs electromagnetic terms. The Higgs potential is contained in the $V(\phi)$ term, and finally, the $\lambda\bar{\psi}\psi\phi$ term is used to give all quarks and leptons mass.

An important requirement of the SM Lagrangian is that it must preserve the internal and external symmetries; or, respect the principle of global and local gauge invariance as well as Lorentz invariance. Group theory is used to describe the gauge invariance of the

²Fun fact, CERN compacted the Lagrangian so efficiently that you can buy it on a mug!

SM Lagrangian, providing the mathematical framework for the symmetries that govern the fundamental interactions. Each gauge symmetry in the SM is associated with a Lie group whose generators correspond to conserved currents and charges via Noether’s theorem [19]. Specifically, the SM is built upon the gauge group

$$SU(3)_C \times SU(2)_L \times U(1)_Y \tag{2.10}$$

where each factor corresponds to one of the fundamental forces: quantum chromodynamics (QCD) for the strong interaction ($SU(3)_C$), and the electroweak theory for the unification of the weak ($SU(2)_L$) and electromagnetic interactions ($U(1)_Y$). The requirement that the SM Lagrangian remains invariant under local transformations of this gauge group dictates the form of the interaction terms and the introduction of gauge bosons, which mediate the forces. The unitary group $U(n)$ consists of all $n \times n$ complex matrices that preserve vector norms under transformation, while the special unitary group $SU(n)$ is the subgroup of $U(n)$ with determinant equal to 1, ensuring conservation laws and the absence of unphysical degrees of freedom in gauge theories.

The subscripts L and R indicate chirality, where L is for *left-handed* (negative) chirality and R is for *right-handed* (positive) chirality. This distinction is especially useful for electroweak theory, where the combination of left- and right-hand spinors into four-component objects (Dirac spinors) describe both particle and antiparticle degrees of freedom. In the context of L_{SM} , the elements of the $SU(2)_L$ act only on the left-handed component of the Dirac spinor. The three generators of $SU(2)_L$ are associated with the weak isospin quantum number. The subscript C stands for “color”, referring to the color charge carried by quarks and gluons in QCD in the $SU(3)$ group. This group has eight generators corresponding

to the eight gluon fields, and quarks transform under its fundamental representation, while gluons transform under the adjoint.

In the SM, representations describe how different particles transform under symmetry groups like $SU(3)_C$, which governs the strong force. Quarks transform under the fundamental representation of $SU(3)_C$, Gluons, the force carriers of the strong interaction, are different. They transform under what is called the adjoint representation of $SU(3)_C$. Instead of having a single color, each gluon carries a combination of a color and an anti-colorlike red-anti-blue or green-anti-red. Because of this, gluons can interact not just with quarks, but also with each other. This self-interaction is a special feature of non-Abelian gauge theories like QCD and is one reason why the strong force behaves very differently from the electromagnetic force (which has a single, non-interacting photon).

The $U(1)_Y$ factor corresponds to weak hypercharge, with Y representing the hypercharge quantum number. Unlike $SU(2)_L$, this group acts on both left- and right-handed fermions, and the assignment of hypercharge values determines the coupling of particles to the corresponding gauge field.

A foundational computation in QFT involves the transition of an initial set of particles into a final set of particles through scattering. Using Fermi's Golden Rule, the differential probability of the scattering from initial state particles $|i\rangle$ to final state particles $|f\rangle$ is

$$dP = \frac{|\langle f|S|i\rangle|^2}{\langle f|f\rangle\langle i|i\rangle} d\Pi, \quad (2.11)$$

where S is the scattering matrix, and $d\Pi$ is the Lorentz invariant phase-space of the states

$$d\Pi = \prod_f \int \frac{d^3 p_f}{(2\pi)^3} \frac{1}{E_f} (2\pi)^4 \delta^4 \left(\sum p_i - \sum p_f \right) \quad (2.12)$$

where \prod_f is the product over all the final states f , p_f is the final state momenta, E_f is the final state energy, and $\sum p_i$ and $\sum p_f$ represents the momentum sum over all initial and final state particles, respectively. The S -matrix can be broken down as such:

$$\langle f|S|i\rangle = \langle f|I|i\rangle + (2\pi)^4 \delta \left(\sum p \right) \langle f|\mathcal{M}|i\rangle, \quad (2.13)$$

Where I is the identity matrix, and thus $\langle f|I|i\rangle$ showcases the case of no scattering, and \mathcal{M} is the the scattering amplitude (thus $\langle f|\mathcal{M}|i\rangle$ is the matrix element for scattering states). To calculate the scattering probability, or the cross-section σ , eq. (2.13) is combined with eq. (2.11). The cross-section is used both by experimentalists (to measure) and theorists (to calculate). In a simple case where there are two incoming particles X_1 and X_2 with energies E_1 and E_2 that scatter into state Y , the cross section is

$$\sigma(X_1 X_2 \rightarrow Y) = \int \frac{|\mathcal{M}_{X_1 X_2 \rightarrow Y}|^2}{2E_1 E_2 v} d\Pi, \quad (2.14)$$

Here, $|\mathcal{M}_{X_1 X_2 \rightarrow Y}|^2$ is the matrix element for the interaction, and v is the relative velocity between the particles³. The resulting decay rate, Γ , of particle X to final states Y can then be calculated as

$$\Gamma(X \rightarrow Y) = \frac{|\mathcal{M}_{X \rightarrow Y}|^2}{2m_X} d\Pi, \quad (2.15)$$

³The relative velocity in this two-particle scattering is given by: $v_{\text{rel}} = \frac{\sqrt{(p_1 \cdot p_2)^2 - m_1^2 m_2^2}}{E_1 E_2}$

Where m_X is the mass of particle X. The total decay width (Γ) is the sum of all partial decays (Γ_i) and is inversely related to its lifetime. The branching ratio, or fraction, (B_i) of a specific decay mode is the fraction of decays occurring via that mode, given by $B_i = \frac{\Gamma_i}{\Gamma}$. The sum of all branching ratios equals 1.

2.1.2 Quantum Electrodynamics

Quantum Electrodynamics (QED) [20] is the theory of electromagnetism describing the interactions between charged fermions and the photon (massless, spin-0 field). It is an Abelian theory based on the symmetry group U(1). For a Dirac field, the Lagrangian is

$$L = \bar{\psi}(i\gamma_\mu\partial^\mu - m)\psi \quad (2.16)$$

which is invariant under global U(1) transformations, $\psi \rightarrow \psi = e^{ig\theta(x)}\psi$. However, the derivative does not transform the same way. Thus to make the theory invariant under such transformations, the covariant derivative is used in lieu of the partial derivative, $\partial_\mu \rightarrow D_\mu$, and can be defined as

$$D_\mu\psi = (\partial_\mu - igA_\mu)\psi \quad (2.17)$$

Where A_μ is an additional spin-1 vector field (also known as a gauge field), and g is the coupling strength between A_μ and ψ . By including this new gauge field in combination with the free-field Lagrangian densities of vector fields (eq. (2.2)) and spinor fields (eq. (2.3)), the resulting Lagrangian is invariant under U(1) symmetry transformations. Additionally, in QED, the mass component of A_μ set to zero, thus corresponding to the electromagnetic four-vector potential that mediates the electromagnetic interaction. By letting g represent

the elementary electric charge e , resulting Lagrangian can therefore be written as

$$L_{\text{QED}} = -\frac{1}{4}F_{\mu\nu}F^{\mu\nu} + i\bar{\psi}\gamma^\mu\partial_\mu\psi - e\bar{\psi}\gamma^\mu A_\mu\psi - m\bar{\psi}\psi. \quad (2.18)$$

2.1.3 Quantum Chromodynamics

Quantum Chromodynamics (QCD) [21, 22] is the quantum field theory describing the strong interaction, based on the non-abelian gauge group $SU(3)_C$, where quarks interact via the exchange of color-charged gluons. Quark field spinors, $\psi_{q,a}$, are used to represent quarks, with q indicating flavor (color or anti-color) and c the color-index (ranging from $a = 1$ to $N_C = 3$, representative of the three colors: red, green, or blue). The gluon vector field consisting of eight components A_μ^C , where the index C , ranging from 1 to $N_C^2 - 1 = 8$, labels the eight generators of the $SU(3)_C$ gauge group, and the index μ denotes the spacetime component of the field, corresponding to the four directions in spacetime: one time component ($\mu = 0$) and three spatial components ($\mu = 1, 2, 3$). Together, these make up the QCD Lagrangian,

$$L_{\text{QCD}} = \sum_q \bar{\psi}_{q,a} \left(i\gamma^\mu\partial_\mu\delta_{ab} - g_s\gamma^\mu t_{ab}^C A_\mu^C - m_q\delta_{ab} \right) \psi_{q,b} - \frac{1}{4}G_{\mu\nu}^A G^{A\mu\nu} \quad (2.19)$$

where m_q is the mass, γ^μ are the Dirac γ -matrices, and repeated indices are summed over. Under the $SU(3)_C$ color symmetry, gluons belong to the adjoint representation, and the eight matrices t_{ab}^C are the generators. The field tensor $G_{\mu\nu}^A$ is given as

$$G_{\mu\nu}^A = \partial_\mu A_\nu^A - \partial_\nu A_\mu^A - g_s f_{ABC} A_\mu^B A_\nu^C \quad (2.20)$$

where f_{ABC} are structure constants from the $SU(3)$ group.

The QCD coupling constant g_s and the strong coupling constant α_s are closely related but serve different purposes in QCD. The parameter g_s is the fundamental gauge coupling that appears in the L_{QCD} and governs the strength of the interaction between quarks and gluons at the theoretical level. In contrast, α_s is the dimensionless version of the strong coupling, defined as $\alpha_s = \frac{g_s^2}{4\pi}$, and is commonly used in calculations involving Feynman diagrams and scattering amplitudes. While g_s sets the interaction strength in the field equations, α_s is more directly tied to measurable quantities and evolves with energy scale; a phenomenon known as running of the coupling,⁴ which leads to asymptotic freedom at high energies. Conversely, at low energy scales or larger distances, the interaction strength grows and leads to quark confinement. Due to this, quarks and gluons cannot be observed bare or by-themselves as free particles, but rather as a formation of colorless bound states called hadrons (mesons or baryons, as described before).

2.1.4 Electroweak Theory

The weak nuclear force, or weak interaction, is one of the four fundamental forces and is responsible for changing the flavor of elementary particles, allowing for processes like beta decay, where a neutron transforms into a proton, electron, and anti-electron-neutrino [23]. The weak interaction is distinct from QCD and QED in several ways, most notably in its massive mediators, the W^\pm and Z bosons, which contrast with the massless photon and gluon. It couples predominantly to left-handed particles and right-handed antiparticles, with the W^\pm bosons coupling exclusively in this manner, while the Z boson also has a smaller coupling to right-handed particles. This chiral preference leads to the violation of parity, a

⁴Sadly, not the kind of running (marathons) this author enjoys.

unique feature of the weak force. Additionally, the weak interaction can induce flavor and generation changes in fermions, enabling processes like radioactive decays. The electroweak theory [24] explains these properties through the Higgs mechanism and spontaneous symmetry breaking [25, 26, 27, 28], which gives mass to the weak force mediators and accounts for the interaction's chiral nature.

2.1.4.1 Electroweak Unification

The weak interaction does not manifest as a gauge symmetry on its own, but rather when unified with the electromagnetic interaction; and this unification has gauge symmetries based on the gauge group $SU(2)_L \times U(1)_Y$ (requiring the invariance of the Lagrangian under local gauge transformations of these groups). Electroweak theory divides SM fermions into left-hand doublets

$$\Psi_i = \begin{pmatrix} \nu_i \\ l_i^- \end{pmatrix} = \begin{pmatrix} u_i \\ d_i^- \end{pmatrix} \quad (2.21)$$

where $d \equiv \sum_j V_{ij} d_j$ (V is the Cabibbo-Kobayashi-Maskawa (CKM) mixing matrix [29]) and right-hand singlets. The conserved quantity associated with the $SU(2)_L$ symmetry is the weak isospin, T . The members of the L doublet are distinguished by the isospin's third component, T_3 , with values of $+1/2$ for neutrinos and the u , c , and t quarks, and $-1/2$ for the charged leptons and the d , s , and b quarks. The three gauge bosons associated with the three generators of this group are the W^1 , W^2 , and W^3 . The right-handed singlets remain invariant under $SU(2)_L$ transformations; however, both the doublets and singlets transform under $U(1)_Y$. Here, the conserved quantity is the weak hypercharge Y and the corresponding gauge boson associated with this symmetry is denoted as B . The actual physical gauge bosons

(mentioned in the Section 2.1) are linear combinations of W^1 , W^2 , and W^3 . The W^+ and W^- bosons are combinations of W^1 and W^2

$$W_\mu^\pm = \frac{1}{\sqrt{2}} (W_\mu^1 \pm iW_\mu^2) \quad (2.22)$$

and the Z boson and the photon are generated by the combination of B and W^3

$$\begin{pmatrix} A_\mu \\ Z_\mu \end{pmatrix} = \begin{pmatrix} \cos \theta_W & \sin \theta_W \\ -\sin \theta_W & \cos \theta_W \end{pmatrix} \begin{pmatrix} B_\mu \\ W_\mu^3 \end{pmatrix} \quad (2.23)$$

where μ indicates the spacetime four-vector (0 for time, and 1, 2, 3 for the spatial directions). The angle θ_W is the weak mixing angle, dependent on the ratio of masses between the W boson and the Z boson ($\cos(\theta_W) = m_W/m_Z$) or the coupling constants for the two gauge groups: g for $SU(2)_L$ and g' for $U(1)_Y$ (with $\tan(\theta_W) = g'/g$). While the photon remains massless, the gauge bosons W^\pm and Z do not, which implies that the electroweak symmetry must be broken. The Higgs mechanism offers the required framework to resolve these problems, shedding light on the origin of particle masses during electroweak symmetry breaking (EWSB).

2.1.4.2 Electroweak Symmetry Breaking and the Higgs Mechanism

The Higgs mechanism explains the spontaneous breaking of electroweak symmetry [30], providing the framework for mass generation of weak bosons and fermions. Proposed by Brout and Englert [25], Higgs [26], and Guralnik, Hagen, and Kibble [27], it predicts the existence of the Higgs field, a complex doublet of scalar fields that interacts with particles to give them mass:

$$H = \begin{pmatrix} \phi_1 + i\phi_2 \\ \phi_3 + i\phi_4 \end{pmatrix} = \begin{pmatrix} \phi^+ \\ \phi_0 \end{pmatrix} \quad (2.24)$$

where the subscripts on ϕ_+ and ϕ_0 denote the electric charge of the respective components. The Higgs terms in the Lagrangian can be written as

$$\mathcal{L}_H = |D_\mu H|^2 + \mu^2 H^\dagger H - \lambda (H^\dagger H)^2 \quad (2.25)$$

with $D_\mu = \partial_\mu - igW_\mu^a \tau^a - \frac{1}{2}ig'B_\mu$ as the covariant derivative (and τ^a the $SU(2)$ generators analogous to Pauli matrices). The Higgs potential can then be re-written using the latter two terms in equation L_H as

$$V(H) = -\mu^2 |H|^2 + \lambda |H|^4 \quad (2.26)$$

with λ as the (dimensionless) self-coupling constant, and μ as the mass parameter. If $\mu < 0$ then it gives rise to a non-zero vacuum expectation value (vev) of $\nu/\sqrt{2} = \mu/\lambda$ ($\nu \approx 256$ GeV [31]), which breaks part of the Electroweak gauge symmetry. After electroweak symmetry breaking, the Lagrangian for fermion fields can be written in a form that includes the Yukawa interaction, which couples fermions to the Higgs field and gives them mass. The general structure of the fermion part of the Lagrangian is:

$$\begin{aligned}
\mathcal{L}_F = & \sum_i \bar{\psi}_i \left(i\phi - m_i - \frac{m_i H}{v} \right) \psi_i \\
& - \frac{g}{2\sqrt{2}} \sum_i \bar{\psi}_i \gamma^\mu (1 - \gamma^5) (T^+ W_\mu^+ + T^- W_\mu^-) \psi_i \\
& - e \sum_i Q_i \bar{\psi}_i \gamma^\mu \psi_i A_\mu \\
& - \frac{g}{2 \cos \theta_W} \sum_i \bar{\psi}_i \gamma^\mu (g_i^V - g_i^A \gamma^5) \psi_i Z_\mu
\end{aligned} \tag{2.27}$$

The fermion fields in the Lagrangian consist of left-handed (ψ_L) and right-handed (ψ_R) components, with the covariant derivative ($D_\mu D^\mu$) accounting for their interactions with the gauge bosons. The Yukawa couplings (y_u , y_d , and y_ℓ) couple the fermions to the Higgs field, with the left-handed quark and lepton doublets (Q_L and L_L) interacting with the Higgs field (ϕ and $\tilde{\phi}$) to give mass to the fermions after symmetry breaking. These interactions lead to mass terms for the fermions. The boson masses are introduced through the expansion of the covariant derivative term of the electroweak Lagrangian ($|D_\mu H|^2$).

2.2 Beyond SM Physics

The SM of particle physics provides a remarkably successful framework for describing the known fundamental particles and their interactions through the electromagnetic, weak, and strong nuclear forces. However, it is widely recognized as incomplete, as it leaves several key phenomena and observations in nature unexplained, motivating a wide range of BSM theories. These BSM models aim to address gaps in the SM, including the hierarchy problem [32] (why gravity is so much weaker than the other fundamental forces), the nature of

dark matter [33] and dark energy [34] (which together make up about 95% of the Universe’s energy density [35]), and the matter-antimatter asymmetry observed in the Universe [36] (why the Universe is made mostly of matter despite theoretical predictions of equal amounts of matter and antimatter).

One common feature of many BSM theories is the prediction of new, heavy, spin-1 gauge bosons. These hypothetical particles, often referred to as Z' or W' bosons, could provide insight into the nature of electroweak symmetry breaking or the potential unification of forces at high energies. The ATLAS detector at CERN is particularly well-suited for searching for these particles, as it can probe the high-energy scales where such new phenomena are expected to manifest. These gauge bosons will be further explored in Subsection 2.2.1.

Additionally, some BSM models propose the existence of extra spatial dimensions as a potential solution to the hierarchy problem. For example, the Randall-Sundrum (RS) model introduces a warped extra dimension to explain why gravity appears so much weaker than the other fundamental forces. This model predicts the existence of a spin-2 graviton (a hypothetical quantum of the gravitational field) and a spin-0 radion (a scalar particle associated with the size of the extra dimension). These particles, along with the theoretical framework of the RS model, will be discussed in Subsection 2.2.2.

Together, these BSM theories represent ambitious attempts to extend the SM and provide a more complete understanding of the fundamental structure of the Universe.

2.2.1 Heavy Gauge Bosons

A Heavy Vector Triplet (HVT) [37] model, based on a simplified Lagrangian [38], is employed to interpret the results of resonance searches. The model introduces three new gauge bosons, W'^{\pm} and Z' , which are assigned to the adjoint representation of $SU(2)_L$, forming a weak-

isospin triplet with a hypercharge $Y=0$. The fields corresponding to these new gauge bosons are labeled V_a , with $a = 1, 2, 3$, where each component of the triplet represents one of the new gauge bosons. Probing the different coupling strengths of those states to quarks, leptons, vector bosons, and Higgs bosons can be showed in the context of the Lagrangian:

$$\begin{aligned}
\mathcal{L}_V = & -\frac{1}{4}D_\mu V_\nu^a D^\mu V^{\nu a} + \frac{m_V^2}{2}V_\mu^a V^{\mu a} \\
& + i g_V g_H V_\mu^a H^\dagger \tau^a \overleftrightarrow{D}^\mu H + \frac{g^2}{g_V^2} g_F V_\mu^a J_F^{\mu a} \quad (2.28) \\
& + \frac{g_V}{2} g_{VVV} \epsilon_{abc} V_\mu^a V_\nu^b D^\mu V^{\nu c} + g_V^2 g_{VVHH} V_\mu^a V^{\mu a} H^\dagger H - \frac{g}{2} g_{V VW} \epsilon_{abc} W_\mu^a V_\mu^b V_\nu^c
\end{aligned}$$

The parameter g_V defines the relative strength of the interactions between the new vector bosons, while g represents the $SU(2)_L$ gauge coupling. The dimensionless factor g_H regulates the interactions of the vector bosons with both the SM vector bosons and the Higgs field. On the other hand, g_F characterizes the direct coupling of the vector bosons to fermions. The interaction between the vector bosons and the SM Higgs and weak vector bosons is determined by the product $g_V g_H$, whereas the coupling between the vector bosons and SM fermions is expressed as $\frac{g^2 g_F}{g_V}$. The parameters g_{VVV} , g_{VVHH} , and $g_{V VW}$ do not contribute to V decays or single production processes, and thus can be disregarded, and rather g_F , g_H , and m_V can be used.

Going line by line through eq. (2.28), the first line contains the kinetic and mass term of the V-field, as well as its coupling to the W/Z bosons through the covariant derivatives

$$D_\mu V_\nu^a = D_\mu V_\nu^a - D_\nu V_\mu^a, \quad D_\mu V_\nu^a = \partial_\mu V_\nu^a + g \epsilon^{abc} W_\mu^b V_\nu^c \quad (2.29)$$

where ϵ^{abc} is the Levi-Civita symbol. The second line provided the interaction of V with the Higgs boson (eq. (2.30)) and the left-handed fermions (eq. (2.31)).

$$iH^\dagger \tau^a \overleftrightarrow{D}^\mu H = iH^\dagger \tau^a D^\mu H - iD^\mu H^\dagger \tau^a H \quad (2.30)$$

$$J_F^{\mu a} = \sum_f \bar{f}_L \gamma^\mu \frac{\sigma^a}{2} f_L \quad (2.31)$$

There are variations, or benchmark models, of the basic HVT framework, each offering distinct mechanisms for the interactions of a new vector triplet of gauge bosons. *Model A* is the minimal version, where the vector triplet couples simply to the SM fields, including the Higgs and fermions, and its mass is generated through the Higgs mechanism. In this model, g_V is fixed to 1, and g_H is represented as $-g^2/g_V^2$. *Model B* extends this by introducing additional couplings or symmetries, allowing for more complex interactions, including flavor-changing or dark matter-related dynamics. Here, $g_V = 3$ and $g_H \sim g_F \sim 1$. Due to this, the coupling of fermions to this new triplet is suppressed. Finally, *Model C* goes further by introducing a new type of interaction: Vector-Boson Fusion (VBF)⁵, making it a powerful tool for exploring exotic phenomena like dark matter, neutrino masses, or new symmetry breaking patterns. For this model, $g_F \sim 0$.

⁵Will be discussed in Chapter 6

2.2.2 Extra Dimension Models

Warped extra dimensions, such as in the Randall-Sundrum (RS) model [39, 40], propose the existence of spatial dimensions beyond the familiar three of space and one of time. In this framework, the extra spatial dimension is warped, meaning its geometry is curved rather than flat, such that the distance between points in these higher-dimensional spaces varies depending on the position within the extra dimension. This warping leads to non-linear scaling of physical quantities, which affects how fields and particles propagate through the extra dimension.

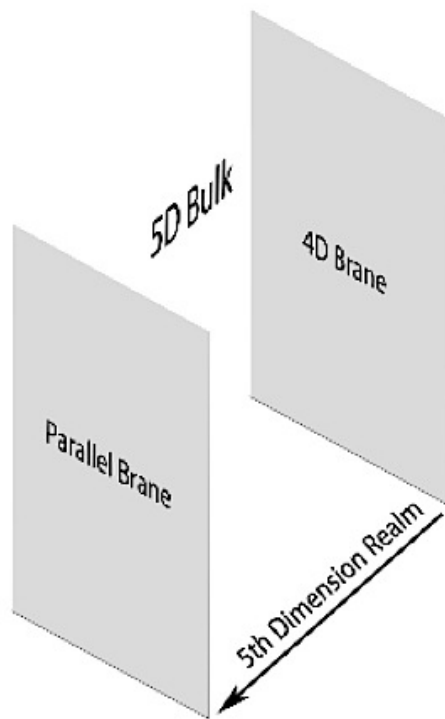


Figure 2.2: Schematic of the Randall-Sundrum model: our observable 4D brane and a parallel brane are embedded in a higher-dimensional 5D bulk. The fifth dimension is warped, with physical scales varying along its length.

As illustrated in Figure 2.2 [41], the RS model envisions our observable universe as being confined to a 4-dimensional brane embedded within a higher-dimensional 5D bulk spacetime.

The extra (fifth) dimension is bounded by two branes: a so-called “Planck brane” at one end, associated with gravity and high-energy physics, and a “TeV brane” at the other end, where the Standard Model fields are localized. The warping of the fifth dimension creates an exponential hierarchy of scales, providing a natural explanation for the large difference between the electroweak and Planck scales. In this scenario, some particles and interactions may be confined to the branes, while others, like gravitons, are free to propagate in the 5D bulk.

The warping factor is typically in the form $e^{-k|y|}$, where k controls the degree of warping and y is the coordinate in the extra dimension. The five-dimensional spacetime metric can be written as

$$ds^2 = e^{-2k|y|} \eta_{\mu\nu} dx^\mu dx^\nu + dy^2 \quad (2.32)$$

where $\eta_{\mu\nu}$ is the Minkowski metric for the 4-D brane and dy^2 represents the contribution from the extra special dimension.

The spin-2 Kaluza-Klein (KK) graviton [42] appears as a tensor fluctuation of the 5-dimensional metric, which when projected onto the 4-dimensional brane, manifests as a spin-2 particle that mediates gravity. These tensor fluctuations are responsible for the gravitational force, and their interactions with the SM fields lead to a warped geometry where gravity is weaker on the brane and stronger in the bulk. This helps explain the nature of gravity and its relationship with the extra dimensions, providing insights into fundamental questions like the hierarchy problem [43] and the behavior of gravity at high energies.

The radion [44] is a spin-0 scalar field that represents fluctuations in the size of the extra

dimension. In the simplest scenarios, the radion is massless, with its fluctuations describing the dynamical behavior of the extra dimension's geometry. These fluctuations describe the changes in the distance between the two branes (Planck and TeV branes) and the overall geometry of the extra-dimensional spacetime. The radion can interact with matter fields and may have observable effects, potentially contributing to dark matter or other new physics phenomena.

Chapter 3. Experimental Apparatus

3.1 CERN and the Large Hadron Collider

Studying the fundamental building blocks of nature requires technology that allows us to probe smaller and smaller scales. The European Organization for Nuclear Research, known as CERN, is at the forefront of this research. First established in 1952, CERN's goal was to unite European scientists following World War II and share the cost of a nuclear physics facility [45]. Located on the French-Swiss border, near Geneva, Switzerland, CERN is an international high energy research facility and is home to the Large Hadron Collider (LHC); the largest particle accelerator and collider in the world. CERN is an international laboratory with a global community of 12,370 users [46] in 950 institutions across 80 different countries [47]. The laboratory has grown a lot both in size as well as person-power since the 1950s, and each new addition has brought bountiful discoveries [48].

The LHC is a superconducting hadron synchrotron accelerator and collider. It is located about 100 meters below the surface, containing 8 straight sections and 8 arcs, with the plane of the tunnel inclined at 0.8° towards Lake Geneva [49]. It accelerates particles to high energies using two beams circulating in opposite directions along its 27 km ring circumference. During the first run of the LHC between 2010 and 2013, known as Run-1, the total center-of-mass energy was $\sqrt{s} = 8$ TeV (4 TeV per beam) [50]. After 2013, CERN entered the Long Shutdown-1 for planned maintenance and upgrades [51]. Two years later, in 2015, CERN started operations for Run-2 with an improved center-of-mass energy of $\sqrt{s} = 13$ TeV (6.5 TeV per beam). Run-2 lasted from 2015-2018 [52]. At the conclusion of Run-2, CERN performed more maintenance and upgrades during Long Shutdown-2 for initially 18

months [53]. Due to the COVID-19 pandemic, Long Shutdown-2 did not end until 2022. Thus, the Run-3 data taking period started in 2022 and is currently ongoing with a center-of-mass energy of $\sqrt{s} = 13.6$ TeV (6.8 TeV per beam) [54], expecting to end in 2026 [55]. The full schematic of CERNs accelerator complex can be seen is Figure 3.1 [56].

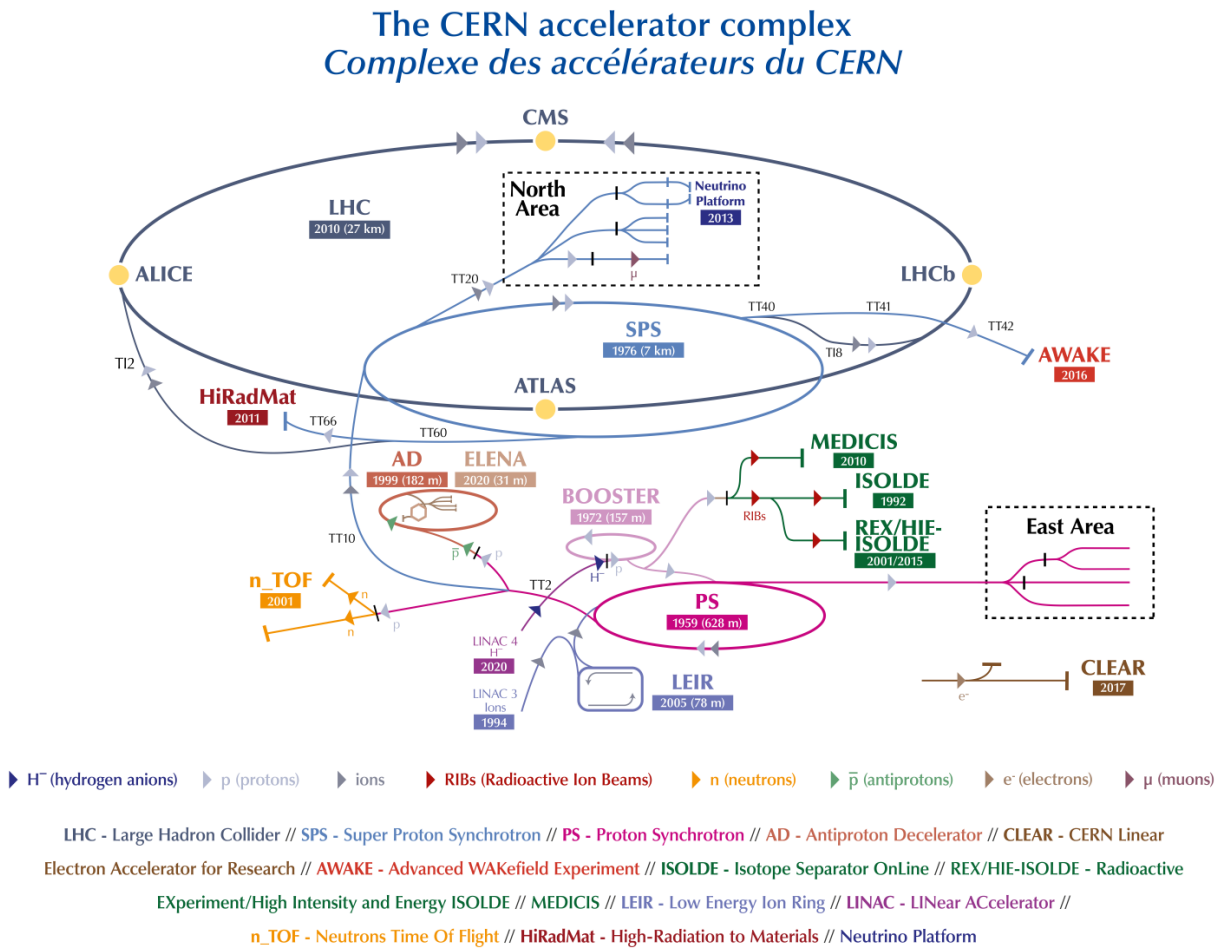


Figure 3.1: The accelerator complex at CERN as of 2022. The schematic shows the process of injecting proton beams into the LHC, and the arrows indicate the direction of the beam [56].

The process first starts with a bottle of hydrogen gas that is ionized into protons. These protons are then accelerated using a linear accelerator (LINAC). From the LINAC, the accelerated particles are accelerated further in the proton synchrotron (PS), before being injected into the super proton synchrotron (SPS). When considering the history of CERN,

one can notice that each upgrade has incorporated the previous generations of work, such that the previous world class accelerators feed into the new upgraded accelerator. Such that following SPS, when the protons have reached an adequate speed, they are injected into the LHC [49]. Particle acceleration is achieved using 16 radiofrequency (RF) cavities housed in cryomodules, enabling them to operate in a superconducting state. These cavities are powered by a 400 MHz electromagnetic field. The oscillating RF field ensures precise timing of particles, and eliminating protons with slight energy deviations. This process organizes the beam into tightly packed "bunches" of protons, enabling high-energy collisions, and can be seen in Figure 3.2 [57].

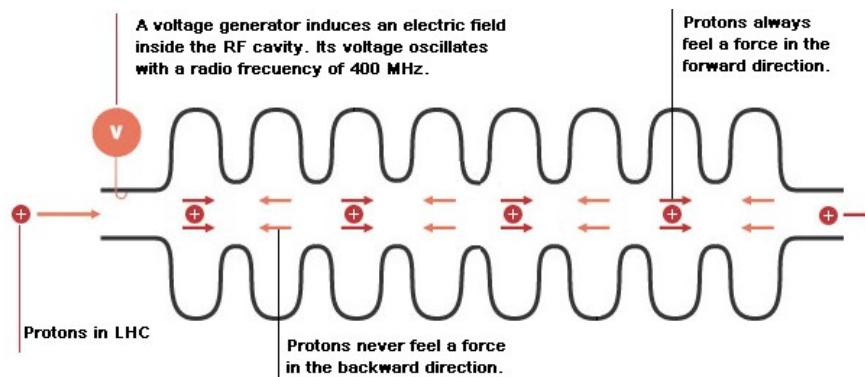


Figure 3.2: Schematic of RF cavity used to accelerate particles. As voltage oscillates, particles are separated out into bunches along the beam [58].

The LHC is designed to run with 2808 bunches per beam separated by a 25 ns gap with each bunch containing 1.2×10^{11} protons, providing a crossing rate of 40 MHz (about 50 collisions per crossing) and about 1 billion collisions per second. 392 quadrupole magnets and 1232 superconducting dipole magnets are used to both squeeze and guide the beam, respectively [59]. The beams are then collided at four interaction points. These specific interaction points house the four main detectors which measure and record particle collisions. There are two general purpose detectors: ATLAS (A Torodial LHC Apparatus) [60] and

CMS (Compact Muon Solenoid) [61] designed to cover a wide range of physics studies, and two specialty detectors: ALICE (A Large Ion Collider Experiment) [62] and LHCb (LHC-beauty) [63] which have more focused physics studies.

For particle physics experiments, an important factor to consider is the number of events, or successful collisions, that occurs. The key quantity used when counting particle collisions is luminosity, or a measure of the number of proton collisions that occur at an interaction point. Luminosity is used in lieu of collision rate because it does not account for the probability of particle interaction, and therefore is just a direct measurement of the machines performance. Luminosity of the LHC can be expressed as

$$L = \frac{f_r n_1 n_2}{2\pi \Sigma_x \Sigma_y} \quad (3.1)$$

where n_1 and n_2 are the number of protons in the colliding bunches, f_r is the collider revolution frequency, and Σ_x and Σ_y are the convoluted beam widths $\Sigma_i = \sqrt{\sigma_{i1}^2 + \sigma_{i2}^2}$ (horizontal σ_{i1}^2 and vertical σ_{i2}^2 geometric widths of the proton beams, respectively) [64]. Integrating, with respect to time, over the amount of time a run takes will yield the amount of data delivered by the LHC during said run; oftentimes called the integrated luminosity. Figure 3.3 shows the total integrated luminosity delivered from the LHC during Full Run-2 (2015-2018), as well as the amount of data the ATLAS detector recorded and the amount of data deemed as “good” for physics analyses (where “good” means all important experiment sub-detectors are working nominally, detector magnets are on, and everything is running smoothly).

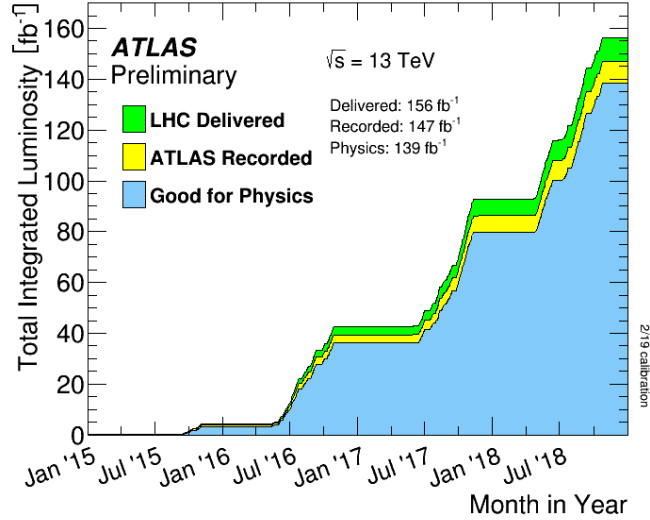


Figure 3.3: Total integrated luminosity, in units of inverse femtobarn, over the time period of Run-2 (2015-2018) delivered by the LHC (green), recorded by ATLAS (yellow), and good for physics (blue) during stable beams for pp collisions at a center of mass energy of $\sqrt{s} = 13$ TeV [65].

3.2 ATLAS Detector

The focus of this thesis uses the ATLAS detector. As mentioned, the ATLAS detector is a general-purpose detector designed to cover a wide range of physics research analyses, from making precision SM measurements to searching for new BSM physics. It is the largest physics detector in the world, measuring 44 meters in length, 25 meters in diameter, and weighing about 7000 tons [66]. Its massive size is displayed in Figure 3.4, where there is a person pictured for scale. Also pictured are the various sub-detector systems that, when combined, create the magnificent detector.

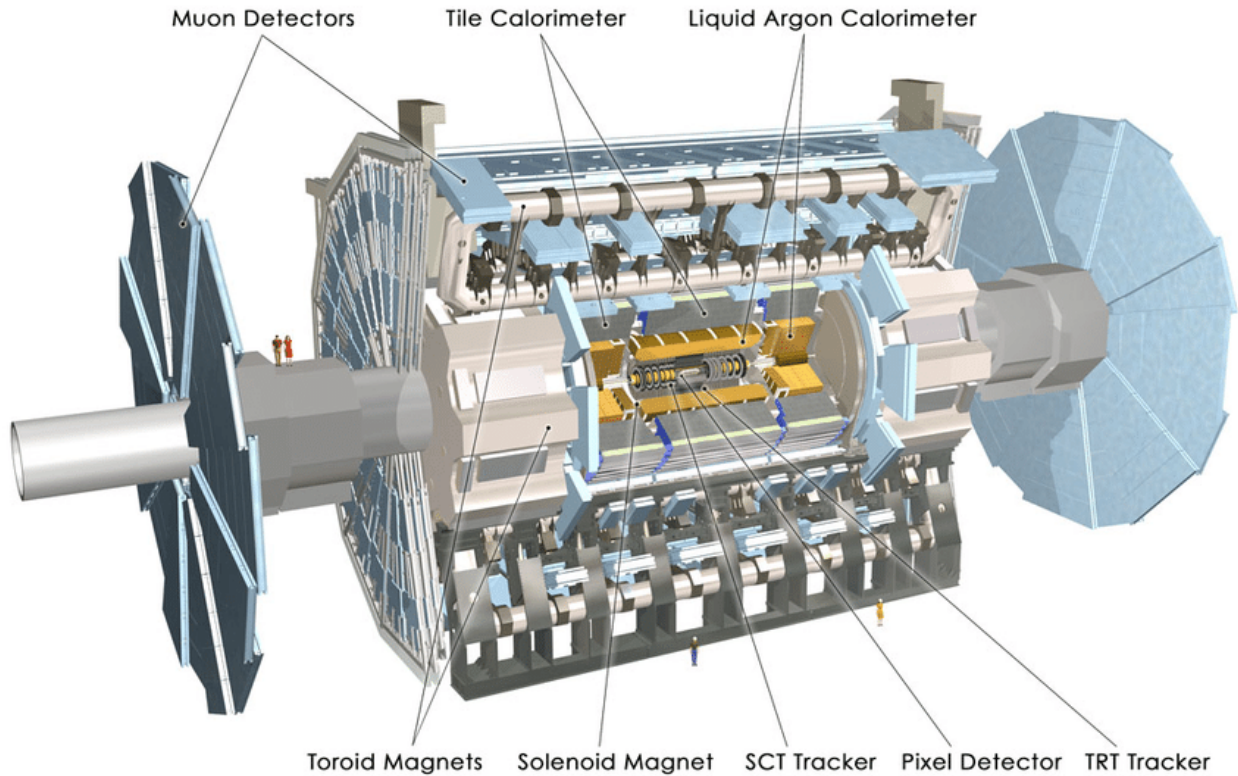


Figure 3.4: Schematic of ATLAS detector showing its size and dimensions as well as the various subcomponents. [67]

The arrangement of the sub-detectors can be thought of like an onion (yes, like the kind you eat). The collisions occur in the center of the detector and radiate outwards, so the detectors are aligned in that nature, working its way from the inside out. Starting from the inside working outwards, the first layer is properly named the inner detector (ID) and is where particle tracks are recorded. From there, particles travel through the calorimetry system, where this twofold system operates and most light-mass electromagnetic particles are absorbed initially, then further out the heavier hadronic interacting particles are absorbed and their energy is recorded. Muons then punch-through the calorimeters into the muon system. The muon system, as named, mostly tracks and measures muons as they leave the ATLAS detector. Neutrinos completely escape the system and are measured by the

missing energy in all the subsystems combined. Importantly, the whole detector is under a magnetic field, and contain various trigger and data acquisition systems. Each layer is equally important in ensuring quality data is being recorded, and will be discussed in further details in the following sections.

3.3 Coordinate System

To describe particles and their directions in the detector, it is useful to define a coordinate system in which to reference. The beam direction is in the z-direction, with the xy-plane perpendicular to the z-direction. From the interaction point to the center of the LHC ring denotes the x-direction. From the interaction point stright upwards denotes the y-direction. Two angles of interest, the azimuthal angle ϕ and the polar angle θ , are the angles around the beam axis and from the beam axis, respectivley. Rapidity is defined as $y = \frac{1}{2} \ln \frac{(E+p_z)}{(E-p_z)}$, and massless particles use pseudorapidity $\eta = -\ln(\theta/2)$. Transverse variables, such as missing transverse energy E_T^{miss} , transverse momentum p_T , and transverse energy E_T , are defined in the xy-plane.

3.4 Magnet System

The ATLAS magnet system is crucial for measuring the momentum of charged particles by providing the bending power required to curve the trajectory of charged particles produced in high-energy collisions. The charged particles will have characteristic paths related to the charge-to-mass ratio, and when combined with the inner dectector information, can help identify particles in reconstruction, further detailed in Section 3.5. The system consists of a central solenoid, a barrel toroid, and two end-cap toroids, shown in Figure 3.5.

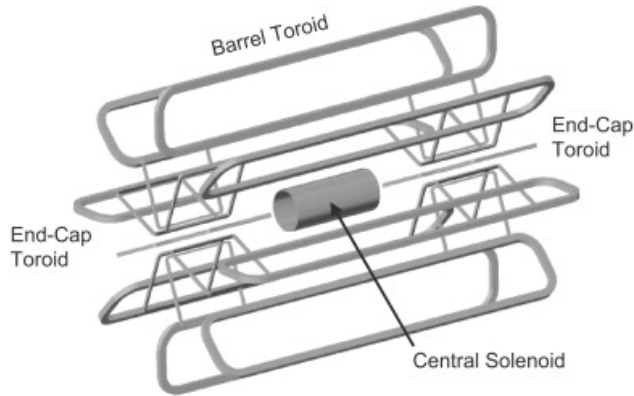


Figure 3.5: Schematic of ATLAS detector’s magnet system [68], highlighting its key components: the central solenoid magnet surrounding the inner detector, and the large toroidal magnets (comprising the barrel and end-cap toroids) that envelop the calorimeter and muon systems. These magnets generate powerful magnetic fields that bend the paths of charged particles, enabling precise momentum measurements and particle identification within the detector.

The solenoid, positioned along the beam axis, generates a magnetic field of 2 T to enable momentum measurements in the inner detector [68]. This solenoid has a compact design with an inner diameter of 2.44 meters and a length of 5.3 meters, minimizing material in front of the calorimeters. Surrounding the calorimeter is the barrel toroid, a large system comprising eight racetrack-shaped coils housed in individual stainless-steel vacuum vessels, each producing a toroidal magnetic field. The barrel toroid spans a length of 25.3 meters and provides an extensive coverage with diameters ranging from 9.4 meters to 20.1 meters. Additionally, two end-cap toroids, each with a length of 5 meters and an outer diameter of 10.7 meters, complement the magnetic field in the forward region. The toroidal magnets produce peak magnetic field strengths of 3.9 T and 4.1 T for the barrel and end-caps, respectively, enhancing the precision of momentum measurements in the Muon Spectrometer. All the coils use aluminum-stabilized niobium-titanium conductors and are operated at cryogenic temperatures, near absolute zero, under vacuum to maintain superconductivity. The magnetic field is modeled with high precision to account for perturbations from surrounding

detector components, ensuring accurate particle tracking throughout the detector.

3.5 Tracking

The first layer of the ATLAS-onion is the inner detector. Closest to the beamline and interaction point, the inner detector is responsible for the tracking information collected. Since it is very close to the interaction point, it has to have both a fine granularity as well as a quick response time in order to track all of the particles emerging from the collision. It provides both primary and secondary vertex measurements. The inner detector can be broken down into three subdetectors: pixel detector, semiconductor tracker (SCT), and transition radiation tracker (TRT), all of which can be seen in Figure 3.6 [69]. Particles leave hits in these different layers of the inner detector, which are used by track reconstruction algorithms to form the trajectory of particles on their journey through the inner detector. Depending on the number and clustering of the hits, different track qualities are assigned depending on how well this trajectory matches said hits.

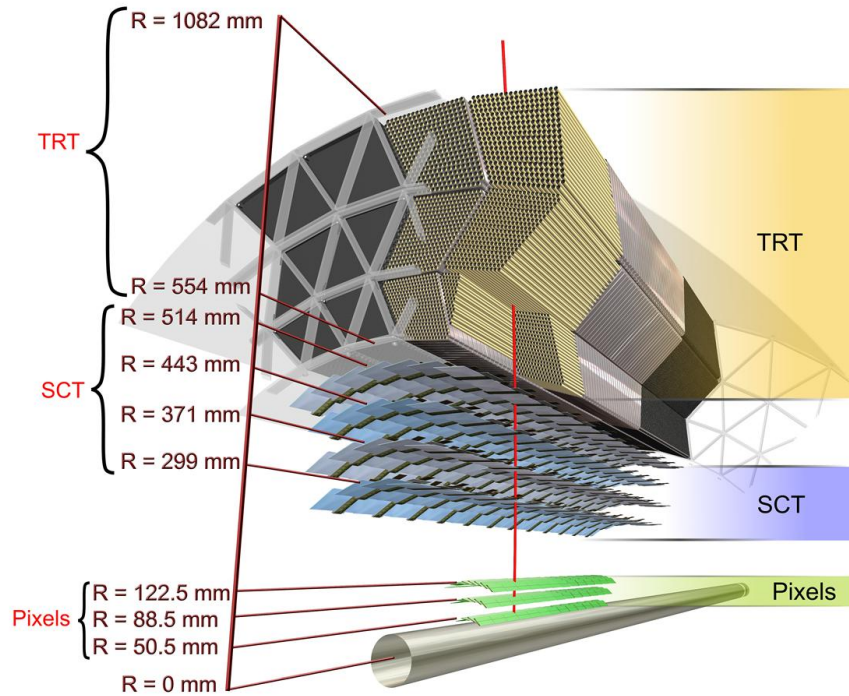


Figure 3.6: Schematic of the ATLAS detector’s inner detector [69], which is responsible for tracking charged particles as they emerge from the collision point. The inner detector is composed of three main subsystems: the Pixel Detector, the Semiconductor Tracker (SCT), and the Transition Radiation Tracker (TRT). These layers are immersed in a uniform magnetic field generated by the central solenoid, allowing for precise reconstruction of particle trajectories and measurement of momentum.

3.5.1 Pixel Detector

The pixel detector is designed to have the highest granularity in the ATLAS inner detector, providing precise measurements closest to the interaction point, where particle tracks are most densely concentrated. This high precision is achieved using 1744 modules of oxygenated silicon sensors arranged in three barrel layers and three end-cap disks, with the innermost layer just 5 cm from the beamline. These silicon sensors are p-n junctions that generate electron-hole pairs as ionizing particles pass through them, producing an electrical signal that

is critical for identifying short-lived particles like B hadrons and τ leptons [69]. However, being closest to the beamline also means the pixel detector experiences the most intense radiation damage, prompting the addition of an Insertable B-Layer (IBL) between the beam pipe and the original pixel detector to improve radiation tolerance.

While the entire inner detector would ideally be composed of these high-precision pixels, this is not feasible due to cost constraints. The Pixel Detector alone is estimated to cost between €100 million and €150 million, driven by the sophisticated technology required, including silicon sensors, front-end electronics, readout systems, and advanced cooling systems. In contrast, the other two inner detector systems, SCT and TRT, are estimated to cost €40 million to €60 million and €30 million to €50 million, respectively, primarily due to their use of different materials and less stringent precision requirements [69].

3.5.2 Semiconductor Tracker (SCT)

The middle portion of the inner detector is the semiconductor tracker (SCT) system. It uses similar technology as the pixel detector, but rather than pixels the system contains silicon strips. It has a slightly larger granularity and also faces large levels of radiation. It has four concentric cylinders in the barrel region and nine disks covering the end-cap region. The module is constructed with the silicone strips glued back-to-back at a slight angle (40 mrad), allowing for a two-dimensional resolution in the η - ϕ plane [69].

3.5.3 Transition Radiation Tracker (TRT)

Finally, the transition radiation tracker (TRT) is the outermost portion of the inner detector. The TRT consists of straw-tube tracking with transition radiation detection capability for

electron identification using Xenon gas [69]. The barrel region contains about 50,000 straws, with a length of 144 cm and 4 mm diameter. The end-caps contain about 320,000 radial straws. Inside each straw contains a 30 μm diameter gold-plated W-Re wire and is filled with gas ($Xe_1CO_2O_2$) [59]. Acting as drift tubes, as ionizing particles pass through the tubes, the gas is ionized and the electrons drift to the center of the tube and are readout as electrical signal. The TRT system complements the other two subsystems by being able to obtain a larger number of hits and have longer track lengths.

3.6 Calorimeters

As protons collide, inelastic scattering due to electromagnetic (EM) and strong interactions produce distinct types of showers, illustrated in Figure 3.7. EM showers and hadronic showers both refer to a cascade of particles as they interact with matter, but the underlying physics and the subsequent forces differ.

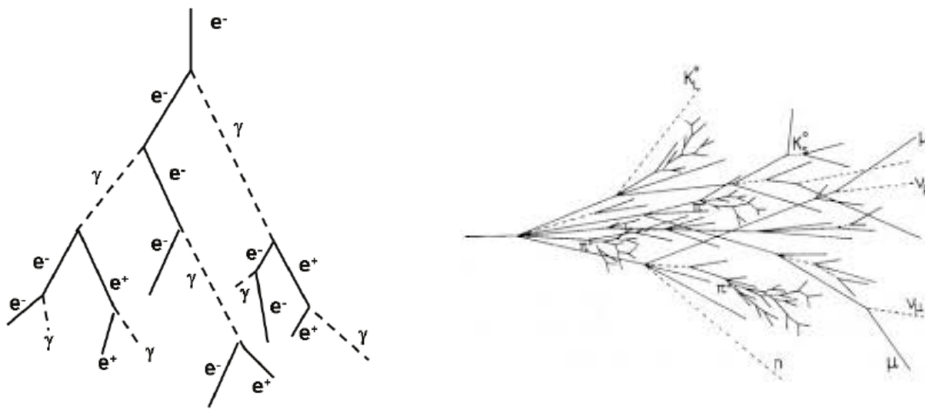


Figure 3.7: Visual comparison of electromagnetic (left) [70] and hadronic (right) [71] showers, highlighting the characteristic development and energy deposition patterns of each.

EM showers are due to photons, electrons, or positrons interacting with matter via the electromagnetic force. It is primarily caused by bremsstrahlung for protons/positrons, and

pair production for photons. As the shower progresses and grows, the energy slowly depletes with each iteration until a minimum threshold is met (1.022 MeV, the pair production energy threshold), and then the shower begins to die out.

Hadronic showers arise from hadron interactions via the strong force. It is primarily caused by decays to pions and muons and secondary hadron production, and the shower continues until the energy falls below the pion production energy threshold. Hadronic showers introduce a new level of complication because of the strong interaction. Production of other particles, mainly pions, occurs, and some of these particles in turn develop showers (EM or otherwise) of their own. There are also decays to neutrinos, which results in missing energy, and muons, which are hard to contain. Hence, their modeling is important for calorimeter design.

The radiation length (X_0) is a key parameter in understanding both electromagnetic (EM) showers and hadronic showers, representing the mean distance an electron or photon travels in a material before losing about 63% of its energy through processes like bremsstrahlung (for electrons) or pair production (for photons) [70]. In hadronic showers, the energy loss occurs via a combination of strong interactions, such as nuclear fragmentation and scattering, which leads to a more complex and extended cascade compared to EM showers. The value of X_0 depends on the material, with heavier elements generally having shorter radiation lengths, causing faster EM shower development. The radiation length X_0 is given by the equation:

$$X_0 = \frac{716.4 \text{ g/cm}^2}{Z \left(\frac{A}{Z}\right) \ln\left(\frac{287}{\sqrt{Z}}\right)} \quad (3.2)$$

where Z is the atomic number and A is the atomic mass number of the material. While X_0

primarily governs the growth of electromagnetic showers, the hadronic interaction length, which is typically longer than the radiation length, controls the development of hadronic showers. X_0 directly influences the design of calorimeters used in particle detectors by determining how thick the material should be to fully contain and measure the shower's energy. Shorter X_0 values lead to faster energy loss and quicker shower growth, while longer values slow the process.

Both the EM calorimeter (ECAL) and the hadronic calorimeter (HCAL) are designed to contain their respective types of showers. Since the EM showers are typically shorter and narrower, the ECAL is placed closer to the interaction point, and is designed to have hadrons (only) deposit a small amount of energy in the ECAL before the hadrons are mostly contained in the HCAL. The ECAL has a finer energy resolution, allowing it to easily identify and measure energy of electrons and photons, while the HCAL has a coarser energy resolution and provides jet reconstruction ¹, and jet and missing transverse energy (MET) measurements. These two calorimeters cover different pseudorapidity ranges, with the EM portion covering the full region $|\eta| < 3.2$, and the hadronic portion covering the barrel ($|\eta| < 1.7$), the end caps ($1.5 < |\eta| < 3.2$), and the forward region ($3.1 < |\eta| < 4.9$) [72]. Both of these calorimeters are shown in Figure 3.8.

¹As protons collide, the impact produces a parton jet consisting of quarks and gluons. However, due to color constraints, these subatomic particles quickly hadronize into mesons, baryons, etc. which we nominally then call the physics jet. These particles then further decay and produce a "shower", or a jet, in the calorimeters. Jets are collimated bunches of stable particles, and are reconstructed using jet algorithms. These algorithms are typically dependent on the jet radius (R). The rule of thumb is as follows: a large-R jet has a radius $R= 1.0$, and a small-R jet has a radius of $R= 0.4$.

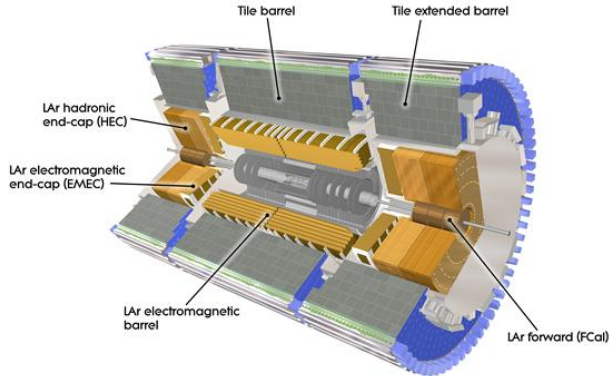


Figure 3.8: Schematic of the ATLAS electromagnetic and hadronic calorimeters, which measure the energy of electrons, photons, and hadrons. The system provides fine spatial and energy resolution across a wide pseudorapidity range.

3.6.1 Electromagnetic Calorimeters

Within the EM calorimeter (ECAL), there is a barrel portion ($|\eta| < 1.475$) and two end-caps ($1.375 < |\eta| < 3.2$), each using liquid-argon (LAr) technology [72]. The end-caps are separated into two coaxial wheels: an outer wheel covering the region $1.375 < |\eta| < 2.5$, and an inner wheel covering $2.5 < |\eta| < 3.2$. It has a unique accordion-shaped design that provides full ϕ symmetry, shown in Figure 3.9. The ECAL uses lead as the absorber material to initiate electromagnetic showers from incoming electrons and photons; its high atomic number makes it effective for inducing showers and also plays a crucial role in determining the radiation length, which sets the scale for how quickly particles lose energy. When particles pass through the ECAL, they ionize the active medium, LAr, causing electrons and ions to drift toward Cu-Kapton electrodes under an applied 2000 V bias, producing a current proportional to the number of ionization interactions.

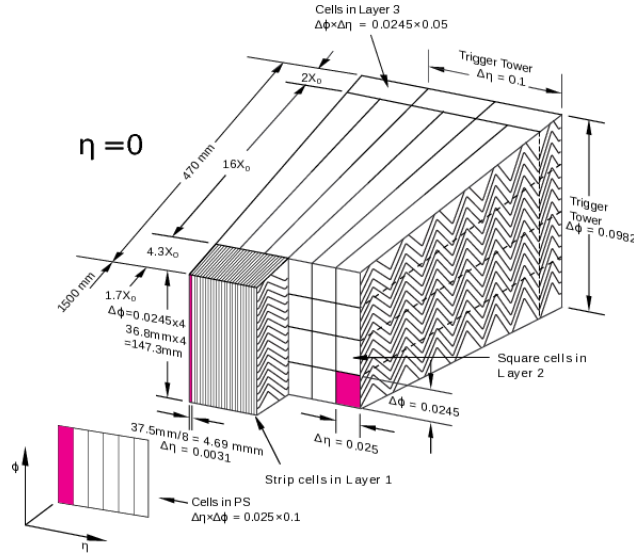


Figure 3.9: This schematic captures the intricate design of the LAr system, showcasing how its accordion shaping, multi-layer segmentation, and presampler work together to deliver precision measurements of electromagnetic showers, crucial for identifying electrons and photons in ATLAS.

3.6.2 Hadronic Calorimeters

For hadronically interacting particles (such as quarks and gluons), their showering occurs in the Hadronic Calorimeter (HCAL). Due to color constraints, these subatomic particles quickly hadronize into mesons, baryons, etc. which we nominally then call the physics jet. These particles then further decay and produce a "shower", or a jet, in the calorimeters. Jet reconstruction techniques will be discussed in Section 5.1.

The HCAL consists the Tile Calorimeter (TILE), the Hadronic End-cap Calorimeter (HEC) and the Forward Calorimeter (FCal) [72]. The Tile Calorimeter, constructed with iron absorbers and scintillating tiles, is optimized for interactions with charged hadrons and provides coverage in the central region ($|\eta| < 1.7$). The HEC, utilizing copper as an absorber, is designed for robust performance in the high-radiation environment of the end-caps ($|\eta| < 3.2$). Finally, the FCal, with modules made of copper and tungsten, extends coverage for

particles scattered at very small angles, enhancing sensitivity to forward-going particles in high-energy events ($3.1 < |\eta| < 4.9$). Together, these components provide full coverage and high energy resolution, which are essential for reconstructing missing transverse energy and for identifying jets and hadronic showers. Each calorimeter is segmented into layers and read out with photomultiplier tubes, allowing for precise spatial and energy measurements across the ATLAS detector.

3.7 Muon Spectrometer

Measuring muons in the ATLAS detector is challenging because of their ability to penetrate large amounts of material with minimal energy loss. Since muons are charged, their trajectories are deflected by the magnetic fields generated by large, superconducting air-core toroid magnets inside the detector (outlined in Section 3.4). Their momentum is derived from the curvature of their trajectory (rather than energy deposition like in other areas of the detector), so the inner tracking information is also used along with the muon system to identify and measure muons.

The muon spectrometer is the outermost layer of the ATLAS-onion. The layout is shown in Figure 3.10, where the geometry consists of a barrel (cylindrical) piece and two endcaps. The barrel chambers are composed of rectangular shape with areas between 2 m^2 and 10 m^2 [73]. They can be further broken down into three concentric cylinders at radii of about 5, 7.5, and 10 meters from the beam axis, and cover the pseudorapidity range $|\eta| < 1$. The end-cap chambers are composed of trapezoidal shape with tapering angles of 8.5° and 14° for the small and large chambers, respectively, and areas ranging from 1 m^2 to 10 m^2 for (with a combination area of 30 m^2 when installed). They are arranged in four disks at

distances of 7.4, 10.8, 14 and 21.5 meters from the center of the detector and cover the pseudorapidity range $1.6 < |\eta| < 2.7$. There is a transition range, or a gap, $1.4 < |\eta| < 1.6$ where a combination of the two fields exist.

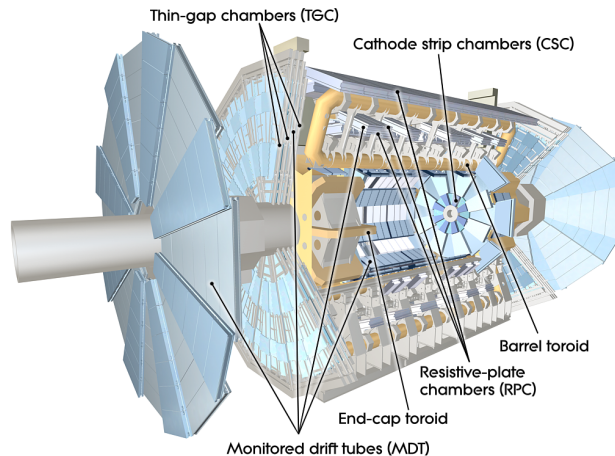


Figure 3.10: A cross-sectional schematic of the ATLAS Muon Spectrometer, showcasing the layout and technologies used to detect and measure muons.

There are two subcategories when thinking about the muon system: the precision-tracking chambers and the trigger chambers. The precision-tracking chambers are used to track the muons momentum while the trigger chambers provide position and time resolution. These two subcategories can be further split: Monitored Drift Tubes (MDTs) and Cathode Strip Chambers (CSCs) for the precision-tracking chambers, and Resistive Plate Chambers (RPCs) and Thin Gap Chambers (TGCs) for the trigger chambers.

The MDTs and CSCs systems together ensure robust and accurate momentum measurements across the entire ATLAS muon system. The MDT chambers in the aid in precision measurement of muon momentum in the barrel region, across the range $|\eta| < 2.7$ [73]. Each MDT chamber consists of multiple layers of drift tubes, typically between three and eight, where individual tubes have a diameter of 30 mm. These aluminum tubes operate by detecting the ionization electrons produced by muons as they pass through the gas-filled tubes of a

non-flammable mixture of Ar (93%) and CO₂ (7%). The position of the muon is determined by measuring the drift time of these electrons. As charged particles pass these tubes, the gas is ionized and the charged electrons drift towards the center of the tubes where it is read out as electrical signal. Each tube providing a position resolution of 80 μm , while the resolution at the chamber level is improved to 35 μm . The CSCs are used in the forward region, or endcaps, ($2 < |\eta| < 2.7$), where higher particle rates and more challenging background conditions exist. The CSCs utilize a multiwire design with segmented cathode strips in orthogonal directions, allowing for the simultaneous measurement of two coordinates. This design enables precise muon tracking even in high-density environments.

To complement the precision-tracking chambers, the trigger chambers are used to prompt signals for triggering, thus providing bunch-cross information. The RPCs provide space-time resolution for the barrel region, $|\eta| < 1.05$, and the TGCs for the end-cap region, $1.05 < |\eta| < 2.7$ [73]. The RPCs are composed of parallel electrode plates separated by tetrafluoroethane ($\text{C}_2\text{H}_2\text{F}_4$) gas, and are attached to the MDTs. The TGCs are multi-wired chambers, and are parallel to the MDTs. The TGCs are used on the endcaps because of the resolution required for higher momenta muons [59].

3.8 Trigger and Data Acquisition

The trigger and data acquisition (TDAQ) system is used to reduce the overload of information that originates from the collisions at the LHC to a manageable amount of data, only saving relevant events.

The goal of TDAQ is to select “interesting” events and reject “boring” events, which rely on underlying physics analysis motivations. This selection of events, or trigger, generates a

prompt to signal the start of the DAQ read-out chain. The trigger system is composed of three levels: Level-1 (L1), Level-2 (L2), and Event Filter (EF). The L2 and EF combine to form the High-Level Trigger (HLT) [74]. The L1 trigger receives all of the 40 MHz collision information from the LHC and reduces down to 100 kHz in about $2.5 \mu\text{s}$. The HLT then further reduces down to about 1 kHz in about 500 ms.

The L1 trigger combines muon trigger chambers (L1-Muon) with calorimeter information (L1-Calo) to be sensitive to signatures from missing transverse energy, candidate electrons, photons, jets and muons [74]. Signals from the L1-Calo and L1-Muon, as well as real-time kinematic and angular selections (L1-Topo), are given as inputs to the central trigger processor (CTP) which then processes L1 accept decisions. The CTP also identifies Regions-of-Interest (ROI), which are regions in the detector that has interesting features. Events passing the L1 selections and the ROI's are then passed to the HLT, which are fast custom-made software that is ran on commercial-grade CPU's. The HLT uses algorithms to reconstruct objects, often guided by ROIs, and applies physics selection. Once an event is accepted by the HLT, it will be recorded and processed at a Tier-0 site and be made available for physics analyses. The Tier-0 site is located at CERN, but the data then gets distributed to 13 Tier-1 sites around the world [75]. Tier-2 sites help to run the MC production (discussed in the next section), together with data/MC reprocessing, and user jobs. MSU and UM together form a Tier-2 site called ATLAS Great Lakes Tier-2 (AGLT2). Some sites, such as MSU, also have a Tier-3 computing site which is exclusively for the MSU users to run analysis jobs.

Chapter 4. Event Generation, Simulation, and Reconstruction

Before diving into analysis, event generation, simulation, and reconstruction are critical steps in the study of high-energy particle collisions produced by the LHC. Event generation involves using theoretical models, such as QCD, to simulate the initial interactions and decay processes resulting from pp collisions. These generated events are then fed into a detailed detector simulation, which models the response of the ATLAS detector using tools like **GEANT4** [76], incorporating the effects of material interactions, energy deposits, and detector noise. The output is a digitized representation of what the detector “sees.” Reconstruction is the process of converting this simulated detector output into meaningful physical observables, such as the momenta of charged particles, energy deposits in calorimeters, and the identification of jets, leptons, or missing transverse energy. These steps are essential for comparing experimental data with theoretical predictions, enabling the search for new physics phenomena and precise measurements of known particles and interactions.

4.1 Event Generation

Monte Carlo (MC) programs are used to model specific signal and background physics processes. Event generation can be thought of as a two-step process. The first step is to model the pp hard scattering by calculating the matrix elements (ME) for a set of Feynman diagrams [77].

This can be done at at leading-order (LO) by using generators such as **Pythia** [78] or **Herwig** [79] and for many background processes evening next-to-leading-order (NLO) by

using generators such as `Powheg` [80], `Sherpa` [81], or `aMC@NLO` [82]. The second step is to model the parton showering and simulate QCD and QED radiation. Generators typically used for this step (even if the hard scattering has been performed by a different generator) are `Pythia`, or `Herwig`.

Parton Distribution Functions (PDFs) represent the probability of finding partons inside a hadron as a function of the fraction of the proton's momentum they carry. PDFs are determined from experimental results on short-distance scattering processes, such as deep inelastic scattering, where high-energy electrons or other particles probe the proton's inner structure. The extraction of PDFs involves sophisticated global fits to data from various experiments, ensuring they accurately reflect the dynamics of partons across a range of momentum fractions and energy scales. These are important in collider measurements because they are a component of the SM theory, and are essential in making predictions about BSM processes. ATLAS uses various sets of PDFs, such as CT14 from the CTEQ Collaboration [83], NNPDF3.0 from the NNPDF Collaboration [84], and MMHT2014 from the MSTW group [85], depending on the type of process being simulated and the specific analysis. Since different PDF sets can yield slightly (sometimes even significantly) different predictions for particle collisions, ATLAS analyses typically account for PDF uncertainties by performing simulations with various PDF sets and evaluating how the results vary. An example of some PDF distributions from the MSTW group is shown in Figure 4.1.

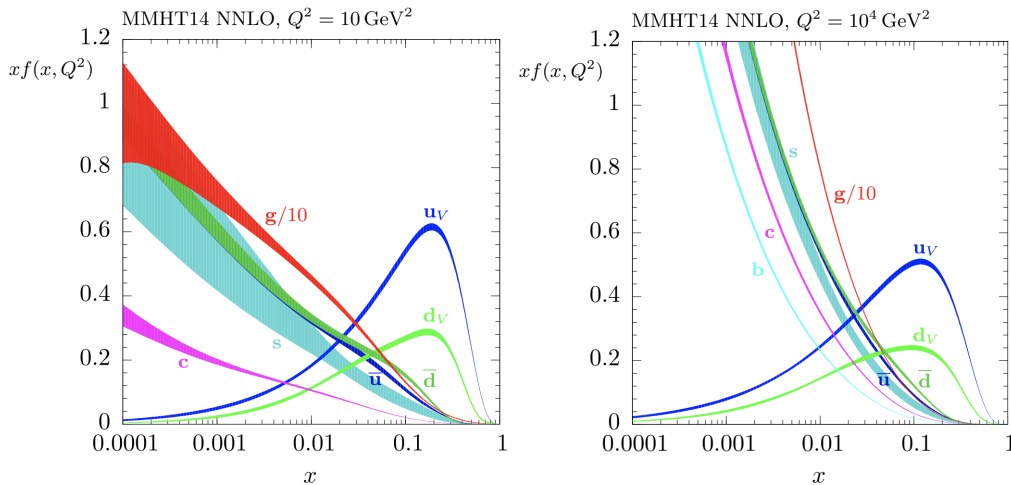


Figure 4.1: The MMHT14 NNLO Parton Distribution set for protons at $Q^2 = 10 \text{ GeV}^2$ (left) and $Q^2 = 10^4 \text{ GeV}^2$ (right) [86]. The thickness of the bands represent various internal PDF uncertainties for this PDF set.

4.2 Event Simulation

Further bridging the gap between theory and measured data, is the simulation of collision events within the ATLAS Detector. A software capable of simulating interactions between particles produced in event generation and a detector is the **GEANT4** (GEometry ANd Tracking) [76] software. **GEANT4** is a toolkit for simulating the passage of particles through matter over a wide energy range [87]. **GEANT4** is widely used in various fields of physics beyond just particle physics, thanks to its ability to simulate virtually limitless detector and accelerator designs. In combination with the event generation methods described above, new simulated particles now more accurately replicate what is seen in actual data; thus providing a more accurate comparison. Figure 4.2 shows schematically how different particles interact with the detector.

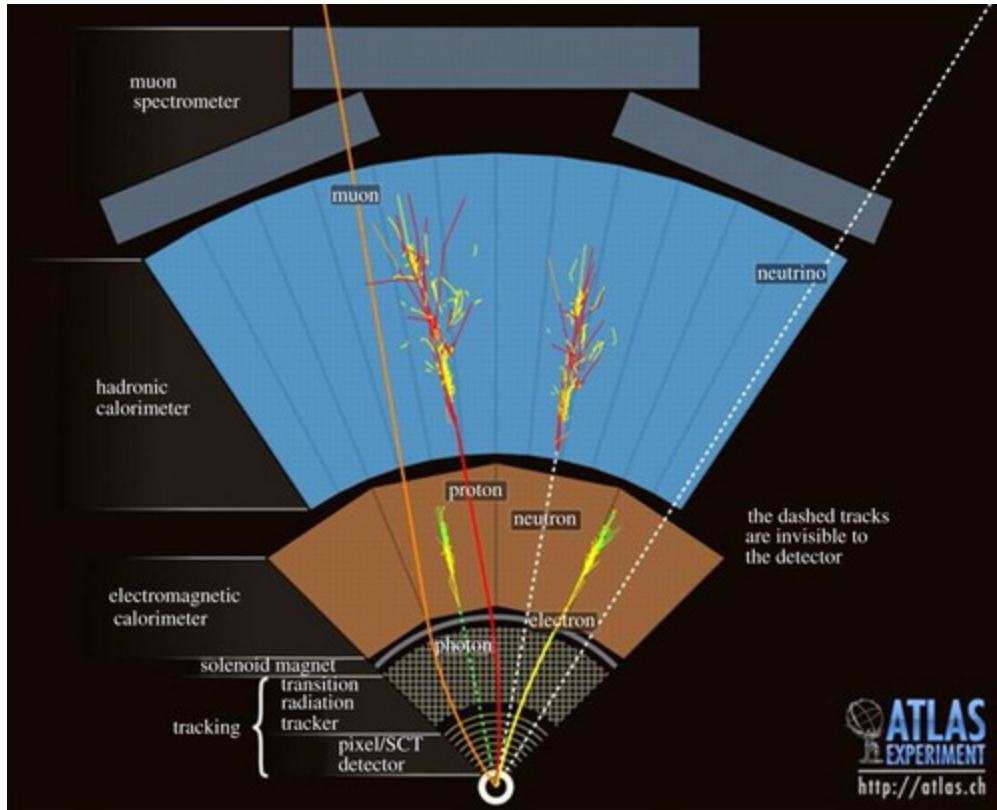


Figure 4.2: ATLAS detector schematic showing how different particles interact with various detector components [88]. Starting from the inner detector at the bottom, then the electromagnetic calorimeter, then the hadronic calorimeter, then finally the muon spectrometer.

Electrons generate “HITS” in the inner detector (ID) due to their electric charge and deposit energy in the electromagnetic calorimeter (ECAL). These “HITS” correspond to the interactions between the electrons and the layers of the Transition Radiation Tracker (TRT). During the reconstruction process, algorithms perform track reconstruction by identifying these hits and associating them with track candidates. The algorithms also determine the number of tracks in a given event, assess the quality of the tracks, and fit the tracks to the clusters of hits. These raw energy deposits in the ECAL are scanned over during reconstruction as well, and the electron, photon, and jet algorithms form energy clusters, ultimately determining the objects to which they correspond. To form a full electron candidate, energy clusters need to be matched in the reconstruction stage to tracks from the inner detector.

Photons however do not leave any “HITS” in the ID, and thus do not generate any tracks, but do also deposit their energy in the ECAL. Thus, photon candidates are based on energy deposits in which no tracks were found. Similarly, neutrons do not leave “HITS” in the ID, but instead deposit their energy in the hadronic calorimeter (HCAL). The raw energy deposit is treated similarly as in the ECAL, and the energy clusters represent particle showers. Protons, being electrically charged, leave “HITS” in the ID and also deposit their energy in the HCAL. Proton candidates thus require tracks in the ID be matched to energy deposits in the HCAL. Muons leave “HITS” in the ID, then pass through the bulk of the detector before interacting with the muon spectrometer (MS), but then leave the detector entirely. These tracks in the MS need to be matched to the tracks in the ID in order to form a “combined muon” candidate.

There is also a question of how completely do we need to model the detector in order to get an accurate representation of the real detector. This is mainly a concern due to CPU computation time. “Full simulation” is the fully simulated detector using the **GEANT4** software, including fully modelled showering in the calorimeter (and is really expensive in terms of CPU cost/time). In scenarios where less precision is required, “fast simulation”, also referred to as “AtFast-II” [89] or “AF2”, is available. This uses a parametrized detector response method to model the showering, the benefit is that such an approach is relatively computationally cheap. AF is continually being improved through comparisons to experimental data and refined parameterizations, including the incorporation of machine learning techniques. This ongoing development allows AF to handle increasingly complex simulations while maintaining accuracy comparable to that of **GEANT4**. The latest version of this fast simulation is AF3, which further enhances its capabilities and brings it closer to the level of precision offered by full detector simulations.

4.3 Reconstruction

Understanding where and how particles interact with the ATLAS detector is key to reconstructing the underlying event. Each detector component captures specific signals, such as trajectories or energy deposits, which are processed by reconstruction algorithms to form high-level physics objects, like electrons, muons, jets, and missing transverse energy. The following section outlines the algorithms used to transform raw detector signals into analyzable physics objects.

4.3.1 Pile-Up

Since protons in the LHC travel in tightly packed “bunches” through the beam pipe, “pileup” can occur when additional pp collisions occur near the primary collision. Pileup can occur both inside the bunch (“in-time pileup”) [90] as well as afterwards (“out-of-time pileup”). Before reconstruction, pile-up mitigation techniques are used to estimate and subtract the extra energy/extra jets coming from pileup [91]. Figure 4.3 shows a visual example of pile-up from the beamline, going from left to right across the image. There are multiple collisions shown along with the various tracks identified for each collision point. Within the mess, we are expected to identify the primary vertex, which will be discussed in the next section, coming from the main pp collision. The average number of pp collisions per bunch crossing over the different years of data taking is shown in Figure 4.4. The increase in the mean number of interactions per crossing over the years shows that the LHC was operating at higher intensities, leading to more pile-up interactions. Despite this increase in pile-up, the increasing luminosity over time allows for more precise measurements and discoveries in particle physics, as more data leads to more statistical power for analyses.

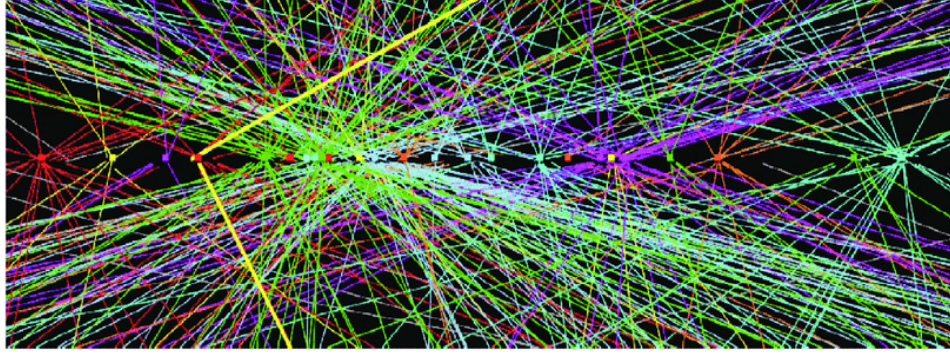


Figure 4.3: Visual example of pile-up in the ATLAS detector of a $Z \rightarrow \mu\mu$ event during Run-1 (with $L = 0.5 \times 10^{34} \text{cm}^{-2}\text{s}^{-1}$ in 8 TeV pp collision) [92].

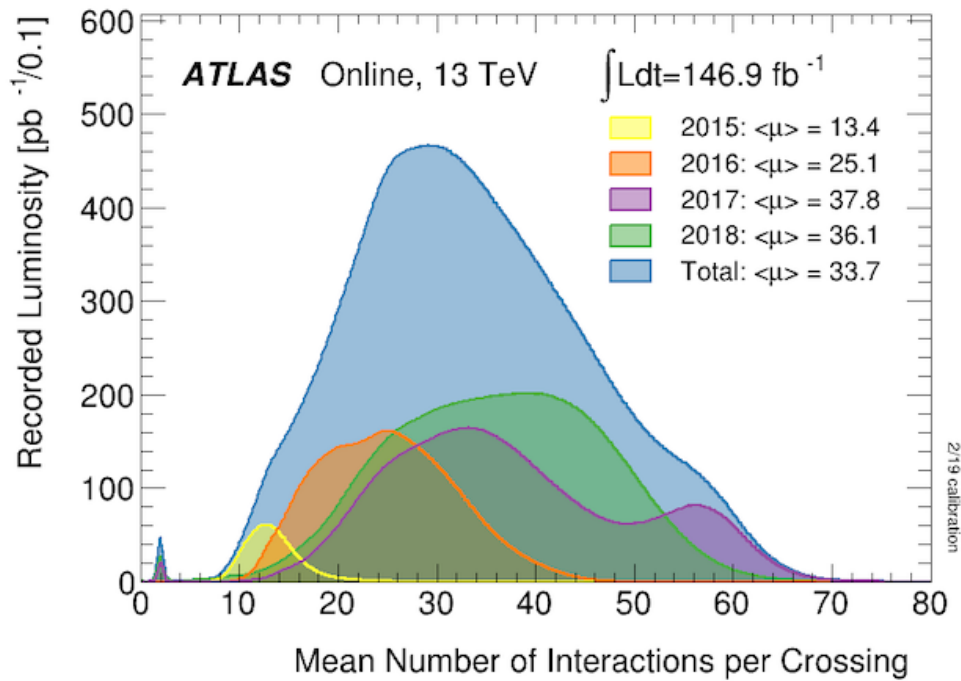


Figure 4.4: The mean number of interactions per bunch crossing, or pile-up, during Run-2 [65]. Showing both the total pile up (blue) and each year: 2015 (yellow), 2016 (orange), 2017 (purple), and 2018 (green).

4.3.2 Tracks and Vertices

Tracking is performed by the inner detector by pattern recognition. It works primarily in an “inside-out” fashion, meaning that tracks are initially reconstructed in the silicon detectors

(SCT) and then extrapolate the trajectory out to the transition radiation tracker (TRT) [93]. Inside the SCT and pixel detectors, clustering measurements are formed (of at least 3 hits) and used to create points in space that represent where a charged particle passed through the active material of the inner detector [94]. From here, track candidates are built, and Kalman filtering [95] and smoothing is used to add to or reject the track candidate (based on nearby hits). As one can imagine, the inner detector has a high pileup environment, and filtering out fake tracks or overlapping track segments with shared hits is important. A dedicated scoring module to resolve this issue is introduced, in which the score corresponds to the chance that a given track candidate represents the trajectory of the charged particle. Tracks that pass the scoring are then used as an input to find candidate tracks in the TRT. Finally, the final fit is conducted using a maximum likelihood that minimizes a global χ^2 .

The points in space of the detector where a pp interaction is said to have occurred are called primary vertices. Primary vertex reconstruction is done in a two-step process: finding and fitting [96, 97]. Finding obtains an estimate of the initial position for the vertex closest to the beamline. Fitting then fits the vertex location to possible compatible tracks, using an iterative procedure and a χ^2 fit.

4.3.3 Electrons and Photons

The electromagnetic calorimeter (ECAL) stops the majority of electrons and photons, and their energy measurements are obtained in the calorimeter using clustering algorithms. These algorithms are designed to group the calorimeter cells and determine the total energy in each cluster. For electrons and photons, ATLAS uses a sliding-window algorithm [98], which scans using a fixed-size rectangular window over the different layers of the electromagnetic calorimeter. Peaks in the energy distribution, indicating localized energy deposits consistent

with EM showers from bremsstrahlung, are identified by comparing the window's energy sum with its surroundings. Once a peak is found, the algorithm defines a candidate energy cluster around the highest-energy cell within the window and collects additional energy from nearby cells. The size and shape of the window are optimized to balance energy resolution and noise suppression, allowing the algorithm to effectively isolate electromagnetic signals from background activity and pileup. The candidate cluster is rejected or accepted based on if the energy is below or above the noise threshold, respectively. Once the candidate is accepted, this energy cluster can be matched to tracks in the inner detector for particle identification:

- If the cluster matches a reconstructed track belonging to a primary vertex: reconstructed as an electron
- If the cluster matches a reconstructed track belonging to a secondary vertex: reconstructed as a photon that decayed into an electron-positron pair
- If the energy cluster does not match any tracks: reconstructed as a photon

If the energy cluster is successfully matched to a track, the momentum of the reconstructed object is recalculated using the cluster energy and the momentum measurement obtained from the ID tracks.

Photons have a unique detector signature, making it hard for other particles to be misidentified as photons. Charged particles will leave tracks in the ID, which then rules them out as being reconstructed as photons. Even neutral hadrons, which do not leave tracks in the ID due to not carrying a charge, deposit their energy in the hadronic calorimeter, also ruling themselves out as being reconstructed as photons. Electrons, however, have a

more imitable detector signature. Charged pions decaying in the ECAL and having tracks associated with a primary vertex can be mis-identified and accidentally reconstructed as an electron. As ATLAS reaches higher luminosities, having a particular electron purity is important. Working points are defined based on electron purity [99]: “loose”, “medium”, and “tight”; which correspond to increasingly restrictive selection requirements:

- “loose” → prioritizing signal efficiency
- “medium” → trade-off between signal efficiency and background rejection
- “tight” → prioritize background rejection (the most “pure”)

As the selection requirements become more stringent, which aids in suppressing background, comes at the cost of also reducing the signal. Isolation variables can be used to quantify the amount of activity around a candidate object. They can be useful to further ensure proper identification. For electrons, there are two types of isolation cuts. The first variable, E_T^{cone20} , is the sum of the transverse energy of the topological clusters in a cone size $\Delta R = 0.2$ around the electron’s direction, subtracting the electrons energy deposit (of itself) and pileup effects. The second variable, $p_T^{varcone20}$, is the scalar sum of the transverse momenta of the ID tracks with $p_T > 1$ GeV associated with the primary vertex. It uses a variable radius cone of size $\Delta R = \min(10\text{GeV}/p_T^e, 0.2)$.

4.3.4 Muons

Muons do not interact with most of the detector, and are reconstructed by matching tracks in the inner detector (ID) with tracks in the muon spectrometer (MS). Both sets of tracks are first formed independently, then extrapolated to cover the full range of the detector, bridging

the sets of tracks together to form muon candidates [100]. In the MS, muon track candidates are built by fitting together hits from segments in the different subdetector layers (Monitored Drift Tubes (MDTs), Cathode Strip Chambers (CSCs), Resistive Plate Chambers (RPCs), and Thin Gap Chambers (TGCs) described in Section 3.7). As long as the tracks do not fall in the transition region between the barrel and end-cap, the track candidates are fitted using a global χ^2 fit.

There are four types of combined tracks are defined depending on which subdetectors were used in the reconstruction: Combined (CB) muons, Segment-tagger (ST) muons, Calorimeter-tagger (CT) muons, and Extrapolated (ME) muons. The combined (CB) muon algorithm combines the ID and MS tracks (which are formed independently), mostly using an outside-in pattern recognition where tracks are first formed in the MS then traced inwards to the ID tracks. The segmented tagged (ST) muon algorithm creates muon candidates if a track in ID is associated with at least one track segment in the MDT or CSC chambers in the MS when extrapolated. Primarily used in cases when a muon has low p_T or passes through a region of the MS where a single layer is hit. The calorimeter-tagged (CT) muon is the lowest purity of the different types of muons because algorithm is used when there is no information available from the MS but an ID track is matched to an energy cluster in the ECAL that is consistent with a minimum-ionizing particle. This category is optimized for the region $|\eta| < 0.1$ and momentum range $15 < p_T < 10$ GeV. The extrapolated (ME) muon algorithm is used when there is a track in the MS, but not a track in the ID. This category of muon is required to traverse at minimum two layers of MS chambers to provide a reliable track measurement, and three layers if in the forward region. It is primarily used in the region $2.5 < |\eta| < 2.7$ (the region not covered by the ID).

Muons are not completely immune to having other particles accidentally be mis-identified

as muons, even though very few particles besides muons and neutrinos actually reach the MS. High energy, charged pions, leaving tracks in the ID, could decay into a muon and neutrino inside the MS and thus be mis-identified and accidentally reconstructed as a muon.

Similar to electrons, muon identification, or purity, is performed by applying quality requirements that suppress background processes: “loose”, “medium”, “tight”, and “High- p_T ”. “Loose”, “medium”, and “tight” are similar to electrons, just for muons instead. “High- p_T ” aims to maximize the momentum resolution in tracks above 100 GeV. Muons also use isolation cuts, such as $E_T^{topcone20}$ and $p_T^{varcone20}$. The first is the calorimeter-based variable, $E_T^{topcone20}$, which is the sum of the transverse energy of the topological clusters in a cone size $\Delta R = 0.2$ around the muon’s direction, subtracting the muons energy deposit (of itself) and pileup effects. The second is the track-based variable, $p_T^{varcone20}$, which is the scalar sum of the transverse momenta of the ID tracks with $p_T > 1$ GeV associated with the primary vertex. It uses a variable radius cone of size $\Delta R = \min(10\text{GeV}/p_T^e, 0.2)$.

4.3.5 Jets

As particles collide, naively one might think there should exist bare stable quarks. However, color confinement negates this and instead the quarks produced in the collision quickly hadronize to form color-neutral bound states. These hadrons then decay to form more quarks (plus gluons), and then the cycle continues. Inside the ATLAS detector, specifically the hadronic calorimeter, this is seen as a shower, which we refer to as a jet. This process is shown in Figure 4.5.

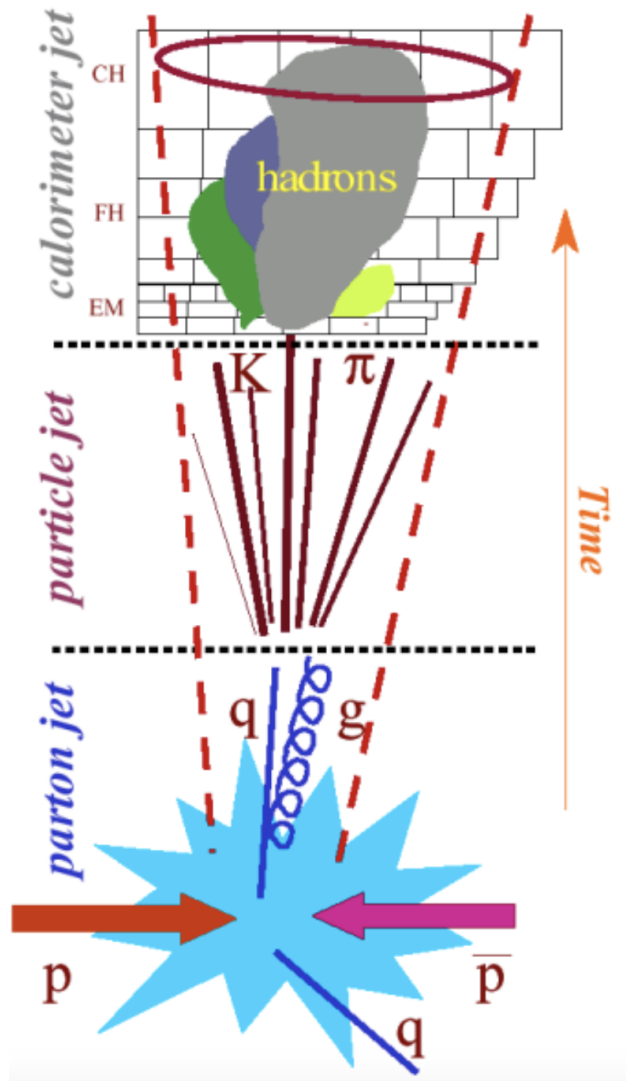


Figure 4.5: This figure illustrates the evolution of a jet from a high-energy parton (quark or gluon) produced in a proton-antiproton collision, which undergoes parton showering and hadronization into a spray of particles (e.g., pions, kaons). These particles form a particle jet, which deposits energy in the electromagnetic and hadronic calorimeters, resulting in a calorimeter jet. The diagram emphasizes the transition from parton-level to detector-level observables over time. Figure adapted from [101]

Clustering algorithms are used to group these particles in a jet with their calorimeter deposits forming energy clusters known as topological clusters, or topoclusters [102]. These algorithms cluster neighboring calorimeter cells based on if the total energy of the cluster is larger than the acceptable level of noise. Both the ECAL and HCAL energy deposits are

used with the purpose of identifying other particles, such as electrons and photons, which could be produced during hadronization.

The basic procedure for clustering algorithms are as follows:

1. The clustering algorithms rely on two distances 1: d_{ij} the distance between two particles or pseudoparticles, i and j , and 2: d_{iB} between i and the beam B .

$$d_{i,j} = \min(k_{t,i}^{-2}, k_{t,j}^{-2}) \frac{\Delta_{i,j}^2}{R^2} \quad (4.1)$$

$$d_{i,B} = k_{t,i}^{-2} \quad (4.2)$$

where $\Delta_{i,j}^2 = (\eta_i - \eta_j)^2 + (\phi_i - \phi_j)^2$, $k_{t,i}$, η_i , and ϕ_i is the transverse momentum, rapidity, and azimuth of particle i , respectively.

2. Calculate $d_{i,j}$ and $d_{i,B}$ for all possible topocluster pairs.
3. Find the minimum distance among all $d_{i,j}$ and $d_{i,B}$, and if
 - $d_{i,j}$ is the minimum \rightarrow objects i and j are removed and combined to form a new object k
 - $d_{i,B}$ is the minimum \rightarrow object i is classified as a jet and removed from the list
4. Repeat.

The different values of parameters result in different algorithms: anti- k_T algorithm, the usual k_T -algorithm, and the Cambridge/Aachen algorithm. In this thesis, the clustering is performed by the anti- k_T algorithm. The anti- k_T algorithm produces jets with circular shapes with radius R . The jet radius can be defined as

$$R = \frac{2p_m}{p_T} \quad (4.3)$$

with respect to the particle's mass m and transverse momentum p_T . In ATLAS, jets are either constructed with a radius parameter of $R = 0.4$ (called small-R jets) or $R = 1.0$ (called large-R jets). Small-R jets contain most of the radiation from quark/gluon jets. Large-R jets captures hadronic decays of heavy, boosted objects such as the top-quark and hadronically decaying W/Z and Higgs bosons.

4.3.5.1 Particle Flow

The Particle Flow (PFlow) [103] algorithm enhances jet reconstruction by combining tracking information from the Inner Detector (ID) with energy measurements from the calorimeters, ensuring minimal overlap between these subsystems. PFlow matches selected ID tracks to topo-clusters based on angular distances $(\Delta\eta, \Delta\phi)$ and evaluates the probability of energy deposition across multiple clusters. For matched tracks, the expected calorimeter energy deposition is subtracted from the topo-clusters, with the algorithm relying on a pion mass hypothesis for charged particles and calibrated using simulated single-pion samples. Unmatched topo-clusters are assumed to originate from neutral particles and remain unmodified. PFlow employs strict quality criteria for tracks, excluding poorly measured tracks, combinatorial fakes, and those from electrons and muons, while removing charged particles not associated with the primary vertex to mitigate pileup. For tracks depositing energy in multiple clusters, the algorithm iteratively subtracts energy from cells within concentric rings in $\eta - \phi$ space, starting with the highest energy density. Clusters are removed if their remaining energy is consistent with fluctuations or if their energy is fully accounted for by

matched tracks. This process results in a refined set of tracks and topo-clusters, effectively reconstructing jets without double-counting energy across subsystems.

4.3.5.2 Track-CaloClusters

Track-CaloClusters (TCCs) [104] are designed to enhance jet substructure reconstruction for high- p_T jets in events involving boosted particles. They combine energy scale information from topo-clusters, calibrated to the local hadronic scale, with angular information from tracks. The algorithm matches tracks to topo-clusters using a two-step process: tracks with extrapolation uncertainties (σ_{track}) larger than the topo-cluster width (σ_{cluster}) are rejected, while matched tracks are assigned a share of the topo-cluster energy based on their momentum fraction relative to other matched tracks. For unmatched topo-clusters or tracks, TCCs are created directly from their respective information. Unlike traditional algorithms, TCCs avoid direct comparisons between subdetectors, instead using scale factors from one detector as weights for the other. This approach improves resolution by leveraging track-to-vertex associations to mitigate pileup effects and focusing on momentum ratios rather than absolute p_T values, addressing challenges like reduced angular separation and insufficient calorimeter granularity at high energies.

4.3.5.3 Unified Flow Objects

While striving for perfect reconstruction algorithms, ATLAS constructed a new reconstruction algorithm to improve upon previous attempts [105]. TCC has good tagging performance at high p_T , but lag in the low p_T regime due to sensitivity in pileup. Whereas jets reconstructed from PFlow objects introduce an overall baseline definition, their poor tagging performance is apparent at high p_T . The Unified Flow Object (UFO) jet definition combines

the optimal aspects of PFlow and TCC, along with additional pileup mitigation algorithms to help optimize the performance across a wide kinematic range.

Pile-up mitigation techniques are applied before jet reconstruction to help reduce contamination from additional pp interactions and improve jet quality. There are three different techniques used to mitigate pileup:

- Constituent Subtraction (CS) [106] method performs area subtraction at the jet constituent level by using a ghost (massless) particles and neighboring topo-clusters.
- SoftKiller (SK) [107] method applies a p_T cut on an event-by-event basis to input objects to help remove soft objects, and is applied after the CS algorithm .
- Soft-Drop (SD) [108] method removed wide-angle soft radiation by employing the Cambridge-Aachen algorithm and re-clusters the constituents of the large-R jet into an angle-ordered jets (from widest to smallest angle radiation), and based on the splitting kinematics, removes the low p_T branch.

The reconstruction of UFOs first begins by applying the PFlow algorithm. When tracking information is included, charged PFlow objects matched to primary vertices can be used to robustly reject charged particles originating from pileup interactions. Then, after tracks that were used in the PFlow subtraction are removed, pileup mitigation algorithms are applied (CS+SK). Then, the TCC algorithm is applied to the remaining collection of both neutral and charged PFlow objects. A flow-chart walking through how the algorithm is performed is shown in Figure 4.6.

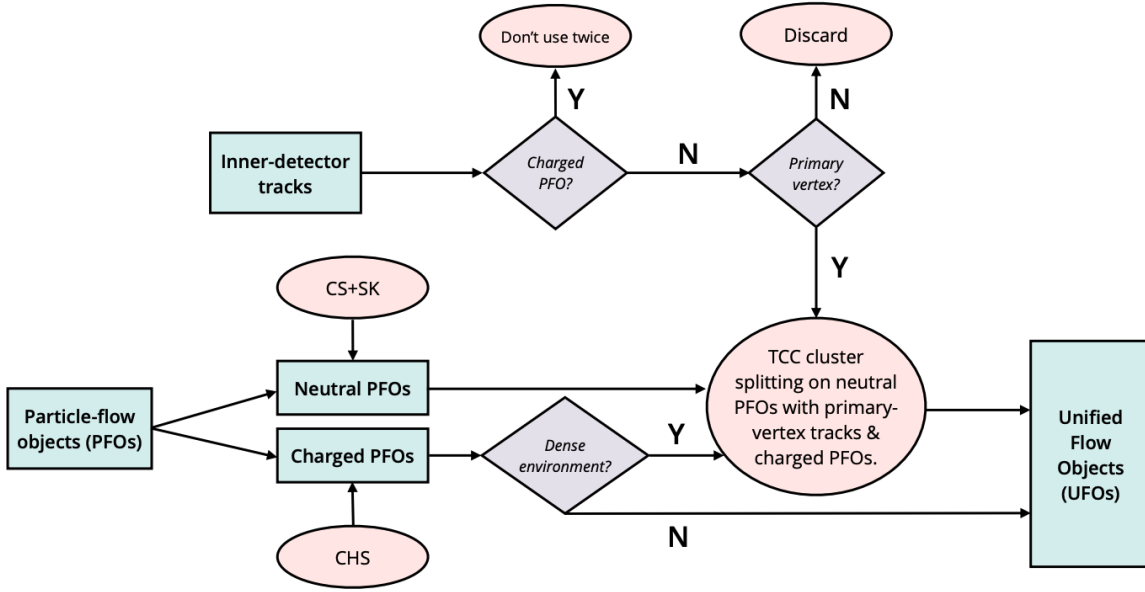


Figure 4.6: Illustration of the UFO reconstruction algorithm [105].

The use of UFO jets brings significant improvements, which will be further explored in Chapter 6.

4.3.6 Missing Transverse Energy

Missing transverse energy [109], MET or E_T^{miss} , can be attributed to particles not interacting with the detector, such as neutrinos, or object mis-reconstruction, such as a mis-reconstructed jet. It is reconstructed by negative sum of the all physics objects and ID tracks not associated with them in the transverse direction. Due to conservation of momentum, the total transverse momentum from all particles produce in the collision must be zero. However, in practicality this is not always the case, due to sources listed earlier, so the amount of MET can be quantified as

$$E_T^{miss} = \sqrt{(p_x^{miss})^2 + (p_y^{miss})^2} \quad (4.4)$$

Where p_x^{miss} and p_y^{miss} are the components of the momentum vector in the transverse plane.

4.4 Data Sets and Formats

The term “big data” has become a buzzword in today’s society. However, in the case of CERN, it is more than just a buzzword. During Run-2 at the LHC, the ATLAS experiment collected about 160 petabytes (PB) of data [110] (1 PB = 1 million GB). For every analysis within ATLAS to run over that amount of data would be (1) very computationally expensive, and (2) take a very long time. Thus, what is actually saved is reduced down. There are about 600 billion collisions per second inside the ATLAS detector, and the trigger is used to filter the data, as mentioned in Section 3.8. Events that get triggered on are then processed through reconstruction, in which physics objects such as electrons, muons, and photons (every track, every parameter of the event) are saved into Analysis Object Data (AODs) [111]. These files still are quite large, on the order of about 400 kB per event [112], and are centrally reduced according to the needs of physics groups, producing Derived-AODs (DAODs). The DAODs keep certain physics objects, without having any analysis-specific restrictions applied which reduces the size in which analysis could have to run over. However, this is then further reduced to Compact-AODs (CAODs) which apply some basic preselection criteria, and this is typically done on the analysis-level. For the full run-2 dataset, we would have to produce about 10 to 50 billion MC events to match the 160 PB of data if none of the size reduction was done.

Reducing information between the derivation steps can be achieved via several techniques [113, 114]:

- *Skimming*: basic event selection where entire events can be removed (usually done between DAOD \rightarrow CAOD)
- *Trimming*: objects can be removed and reduces the size of each individual event (usually done between AOD \rightarrow DAOD)
- *Slimming*: variables within the objects can be removed, such as when very detailed information about the object is no longer needed
- *Thinning*: only selected object information is saved, and other information not pertaining to those objects are removed

All the different variations of “AODs” are considered object-oriented, meaning that the data is structured as collections of high-level physics objects (e.g., electrons, muons, jets), each with associated attributes and methods that reflect their physical properties. In the final reduction step, producing N-tuples, the data is no longer organized in this hierarchical, object-based way but rather in a flat format, where quantities are stored in vectors with each element corresponding to a different collision event. This flat structure ensures consistency across vectors, where the same index in different variables refers to the same event, allowing for efficient access and analysis tools like ROOT [115]. Another advantage to using this non-object-oriented framework is that it is quite small in size and only contains relevant information to the physics analysis. From N-tuples, physics analyses, such as the VV+VH Semi-leptonic analysis, can easily run over data efficiently and optimize the analysis with subsequent iterations of analyzing data and MC.

Chapter 5. $t\bar{t}$ Jet-Tagging Scale Factors

5.1 Introduction

Identifying jets from hadronic decays of top quarks and W/Z bosons is essential for enhancing the sensitivity of physics analyses within ATLAS. Jet reconstruction algorithms play a key role in revealing the internal structure of physics jets, enabling us to exploit this substructure to probe deeper into the underlying physics. Jet reconstruction is a complex task, outlined in Chapter 4. Until recently, ATLAS relied solely on the TCC algorithm for large-R jets, and PFlow for small-R jets [116]. Both algorithms used inner detector tracks and calorimeter measurements to reconstruct the jets, but were optimized in two different kinematic ranges. Specifically, TCC was found to have a poor jet mass resolution for top-jets (W-jets) for $p_T < 1500$ (800) GeV. The introduction of a new jet definition, the Unified Flow Object (UFO), enhances overall jet reconstruction by unifying both TCC and PFlow together, achieving an optimal performance across a broad kinematic range. The UFO jet definition enhances the reconstruction of various jet substructure (JSS) variables by providing a more precise and detailed representation of the jet's internal structure. This improvement is particularly valuable in the context of boosted top quark and W/Z boson tagging, where decay products are highly collimated and traditional reconstruction techniques may struggle to resolve the substructure. By leveraging combined information from the calorimeter and inner detector, the UFO algorithm enables more accurate identification of substructure patterns such as mass, energy flow, and splitting scales, ultimately leading to better signal discrimination in complex final states.

This work, which was used to fulfill the ATLAS authorship qualifications ¹, presents a detailed signal efficiency measurement of boosted object taggers, which are designed to leverage a variety of jet substructure (JSS) variables within large-R UFO jets. The signal efficiency measurement quantifies the taggers’ ability to correctly identify true signal events, such as hadronically decaying top quarks or W/Z bosons, while distinguishing them from background processes. This involves evaluating the taggers’ performance across different kinematic regions and assessing how well they retain genuine boosted objects, which is critical for optimizing selection criteria in physics analyses. The efficiency is calculated for both data and MC, and the differing in values is used as a corrective factor, also known as a scale factor, which is used to calibrate the jets. Uncertainties are discussed in Subsection 5.3.2. Performance of the taggers is shown in Subsection 5.3.4.2. Finally, the resulting signal efficiencies and scale factors are shown in Subsection 5.3.4.3.

5.1.1 Jet Substructure Variables

Jet substructure refers to the internal structure of a jet. JSS variables are observables which correspond to the radiation pattern inside hadronic jets, and have been constructed to probe the hard structure of a jet. JSS variables are used to derive selection cuts for cut-based taggers and are inputs features into DNN-based taggers. Some relevant JSS variables considered here are:

- Jet Mass The jet invariant mass is defined as

$$m^2 = \left(\sum_i k_i \right)^2 \tag{5.1}$$

¹every member of the ATLAS collaboration has to perform a task which is a benefit to the whole collaboration, and in return receives authorship for ATLAS papers

which is the sum over all the particles, k_i , clustered in the jet [117].

- N-subjettiness Using the number of subjets, N , in a jet could be used to discriminate between jets [118]. The jet axis is an important characteristic of this variable and is based on the momentum. N-subjettiness can be defined as:

$$\tau_N^\beta = \frac{1}{p_{T,J}} \sum_{i,N} p_{T,i} \min(R_{i,1}, R_{i,2}, \dots, R_{i,N})^\beta \quad (5.2)$$

for a jet J with transverse momentum $p_{T,J}$ along with particles i each with $p_{T,i}$. The distance between particle i and the closets subjet in the $n - \phi$ plane in $R_{i,N}$, and the sensitivity to collinear radiation is β . In this thesis, the jet axis used is known as the winner-takes-all (WTA) jet axis, which is determined by reclustering the jet using the k_t algorithm followed by a WTA recombination scheme. Jet reclustering involves taking the original jet constituents and applying a sequential clustering algorithm, such as the k_t algorithm, to reorganize their structure, often to extract features like subjets or to define a more robust jet axis. The WTA recombination scheme differs from traditional schemes by assigning the direction of each clustered pair to the constituent with the higher transverse momentum, rather than computing a momentum-weighted average. This approach leads to a jet axis that is less sensitive to soft radiation and pile-up, providing a more stable and physically meaningful axis for jet substructure analyses. Using this WTA axis, jet substructure variables, denoted as $\tau_1, \tau_2, \tau_3, \tau_4$, are computed. These N-subjettiness variables quantify how well a jet can be described as being composed of 1, 2, 3, or 4 subjets, respectively, and play a crucial role in distinguishing between different types of boosted objects, such as top quarks or W/Z bosons. Another quantity used is the ratios of subsequent n-subjettiness

$$\tau_{N,N-1}^\beta = \frac{\tau_N^\beta}{\tau_{N-1}^\beta} \quad (5.3)$$

denoted as $\tau_{12}, \tau_{23}, \tau_{34}$.

- Splitting Scales These are determined using anti- k_t clustering objects together according to their distance from each other. The splitting scale observables ($\sqrt{d_k} = \min(\sqrt{d_{i,j}}, \sqrt{d_{i,B}})$) and the ratio of observables ($\sqrt{d_{12}}, \sqrt{d_{23}}, \sqrt{d_{34}}$), are used to help with modelling of QCD effects [119]. The splitting scale helps distinguish QCD jets from signal jets by quantifying the hardness of the jet's internal structure, where signal jets tend to have larger splitting scales due to energetic substructure. It also serves as a tool to validate and tune QCD modeling in MC simulations by comparing predicted and observed radiation patterns.
- Energy Correlation Functions Generalized N-point correlation functions (ECFs) which identify N-prong jet substructure by using energies and pair-wise angles of particles, without a subjet finding procedure [120]. It is defined as

$$ECF(n, \beta) = \sum_{i_1 < i_2 < \dots < i_n} \left(\prod_{a=1}^n p_{T,i_a} \right) \left(\prod_{b=1}^{n-1} \prod_{c=1}^n R_{i_b i_c} \right)^\beta \quad (5.4)$$

where n is the number of particles to be correlated, $R_{i,j}$ is the distance between particle i and particle j , and β is the angular weight of the distance between particles.

Ratios of EFCs can be used to construct a variety of jet substructure observables that provide insight into the internal composition of jets, particularly their N-prong topology:

$$e_n^{(\beta)} = \frac{ECF(n, \beta)}{ECF(1, \beta)^n} \quad (5.5)$$

These observables are designed to quantify how the energy is distributed among jet constituents and how that distribution reflects the underlying particle decay structure. For example, in the case of two-prong decays, such as those from boosted W or Z bosons, the D_2 and C_2 (shown in eq. (5.6)) variables are particularly effective as they probe the energy correlations at different angular scales to distinguish signal jets from the typically more diffuse QCD background. For three-prong structures, like those from hadronic top quark decays, the C_3 variable is sensitive to the more intricate radiation patterns associated with the three-prong topology. In addition to these traditional observables, the L-series (L_1 through L_5 shown in eq. (5.7)) has been introduced, defined through ratios of Energy Flow Correlator Generalizations (ECFGs), offering a more flexible and fine-grained approach to analyzing jet structure. Notably, L_2 and L_3 have been incorporated as input features in deep neural network (DNN) top taggers, where their sensitivity to substructure enhances classification performance in identifying boosted top quarks.

$$C_2^{(\beta)} = \frac{e_3^{(\beta)}}{\left(e_2^{(\beta)}\right)^2}, \quad D_2^{(\beta)} = \frac{e_3^{(\beta)}}{\left(e_3^{(\beta)}\right)^3}, \quad (5.6)$$

$$L_1 = \frac{e_2^{(\beta=1)}}{e_1^{(\beta=2)}}, \quad L_2 = \frac{e_3^{(\beta=1)}}{\left(e_1^{(\beta=2)}\right)^{3/2}}, \quad (5.7)$$

$$L_3 = \frac{e_1^{(\beta=1)}}{\left(e_3^{(\beta=1)}\right)^{1/3}}, \quad L_4 = \frac{e_2^{(\beta=2)}}{\left(e_3^{(\beta=1)}\right)^{4/3}}, \quad L_5 = \frac{e_2^{(\beta=2)}}{e_4^{(\beta=1)}}.$$

- Planar Flow A measure of the degree to which a jets energy is evenly spread across the plane of the jet with respect to being spread linearly [121]. First constructing a two-dimensional matrix I:

$$I_w^{kl} = \frac{1}{m_J} \sum_i \frac{p_{i,k} p_{i,l}}{w_i w_i} \quad (5.8)$$

where m_J is the jet mass, w_i is the energy of the i th jet, and $p_{i,k}$ and $p_{i,l}$ are the k and l components of its transverse momentum (with respect to the jet axis). The Planar flow is then

$$P = \frac{4\det(I_w)}{\text{tr}(I_w)^2} \quad (5.9)$$

- Fox-Wolfram moments Rotationally invariant observables which describe how compatible the event topology is with each of the spherical harmonics [122].
- N_{trk}^{500} The number of inner detector tracks with $p_T > 500$ MeV.
- Q_w The invariant mass associated with a three-body decay or splitting process, specifically in the case of $M \rightarrow A + B + C$, where a parent particle M decays into three daughter particles. [123] This quantity is calculated using the four-momenta of the decay products A , B , and C , and reflects the total energy and momentum content of the system in a Lorentz-invariant way. It helps identify boosted top quarks by reconstructing an on-shell W boson within a top quark jet.
- Thrust Major Thrust Major (TM) is a jet substructure variable that characterizes the spread of energy flow within a jet by measuring how jet constituents are distributed in

the transverse plane, perpendicular to the main thrust axis. [124] It is defined as

$$T_{\text{Major}} = \max_{\vec{n}_\perp} \left(\frac{\sum_i |\vec{p}_{T,i} \cdot \vec{n}_\perp|}{\sum_i |\vec{p}_{T,i}|} \right) \quad (5.10)$$

where $\vec{p}_{T,i}$ is the transverse momentum of each jet constituent, and \vec{n}_\perp is a unit vector orthogonal to the thrust axis. TM reflects how widely the constituents are spread perpendicular to the dominant momentum direction—lower values indicate narrow, pencil-like jets typical of QCD backgrounds, while higher values suggest broader, more isotropic jets often associated with boosted W/Z bosons or top quark decays. As such, TM is a useful observable for identifying jets with multi-prong substructure in tagging applications.

5.2 Taggers

Tagger algorithms apply a certain selection, or cuts, on jet variables, such as mass or p_T , in order to determine if a jet was originated by a certain particle. A top tagger has been optimized to identify jets originating from top quark decays, while a W boson tagger has been optimized to identify jets originating from hadronic decays of W bosons. Both taggers have to be robust in rejecting quark or gluon initiated jets (QCD jets). Since switching to the new UFO jet definitions, the taggers are able to exploit various jet substructure (JSS) variables for performance gain. ATLAS analyses use a combination of both cut based and machine learning taggers.

5.2.1 Truth Information

At truth-level two categories of top-quark jets are used based on the topology of the decay product: contained jets and inclusive jets. A contained top-jet is a jet where the full decay product is contained inside the large-R jet. An inclusive top-jet is when only when there is only a partial containment of the top decay product inside the reconstructed jet.

5.2.2 Top Taggers

The top tagger is actually composed of two deep neural network (DNN) taggers: one to identify the inclusive top quark jets and the other to identify the fully contained top quark jets. The JSS variables found to have the most impact in discriminating between top quark jets and QCD jets are: N-subjettiness ($\tau_1, \tau_2, \tau_3, \tau_4$), the generalized energy correlation functions and their ratios (ECF1, ECF2, ECF3, C2, D2, L2, L3), Q_w and thrust major TM [125]. Other variables used are the splitting scales $\sqrt{d_{12}}$ and $\sqrt{d_{23}}$.

5.2.3 W Taggers

There are three main types of W/Z taggers for UFO jets: a three variable (3-var) cut-based tagger, a deep neural network (DNN) W tagger, and an adversarial deep neural network (ANN) W/Z tagger. The 3-var tagger uses rectangular cuts in large-R jet mass, D2, and the number of ID tracks with $p_T > 500$. The DNN W tagger is not used on its own, but rather to compete with a trained adversarial network, then the ANN is trained to infer the jet mass from the outputs of the DNN thus making its mass decorrelated. The ANN is minimized using a loss function. The DNN consists of 3 fully connected layers of 32 nodes, and uses the JSS variables: D_2 , C_2 , τ_{21} , Fox-Wolfram moment R_2^{FW} [126], planar flow P [127], angularity

α_3 [128], aplanarity A , Z_{cut} [129], the splitting scale $\sqrt{d_{12}}$ [130] and $kt\Delta R$ [131].

5.3 Scale Factor Determination

5.3.1 Strategy

Many ATLAS analyses rely on MC simulation to reliably reproduce data. Algorithms are designed to select physics objects within a collision event, both in real data and simulation. Thus, there is a risk of difference in performance due to imperfect detector knowledge and inaccuracies in the physics understanding of these complex processes. This difference is quantified by measuring the efficiency, ϵ , of different objects as a function of p_T :

$$\epsilon = \frac{N_{tagged}}{N_{total}} \quad (5.11)$$

where N_{tagged} is the number of objects tagged, or selected, and N_{total} is the total number of objects [125].

The difference in efficiency between data and MC is used to correct the MC using a quantity called a scale factor:

$$SF = \frac{\epsilon_{data}(p_T)}{\epsilon_{MC}(p_T)} \quad (5.12)$$

which is the ratio of the efficiency in data, ϵ_{data} , to the efficiency in MC, ϵ_{MC} , as a function of p_T [125].

In practice there are two methods used to actually accomplish this: Tag and Probe, and Template Fit method. The tag-and-probe method and template fit method are used together to produce accurate $t\bar{t}$ scale factors.

The tag-and-probe method is used to create a clean, well-defined sample by selecting $t\bar{t}$ events where one top quark decays leptonically (tag) and the other hadronically (probe). In this approach, the leptonic decay, $t \rightarrow Wb \rightarrow \ell\nu b$, is used as the tag, providing a clean, well-identified reference point with high signal purity. The hadronic decay, $t \rightarrow Wb \rightarrow qq'b$, serves as the probe, which is then evaluated for tagging efficiency. The probe jets are categorized based on their angular separation, typically using ΔR : top jets have a broader structure with $\Delta R > 1$, while W jets are more collimated with $\Delta R < 1$. The probe sample is then split into passing and failing categories based on whether the jets meet the tagging criteria, where “passing” is considered being top/W tagged. This approach provides a robust, data-driven measurement of the tagging efficiency for the hadronic top decay, reducing reliance on simulation.

The template fit method is then applied to the probe sample, fitting the observed distributions of discriminating variables, such as jet mass, N-subjettiness, or top-tagging scores, to separate signal (top jets) from background. These templates, typically based on MC simulations or control regions in data, capture the characteristic shapes of the expected signal and background distributions. The observed distribution is then decomposed into its signal and background components using a likelihood fit, which adjusts the relative contributions of each template to best match the data (using a χ^2 test ²). This approach provides a robust, data-driven estimate of the tagging efficiency and background contamination, reducing reliance on purely simulation-based estimates and allowing for more precise measurements.

²A χ^2 test is a goodness-of-fit test used to reflect the level of agreement between observed and expected histograms [132]:

$$\chi^2 = \sum_{i=1}^N \frac{(n_i - \nu_i)^2}{\nu_i} \quad (5.13)$$

Where i is the number of bins, $\mathbf{n} = (n_1, \dots, n_N)$ is the data, and $\mathbf{v} = (v_1, \dots, v_N)$ is the mean values. More information can be found in [132].

This combination allows for precise extraction of the signal fraction, leading to an accurate measurement of the tagging efficiency and resulting scale factors. These scale factors are essential for correcting MC simulations to match real-world data.

5.3.2 Systematic Uncertainties

There are various uncertainties associated with jets and are therefore important to propagate to the SF values. They can be split between experimental and theory (or modeling) uncertainties.

The experimental uncertainties refer to the uncertainties associated to the reconstruction of physical objects identified in the ATLAS detector. With many of these uncertainties, there is uncertainty in both the resolution (peak width) and the scale (where the measurement falls on the x-axis). For electrons and muon triggers, the tag and probe method is used to evaluate systematic uncertainties on the trigger efficiency.

For jets, there are also the following experimental uncertainties to consider:

- Energy Scale: median shift in the scale measurement
- Energy resolution: uncertainty in the resolution of the jet energy distribution
- Pile up: extra energy comes from the initial hard scattering or extra jets could be detected, so pile-up refers to the estimation of this extra energy and is subtracted using pileup subtraction/ suppression methods (previously described in Section 4.3)
- Punch-through: some energetic jets can punch through the calorimeter into other subdetectors (or punch through all of ATLAS), and we gain an understanding of how much energy can be lost on average due to this effect so that we can account for it

- Flavor composition/ response: uncertainty in the detector responding differently to the internal composition of the jet (i.e. the response will differ if it is composed of more heavy quarks/ hadrons versus lighter quarks/ hadrons)
- High p_T : uncertainty coming from single-pion measurements of the E/p (or, the measurement/calibration of calorimeter (E) via track momentum matching (p)), which is the dominant JES uncertainty at high- p_T
- Jet η inter-calibration: to balance forward and central jets, there is a calibration in place to ensure there is a uniform distribution in *eta*
- MET soft track terms: due to pile up at low energy (for soft collisions), we have a large uncertainty at low MET
- B-tagging: b-jets behave differently than other quark-jets (in tracking, etc.), so we have to add in a special factor to account for this, and the b-tagging uncertainty is the uncertainty to this extra factor

There is also uncertainty related to the MC generators used to produce the signal and background processes, referred to above as the modeling uncertainties. The nominal generator for $t\bar{t}$ and s-channel, t-channel, and W t-channel single top production events in semileptonic final states are generated with `Powheg+Pythia8` (with the A14 tune), where `Powheg` handles the matrix element (hard scattering), and `Pythia8` handles the showering and hadronization. There are other generators which model nature slightly differently, as mentioned in Chapter 4 and serve as alternate predictions. The main result uses the nominal generator, and then compared to results from other event generators, resulting in a comprehensive result that contains all variations, covering ideally all possible variations that

could arise in nature. The generator `Powheg+Herwig` (with H7UE tune) is used to study the uncertainties in parton showering and hadronization modeling. The uncertainty in the choice of NLO matching between the matrix element and parton showering is explored using samples generated with `aMCNLO` (+`pythia8` for the parton showering). Uncertainty from the different NLO corrections for initial state radiation (ISR) and final state radiation (FSR) in `Pythia` is included as an independent uncertainty.

5.3.3 Event Selection

Events are selected in order to provide the highest purity of signal top quark jets in both data and MC. The first requirement imposed is to pass either the electron or muon trigger, based on the p_T thresholds. Then, there are requirements to separate into electron and muon channels. There must be exactly one electron [muon] with $p_T > 25$ GeV and no additional muons [electrons] with $p_T > 25$ GeV, and also be matched to the triggering lepton in order for the event to be considered in the electron [muon] channel.

Small-R jets are reconstructed from PFlow objects, described in Subsection 4.3.5.1, using the anti-kt algorithm with a radius parameter $R = 0.4$. The small-R jet events are required to have at least one small-R jet b-tagged using the DL1r algorithm with a 77% efficiency working point. Large-R jets are reconstructed from UFO objects using the anti-kt algorithm with a radius parameter $R = 1.0$, and are groomed with CS+SK and SoftDrop. The large-R jet events are selected if they contain at least one large-R jet with $p_T > 150$ GeV.

Missing transverse energy (MET), E_T^{miss} , in the event is reconstructed as the negative sum of the pT of the leptons and jets. A minimum requirement of $E_T^{miss} > 20$ GeV is imposed on events, as well as the sum of the MET and the transverse mass of the leptonically decaying W boson, $m_{W,T}$, is imposed:

$$E_T^{miss} + m_{W,T} > 60\text{GeV} \quad (5.14)$$

and $m_{W,T}$ is defined as $m_{W,T} = \sqrt{2p_T^l E_T^{miss}(1 - \cos \Delta\phi)}$, and p_T^l is the transverse momentum of the lepton, and $\Delta\phi$ is the azimuthal angle difference between the lepton momentum and the direction of MET of the event [125].

Finally, ΔR is used to separate the top and W enriched regions, in which the large-R jets originate from the hadronic top quark and W boson decay, respectively.

- Top Selection: $\Delta R(b - jet, large - Rjet) < 1.0$, sample is enriched in boosted top quarks
- W Selection: $\Delta R(b - jet, large - Rjet) > 1.0$, sample is enriched in boosted W jets

Additionally, a selection on large-R jet of p_T range to only include jet with $p_T > 350$ GeV is applied in the top selection.

5.3.4 Results

The JSS variables from Subsection 5.1.1 are shown in Figure 5.1 to Figure 5.7 and provide a good visualization of the input variables for the different taggers. The resulting tagger performance plots for these taggers are shown in Figure 5.8 to Figure 5.10, which demonstrates the accuracy of the tagger being used. Then the resulting efficiencies, and the final SF values for each tagger are presented.

The $t\bar{t}$ and single-top MC samples are categorized based on whether partons from the top-quark decay are contained within the large-R jet, with classification determined using the truth jet that is matched to the reconstructed large-R jet. The $t\bar{t}(\text{top})$ category refers to

if all partons from the top decay, and the $t\bar{t}(W)$ and single-top (W) category refers to if the two light quarks from the W decay are contained within the truth jet. The $t\bar{t}(\text{other})$ and single-top (other) categories contain if there is no truth jet matched to the reco-level large-R jet.

5.3.4.1 Kinematic Variables

As mentioned previously, various substructure variables are used as inputs to the top- and W- taggers.

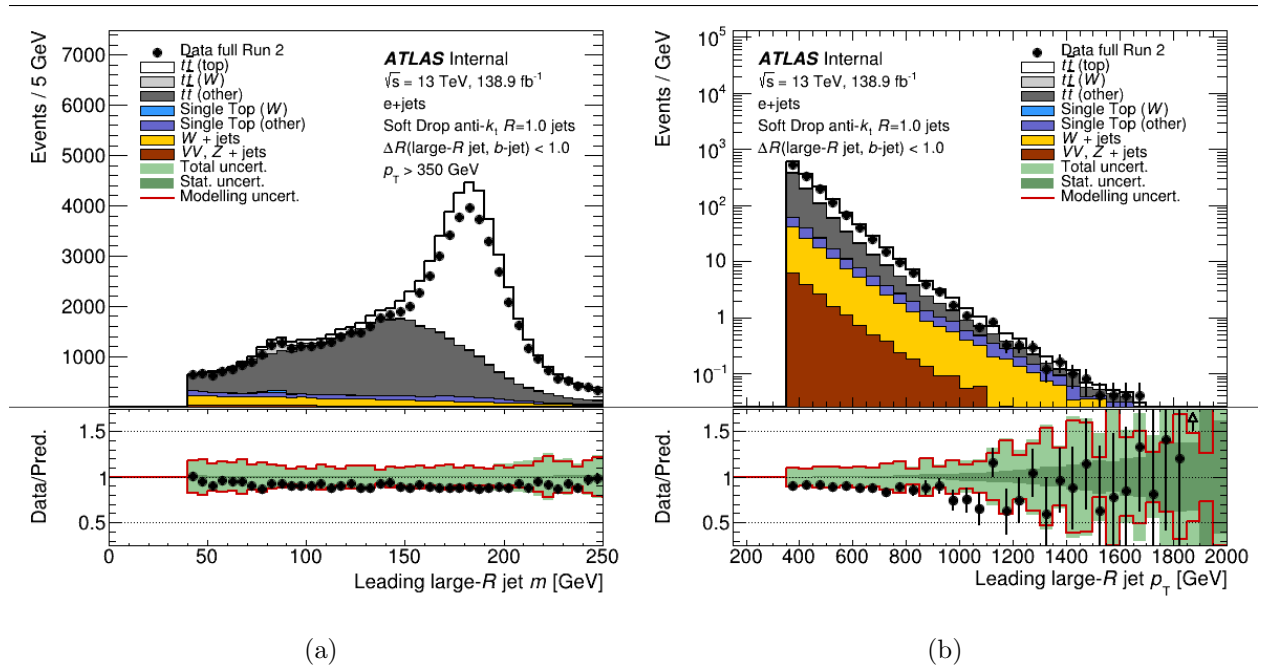


Figure 5.1: Distribution of mass (a) and p_T (b) in data and MC simulation for the leading large-R jet in events that pass selection criteria for a top-enhanced single-electron $t\bar{t}$ events. The statistical uncertainty is shown by the dark green, and total uncertainty is shown by light green. The red line which shows the $t\bar{t}$ modelling uncertainty is also overlaid on top of the statistical uncertainty, highlighting that it is the dominant systematic almost everywhere.

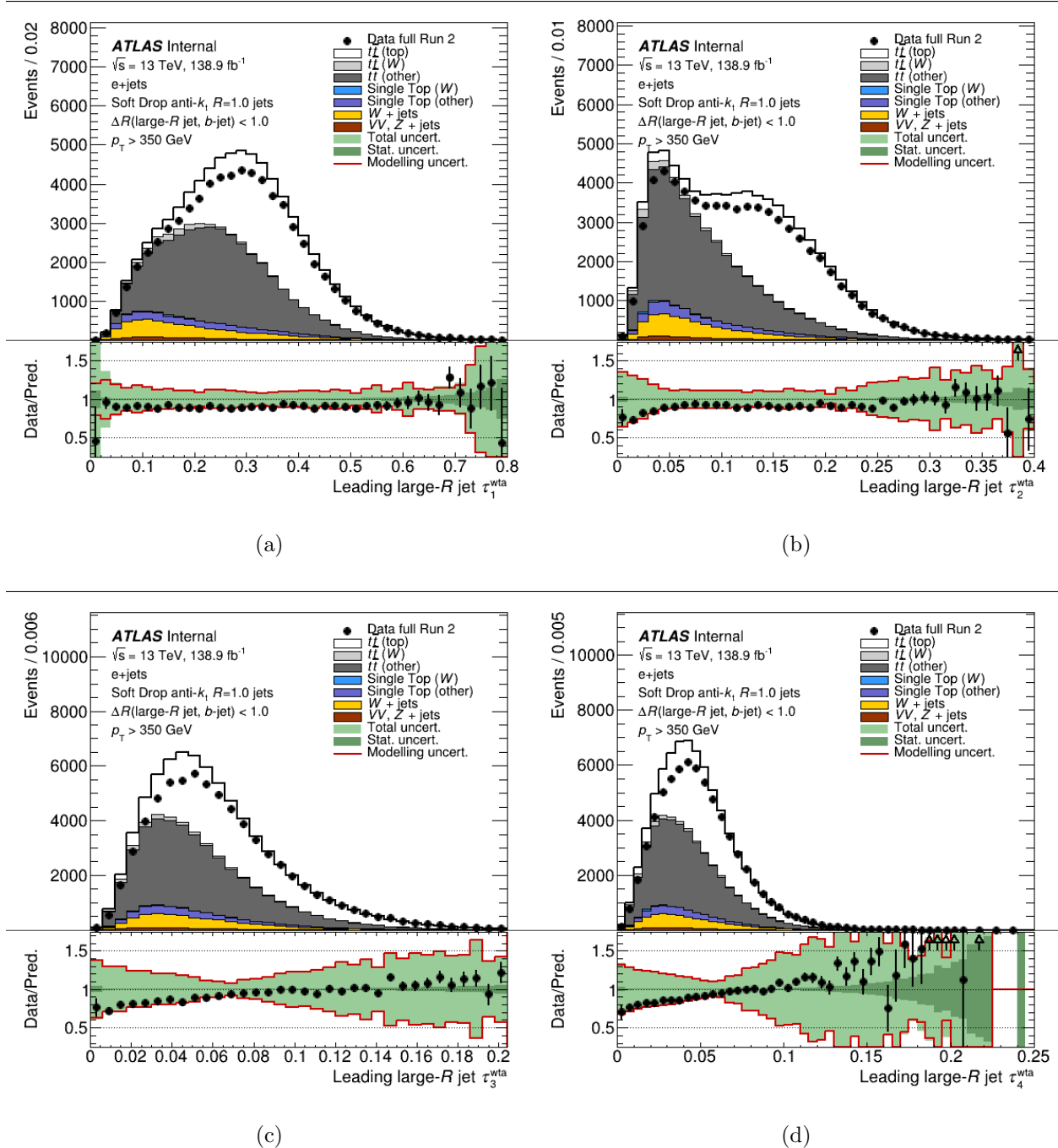


Figure 5.2: Distribution of N -subjettiness and their ratios in data and MC simulation for the leading large- R jet in events that pass selection criteria for a top-enhanced single-electron $t\bar{t}$ events. The statistical uncertainty is shown by the dark green, and total uncertainty is shown by light green. The red line which shows the $t\bar{t}$ modelling uncertainty is also overlaid on top of the statistical uncertainty, highlighting that it is the dominant systematic almost everywhere.

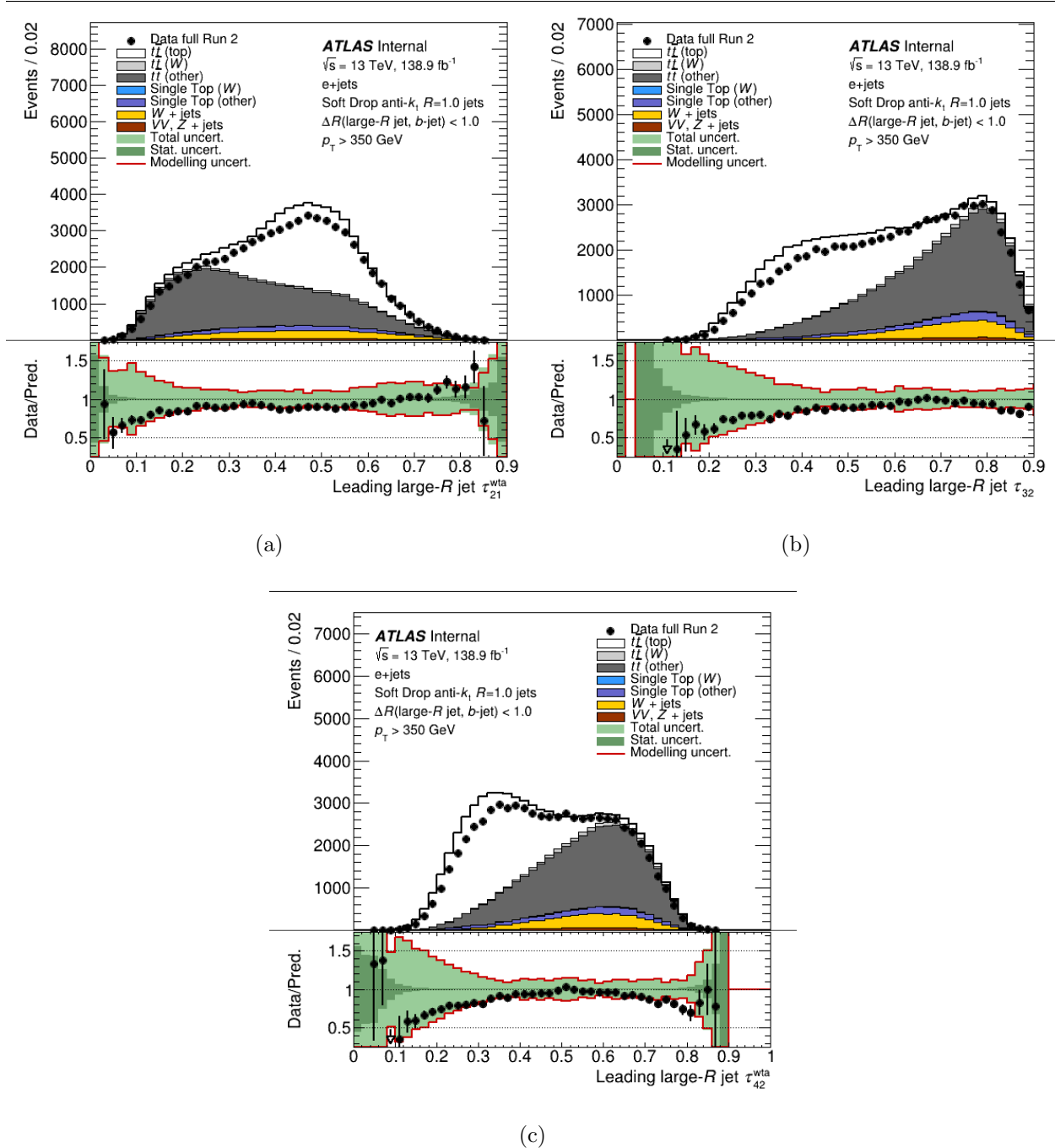


Figure 5.3: Continuation of Figure 5.2. Distribution of N-subjettiness and their ratios in data and MC simulation for the leading large-R jet in events that pass selection criteria for a top-enhanced single-electron $t\bar{t}$ events. The statistical uncertainty is shown by the dark green, and total uncertainty is shown by light green. The red line which shows the $t\bar{t}$ modelling uncertainty is also overlaid on top of the statistical uncertainty, highlighting that it is the dominant systematic almost everywhere.

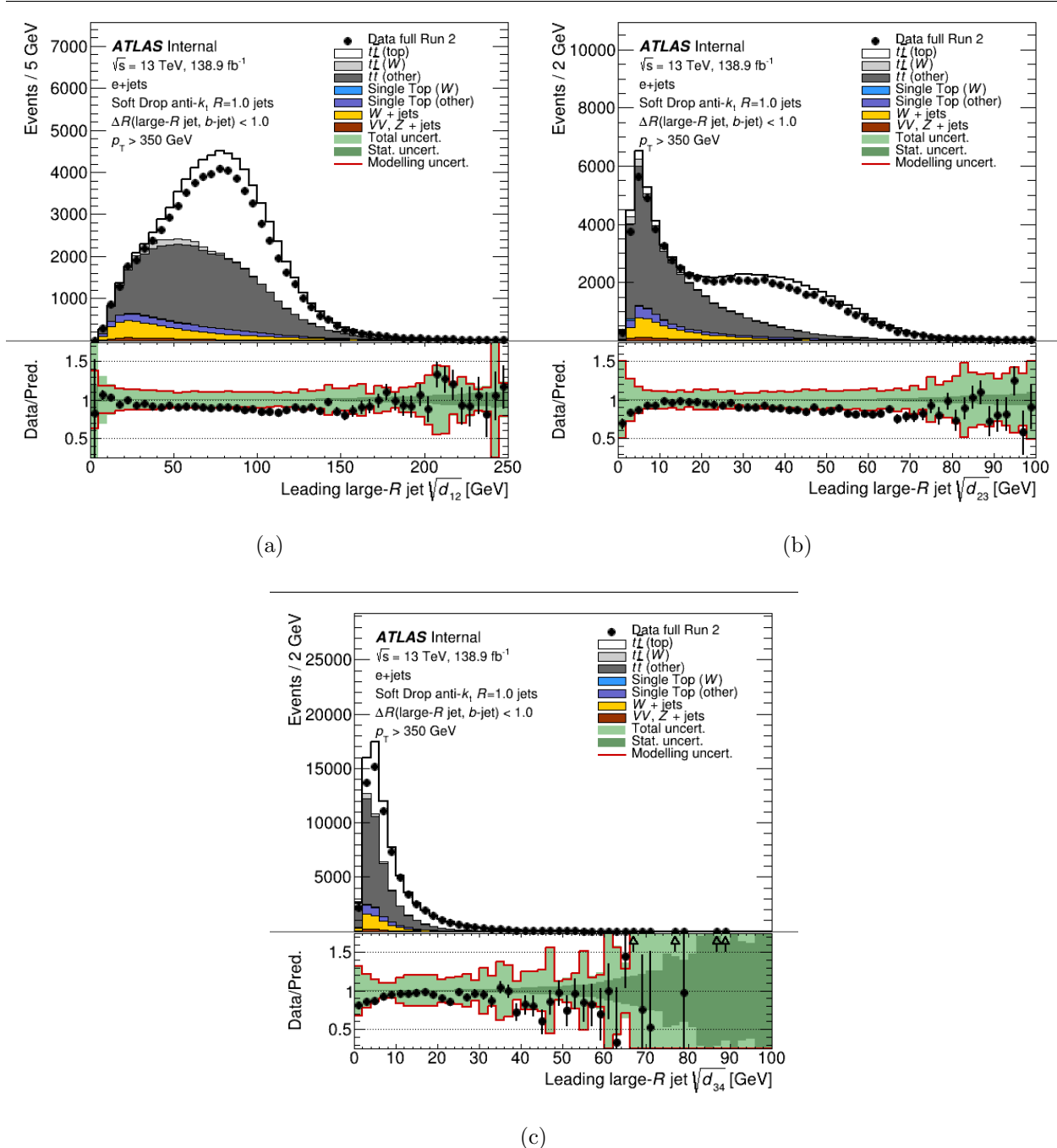


Figure 5.4: Distribution of splitting scales in data and MC simulation for the leading large-R jet in events that pass selection criteria for a top-enhanced single-electron $t\bar{t}$ events. The statistical uncertainty is shown by the dark green, and total uncertainty is shown by light green. The red line which shows the $t\bar{t}$ modelling uncertainty is also overlaid on top of the statistical uncertainty, highlighting that it is the dominant systematic almost everywhere.

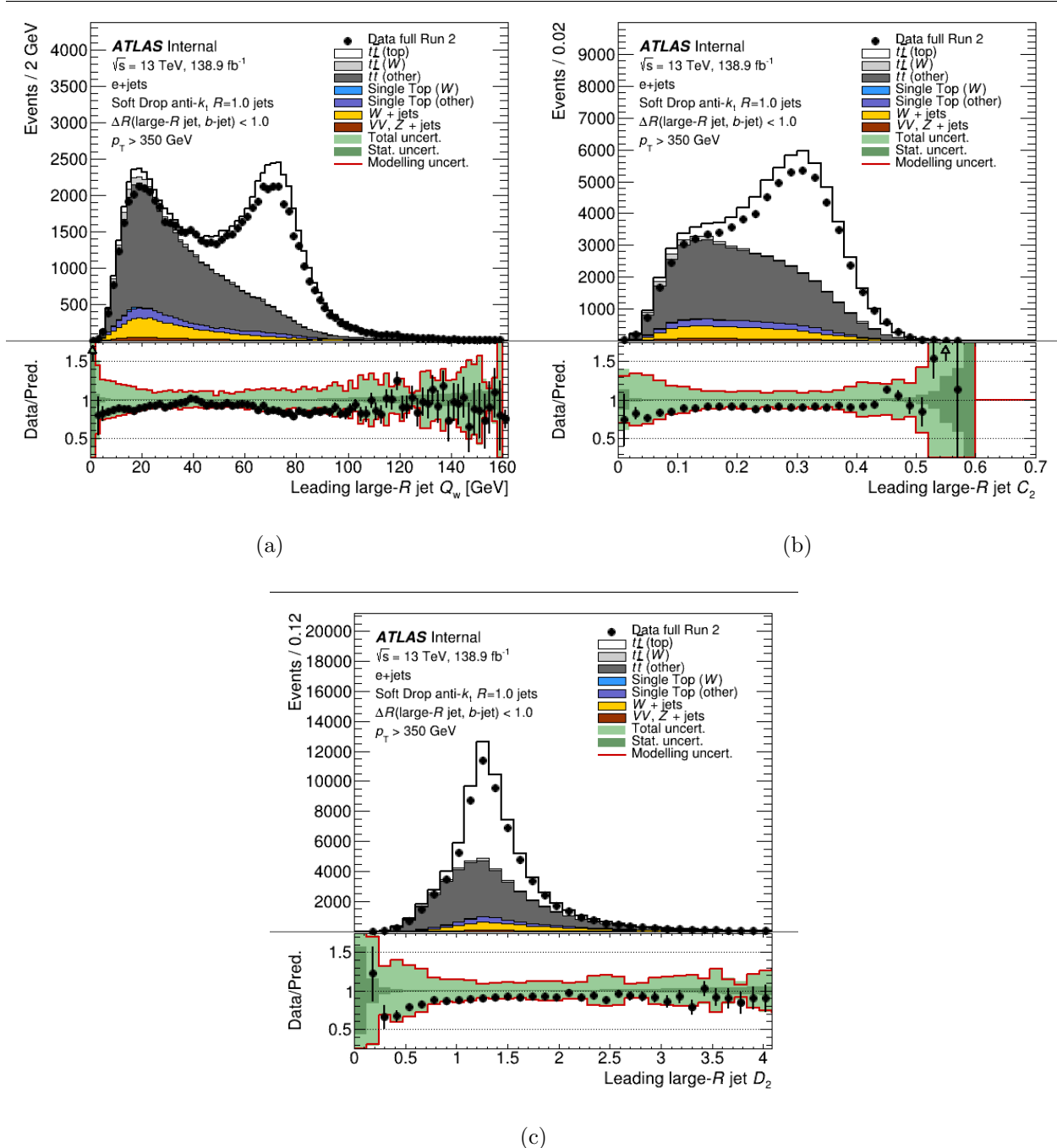


Figure 5.5: Distribution of Q_W (a), C_2 (b), and D_2 (c) in data and MC simulation for the leading large-R jet in events that pass selection criteria for a top-enhanced single-electron $t\bar{t}$ events. The statistical uncertainty is shown by the dark green, and total uncertainty is shown by light green. The red line which shows the $t\bar{t}$ modelling uncertainty is also overlaid on top of the statistical uncertainty, highlighting that it is the dominant systematic almost everywhere.

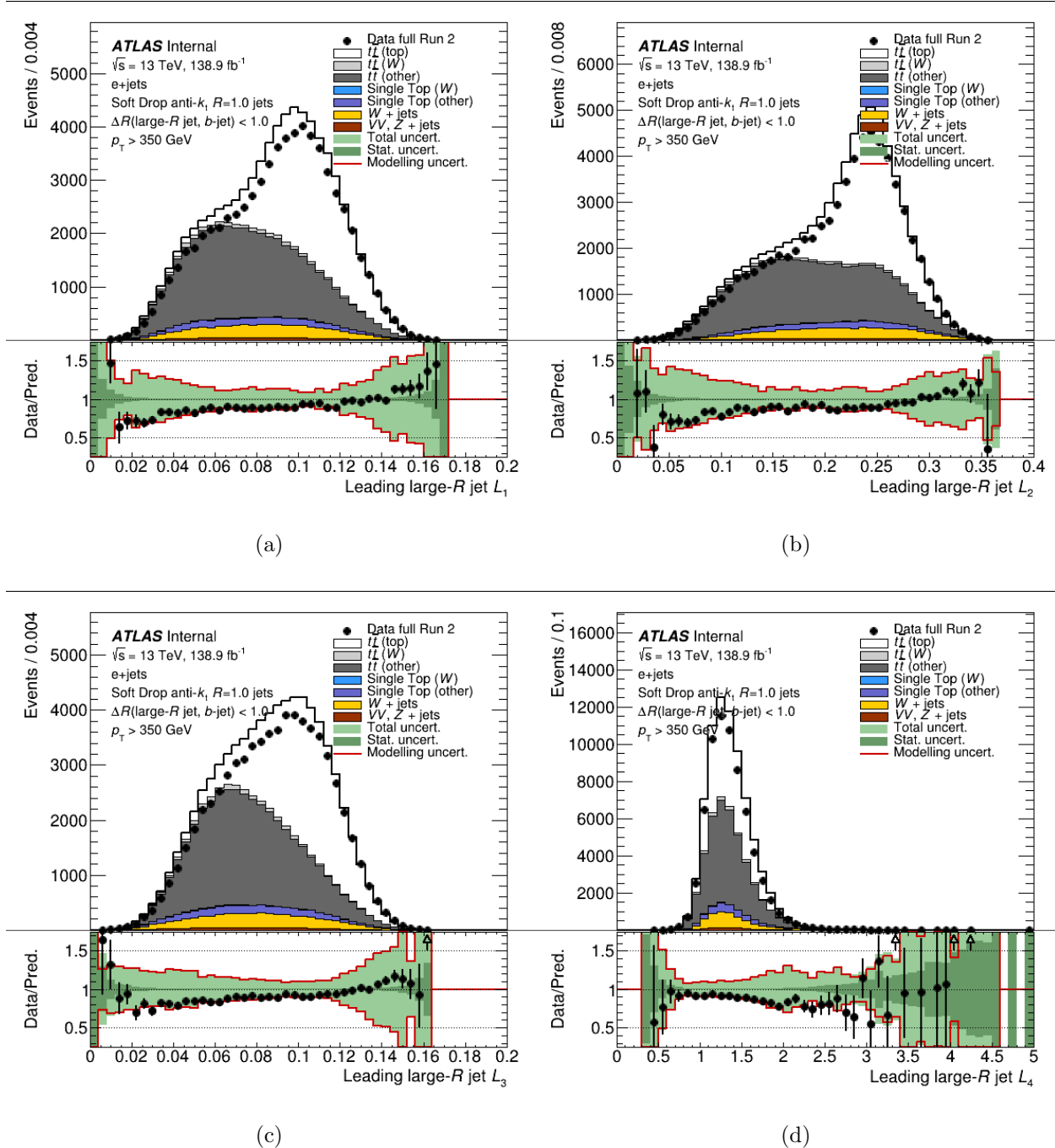


Figure 5.6: Distribution of the L-series (ratios of ECFGs) in data and MC simulation for the leading large-R jet in events that pass selection criteria for a top-enhanced single-electron $t\bar{t}$ events. The statistical uncertainty is shown by the dark green, and total uncertainty is shown by light green. The red line which shows the $t\bar{t}$ modelling uncertainty is also overlaid on top of the statistical uncertainty, highlighting that it is the dominant systematic almost everywhere.

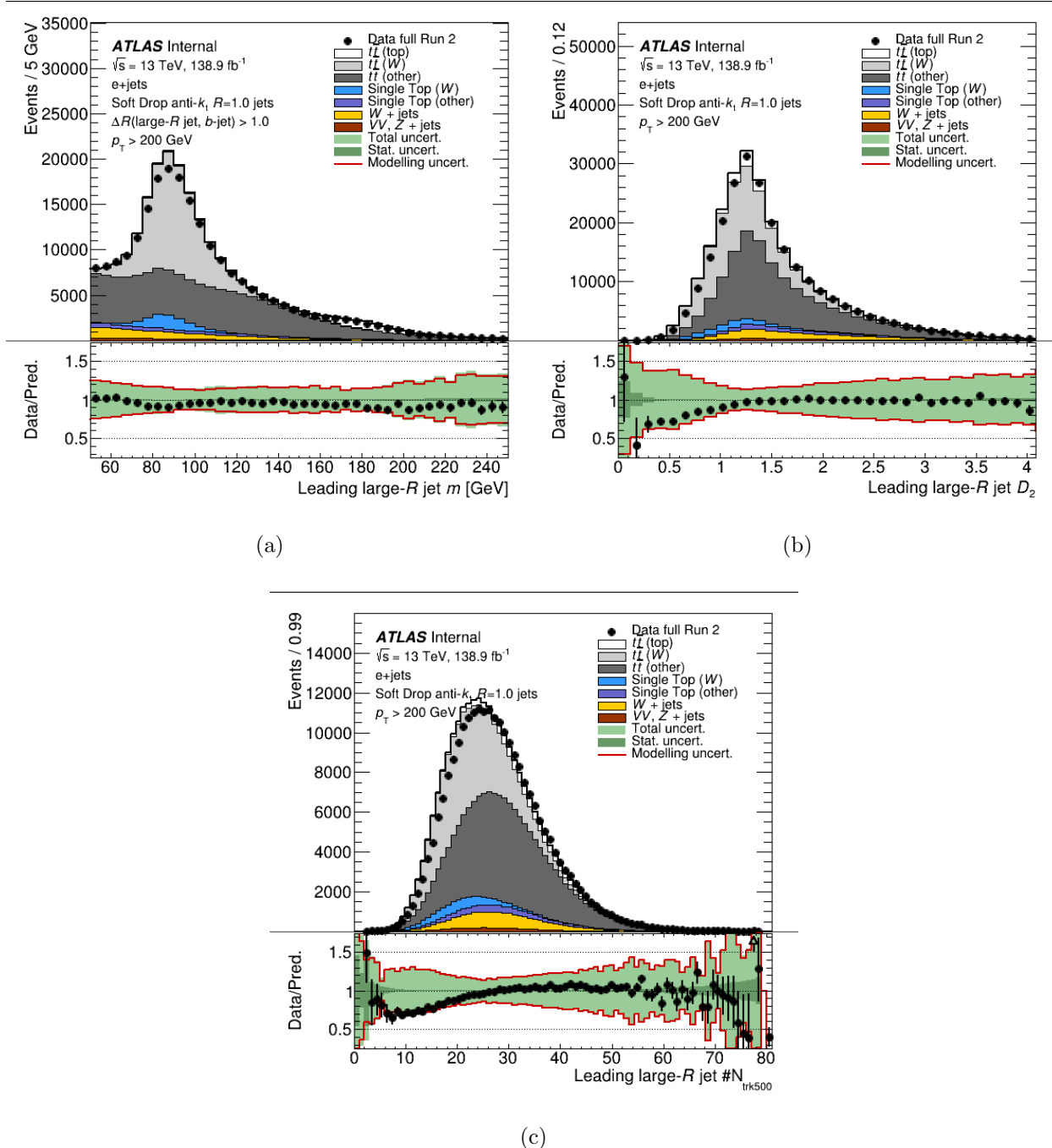


Figure 5.7: Distribution of mass (a), D_2 (b), and N_{trk}^{500} (c) in data and MC simulation for the leading large-R jet in events that pass selection criteria for a W -enhanced single-electron $t\bar{t}$ events. The statistical uncertainty is shown by the dark green, and total uncertainty is shown by light green. The red line which shows the $t\bar{t}$ modelling uncertainty is also overlaid on top of the statistical uncertainty, highlighting that it is the dominant systematic almost everywhere.

The kinematic variables for the DNN top tagger are shown in Figure 5.1, Figure 5.2, Figure 5.4, Figure 5.5, and Figure 5.6, and the 3-variable W-tagger are shown in Figure 5.7. These distributions are before the tagger is applied, but after the event selection process in Subsection 5.3.3. We see good data-MC agreement within the uncertainties for all input variables. The largest source of uncertainty is from the $t\bar{t}$ modeling.

5.3.4.2 Tagger Performance

After applying the tagger, we can confirm that the tagger aligns with what we expect to see; i.e. mostly top-selected events being selected by the top-tagger and mostly W-events selected by the W-taggers.

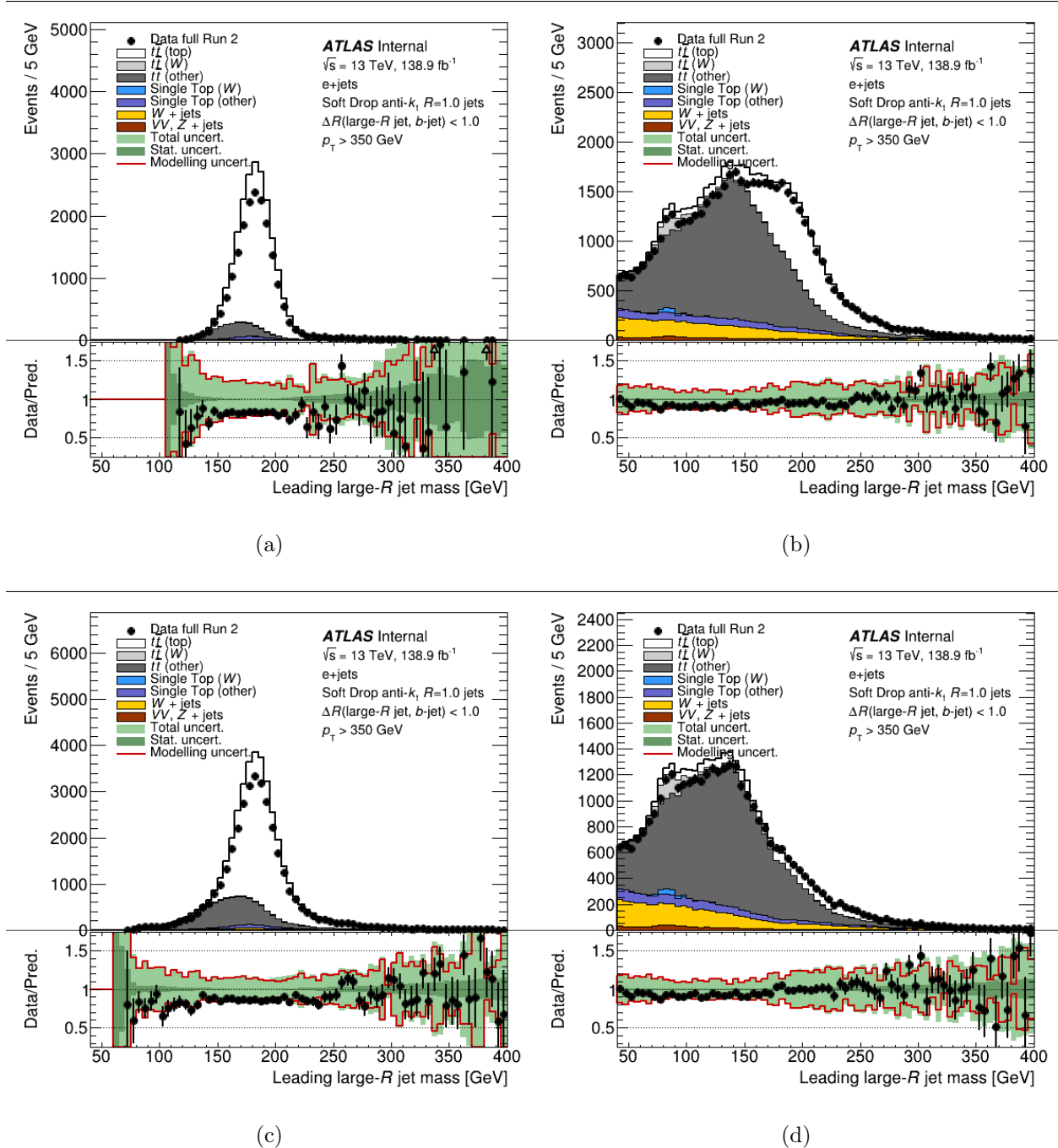


Figure 5.8: Tagger performance in data and MC simulation for the DNN top-tagger on leading large-R jet single-electron $t\bar{t}$ events. Events passing the tagger at the 50% WP (a) and 80% WP (c) show mostly $t\bar{t}$ top-events, as expected. Events not passing the tagger at the 50% WP (b) and 80% WP (d) contain mostly everything but $t\bar{t}$ top-events. The statistical uncertainty is shown by the dark green, and total uncertainty is shown by light green. The red line which shows the $t\bar{t}$ modelling uncertainty is also overlaid on top of the statistical uncertainty, highlighting that it is the dominant systematic almost everywhere.

Figure 5.8 shows the tagger performance (pass/fail) plots for the DNN top tagger as a function of leading large-R jet mass for the 50% WP and 80% WP, respectively. The largest source of uncertainty is again from modeling, but any data-MC disagreement is completely covered by the uncertainties. We can confirm that the top-tagger is working appropriately since most of the events selected indeed are from $t\bar{t}$ top, while in the fail plots contain mostly everything else. The 80% WP has tighter restrictions which are exemplified by the fail plots, where there is significantly less $t\bar{t}$ top events present in the fail plots.

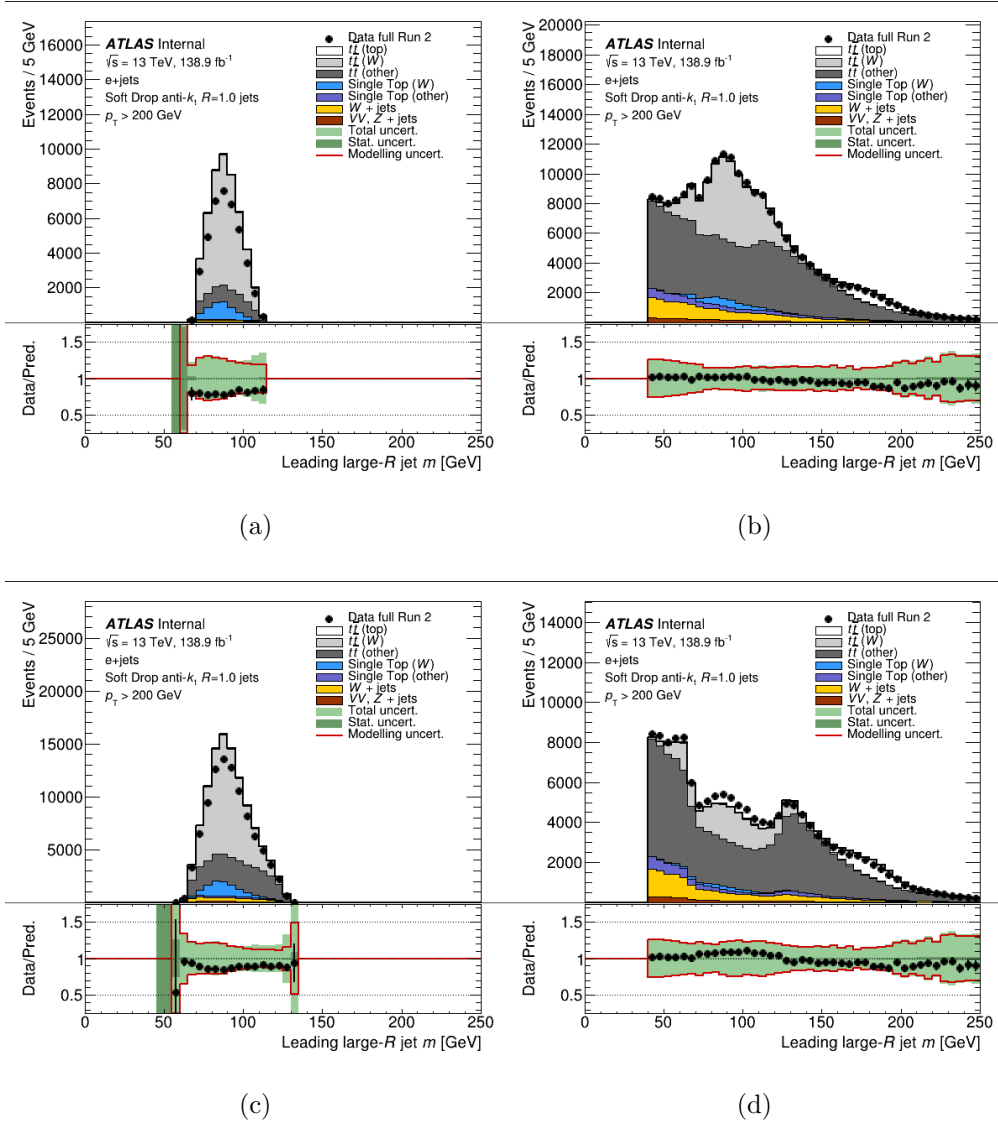


Figure 5.9: Tagger performance in data and MC simulation for the 3-variable W -tagger on leading large- R jet single-electron $t\bar{t}$ events. Events passing the tagger at the 50% WP (a) and 80% WP (c) show mostly $t\bar{t}W$ -events, as expected. Events not passing the tagger at the 50% WP (b) and 80% WP (d) contain mostly everything but $t\bar{t}W$ -events. The statistical uncertainty is shown by the dark green, and total uncertainty is shown by light green. The red line which shows the $t\bar{t}$ modelling uncertainty is also overlaid on top of the statistical uncertainty, highlighting that it is the dominant systematic almost everywhere.

Similarly, for the 3-Variable W -tagger, Figure 5.9 shows the tagger performance (pass/fail) plots for this tagger as a function of leading large- R jet mass for the 50% WP and 80% WP, respectively. The largest source of uncertainty is from modeling, but any data-MC

disagreement is completely covered by the uncertainties. Instead of focusing on the $t\bar{t}$ top contribution, the W-tagger is selecting $t\bar{t}$ -W events, which the pass/fail plots show the tagger accurately tagging the $t\bar{t}$ -W events with everything else ending up in the fail plot.

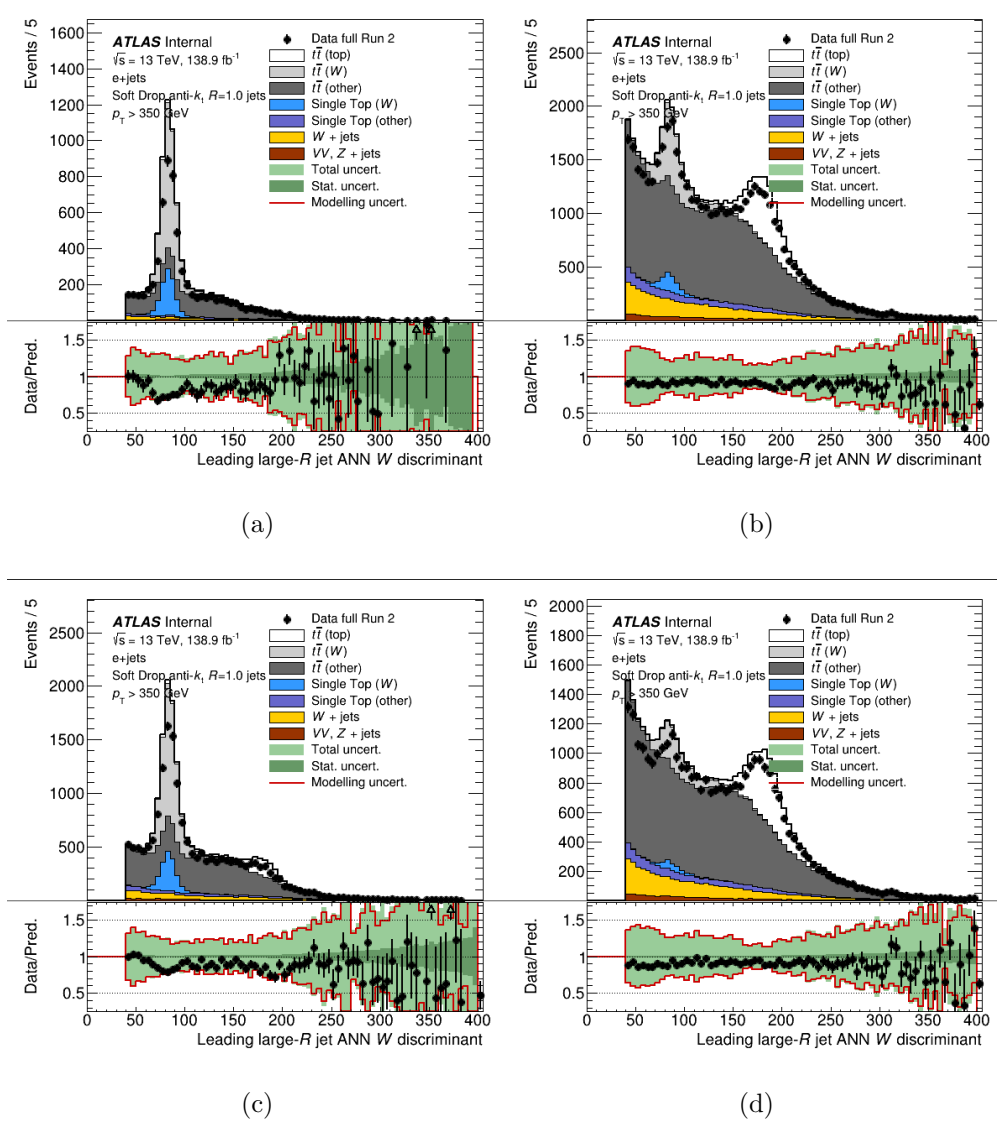


Figure 5.10: Tagger performance in data and MC simulation for the ANN W-tagger on leading large-R jet single-electron $t\bar{t}$ events. Events passing the tagger at the 50% WP (a) and 80% WP (c) show mostly $t\bar{t}$ W-events, as expected. Events not passing the tagger at the 50% WP (b) and 80% WP (d) contain mostly everything but $t\bar{t}$ W-events. The statistical uncertainty is shown by the dark green, and total uncertainty is shown by light green. The red line which shows the $t\bar{t}$ modelling uncertainty is also overlaid on top of the statistical uncertainty, highlighting that it is the dominant systematic almost everywhere.

The ANN W-tagger pass/fail plots are shown in Figure 5.10 for the 50% and 80% WPs. As expected, the largest source of uncertainty is from modeling, and any data-MC disagreement is completely covered by the uncertainties. Looking again at the $t\bar{t}$ -W contribution, the pass/fail plots show the tagger accurately tagging the $t\bar{t}$ -W events in the pass plot with everything else ending up in the fail plot.

5.3.4.3 Signal Efficiency and Scale Factors

By using the event selection outlined in Subsection 5.3.3, enriched top-quark and W-boson samples enables the measurement of the signal efficiency in data by using the tag-and probe method described in Subsection 5.3.1. The efficiency can then be used in conjunction with the efficiency calculated from using MC generated samples, to obtain a corrective factor, also known as the efficiency scale factor. Various physics analyses can use these corrective factors to help correct some MC mis-modeling. The DNN top-tagger, 3-variable W-tagger, and ANN W-tagger, described in Section 5.2 and shown in Subsection 5.3.4.2, are the top- and W-taggers in which this efficiency measurement, and subsequent scale factor measurements, are given.

Signal efficiency as a function of leading large-R jet p_t for the DNN top-tagger is shown in Figure 5.11 for the 50% and 80% WPs. Table 5.1 and Table 5.2 show the nominal SF values for the DNN top-tagger along with the breakdown of systematics for the 50% and 80% WPs, respectively. A more detailed breakdown of each type of systematic uncertainties are in ???. The scale factors for the top taggers defined at the 50% WP tend to be slightly lower than those defined at the 80% WP, but both are close to unity with the 50% WP within 15% and the 80% WP within 10%. The total scale factor uncertainty for the 50% WP is around 20 – 30%, and slightly lower around 10% or less for the 80% WP.

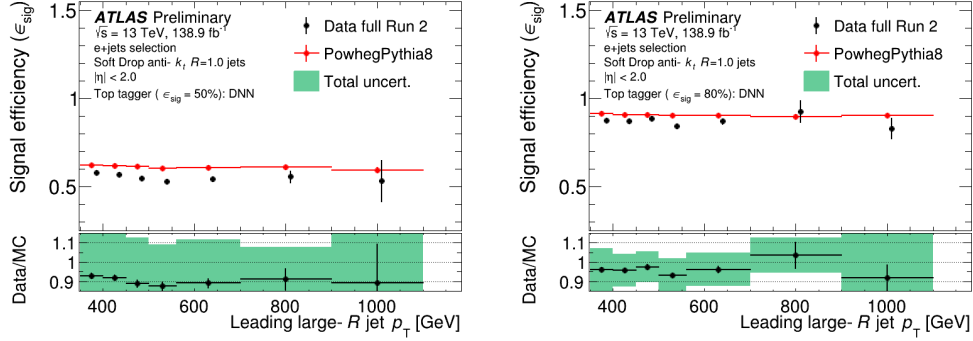


Figure 5.11: The measured efficiencies for the 50% contained top (a), and the 80% contained top (b) taggers are shown on the top panel. The bottom panel shows the tagger efficiency scale factors with the total uncertainty bands.

Systematic Group	Contained top-tagger p_T bins [GeV]					
	[350,400]	[400,450]	[450,500]	[500,560]	[560,700]	[700,900]
Statistical	0.0143	0.0160	0.0194	0.0222	0.0239	0.0549
$t\bar{t}$ modeling	0.2573	0.2325	0.2311	0.2098	0.2181	0.1489
Large-R jet	0.0252	0.0226	0.0278	0.0211	0.0253	0.0202
Other experimental	0.0496	0.0327	0.0332	0.0293	0.0295	0.0346
b -tagging	0.0028	0.0042	0.0098	0.0061	0.0151	0.0272
Total Uncertainty	0.2637	0.2365	0.2361	0.2141	0.2233	0.1659
Nominal SF Value	0.9297	0.9204	0.8901	0.8770	0.8926	0.9117

Table 5.1: The impact of the individual systematic uncertainty components on the 50% contained top tagger. Each uncertainty group row shows the uncertainty obtained by adding in quadrature all the uncertainties in the group. The nominal SF value is shown along with the total uncertainty for the value.

Signal efficiency as a function of leading large-R jet p_T for the 3-variable W-tagger is shown in Figure 5.12 for the 50% and 80% WPs. Table 5.4 and ?? show the nominal SF values for the 3-Variable W-tagger along with the breakdown of systematics for the 50% and 80% WPs, respectively. A more detailed breakdown of each type of systematic uncertainties are in ?. The scale factors for the 3-var W-tagger defined at the 50% WP tend to be slightly lower than those defined at the 80% WP, but both are close to unity with the 50% WP within 20% and the 80% WP within 15%. The total scale factor uncertainty is around

Systematic Group	Contained top-tagger p_T bins [GeV]					
	[350,400]	[400,450]	[450,500]	[500,560]	[560,700]	[700,900]
Statistical	0.0080	0.0088	0.0135	0.0123	0.0167	0.0684
$t\bar{t}$ modeling	0.1005	0.0793	0.0709	0.0842	0.0785	0.0366
Large-R jet	0.0178	0.0119	0.0152	0.0111	0.0081	0.0203
Other experimental	0.0407	0.0256	0.0285	0.0215	0.0203	0.0319
b -tagging	0.0030	0.0065	0.0083	0.0055	0.0220	0.0293
Total Uncertainty	0.1103	0.0849	0.0795	0.0886	0.0861	0.0911
Nominal SF Value	0.9598	0.9584	0.9754	0.9321	0.9622	1.0344

Table 5.2: The impact of the individual systematic uncertainty components on the 80% contained top tagger. Each uncertainty group row shows the uncertainty obtained by adding in quadrature all the uncertainties in the group. The nominal SF value is shown along with the total uncertainty for the value.

15 – 30% for both the 50% and 80% WP.

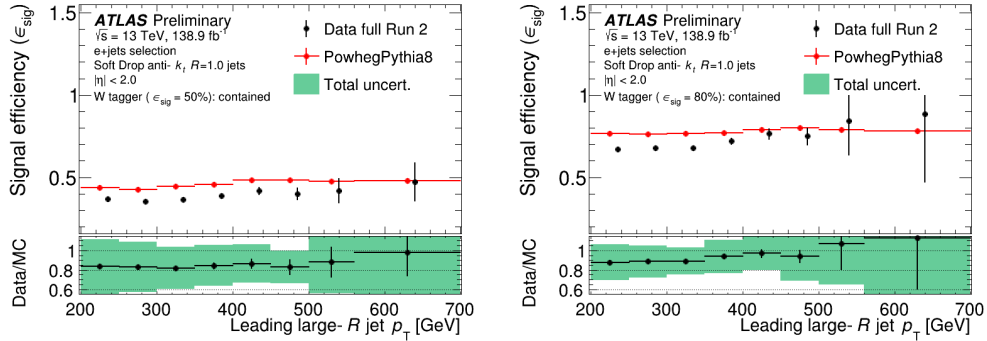


Figure 5.12: The measured efficiencies for the 50% (a) and 80% (b) 3-Variable W -taggers are shown on the top panel. The bottom panel shows the tagger efficiency scale factors with the total uncertainty bands.

Signal efficiency as a function of leading large- R jet p_T for the ANN W -tagger is shown in Figure 5.13 for the 50% and 80% WPs. Results for the 60%, 70%, and 90% WPs are included in the appendix Appendix A, and only the 50% and 80% WPs are shown in the main text here. Table 5.5 and Table 5.6 show the nominal SF values for the ANN W -tagger along with the breakdown of systematics for the 50% and 80% WPs, respectively. A more detailed breakdown of each type of systematic uncertainties are in ???. The scale factors for

Systematic Group	3-variable W -tagger p_T bins [GeV]							
	[200,250]	[250,300]	[300,350]	[350,400]	[400,450]	[450,500]	[500,560]	[560,700]
Statistical	0.0098	0.0134	0.0190	0.0311	0.0486	0.0758	0.1574	0.2438
$t\bar{t}$ modeling	0.2793	0.2548	0.2135	0.2003	0.1734	0.0977	0.2481	0.2382
Large-R jet	0.0018	0.0043	0.0036	0.0067	0.0083	0.0250	0.0242	0.0453
Other experimental	0.0398	0.0247	0.0265	0.0313	0.0409	0.0457	0.0608	0.1116
b -tagging	0.0083	0.0080	0.0229	0.0421	0.0747	0.0974	0.1204	0.2379
Total Uncertainty	0.2824	0.2565	0.2172	0.2095	0.1994	0.1658	0.3242	0.4328
Nominal SF Value	0.8358	0.8309	0.8203	0.8450	0.8649	0.8297	0.8813	0.9824

Table 5.3: The impact of the individual systematic uncertainty components on the 50% 3-variable W -tagger. Each uncertainty group row shows the uncertainty obtained by adding in quadrature all the uncertainties in the group. The nominal SF value is shown along with the total uncertainty for the value.

Systematic Group	3-variable W -tagger p_T bins [GeV]							
	[200,250]	[250,300]	[300,350]	[350,400]	[400,450]	[450,500]	[500,560]	[560,700]
Statistical	0.0098	0.0134	0.0190	0.0311	0.0486	0.0758	0.1574	0.2438
$t\bar{t}$ modeling	0.2793	0.2548	0.2135	0.2003	0.1734	0.0977	0.2481	0.2382
Large-R jet	0.0018	0.0043	0.0036	0.0067	0.0083	0.0250	0.0242	0.0453
Other experimental	0.0398	0.0247	0.0265	0.0313	0.0409	0.0457	0.0608	0.1116
b -tagging	0.0083	0.0080	0.0229	0.0421	0.0747	0.0974	0.1204	0.2379
Total Uncertainty	0.2824	0.2565	0.2172	0.2095	0.1994	0.1658	0.3242	0.4328
Nominal SF Value	0.8358	0.8309	0.8203	0.8450	0.8649	0.8297	0.8813	0.9824

Table 5.4: The impact of the individual systematic uncertainty components on the 50% 3-variable W -tagger. Each uncertainty group row shows the uncertainty obtained by adding in quadrature all the uncertainties in the group. The nominal SF value is shown along with the total uncertainty for the value.

the 3-var W -tagger defined at the 50% WP tend to be slightly lower than those defined at the 80% WP, but both are close to unity with the 50% WP mostly within 20% and the 80% WP mostly within 10%. The total scale factor uncertainty for the 50% WP is around 20 – 30%, and slightly lower around 15% or less for the 80% WP.

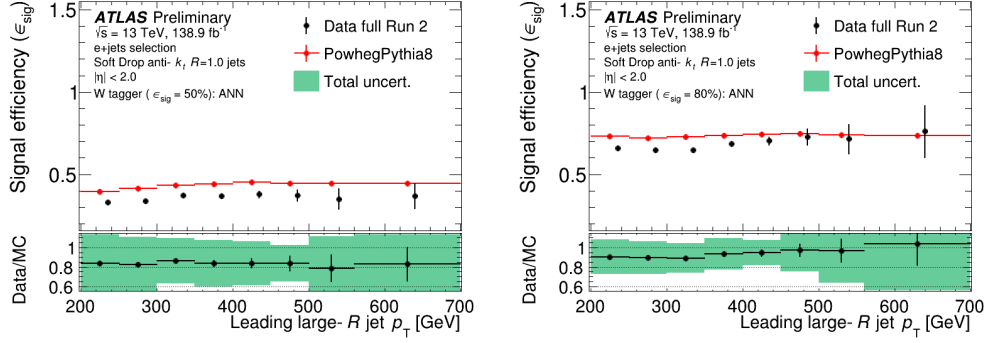


Figure 5.13: The measured efficiencies for the 50% (a) and 80% (b) ANN W -taggers are shown on the top panel. The bottom panel shows the tagger efficiency scale factors with the total uncertainty bands.

Systematic Group	ANN W -tagger p_T bins [GeV]							
	[200,250]	[250,300]	[300,350]	[350,400]	[400,450]	[450,500]	[500,560]	[560,700]
Statistical	0.0105	0.0135	0.0195	0.0317	0.0488	0.0766	0.1398	0.1720
$t\bar{t}$ modeling	0.2944	0.2830	0.2310	0.2292	0.2053	0.1366	0.2725	0.1730
Large-R jet	0.0041	0.0021	0.0027	0.0067	0.0101	0.0121	0.0252	0.0155
Other experimental	0.0350	0.0218	0.0275	0.0319	0.0361	0.0474	0.0622	0.0690
b -tagging	0.0100	0.0153	0.0314	0.0537	0.0733	0.0916	0.1024	0.1732
Total Uncertainty	0.2968	0.2846	0.2356	0.2398	0.2265	0.1879	0.3298	0.3074
Nominal SF Value	0.8358	0.8211	0.8633	0.8362	0.8392	0.8368	0.7857	0.8298

Table 5.5: The impact of the individual systematic uncertainty components on the 50% ANN W -tagger. Each uncertainty group row shows the uncertainty obtained by adding in quadrature all the uncertainties in the group. The nominal SF value is shown along with the total uncertainty for the value.

Systematic Group	ANN W -tagger p_T bins [GeV]							
	[200,250]	[250,300]	[300,350]	[350,400]	[400,450]	[450,500]	[500,560]	[560,700]
Statistical	0.0057	0.0080	0.0119	0.0216	0.0348	0.0647	0.1201	0.2142
$t\bar{t}$ modeling	0.1777	0.1663	0.1440	0.1464	0.0836	0.1708	0.2627	0.3467
Large-R jet	0.0007	0.0022	0.0019	0.0067	0.0064	0.0191	0.0263	0.0363
Other experimental	0.0269	0.0162	0.0190	0.0274	0.0375	0.0525	0.0718	0.0982
b -tagging	0.0117	0.0205	0.0398	0.0639	0.0853	0.1172	0.1417	0.2222
Total Uncertainty	0.1802	0.1686	0.1511	0.1636	0.1301	0.2241	0.3307	0.4758
Nominal SF Value	0.9045	0.8976	0.8899	0.9333	0.9447	0.9748	0.9669	1.0346

Table 5.6: The impact of the individual systematic uncertainty components on the 80% ANN W -tagger. Each uncertainty group row shows the uncertainty obtained by adding in quadrature all the uncertainties in the group. The nominal SF value is shown along with the total uncertainty for the value.

5.4 Summary

Identifying jets from hadronic decays of top quarks and W/Z bosons is critical for enhancing analysis sensitivity in ATLAS, especially in boosted topologies where decay products are highly collimated. This work, completed as part of the ATLAS authorship qualification task, focuses on measuring the signal efficiency of boosted object taggers using the new UFO jet definition, which improves jet substructure resolution by combining calorimeter and tracking information. Tagger performance was evaluated in $t\bar{t}$ events, with scale factors derived from differences between data and MC to correct for mismodeling. The DNN Top Tagger achieved about 10% uncertainty, while the 3-Variable and ANN W-Taggers had 20-30% and 15-30% uncertainty, respectively, across the jet p_T spectrum. These finalized scale factors are now used in multiple analyses, including the heavy resonance search described in this dissertation. The task also involved improving and debugging centralized code, deepening my understanding of scale factor methodology and allowing me to support incoming students working on similar efforts for Run 3.

Chapter 6. Search for heavy resonances decaying into two SM bosons in semi-leptonic final states

6.1 Analysis Overview

This thesis investigates the ongoing search for a new heavy resonance decaying through a pair of bosons, VV or VH (where V represents a SM W or Z boson, and H represents the SM Higgs boson), into semileptonic final states. Semileptonic final states implies that one of the vector bosons decays leptonically while the other boson or Higgs boson decays hadronically. If both pairs of bosons decayed to a pair of leptons, then the final states would be referred to as fully leptonic. If instead both pairs of bosons decayed to quarks, then the final states would be referred to as fully hadronic. Both fully-hadronic and fully-leptonic final states searches exist within ATLAS, however that is not the focus of this dissertation. In semileptonic final states, the leptonic decay allows for a clear signature, since it can be easily reconstructed, whereas the hadronic decay allows for a higher cross section, from higher decay branching ratio (BR), making this search sensitive across a large mass range of 200 GeV to 5 TeV. The leptonic decay of either the W or Z boson proceed as $Z \rightarrow \nu\bar{\nu}$, $W \rightarrow l^\pm \nu^{(-)}$, or $Z \rightarrow l^+l^-$, where l is a light charged lepton: either an electron or muon. The hadronic decay of either a W or Z boson decay as $W \rightarrow qq$ or $Z \rightarrow q\bar{q}$. The Higgs boson also decays hadronically, and this analysis targets the b-quark decay: $H \rightarrow b\bar{b}$. Two reconstruction techniques of the hadronic decays of the second boson are utilized based on the transverse momentum of the boson. For low transverse momentum bosons, the hadronic decay is reconstructed as two small-radius

(small-R) jets (with the radius parameter $R=0.4$). For high transverse momentum bosons, the hadronic decay is reconstructed as one large-radius (large-R) jet (with radius parameter $R=1.0$).

Several beyond the Standard Model (BSM) signal interpretations are considered, with production mechanisms including Drell-Yan (DY), gluon-gluon fusion (ggF), vector boson fusion (VBF), and associated production with b-quarks (bbA). A search for a heavier version of the Standard Model W and Z bosons, denoted W' and Z' , is conducted using the Heavy Vector Triplet (HVT) framework in both diboson (VV) and boson+Higgs (VH) final states. The radion (R), a neutral scalar resonance predicted in certain Randall-Sundrum (RS) models, is considered as a signal decaying to VV final states (WW or ZZ). Another interpretation involves a spin-2 graviton (G_{KK}), corresponding to the first KK excitation in a bulk RS model, also decaying to WW or ZZ.

Previous searches in the same final states have been conducted using this dataset by ATLAS through either VV or VH processes separately. The VV searches were performed with the 36.1 fb^{-1} ($\sqrt{s} = 13 \text{ TeV}$) [133, 134] and the 139 fb^{-1} ($\sqrt{s} = 13 \text{ TeV}$) [135] dataset, while the VH searches were performed using the 3.2 fb^{-1} ($\sqrt{s} = 13 \text{ TeV}$) [136], 36.1 fb^{-1} ($\sqrt{s} = 13 \text{ TeV}$) [137], and 139 fb^{-1} ($\sqrt{s} = 13 \text{ TeV}$) [138] dataset. Similar searches were performed by the CMS collaboration ($\sqrt{s} = 13 \text{ TeV}$) in the WZ/WW/WH [139] and in the ZH [140] final state. The search presented uses the full Run-2 dataset collected from 2015-18 with an integrated luminosity of 139 fb^{-1} ($\sqrt{s} = 13 \text{ TeV}$). A new revision was motivated by several developments, including improved jet collections and a new optimized event selection.

6.2 Analysis Strategy

The VV+VH analysis searches for localized excesses in the data when compared to the known SM background, also known as a “bump search.” The search starts by executing an event selection, where a series of cuts are applied in order to define final regions of the analysis. These cuts consist of requirements on kinematic properties of the event variables which result in a phase space similar to the signal under investigation. Two strategies are used to maintain sensitivity for both high- and low-mass resonances. One strategy uses final state objects which reconstruct the hadronically decaying boson as two small-R jets, referred to as the “resolved” event topology. In boosted topologies, the second strategy uses final state objects which reconstruct the hadronically decaying boson with large-R jets, referred to as the “merged” event topology. In addition to kinematic cuts and the different strategies for the hadronic decay, each production mode has a specific event selection defining channels. These channels are subsequently defined if the process is VV or VH, and according to the number of charged leptons (0/1/2) in the final state, resulting in six channels.

Following event selection, the different types of final regions are defined and events are categorized based on particular signatures. Signal regions (SR) contain events selected in order to maximize the signal significance. Control regions (CR) are regions which look very similar to the signal region but have some slightly different selection to enrich a particular background, which is orthogonal to the signal region. This is often done by inverting a single cut in which the analysis is sensitive to, thus drastically removing the signal in that region. Specific to this analysis, there are two control regions: mass-control region (MCR) and top-control region (TCR). These regions along with the SR are depicted in Figure 6.1.

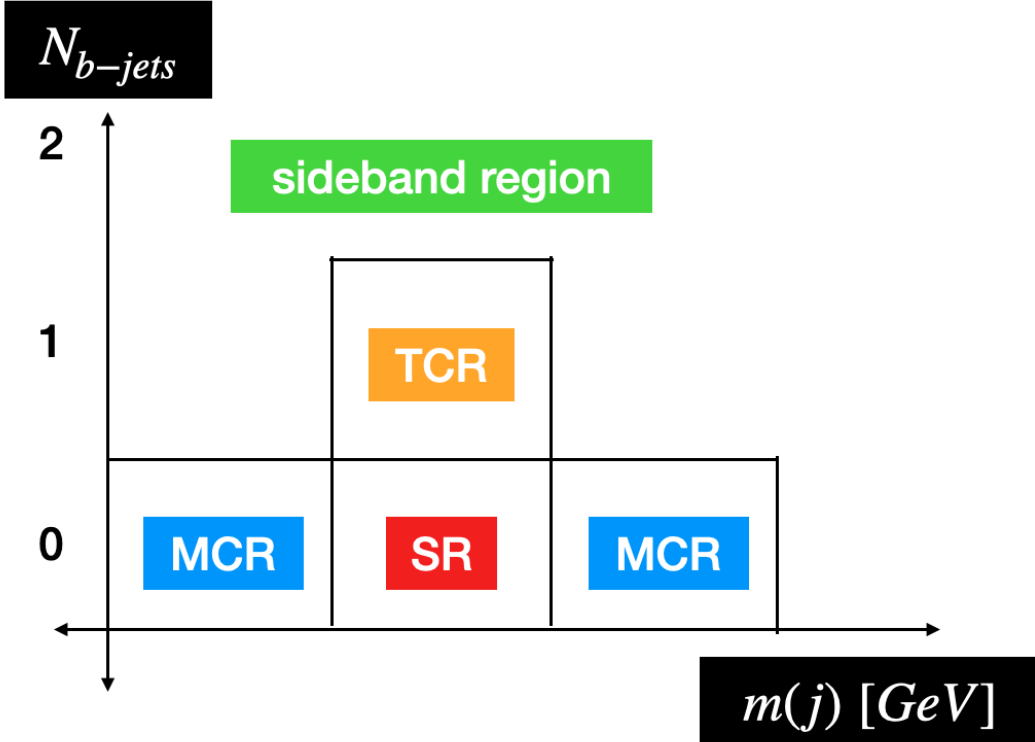


Figure 6.1: Schematic depicting the signal region (SR), mass control regions (MCR), and the top-control region (TCR) in the mass-number-of-b-jets phase-space.

The SR contains V/H decays selected by a mass window and is further split by the number of b-tags (N_{b-jets}). The MCR are the two regions on either side of the SR mass window. The TCR is with the same mass window as the SR, but inverts the additional-b-veto ¹. Splitting by the number of b-jets allows for better isolation of V+jets contributions according to the number of light and heavy flavor jets. Defining these regions is important for the analysis, especially for optimization when the analysis is blinded, or deliberately not looking at data in particularly sensitive regions in order to stay unbiased. The control regions provide a space that is used to apply and validate background MC modeling and analysis techniques. Then, they are used to constrain background normalizations in the final fit. Since this

¹The b-veto in this context means that the number of b-jets, N_{b-jets} , is equal to zero. Thus, by inverting the b-veto means that there is in fact a b-jet, or N_{b-jets} is equal to one.

analysis is the first time the VV and VH final states are being considered simultaneously, the complexity of the analysis increases and it is possible that some of the regions unintendedly overlap. To combat this issue, the analysis deploys a multi-class classifier (MCT) tool used to orthogonalize the VV and VH final regions. Considering the number of charged leptons (0/1/2) in the final state, the hadronic configuration (resolved/merged), the mass of the di-jet system or large-R jet, the number of b-tagged jets in the event, if there is a W/Z-tagged large-R jet, and the properties of any additional jets in the event, there are 63 signal regions and 78 control regions. A detailed outline of this is shown in Figure 6.2.

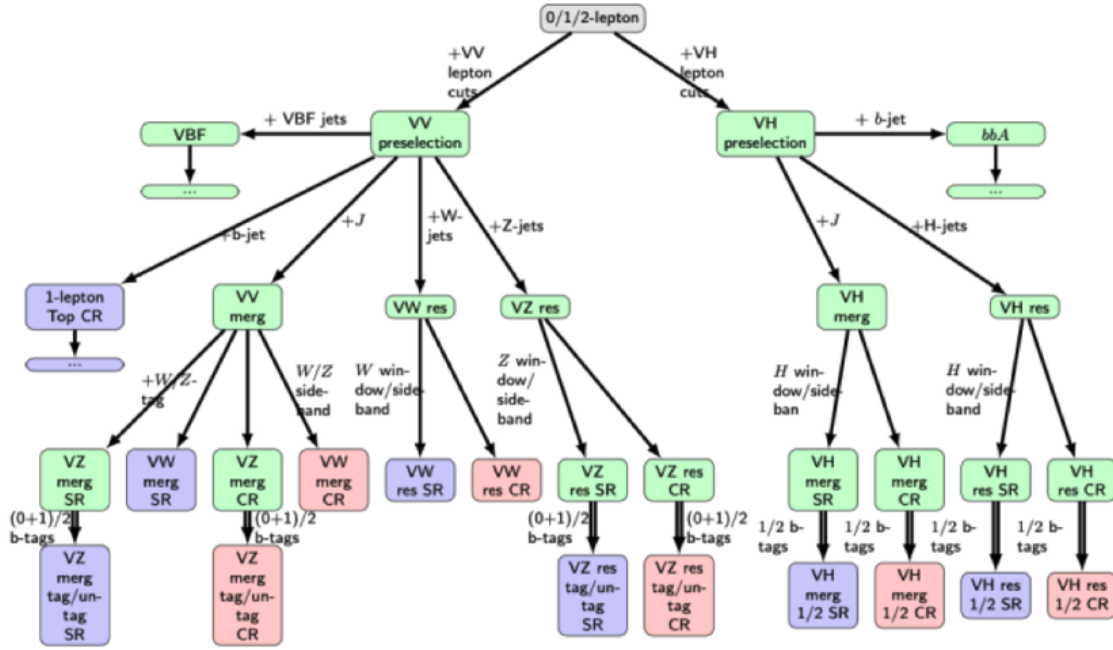


Figure 6.2: Flow chart illustrating the 63 signal regions and 78 control regions of the VV+VH analysis.

Once all of the regions are defined, the statistical interpretation is performed using a binned maximum-likelihood fit to data. MC simulated events that pass the event selection make up the SM background, and the normalization is done through fitting in the CR. Data is passed through the same event selection process, both in the SR and CR. If an excess is

found, the fit provides a p-value (the probability that the background could fluctuate to at least the excess observed, with no signal present). Finally, in the absence of a significant excess, exclusion limits are set on the upper bounds of the signal production cross sections times the branching ratios to WW , ZZ , WZ , WH , or ZH are derived.

6.3 Signal Models, Backgrounds, and Data

6.3.1 Signal Models

Many BSM models in particle physics predict heavy particles that could decay into VV or VH final states. Production of these heavy particles can happen through gluon-gluon fusion (ggF), Drell-Yan (DY), vector-boson fusion (VBF), or b-associated (bbA) production processes. In gluon-gluon fusion, two gluons from the colliding protons interact to produce a heavy resonance. Drell-Yan production involves the annihilation of a quark and antiquark, subsequently producing a heavy particle. Vector-boson fusion occurs when two incoming quarks each emit a vector boson that interact to produce the heavy particle. In b-associated production, the heavy particle is produced in association with one or more b-quarks. Each mechanism probes different couplings and offers complementary sensitivity in the search for new physics. Feynman diagrams for these production processes are shown in Figure 6.3 (for VV) and Figure 6.4 (for VH).

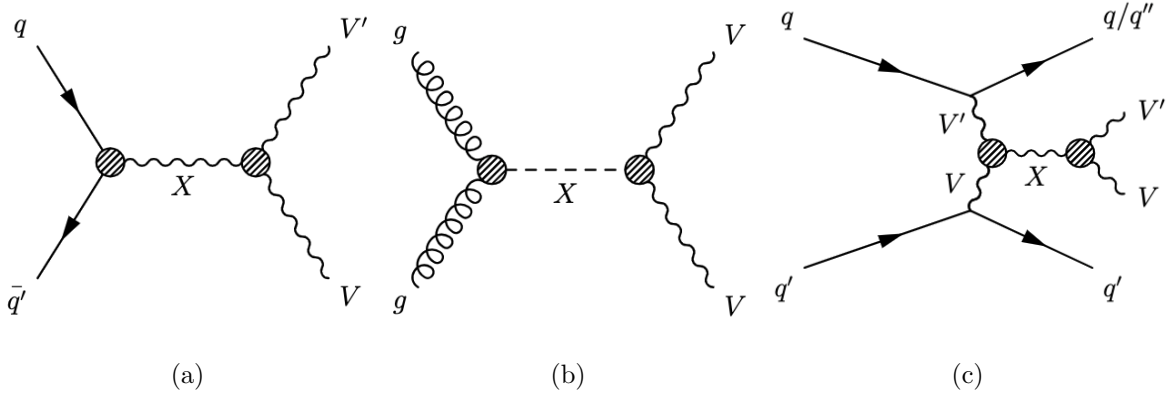


Figure 6.3: Representative Feynman diagrams for the production of heavy resonances, X , with their decays into VV semileptonic final states. Production mechanisms for (a) Drell-Yan, (b) gluon-gluon fusion, and (c) vector-boson-fusion, are shown.

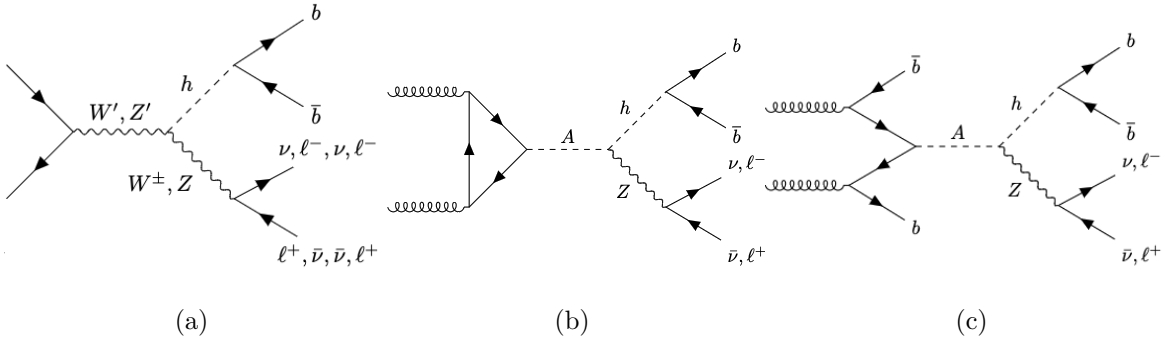


Figure 6.4: Representative Feynman diagrams for the production of heavy resonances, X , with their decays into VH semileptonic final states. Production mechanisms for (a) Drell-Yan, (b) gluon-gluon fusion, and (c) b -associated production, are shown.

The heavy vector triplet model [141] consists of two states nearly degenerate in mass: new electrically charged W' or electrically neutral Z' vector boson, which decay into SM bosons. Possible decay modes are $W' \rightarrow WZ$, $W' \rightarrow WH$, $Z' \rightarrow WW$, and $Z' \rightarrow ZH$. Both DY and VBF production modes are considered for HVT bosons. The coupling of the HVT particles to the SM particles is parameterized by the parameter g_V , which represents the strength of the interaction. The coupling of new particles to SM bosons and fermions is

given by $g_H = g_V c_H$ and $g_F = g^2/g_V c_F$, respectively, where c_H and c_F are fixed to values of order one. There are three models used for interpretation:

- *Model A*: predicts comparable BRs for fermions and bosons
- *Model B*: a composite model, with dominant BRs to dibosons and the couplings to fermions suppressed
- *Model C*: focuses on VBF production, with $g_H = 1$ and $g_F = 0$

Model A and *B* are primarily produced with DY, or quark-anti-quark annihilation, whereas *Model C* allows for VBF production to be studied; which is the first time this production mode is considered in the ATLAS VH analysis. By constraining g_F and g_H , the analysis is able to set upper limits on the production cross-section of HVT resonances within the mass range of 300 GeV and 5 TeV. HVT Z' and W' signal samples for *Model A* via DY production are generated at leading-order (LO) in QCD using MadGraph5 2.3.3 (MG5) interfaced to Pythia 8.186 with the parton shower tune A14 and the NNPDF2.3 PDF set. For *Model B*, the differences in the final state kinematics as compared to *Model A* are considered negligible, once detector resolution effects are considered, so the same set of signal samples is used for comparison (but with their cross-sections and branching ratios scaled appropriately for the specific model). The decay of the Higgs boson into b - and c - quarks is considered, with branching ratios of $\mathcal{B}(h \rightarrow b\bar{b}) = 0.569$, $\mathcal{B}(h \rightarrow c\bar{c}) = 0.0287$, respectively, and the mass $m_H = 125$ GeV was assumed. Another set of samples for *Model C* is generated for VBF production only.

There are two other signal interpretations for the VV-portion of the analysis yielding from the Randall-Sundrum model [142, 143, 42]: the Graviton and the Radion. The neutral spin-2 Graviton is the first mode of the KK excitation, explained in Section 2.2. The Radion,

a neutral scalar resonance, is a scalar field corresponding to fluctuations in the size of the extra dimension. Both have dominant BRs to WW and ZZ final states, are produced via ggF or VBF, and the search is over the mass range of 300 GeV and 5 TeV. The RS Graviton signal samples (both ggF and VBF) are generated with `MadGraph5-2.2.2` interfaced to `Pythia 8.186` using the `NNPDF2.3 LO PDF`. The Radion samples (both ggF and VBF) are generated with `MadGraph5-2.6.0` interfaced to `Pythia 8.212`.

For the VH-portion of the analysis, there is a search for a new pseudoscalar CP-odd scalar boson A ; a heavier Higgs boson predicted by the Two-Higgs-Doublet Model (2HDM) model. This resonance decays to a ZH final state, and targets both gluon-gluon fusion (here, ggA) and bbA over the mass range of 220 GeV and 2 TeV. The ggA signal samples are generated with the narrow width approximation using the `MadGraph5 2.3.3` generator at LO accuracy in QCD, with the `2HDM_GF FeynRules` model [144] and the `NNPDF2.3 LO PDF` set. The bbA signal samples are generated in the 4-flavour scheme at next-to leading order (NLO) in QCD using the `MadGraph5_aMC@NLO` generator and the `NNPDF2.3NLO PDF` set.

6.3.2 Backgrounds

Along with the various signals, there are several background processes to consider when attempting to select and reconstruct the production of heavy particles decaying into semileptonic final states, due to several of these background processes having similar final states as the signals. The major background processes include:

- $W + jets, Z + jets$: W and Z boson production in association with jets (also collectively referred to as $V + jets$)
- $t\bar{t}$: Top-quark pair production

- *stop*: Single-top production
- *Diboson*: non-resonant diboson production (WW, WZ, or ZZ) with semileptonic decays
- *Multijet* production (can mimic signal-like signatures through mis-reconstructed jets or fake missing energy in events with many jets)

Other minor background processes are: $t\bar{t}+h$, $t\bar{t}+V$ ($V = W, Z$), and the irreducible SM background $V+h$. The backgrounds are modelled with MC simulation, further described in Chapter 4. All simulated events are generated at a center-of-mass energy \sqrt{s} of 13 TeV and are passed through the full GEANT-4 ATLAS detector simulation. A summary of the MC generators used to produce the various background processes is given in Table 6.1. The MC production undergoes the same event reconstruction as data. Simulated events are corrected for differences with data, and this correction is applied as a multiplicative factor to the event weight, one example of which was further discussed in Chapter 5.

6.3.3 Data Samples

This analysis uses pp collision data from the full Run-2 dataset collected at $\sqrt{s} = 13$ TeV during 2015 (3.2 fb^{-1}), 2016 (33.0 fb^{-1}), 2017 (44.3 fb^{-1}), and 2018 (58.5 fb^{-1}), which combines to a total integrated luminosity of 139.0 fb^{-1} . Events in the datasets are required to pass the “All_Good” Good Run List (GRL), which ensure quality, stable beam and detector conditions.

Process	Generator	Prediction order of σ_{prod}
Vector boson + jets		
$W \rightarrow \ell\nu$	SHERPA2.2.1	NNLO
$Z \rightarrow \ell\ell$	SHERPA2.2.1	NNLO
$Z \rightarrow \nu\nu$	SHERPA2.2.1	NNLO
Top quark		
$t\bar{t}$	POWHEG+PYTHIA8	NNLO+NNLL
single top (s -channel)	POWHEG+PYTHIA8	NLO
single top (t -channel)	POWHEG+PYTHIA8	NLO
Wt -channel	MADGRAPH5_AMC@NLO + PYTHIA 8	NLO (QCD) and NLO (EW)
$t\bar{t} + h$	MADGRAPH5_AMC@NLO + PYTHIA 8	NLO
$t\bar{t} + V$	MADGRAPH5_AMC@NLO + PYTHIA 8	NLO
Diboson		
$gg/q\bar{q} \rightarrow WW \rightarrow \ell\nu\ell\nu$	SHERPA2.2.1	NLO
$gg/q\bar{q} \rightarrow WZ \rightarrow \ell\nu qq$	SHERPA2.2.1	NLO
$gg/q\bar{q} \rightarrow WZ \rightarrow \ell\nu\ell\ell$	SHERPA2.2.1	NLO
$gg/q\bar{q} \rightarrow ZZ \rightarrow qq\ell\ell$	SHERPA2.2.1	NLO
$gg/q\bar{q} \rightarrow ZZ \rightarrow \nu\nu qq$	SHERPA2.2.1	NLO
$gg/q\bar{q} \rightarrow ZZ \rightarrow \ell\ell\ell\ell$	SHERPA2.2.2	NLO
$gg/q\bar{q} \rightarrow \ell\nu qq$	SHERPA2.2.2	NLO
SM Higgs		
$gg \rightarrow Wh \rightarrow \ell\nu bb$	POWHEG+PYTHIA8	NNLO (QCD) and NLO (EW)
$qq \rightarrow Wh \rightarrow \ell\nu bb$	POWHEG+PYTHIA8	NNLO (QCD) and NLO (EW)
$gg \rightarrow Zh \rightarrow \nu\nu bb$	POWHEG+PYTHIA8	NLO+NLL
$qq \rightarrow Zh \rightarrow \nu\nu bb$	POWHEG+PYTHIA8	NLO+NLL

Table 6.1: Overview of processes, generators, and prediction orders. The multijet background is not included here since it is estimated using a data-driven method, (not detailed as I was not directly involved in its development).

6.4 Object Selection

Object reconstruction and selection requirements is the same for both data and simulated samples. ATLAS event reconstruction is described in Section 4.3, and analysis specific object selection requirements is provided in this section.

6.4.1 Large-R Jets

In the previous iteration of this analysis, the Track-Calo Clusters (TCCs)² algorithm was used to reconstruct the Large-R jet candidate. However, a new jet collection recommendation, which optimizes desirable aspects of PFlow and TCC reconstruction, is implemented instead: Unified Flow Objects (explained in Subsection 4.3.5.3). Thus, the large-R jets are reconstructed with the anti- k_t algorithm, with $R = 1.0$ using UFO input objects.

Before jet reconstruction, the input objects are pre-processed using constituent-level pileup-suppression algorithms, outlined in Subsection 4.3.5.3. First, the CS method is applied to the p_T of each constituent and adjusted. Then, the SK algorithm applies an event dependent p_T cut to remove low- p_T constituents, utilizing a grid granularity of $\Delta\eta \times \Delta\phi = 0.6 \times 0.6$. After that, the Soft-Drop algorithm is applied to remove constituents associated with soft and wide-angle radiation.

6.4.2 Small-R Jets

Small-R jets are reconstructed with the anti- k_t algorithm, with $R = 0.4$ using PFlow input objects. Jets reconstructed in the central eta region ($|\eta| < 2.5$) of the detector, also referred to as signal jets, are required to pass the selection of $p_T > 20$ GeV. Jets reconstructed in the forward eta region ($2.5 < |\eta| < 4.5$) of the detector, aptly named forward jets, are required to pass the selection of $p_T > 30$ GeV. Additionally, jets with $p_T < 60$ GeV and $|\eta| < 2.4$ are required to pass a jet-vertex tagging (JVT) selection to reduce the contamination from jets originating from pile-up vertices.

²TCC is further explained in Subsection 4.3.5.2.

6.4.3 Electrons

Electrons are reconstructed from tracks in the ID that match topological clusters in the EM calorimeter. The electron candidates are required to have an $E_T > 7$ GeV and $|\eta| < 4.47$ (excluding the barrel- end-cap gap region). Additionally, there are requirements the absolute value of the longitudinal impact parameter, $|z \sin \theta| < 0.5$ mm, and the transverse impact parameter significance, $|d\theta|/\sigma_{d\theta} < 5$. In the context of this analysis, two electron identification criteria are used: “tight” and “loose”. The “tight” selection is used to select $W \rightarrow e\nu$ candidates in 1-lepton channel with $p_T > 30$ GeV. The “loose” selection is used to select $Z \rightarrow e^+e^-$ candidates in 2-lepton channel, with looser identification and no isolation requirement for electrons with $p_T > 100$ GeV. The “loose” selection is also used to veto events with additional leptons in 0- and 1-lepton channels.

6.4.4 Muons

Muons are reconstructed by matching tracks in the ID with tracks in the muon spectrometer (MS). Both sets of tracks are first formed independently, then extrapolated to cover the full range of the detector, bridging the sets of tracks together to form muon candidates. The muon candidates are required to have $E_T > 7$ GeV and $|\eta| < 2.5$. Like electrons, there are two identification criteria are used: “tight” and “loose”. The “tight” selection is used to select $W \rightarrow \mu\nu$ candidates in 1-lepton channel, with $p_T > 30$ GeV and medium identification working point and tight isolation criteria. The “loose” selection is used to select $Z \rightarrow \mu^+\mu^-$ decays in the 2-lepton channel, with looser identification and isolation working points, and no isolation requirement for electrons with $p_T > 100$ GeV. The “loose” selection is also used to veto events with additional leptons in 0- and 1-lepton channels.

6.4.5 Missing Transverse Energy

The presence of neutrinos in the final state can be inferred by the momentum imbalance in the transverse plane, described in Subsection 4.3.6. Missing transverse energy and momentum, E_T^{miss} (or MET) and p_T^{miss} , are reconstructed by negative sum of the all physics objects and ID tracks not associated with them in the transverse direction. Missing energy is calculated from the calorimeter cells of the hard interaction as well as cells for the track-based soft terms. Missing momentum is calculated from the sum of the transverse momenta of all the tracks associated to the primary vertex. Another observable that is useful to decrease contributions from background with large E_T^{miss} is E_T^{miss} significance, S :

$$S = \frac{E_T^{miss}}{\sqrt{\sum E_T}} \quad (6.1)$$

Where E_T^{miss} is the reconstructed magnitude of the missing transverse momentum, and $\sqrt{\sum E_T}$ is the event based approximation to the total E_T^{miss} resolution. The significance separates events in which the reconstructed MET originates from weakly interacting particles, or other sources (resolution and inefficiencies), such as mismeasurements of leptons and jets energies.

6.4.6 Tracks

Tracks are reconstructed from hits in the ID using the `Primary` tracking algorithm with the `Tight` track quality selection and the `Tight` track-vertex association criteria. Additional requirements for tracks include: $|\eta| < 2.5$ and $p_T > 5$ GeV.

6.4.7 Variable-Radius Track-Jet

Variable-radius (VR) track jets are used to identify b-quark jets in large-R jets. They apply the anti- k_T algorithm on the tracks with a p_T -dependent radius parameter:

$$R_{eff}(p_T, i) = \frac{\rho}{p_{T,i}} \quad (6.2)$$

Where $\rho = 30$ GeV, and an upper and lower cone-size limit of $R = 0.4$ and $R = 0.02$, respectively. Additional requirements on VR jets include: $p_T > 10$ GeV, $|\eta| < 2.5$, and the number of associated tracks $n_{Trk} > 1$. Collinear VR track jets can develop, and their interaction with the track-association portion of b-tagging algorithms is not well established. An ATLAS Combined Performance group provide recommendations addressing this issue. Under their recommendation, this analysis removes events that have overlapping track jets used for b-tagging, where the following is applied:

$$\Delta R_{i,j} < \min(R_{eff,i}, R_{eff,j}) \quad (6.3)$$

where the indices i, j run on all VR track jets with $p_T > 5$ GeV and $n_{Trk} > 1$.

6.4.8 Flavor Tagging

Two different jet collections are used for b-tagging: small-R jets in the resolved category and VR track jets in the merged category (which target boosted $Z \rightarrow b\bar{b}$ and $H \rightarrow b\bar{b}$ decays). The DL1r b-tagging algorithm is applied to both $R = 0.4$ calorimeter jets and VR track jets, with a 77% efficiency operating point evaluated in simulated $t\bar{t}$ events. The rejection rates for light-flavor hadrons or gluons are 192 for small-R jets and 200 for VR track jets,

while for jets containing c-hadrons, they are approximately 5 and 7, respectively. A muon-in-jet correction is applied as in the previous VH paper. The DL1r algorithm uses a score threshold to identify b-tagged jets, with a 70% efficiency working point (WP) for signal jets and an 85% WP for VR track jets, where a higher WP increases both signal and background acceptance.

6.4.9 Vector-Boson Tagging

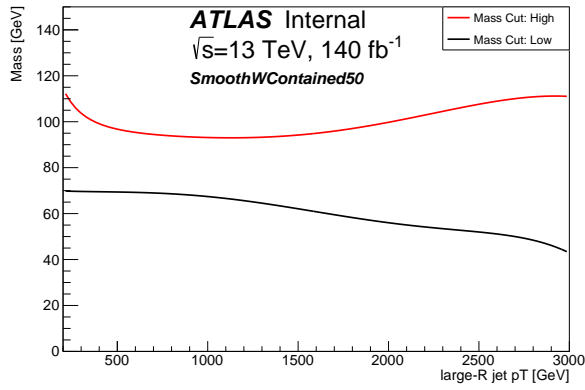
To further aid in background rejection for large-R jets, the 3-variable cut-based boson tagger is used to selection $V \rightarrow qq$ jets (further described with details in Chapter 5).

The 3-variable tagger applies cuts on the large-R jet mass, $m(J)$, and two jet sub-structure variables (both described in Chapter 5), D_2 and N_{Trk} . The upper and lower boundaries of the mass-window requirements and the N_{trk} requirements for the 3-variable tagger as a function of large-R jet p_T is shown in Figure 6.5 and Figure 6.6.

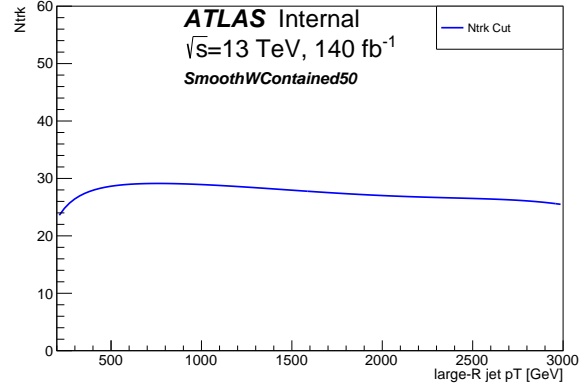
In this analysis, the 50% working point is used, such that large-R jets are considered “tagged” if they pass the 50% WP threshold.

6.4.10 Overlap-Removal

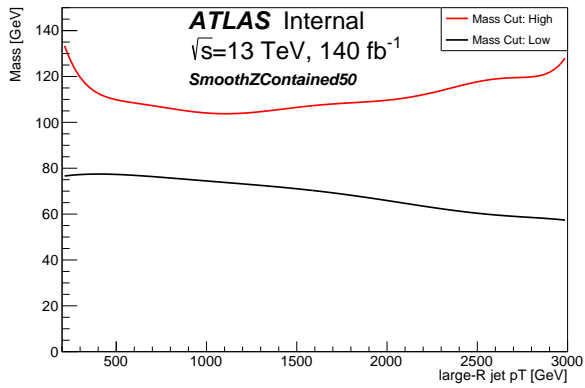
As the different objects are reconstructed and selected independently, there is a chance that different objects are built from the same inputs. Thus, to avoid double counting energy, an overlap-removal procedure based on the angular separation ΔR in the $\eta\phi$ -plane between two reconstructed objects, is applied. A τ -lepton is removed if it overlaps with a muon within $\Delta R < 0.2$, unless the τ has $p_T > 50$ GeV and the muon is not a combined muon. Electrons are removed if they share an ID track with a muon. A small-R jet is removed if it is



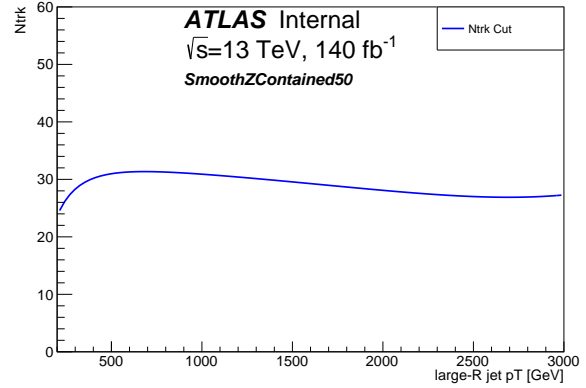
(a)



(b)

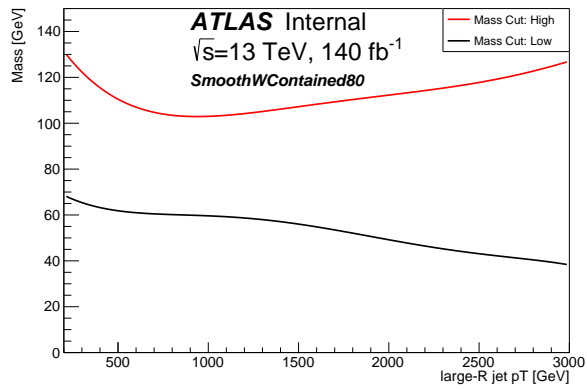


(c)

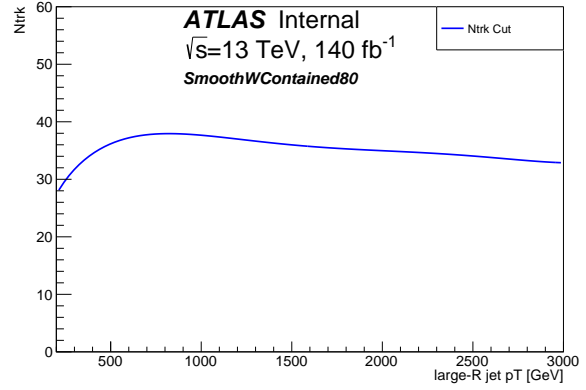


(d)

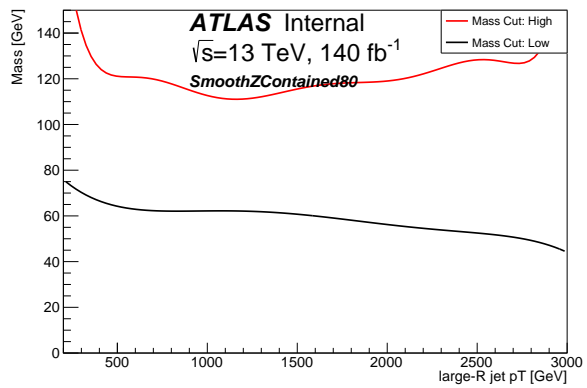
Figure 6.5: Mass window (a)(c) and sub-structure (b)(d) requirements for the 3-Variable tagger with a 50% efficiency for the W-tagger (top) and Z-tagger (bottom).



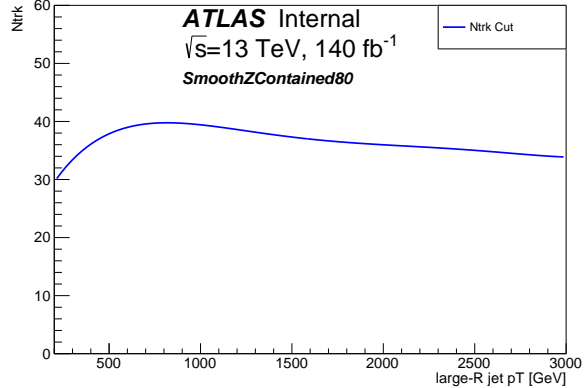
(a)



(b)



(c)



(d)

Figure 6.6: Mass window (a)(c) and sub-structure (b)(d) requirements for the 3-Variable tagger with a 80% efficiency for the W-tagger (top) and Z-tagger (bottom).

within $\Delta R < 0.2$ of an electron or a muon that has passed isolation requirements. In order to retain jets originating from leptonic b-hadron decays, jets are only removed if they have fewer than three associated tracks, or if more than 70% of the transverse momentum sum of the associated tracks comes from the muon. Last but not least, electrons and muons are removed if they overlap with any of the remaining jets within $0.2 < \Delta R < \min(0.4, 0.04 + 10\text{GeV}/p_T)$.

6.5 Event Selection

After the final state objects have been reconstructed, the next step is to define the final regions of the analysis by performing a selection on the events. There are general requirements common to all regions, as well as specific selections to target each decay channel. There are 3 channels across lepton multiplicity according to the number of reconstructed charged leptons:

- $Z \rightarrow \nu\nu$ in the 0-lepton channel
- $W \rightarrow e\nu$ or $W \rightarrow \mu\nu$ in the 1-lepton channel
- $Z \rightarrow ee$ or $Z \rightarrow \mu\mu$ in the 2-lepton channel

which can be further divided into 2 channels across reconstructed jet techniques: resolved or merged. Previous iterations of this analysis separated based on the reconstructed hadronic candidate, if reconstructed as a Higgs boson (H) it was considered part of the “VH analysis”, and if reconstructed as a W or Z boson then it was considered part of the “VV analysis”. Now in this combined effort, as the “VV+VH analysis”, all reconstructed bosons are considered, and a prioritization of either the resolved or merged region allow for orthogonal final regions.

Additionally, optimization and harmonization of the VV and VH regions has been conducted to maximize the analysis sensitivity.

6.5.1 Preselection

An initial preselection is applied to all events. Events are required to be on ATLAS' Good-Runs List, mentioned in Section 3.8, to reject bad or corrupted data events. Events are also required to have a primary vertex with at least two associated tracks in order to ensure an event with a hard proton-proton collision. Jet cleaning, further discussed in Subsection 6.5.3.1, is also applied with the “loose” event flag in all lepton channels (but adjusted later for the 0-lepton channel).

6.5.2 Jet Requirements

Two channels are used to reconstruct the W/Z/H hadronic decay as either a single large-R jet or two small-R jets, referred to as merged or resolved, respectively. The difference is attributed to the reconstruction strategy.

6.5.2.1 Resolved Regime

For the resolved region, candidate bosons are reconstructed from small-R jets, all of which are required to have a jet $p_T > 45$ GeV. Candidate W/Z jets are reconstructed from the two leading small-R jets in the event, whereas candidate H jets are reconstructed from the two leading b-tagged small-R jets. If there is only one b-tagged jet, candidate H jets are reconstructed from the b-tagged jet and the leading non-b-tagged jet.

The reconstructed dijet system (jj) required invariant mass windows consistent with the W/Z/H bosons:

- W boson: $62 < m_{jj} < 97$ GeV
- Z boson: $70 < m_{jj} < 105$ GeV
- H boson: $110 < m_{jj} < 140$ GeV (0/1-lepton), $100 < m_{jj} < 145$ GeV (2-lepton)

6.5.2.2 Merged Regime

For the merged region, candidate bosons are reconstructed from a leading- p_T large-R jet, which is required to have a jet $p_T > 200$ GeV ($p_T > 250$ GeV) in the VV (VH) analysis. In the VH analysis, the Higgs candidate is selected by imposing a mass window of $75 \text{ GeV} < m_J < 145 \text{ GeV}$. In the VV analysis, the mass windows are defined using the p_T -dependent W and Z mass cuts from the W/Z Tagger, mentioned in Subsection 6.4.9. The mass windows as a function of p_T are shown in Figure 6.5 and Figure 6.6. Events passing both the mass window and D_2 cuts are defined as High-Purity (HP), while events that pass the mass cut but fail the D_2 cut are classified as Low-Purity (LP). The HP region is optimized to enhance signal purity by selecting events with jet substructure characteristics consistent with hadronic decays of boosted bosons, thereby improving the signal-to-background ratio and increasing sensitivity in regions where backgrounds can be suppressed. However, this strict selection comes at the cost of reduced overall efficiency, as some genuine signal events are excluded. The LP region, while less pure due to relaxed D_2 criteria, captures additional signal events that do not meet the HP requirements.

6.5.3 Lepton Requirements

This thesis presents the optimization of the 0-lepton channel, where the resulting selection criteria are used in the analysis. Similar studies were performed for the 1-lepton and 2-lepton

channel by other analyzers, and thus only the final selection is presented.

6.5.3.1 0-Lepton Optimization and Selection

The 0-lepton region is defined as selecting events with $Z \rightarrow \nu\nu$ decay. The main cuts of interest are the lepton, jet, and MET cuts. One goal for the optimization of the 0-lepton selection was to reduce the number of cuts required to retain, or possibly improve upon, the same signal acceptance and background rejection. Reducing the number of selection cuts would enhance the analysis by simplifying the procedure and minimizing potential redundancies that could unnecessarily eliminate signal events. The cuts applied during the previous iteration of the analysis can be found in Appendix B.

The methodology for this reduction consisted of first identifying a baseline, or a set list of cuts that are considered bare minimum to be included, then successively adding onto the baseline until a good agreement is reached. MET is a commonly used observable to detect and identify weakly interacting particles. The MET significance separates events in which the reconstructed MET originates from the weakly interacting particles, against other sources such as mis-reconstructed events. An optimal cut in MET significance could improve the signal to background ratio, particularly against QCD multijet production and V+jets. The multijet background describes the interactions of colored particles (quarks), and the interactions are mediated by gluons. It is an important source of uncertainty for both W +jets and Z +jets. QCD branching happens all of the time as an attempt to undo parton fragmentation, and MC has a hard time modeling this. Therefore, MET Significance was identified to possibly have the capability of replacing several anti-QCD cuts in the previous round of the analysis used to reject the QCD multijet and non-collision background for the 0-lepton channel. The main backgrounds are non-collision backgrounds, such as beam induced

background (BIB) and cosmic-ray showers, and calorimeter noise.

The purpose of having a baseline list of cuts is to establish and identify very basic cuts which are used throughout most ATLAS searches and which are not anti-QCD related. Here, we split between the merged and resolved channel due to underlying physics (and number of jets). The baselines are:

- Merged: Pass Trigger, MET > 200 GeV, >= 1 Large-R jet, Leading jet $p_T > 250$ GeV
- Resolved: Pass Trigger, MET > 150 GeV, >= 2 Signal jets

In addition, we apply a jet mass cut to eliminate the jets below 50 GeV, since above this threshold is the region of support for large-R jet mass recommendations [145]. From the baseline, we then applied several different MET significance cuts. After each MET Significance cut, the signal significance was calculated for various signal masses and compared together. By plotting the signal significance versus the MET significance cut, we could look at trends between the different signal samples, and identify if there was either a drop in significance at a too tight of MET significance threshold or an increase of significance at an optimal cut. A simplified significance equation was used to calculate the signal significance for various signal masses:

$$\sigma_{tot} = \sqrt{\Sigma\sigma_i^2}, \quad (6.4)$$

$$\sigma_i = \frac{s_i}{\sqrt{s_i^2 + b_i^2 + \delta_i^2}}, \quad (6.5)$$

where σ_{tot} represents total significance; σ is significance, s is number of signal events, b is number of background events, δ is statistical uncertainty, each defined for bin i . To balance the data/MC agreement with signal significance, χ^2/ndf was used to compare the goodness

of fit between data and MC with each subsequent MET significance cut (where the degrees of freedom is the same as the number of bins). A plot summarizing the results of this study is presented in Figure Figure 6.7.

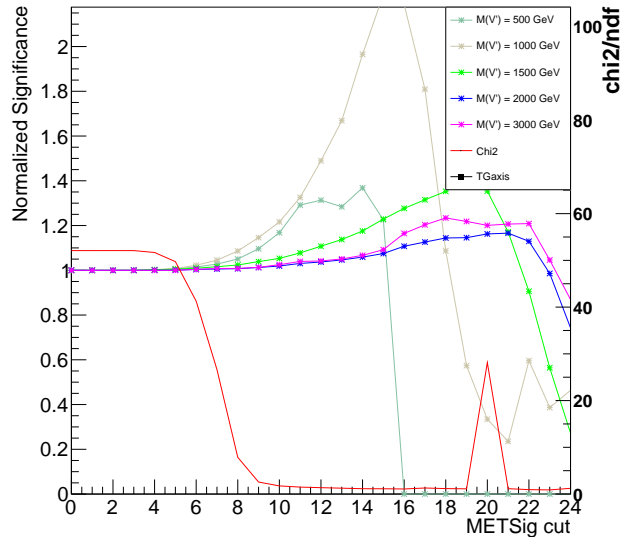


Figure 6.7: Various cuts on MET Significance vs normalized signal significance (left) and the χ^2/ndf of the data-to-simulation agreement (right, red line) for the VH merged, 1 b-tagged, ggF production region. As the MET Significance cuts get tighter, there is an optimal cut of 10 which allows for increased signal sensitivity while retaining good agreement with the χ^2/ndf .

By increasing the MET Significance cut, improvements in the signal significance can be seen after a cut of 6 is applied, and the χ^2/ndf improves (using the right-side axis in Figure 6.7), tending towards lower values, thus a better agreement. Beyond a cut of 10 the agreement becomes constant, but the signal significance for certain signal masses tend to decrease. Therefore, a MET Significance cut of 10 was found to have an optimal signal significance while also retaining a good χ^2/ndf value.

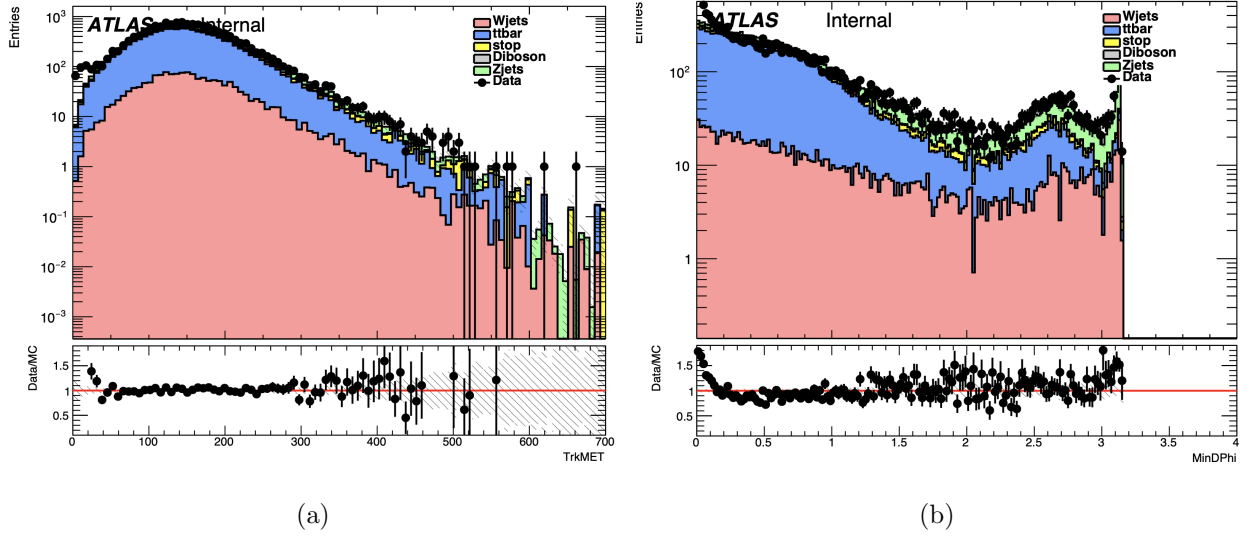


Figure 6.8: Observed and expected kinematic distributions of (a) TrkMET and (b) MinDPHi showing the data vs MC agreement with just the baseline and MET Significance cuts applied for Full Run-2.

After discovering the optimal MET significance cut, there were still disagreements between data and MC especially in the kinematic distributions $\min[\Delta\phi(\vec{E}_T^{miss}, R = 0.4jet)]$ (MinDPHi) and low \vec{p}_t^{miss} (TrkMET), as seen in Figure 6.8. Both $\min[\Delta\phi(\vec{E}_T^{miss}, R = 0.4jet)]$ and \vec{p}_t^{miss} were used in the previous analysis, which can be seen in Table B.1 for VV and Table B.2 for VH .

To first investigate the disagreement, a cut on low $\min[\Delta\phi(\vec{E}_T^{miss}, R = 0.4jet)]$ was applied, and found to have improved the agreement while maintaining good signal acceptance, which can be seen in Figure 6.9.

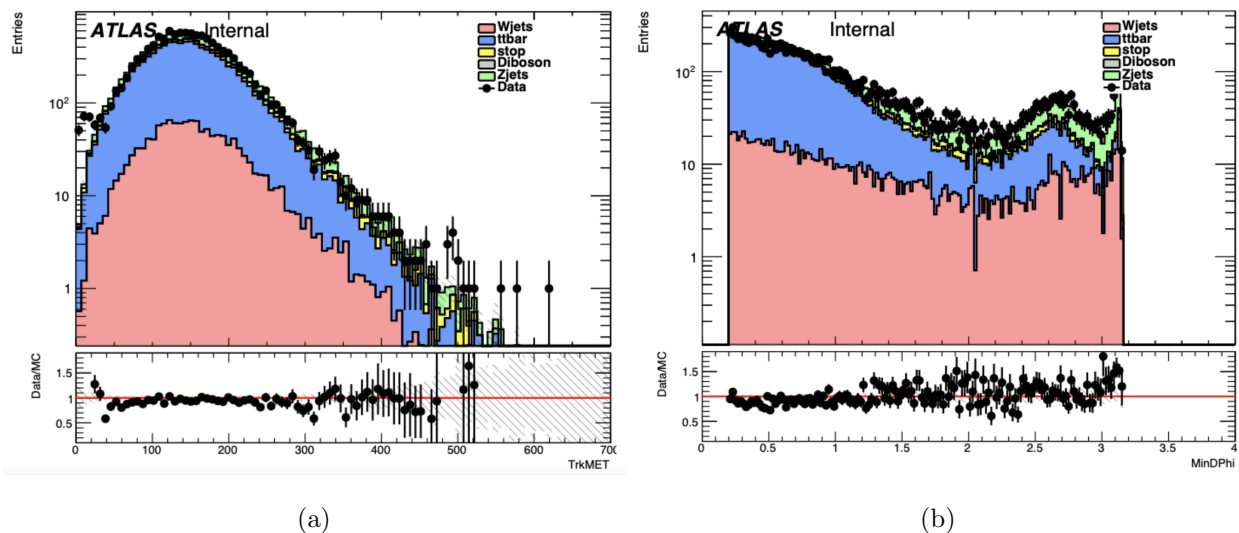


Figure 6.9: Observed and expected kinematic distributions of (a) TrkMET and (b) MinDPHi showing the data vs MC agreement with the addition of the MinDPHi cut applied (along with the baseline + MET Significance cuts) for Full Run-2.

A cut on \vec{p}_t^{miss} was also applied and investigated; however, \vec{p}_t^{miss} is currently not a supported variable (e.g. the ATLAS performance groups are not confident enough in its modelling such that it is not recommended to make selections based on this variable if possible). Rather, exploring the jet-cleaning requirement was proposed to circumvent the issues with \vec{p}_t^{miss} . Since we are dealing with collision events, the high transverse momenta jets must be distinguished from the relevant backgrounds. Jet cleaning is the idea of efficiently rejecting jets from these background processes while keeping the jets produced in proton-proton collisions. In the analysis, as well as the previous round, a loose jet-cleaning cut is already applied with 99.9% efficiency for signal jets. The tight cut is 95% efficient for 20 GeV jets. To implement a tighter jet-cleaning requirement into the analysis, the resolved channel and merged channel were again treated slightly different.

In the resolved channel, two signal jets are clear, so we just apply a cut on the leading signal jet. However, when applying that same process to the merged channel, we observed

the signal efficiency dropping. This was due to the leading small- R jet and the selected large- R jet being far in ΔR , meaning that they don't connect to the same underlying truth jet/hadron, and we were applying the cut on the jet not closest to the true selected jet. To rectify this issue in the merged channel, we first find the closet ΔR small- R jet and then apply the cut to that jet. This ensured that the data/MC agreement was improved, while the signal selection efficiency did not drop due to the tight jet cleaning requirement. This improvement is reflected in Figure 6.10.

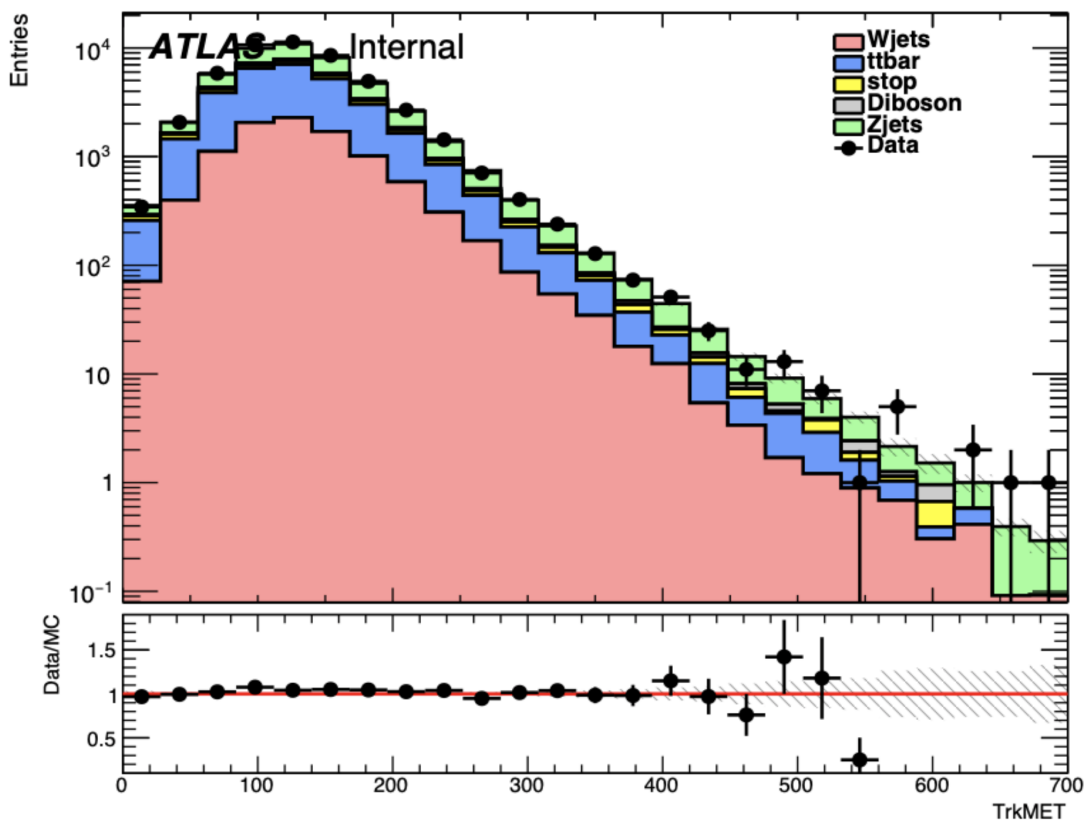


Figure 6.10: Observed and expected kinematic distributions of TrkMET showing the data vs MC agreement with the addition of the jet cleaning cut applied (along with the baseline + MET Significance + MinDPhi cuts) for Full Run-2.

A $\min[\Delta\phi(\vec{E}_T^{miss}, R = 0.4jet)]$ cut of 0.2, and tight jet cleaning cut was decided to be used, in conjunction with the baseline and simplified MET Significance cut. This reduced

the overall number of cuts in the analysis by 3 and simplified the MET Significance cut, while also retaining similar signal efficiency, background rejection, and level of data/MC agreement. The finalized list of cuts for both VV and VH is shown in Table 6.2.

Table 6.2: Finalized signal region event selection for the 0-lepton channel.

Selection	Merged	Resolved
Trigger	Pass	
MET Significance	10	
E_T^{miss}	> 200 GeV	> 150 GeV
$m(J)$	> 50 GeV	
$\min(\Delta\Phi(E_T^{miss}, \text{small-R jets}))$	> 0.2	
Jet Cleaning	Pass	
Number of jets	≥ 2 small- R jets	≥ 1 large- R jet

6.5.3.2 1-Lepton Selection

The 1-lepton region is defined as selecting events with $W \rightarrow l\nu$ decays. These events are required to have exactly one “tight” isolated lepton (electron or muon) with $p_T > 30$ GeV, and no additional “loose” leptons (electrons or muons). To select W decays in the merged (resolved) regions, additional requirements include a constraint on $E_T^{miss} > 100(60)$ GeV and on the W candidate $p_T > 200(75)$ GeV.

Contamination arising from $t\bar{t}$ is suppressed by removing events with additional b-tagged jets in the resolved regime, or additional b-tagged VR jets outside the large-R jet in the merged regime. To further optimize the 1-lepton resolved regime, several angular requirements are applied to suppress QCD-multijet contributions. To contain the leptonic and hadronic decays, cuts on $\Delta\phi(l, E_T^{miss}) < 1.5$ and $\Delta\phi(j_1, j_2) < 1.5$ are applied to events. For events with well separated leptonic and hadronic decays, cuts on $\Delta\phi(l, j_1/j_2) > 1.0$ and $\Delta\phi(E_T^{miss}, j_1/j_2) > 1.0$ are also applied. For electrons only, there is an additional require-

ment of $E_T^{miss}/p_T(W) > 0.2$ applied. The final discriminant for the 1-lepton region is the invariant mass of the reconstructed diboson system: $m(VV/VH)$.

6.5.3.3 2-Lepton Selection

The 2-lepton region is defined as selecting events with $Z \rightarrow ll$ decays. These events are required to have 2 “loose” leptons of the same flavor (electron or muon) with a leading lepton $p_T > 27$ GeV, and sub-leading lepton $p_T > 25(20)$ GeV for the merged (resolved) region. Events with additional leptons are vetoed. For events with two muons, they are required to have opposite charge. This does not apply to electron pairs on account of their higher rate of charge misidentification due to possible converted photons from bremsstrahlung radiation.

The dilepton invariant mass, m_{ll} , is required to be consistent with the Z boson mass for the 2-lepton system. A fixed m_{ll} window of $83 < m_{ee} < 99$ GeV is applied for di-electrons. For di-muons, to account for the mass resolution degradation at high Z transverse momentum, a $p_T(ll)$ -dependent mass window (in GeV) is used:

$$85.6 - 0.0117p_T(ll) < m_{\mu\mu} < 94.0 + 0.0185p_T(ll) \quad (6.6)$$

Along with an additional cut to further suppress the backgrounds:

$$R = \frac{\min(p_T(W_{lep}), p_T(W/Z/h_{had}))}{m(VV/VH)} > 0.35 \quad (6.7)$$

similarly in the 1-lepton channel, but is relaxed at higher signal masses to recover signal efficiency.

A requirement on the object-level MET significance to be $S < 4$ suppresses $t\bar{t}$ background contamination by removing events consistent with the presence of E_T^{miss} . The final discrim-

inant for the 2-lepton region is the invariant mass of the reconstructed diboson system: $m(VV/VH)$.

6.5.4 Multi-Class Classifier (MCT)

As mentioned during Section 6.2, different types of final regions are defined and events are categorized into signal regions or control regions. However, due to the complexity of the analysis there exists some overlap of the regions unintentionally, which is where the multi-class classifier (MCT) is deployed. The MCT is a five-class neural network (NN) designed to identify the hadronic decays coming from a Higgs boson, W boson, Z boson, top-quark, or QCD. In the VV+VH analysis, the jet mass windows overlap, thus the MCT aides with the orthogonalization of the final regions. The identification of the hadronic decays are useful for sorting events into either the SR or CR categories, and a prioritization strategy is also implemented. This thesis does not focus on the construction or implementation of this NN, (contribution by a former MSU graduate student, Maria Mazza); however, the analysis as a whole benefit immensely from its inclusion.

6.6 Systematic Uncertainty

Systematics are an important piece in the analysis-puzzle as they affect the normalization and shape of final discriminating variables, background estimates, and signal selection efficiencies, overall influencing the search sensitivity. In a nutshell, systematic uncertainties parameterize our ignorance based on imperfect knowledge of theory and experiment, to temper claims of significant excesses or deficits unless they are clearly beyond those uncertainties. Similarly to Subsection 5.3.2, systematics can be thought of as either falling into the category of

experimental or theory uncertainties. Most of the theory uncertainties discussed here happen to be modelling uncertainties, where the shape of the distributions changes due to changing generator parameters. Experimental uncertainties are those that are related to the detector and reconstruction performance. In the statistical analysis (the following section), each of the systematics are treated as a nuisance parameter, and the systematic variations are estimated on the final discriminate.

6.6.1 Experimental Uncertainties

Luminosity: The total integrated luminosity uncertainty is 0.83% [146] with each individual data taking year's uncertainty ranging from 0.9% to 1.1%. This uncertainty is applied to backgrounds estimated from simulation and the signal samples.

Pile-up: The uncertainty associated with pileup, first introduced and explained in Subsection 4.3.1, is the correction for the differences between the pileup distribution in data and simulation, and is done by applying a weight to each MC event [147].

Muon and Electron Efficiencies: The tag-and-probe method, described in Subsection 5.3.1, is used to model the electron and muon uncertainties deriving from the reconstruction, identification, and isolation efficiencies. These uncertainties are small (around 1%) and are applied to the simulation, taking into account the differences between data and MC [148, 149].

Missing Transverse Energy: The uncertainties on E_T^{miss} are derived from the reconstruction and identification uncertainties of the individual physics objects that contribute to its calculation [150].

Small-R jet energy scale and resolution: Small-R jet energy scale (JES) and resolution (JER) uncertainties quantify how accurately and precisely the energy of jets reconstructed with a small radius parameter ($R = 0.4$) is known [151]. These uncertainties arise from factors such as detector response, pileup, and calibration procedures, and are evaluated using both simulation and *in-situ*³ techniques with data to ensure reliable jet measurements in physics analyses. For central jets with $p_T > 20$ GeV, the overall relative JES uncertainty fluctuates in the range of 1-4%, with an additional 2-4% uncertainty for forward jets. The JER uncertainty ranges from 20% for low- p_T jets (around 20 GeV) to less than 5% for $p_T > 200$ GeV.

Large-R jet energy scale and resolution: Large-R jet energy scale (JES) and resolution (JER) uncertainties reflect the accuracy and precision of energy measurements for jets reconstructed with a larger radius parameter ($R = 1.0$), which are often used to capture boosted objects. These uncertainties, as well as the jet mass resolution (JMR) uncertainty, are assessed by comparing the calorimeter and track-based energy and mass measurements in data and MC [152]. The JES uncertainty for $200 \text{ GeV} < p_T < 2 \text{ TeV}$ jets is 1-2%. The JER and JMR uncertainties for the same p_T -range are 2% and 2-10%, respectively.

b-tagging: Hadrons containing *b*-quarks are different than other hadrons, typically having larger masses, lifetimes, and multiplicities of decay products. There are several techniques em-

³In this context, *in-situ* refers to data-driven techniques used to refine the JES and estimate JER uncertainties. These methods leverage well-measured reference objects, such as photons or Z-bosons, in events like $\gamma + \text{jet}$, $Z + \text{jet}$, and multijet systems to balance and calibrate jet responses directly in data. For JES, in-situ measurements correct residual discrepancies between data and simulation and provide a key component of the total JES uncertainty. Similarly, in-situ JER uncertainties are derived by comparing jet resolutions in data and MC using methods like dijet asymmetry. These in-situ techniques improve the precision and realism of jet calibrations by reducing reliance on simulation and anchoring corrections to the actual detector performance.

ployed to identify jets containing b -hadrons (referred to as b -tagged jets), which is important for many physics processes, such as the identification of top-quarks (which primarily decay into a W -boson and b -quark). Differences in the b -tagging efficiency and misidentification rate measured in data and MC are treated as corrective factors for b -jets, as well as for c -jets and light flavor jets (u -, d -, g -induced-jets). Uncertainties in these correction factors are derived from $t\bar{t}$ control samples [153, 154, 155], and have uncertainties of 1-8%, 10-15%, and up to 50% for b -jets, c -jets, and light flavor-jets, respectively.

6.6.2 Modeling Uncertainties

Modeling uncertainties arise from the intrinsic assumptions and approximations made during the MC event generation process. These uncertainties capture the potential variations in both the overall normalization and the detailed shape of the predicted distributions, reflecting differences that can arise from the choice of the MC generator, the underlying physics models, and the specific parameter configurations used in the simulations. These variations account for factors such as the treatment of parton showering, hadronization, parton distribution functions (PDFs), and underlying event modeling, all of which can significantly influence the accuracy of the generated predictions compared to real experimental data.

For my contributions in particular, these effects are quantified and studied for $t\bar{t}$ and single-top. The modeling uncertainties are determined by measuring the difference between the nominal MC generator with alternative generators. The alternative generator samples are typically generated with AF2 (“fast simulation”, described in section Section 4.2).

6.6.2.1 $t\bar{t}$ and single-top Modeling

The $t\bar{t}$ and single-top normalizations are free parameters in the fit, described in the next section, thus the normalizations of systematic variations are scaled to the nominal sample in the $t\bar{t}$ or single-top control region, such that only shape changing effects are taken into account here. The changes between different generators are compared by taking the ratio of the shape systematic to the base MC sample.

For $t\bar{t}$, the uncertainty corresponding to the matching of the matrix element and the parton shower is accounted for by comparing the default POWHEG sample with the distribution obtained using AMC@NLO as an alternative generator. Additional systematic uncertainties are evaluated by comparing the nominal sample showered with PYTHIA to one showered with HERWIG. The ratio between the normalized nominal AF2 and each normalized systematic is taken as:

- Variation of hadronization (PHH7): PYTHIA8 \rightarrow HERWIG7
- Variation of generator (AMC@NLO): POWHEG \rightarrow AMC@NLO
- Higher initial state radiation in POWHEG + PYTHIA8 (PHPYRAD)

For single-top, the uncertainty corresponding to the matching of the matrix element and the parton shower is accounted for by comparing the default POWHEG sample with the distribution obtained using MADGRAPH as an alternative generator. Additional systematic uncertainties are evaluated by comparing the nominal sample showered with PYTHIA to one showered with HERWIG. Differing from $t\bar{t}$, the modeling of single-top production also includes a theory uncertainty associated with the treatment of overlapping phase space between single-top and $t\bar{t}$ bar processes. This is handled using the DIAGRAM SUBTRACTION

(DS) scheme, which subtracts overlapping contributions at the matrix element level to avoid double-counting. The ratio between the normalized nominal AF2 and each normalized systematic is taken as (except for DS, which is compared to the full simulation rather than the AF2 version):

- Variation of hadronization (*PowhegH7*): PYTHIA8 \rightarrow HERWIG7
- Variation of generator (*MGPy*): POWHEG \rightarrow MADGRAPH
- Theory uncertainty for $t\bar{t}$ overlap (*DS*): DIAGRAM SUBTRACTION

As there is a lot of variation in some of the ratios, a fit is performed to capture most of the important information about the uncertainty while maintaining something that is viable to use in the statistical machinery. A few different functions were tried (degree-1 polynomial, degree-2 polynomial, square-root function) and chosen based on the χ^2 of all the fits. From those studies, a linear (degree-1 polynomial) fit was chosen. However, a heavy-side function was also incorporated to limit the linear fit, such that when the relative statistical uncertainty was larger than 30%, then the last value is kept for the rest of the distribution. In general, there is a good agreement between the nominal and variation. Where there is some disagreement, the fits are on the conservative side, and the regions do not have a dominant effect on the overall uncertainty when considered in the context of the full background distribution.

Figure 6.11 to Figure 6.18 show the un-normalised main distributions of each, the ratios after all have been normalized to the integral of the nominal, and the fit applied for VV and VH, merged and resolved, all lepton channels, and relevant SR and CRs for $t\bar{t}$. Figure 6.19 to Figure 6.26 show the un-normalised main distributions of each, the ratios after all have

been normalized to the integral of the nominal, and the fit applied for VV and VH, merged and resolved, all lepton channels, and relevant SR and CRs for single-top. The AF2 sample (in black) is treated as the nominal $t\bar{t}$ or single-top sample for comparison, and DS is compared to the full simulation rather than the AF2 version.

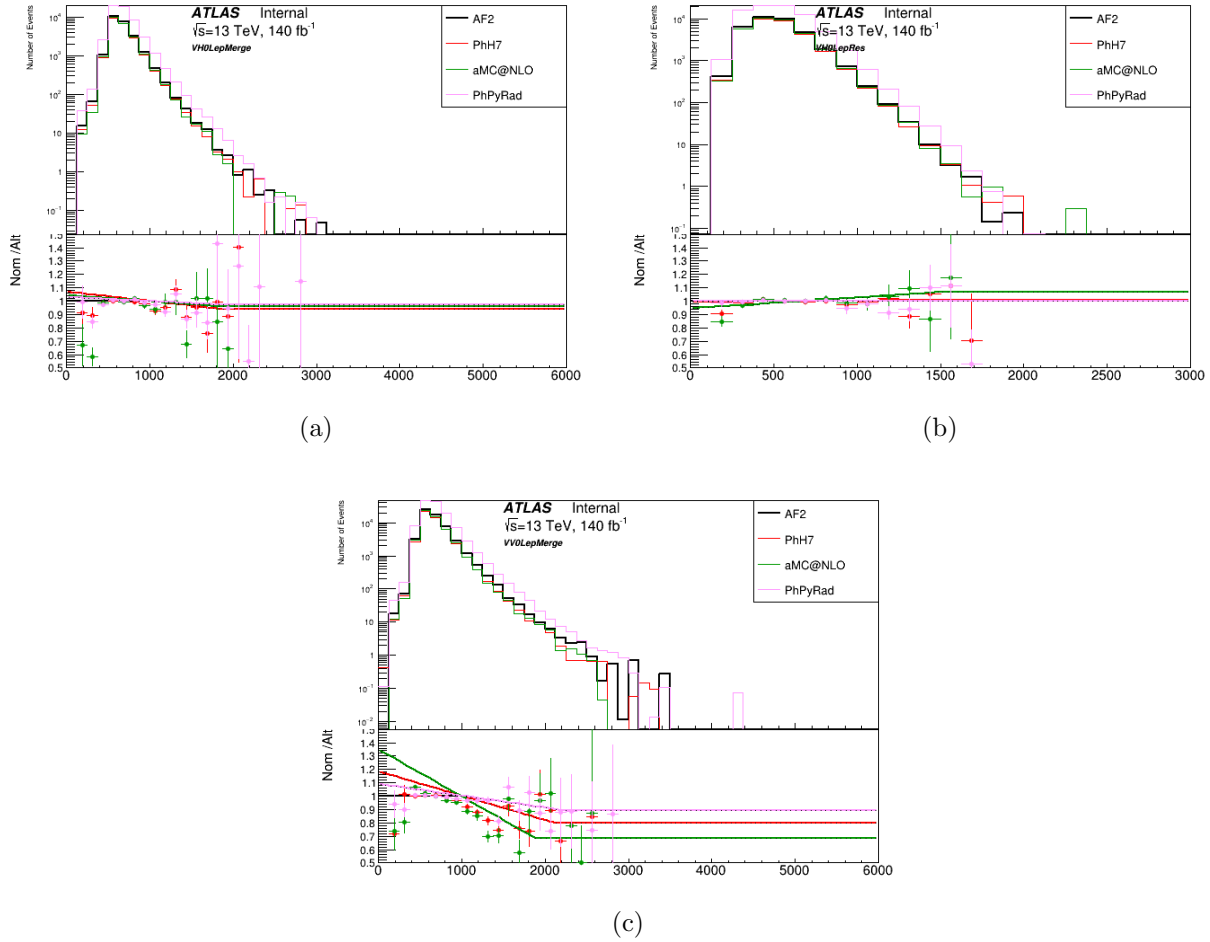


Figure 6.11: Comparisons of the $t\bar{t}$ AF2 sample with each systematic uncertainty in m_{VV} or m_{VH} for each SR of the 0-lep channel. The bottom panel shows the normalized ratio (after all have been normalized to the integral of the nominal) of each systematic to the nominal AF2 sample after normalisation and a degree-1 polynomial fit is applied. Figures (a) and (b) show results for VH 0-lep in the merged (left) resolved (right) region. Figure (c) show results for the VV 0-lep merged region (center).

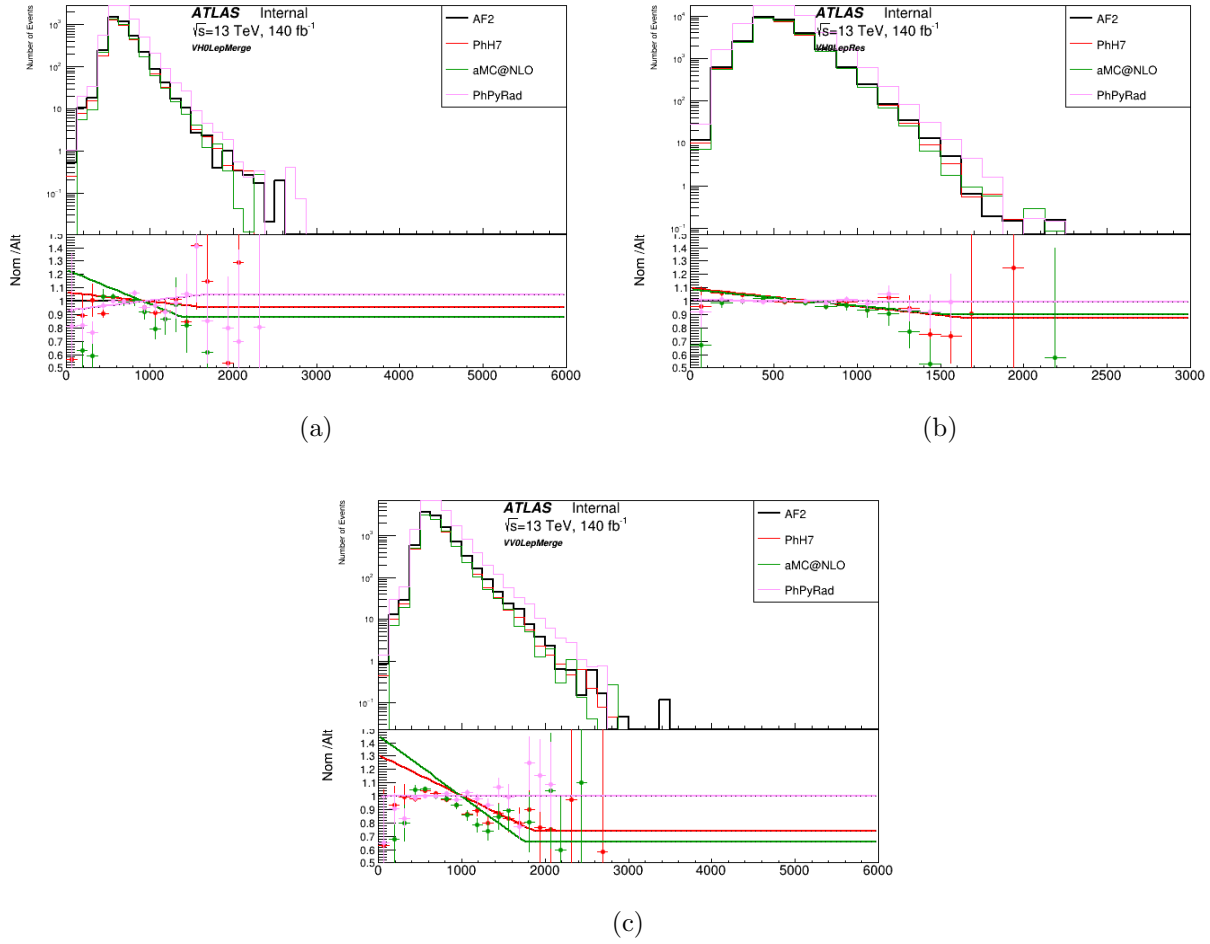


Figure 6.12: Comparisons of the $t\bar{t}$ AF2 sample with each systematic uncertainty in m_{VV} or m_{VH} for each MCR of the 0-lep channel. The bottom panel shows the normalized ratio (after all have been normalized to the integral of the nominal) of each systematic to the nominal AF2 sample after normalisation and a degree-1 polynomial fit is applied. Figures (a) and (b) show results for VH 0-lep in the merged (left) resolved (right) region. Figure (c) show results for the VV 0-lep merged region (center).

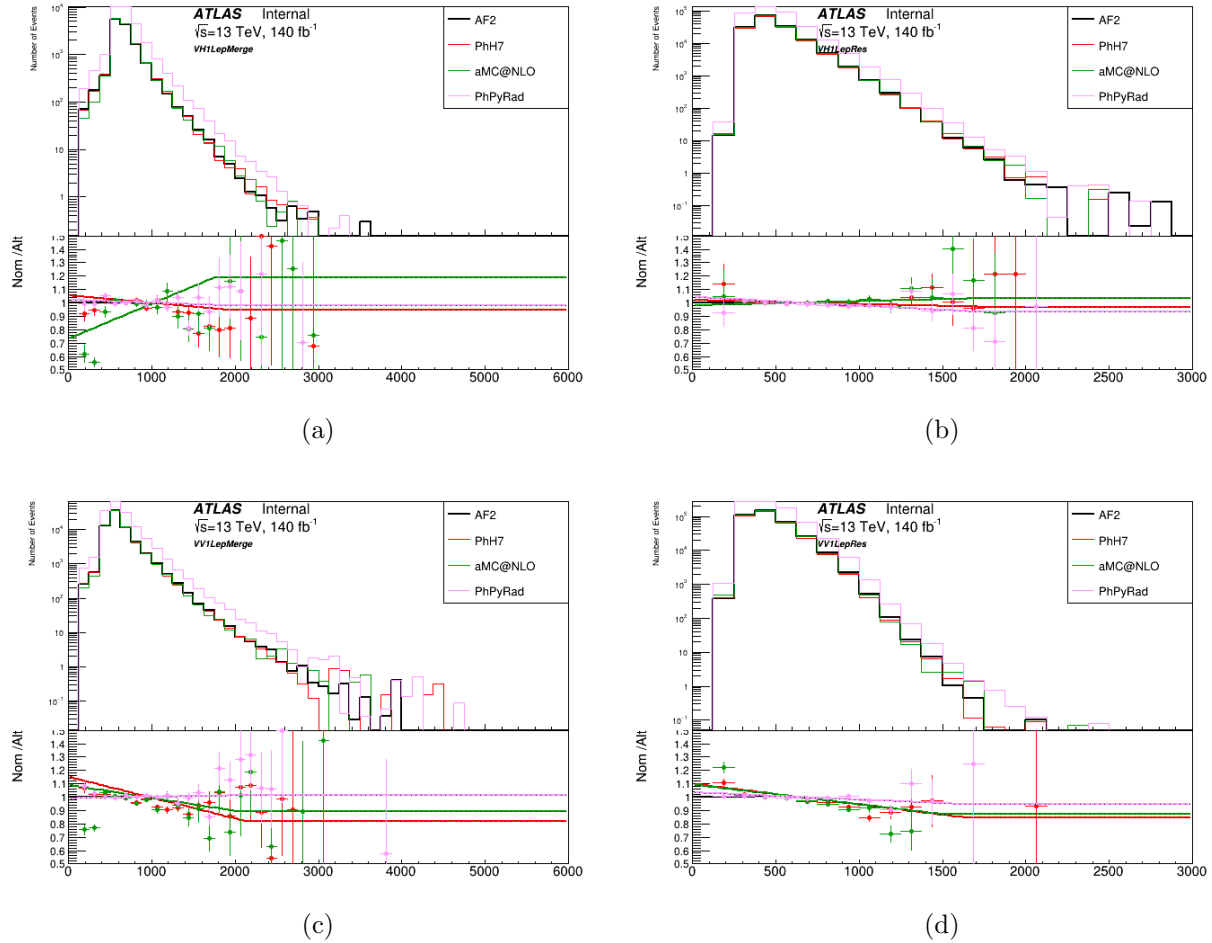


Figure 6.13: Comparisons of the $t\bar{t}$ AF2 sample with each systematic uncertainty in m_{VV} or m_{VH} for each SR of the 1-lep channel. The AF2 sample in black is used as the nominal for comparison. The bottom panel shows the normalized ratio (after all have been normalized to the integral of the nominal) of each systematic to the nominal AF2 sample after normalisation and a degree-1 polynomial fit is applied. Figures (a) and (b) show results for VH 1-lep in the merged (left) and resolved (right) region. Figures (c) and (d) show results for the VV 1-lep merged (left) and resolved (right) region.

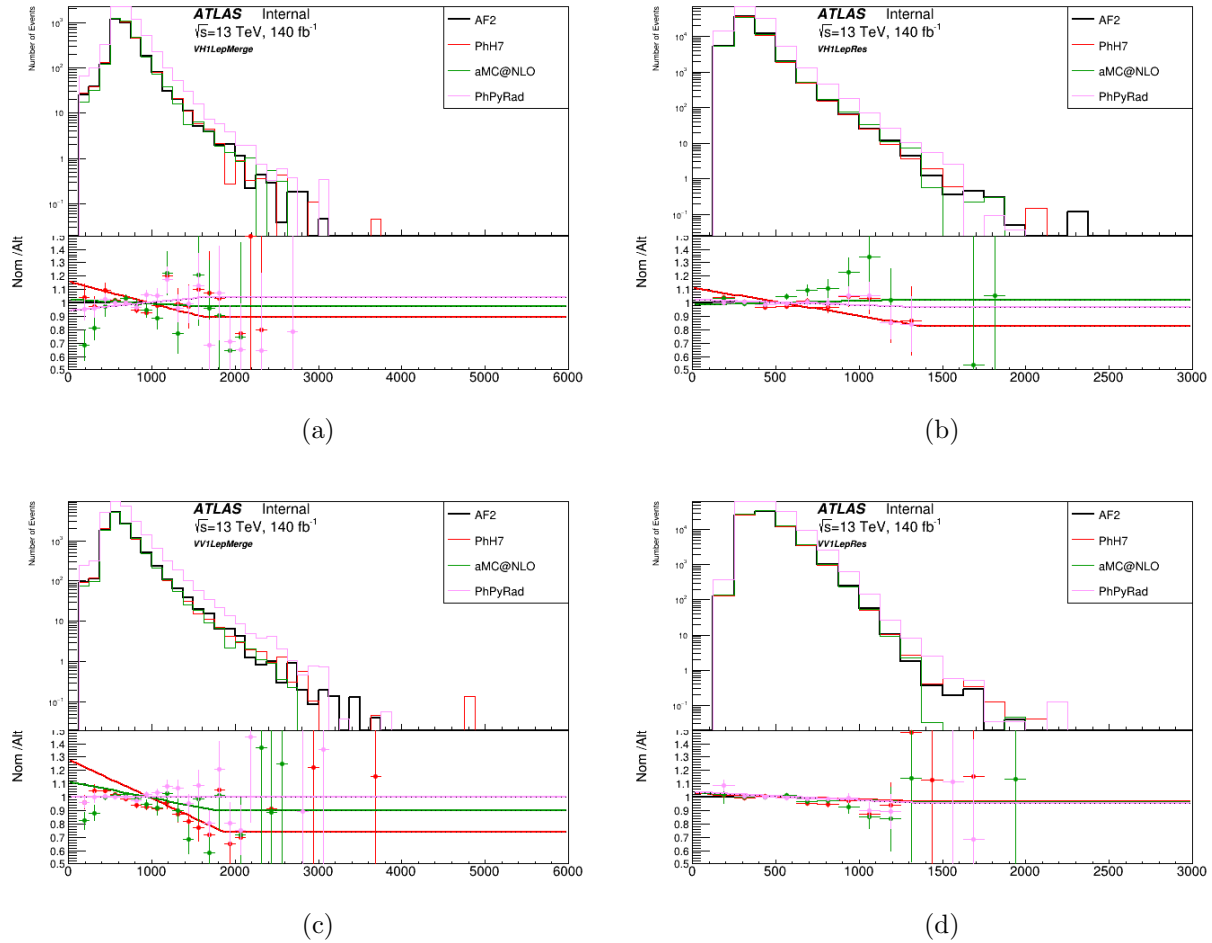


Figure 6.14: Comparisons of the $t\bar{t}$ AF2 sample with each systematic uncertainty in m_{VV} or m_{VH} for each MCR of the 1-lep channel. The AF2 sample in black is used as the nominal for comparison. The bottom panel shows the normalized ratio (after all have been normalized to the integral of the nominal) of each systematic to the nominal AF2 sample after normalisation and a degree-1 polynomial fit is applied. Figures (a) and (b) show results for VH 1-lep in the merged (left) and resolved (right) region. Figures (c) and (d) show results for the VV 1-lep merged (left) and resolved (right) region.

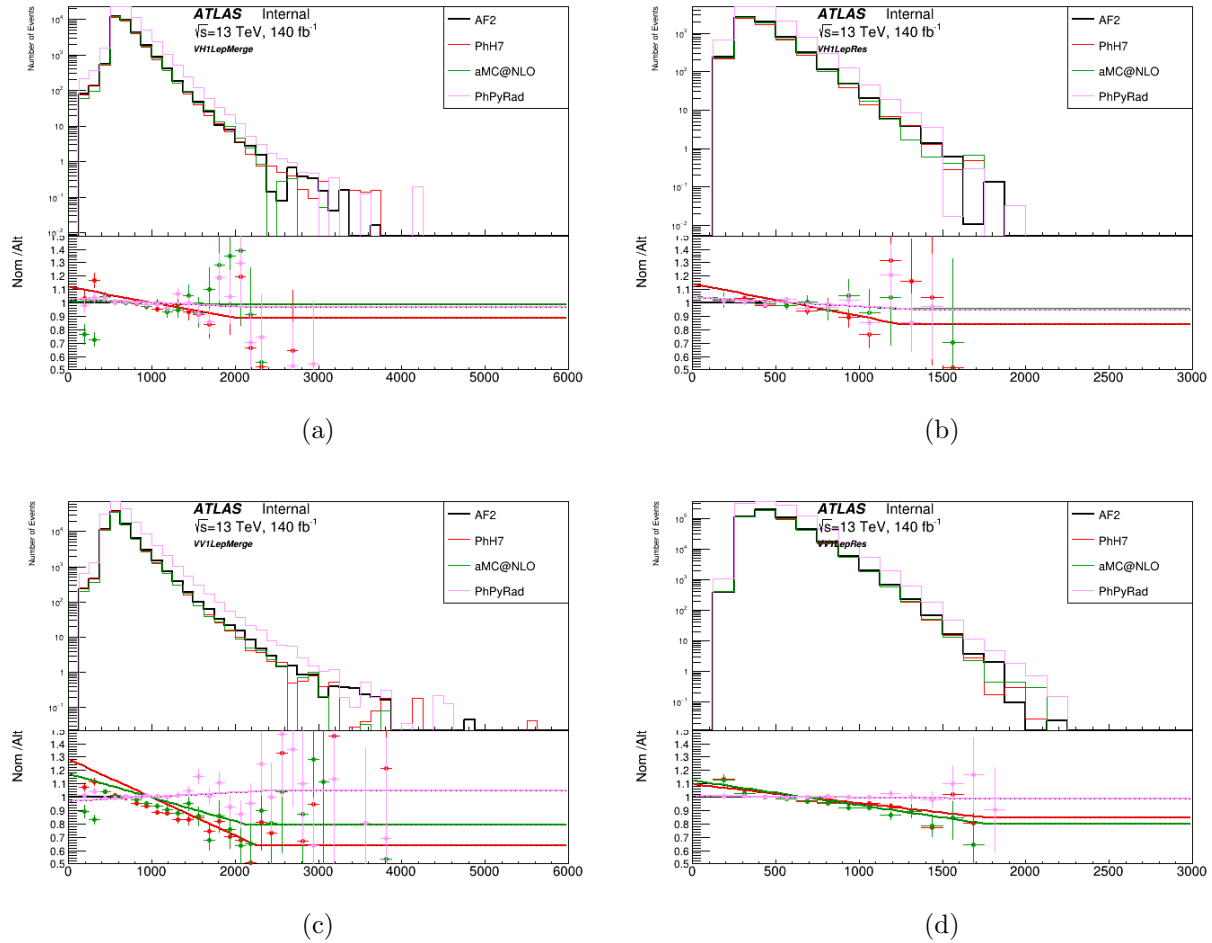


Figure 6.15: Comparisons of the $t\bar{t}$ AF2 sample with each systematic uncertainty in m_{VV} or m_{VH} for each TCR of the 1-lep channel. The AF2 sample in black is used as the nominal for comparison. The bottom panel shows the normalized ratio (after all have been normalized to the integral of the nominal) of each systematic to the nominal AF2 sample after normalisation and a degree-1 polynomial fit is applied. Figures (a) and (b) show results for VH 1-lep in the merged (left) and resolved (right) region. Figures (c) and (d) show results for the VV 1-lep merged (left) and resolved (right) region.

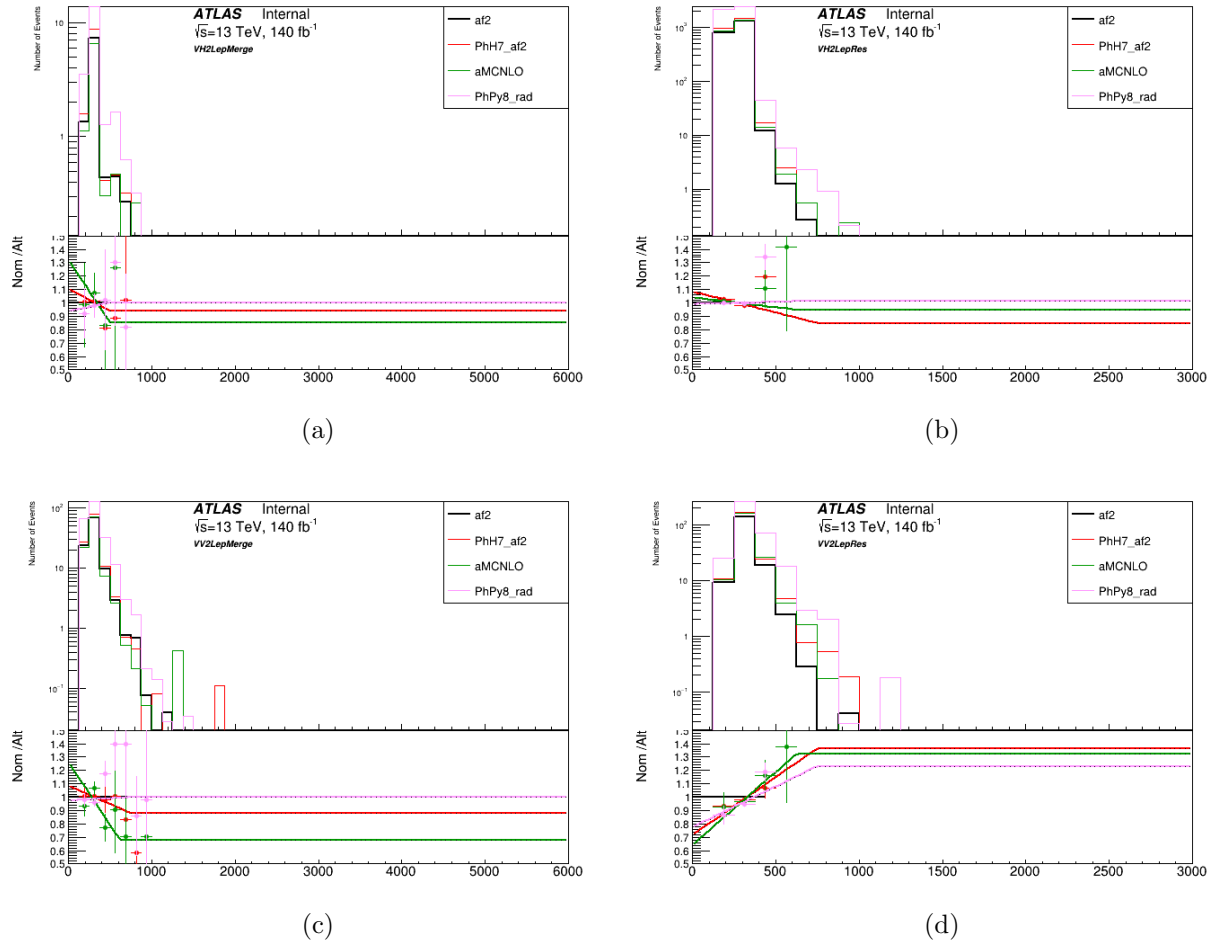


Figure 6.16: Comparisons of the $t\bar{t}$ AF2 sample with each systematic uncertainty in m_{VV} or m_{VH} for each SR of the 2-lep channel. The AF2 sample in black is used as the nominal for comparison. The bottom panel shows the normalized ratio (after all have been normalized to the integral of the nominal) of each systematic to the nominal AF2 sample after normalisation and a second degree polynomial fit is applied. Figures (a) and (b) show results for VH 2-lep in the merged (left) and resolved (right) region. Figures (c) and (d) show results for the VV 2-lep merged (left) and resolved (right) region.

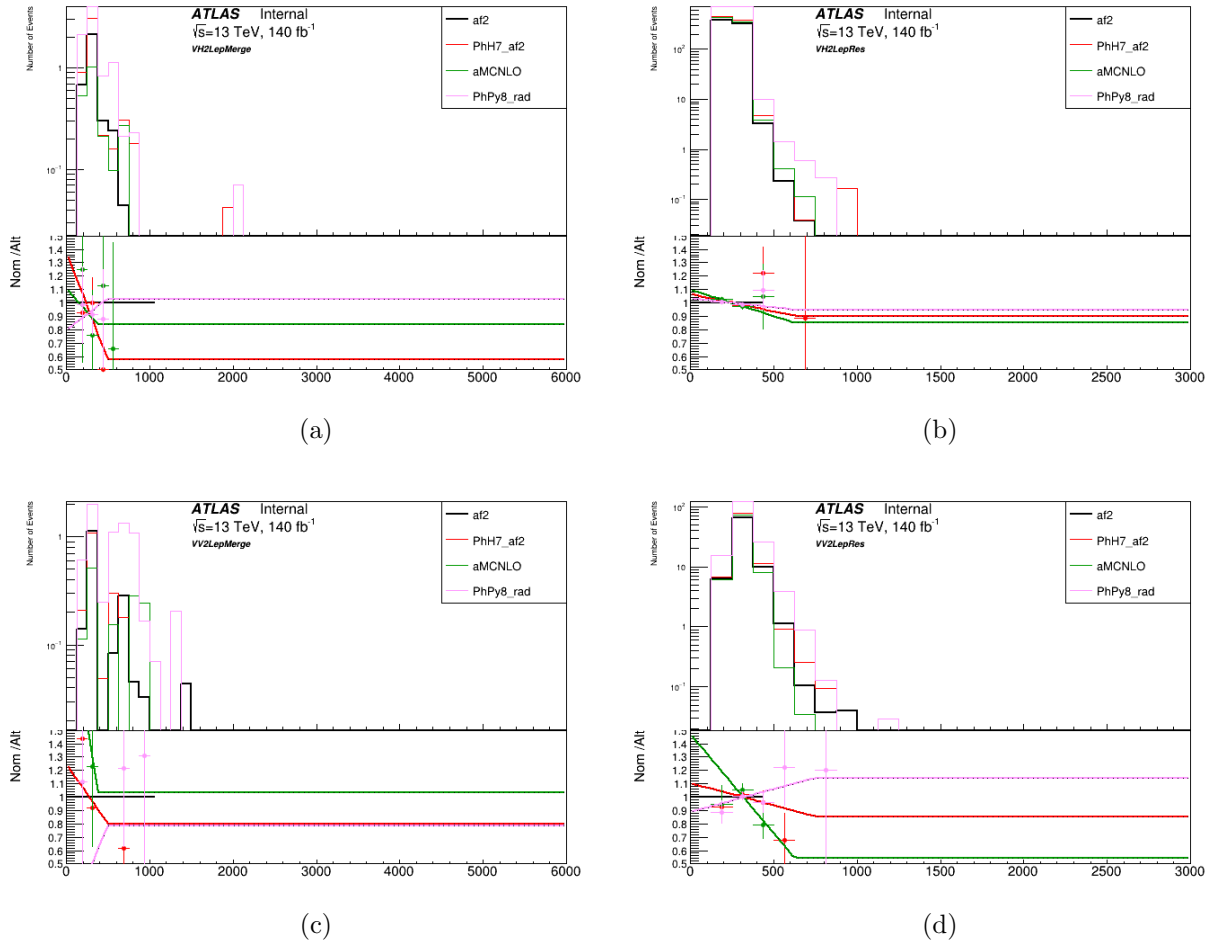


Figure 6.17: Comparisons of the $t\bar{t}$ AF2 sample with each systematic uncertainty in m_{VV} or m_{VH} for each MCR of the 2-lep channel. The AF2 sample in black is used as the nominal for comparison. The bottom panel shows the normalized ratio (after all have been normalized to the integral of the nominal) of each systematic to the nominal AF2 sample after normalisation and a second degree polynomial fit is applied. Figures (a) and (b) show results for VH 2-lep in the merged (left) and resolved (right) region. Figures (c) and (d) show results for the VV 2-lep merged (left) and resolved (right) region.

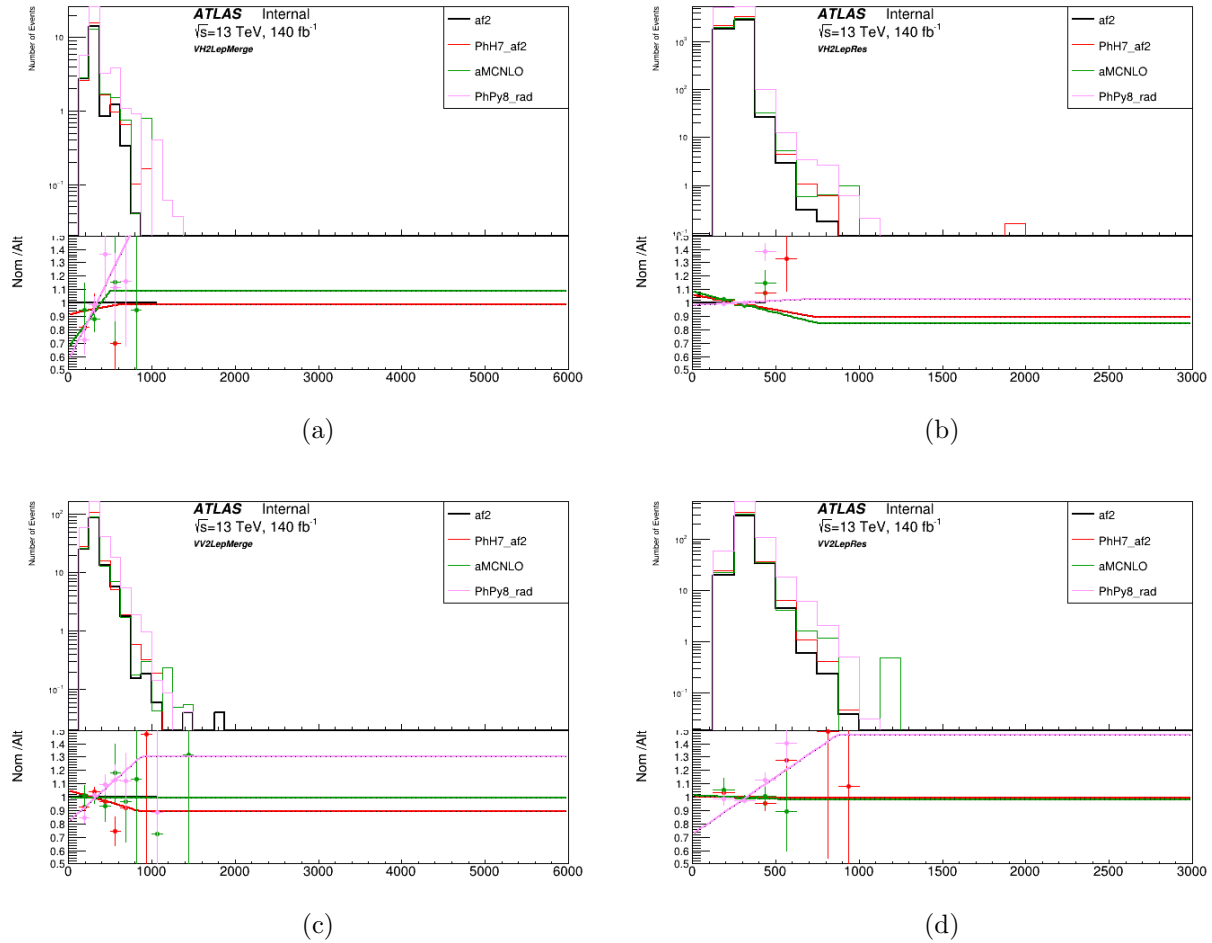


Figure 6.18: Comparisons of the $t\bar{t}$ AF2 sample with each systematic uncertainty in m_{VV} or m_{VH} for each TCR of the 2-lep channel. The AF2 sample in black is used as the nominal for comparison. The bottom panel shows the normalized ratio (after all have been normalized to the integral of the nominal) of each systematic to the nominal AF2 sample after normalisation and a second degree polynomial fit is applied. Figures (a) and (b) show results for VH 2-lep in the merged (left) and resolved (right) region. Figures (c) and (d) show results for the VV 2-lep merged (left) and resolved (right) region.

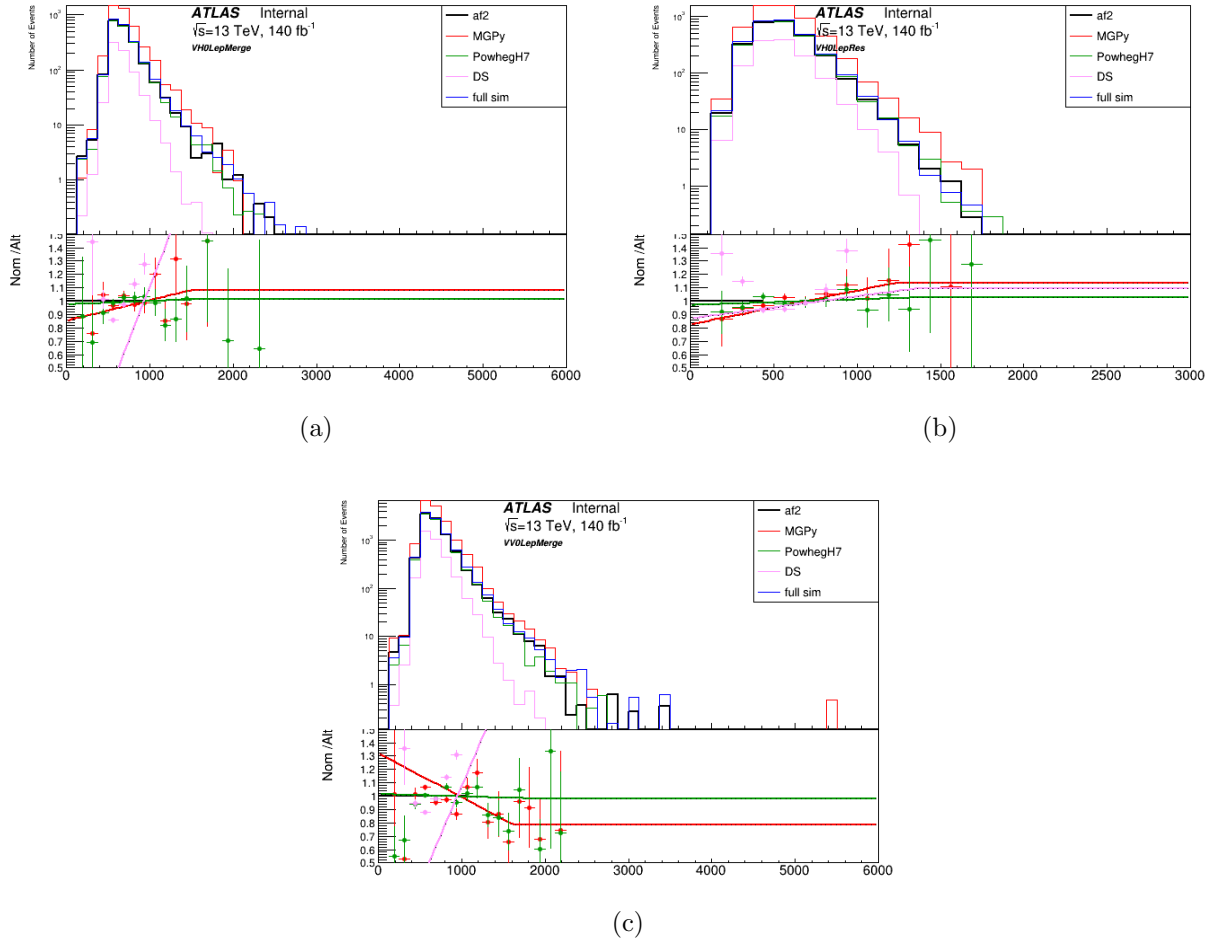
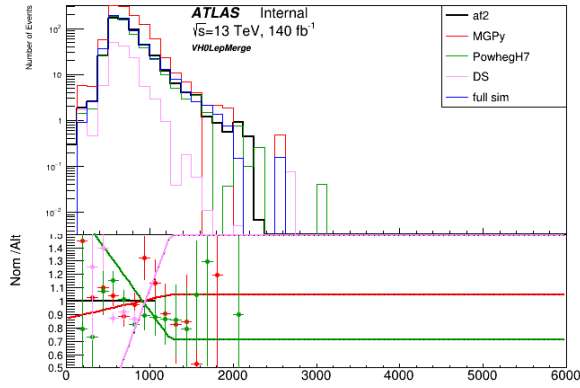
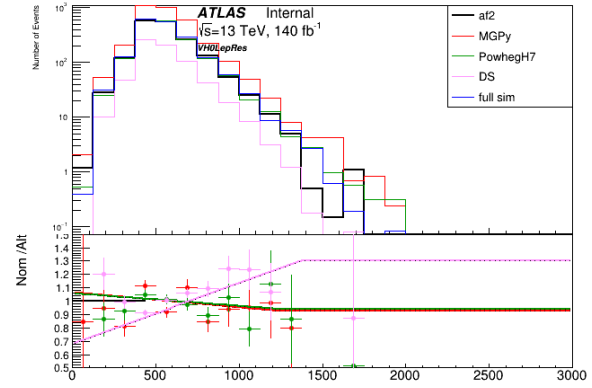


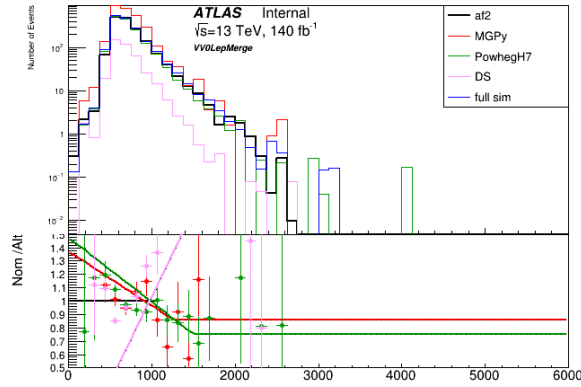
Figure 6.19: Comparisons of the single top AF2 sample with each systematic uncertainty in m_{VV} or m_{VH} for each SR of the 0-lep channel. The bottom panel shows the normalized ratio (after all have been normalized to the integral of the nominal) of each systematic to the nominal AF2 sample after normalisation (or FULL SIM for DS), and a degree-1 polynomial fit is applied. Figures (a) and (b) show results for VH 0-lep in the merged (left) and resolved (right) region. Figure (c) show results for the VV 0-lep merged region (center).



(a)



(b)



(c)

Figure 6.20: Comparisons of the single top AF2 sample with each systematic uncertainty in $m_{V\bar{V}}$ or $m_{V\bar{H}}$ for each MCR of the 0-lep channel. The bottom panel shows the normalized ratio (after all have been normalized to the integral of the nominal) of each systematic to the nominal AF2 sample after normalisation (or FULL SIM for DS), and a degree-1 polynomial fit is applied. Figures (a) and (b) show results for VH 0-lep in the merged (left) and resolved (right) region. Figure (c) show results for the VV 0-lep merged region (center).

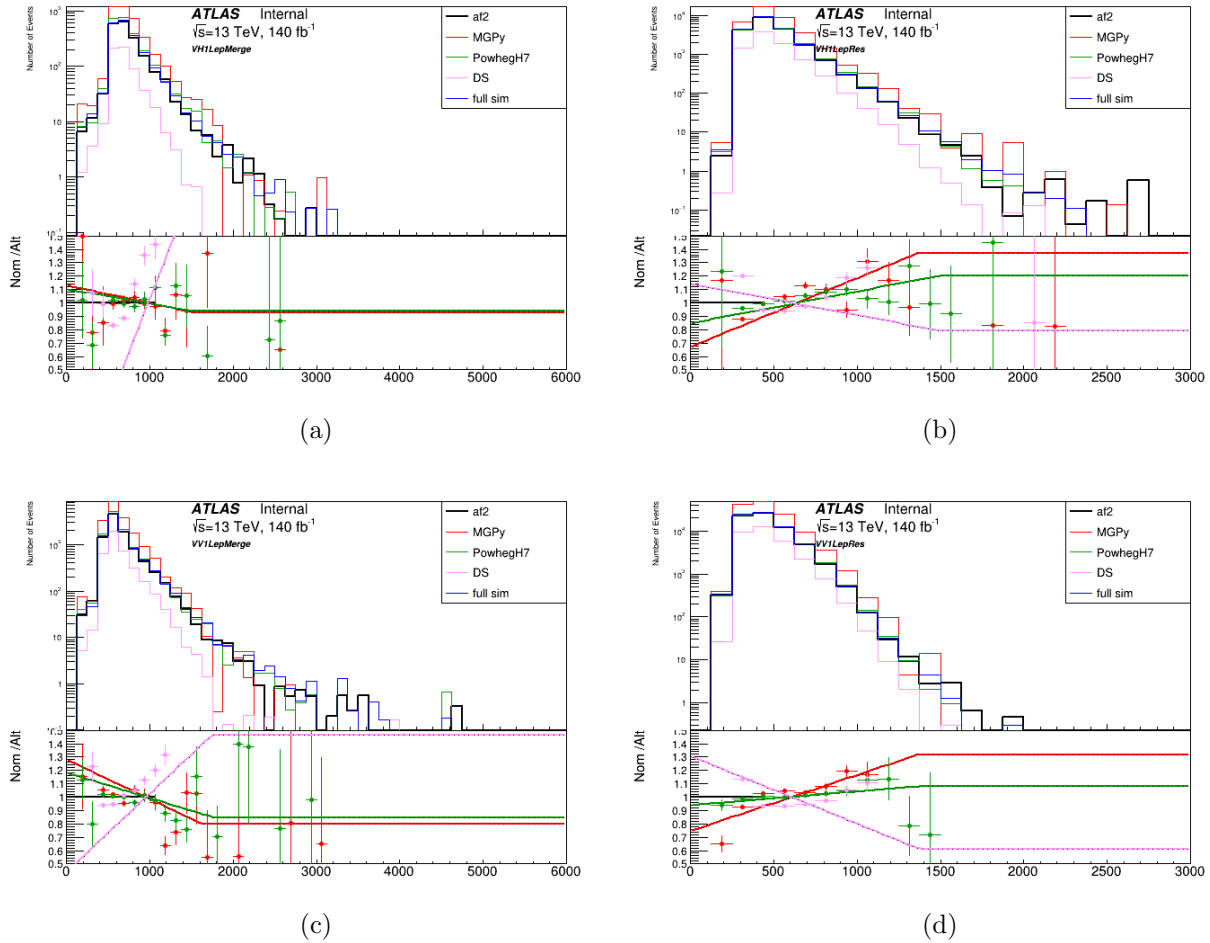


Figure 6.21: Comparisons of the single top AF2 sample with each systematic uncertainty in m_{VV} or m_{VH} for each SR of the 1-lep channel. The bottom panel shows the normalized ratio (after all have been normalized to the integral of the nominal) of each systematic to the nominal AF2 sample after normalisation (or FULL SIM for DS), and a degree-1 polynomial fit is applied. Figures (a) and (b) show results for VH 1-lep in the merged (left) and resolved (right) region. Figures (c) and (d) show results for the VV 1-lep merged (left) and resolved (right) region.

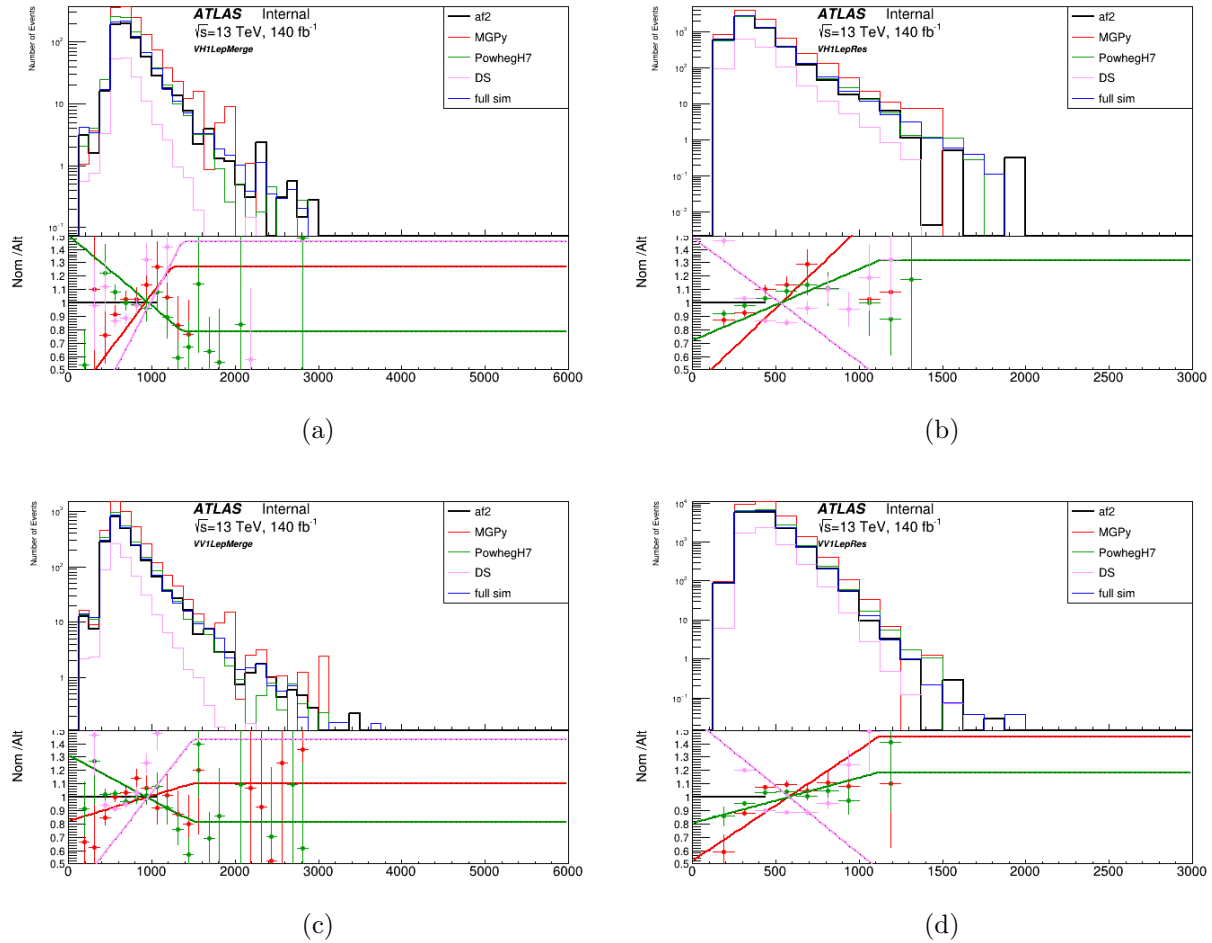


Figure 6.22: Comparisons of the single top AF2 sample with each systematic uncertainty in m_{VV} or m_{VH} for each MCR of the 1-lep channel. The bottom panel shows the normalized ratio (after all have been normalized to the integral of the nominal) of each systematic to the nominal AF2 sample after normalisation (or FULL SIM for DS), and a degree-1 polynomial fit is applied. Figures (a) and (b) show results for VH 1-lep in the merged (left) and resolved (right) region. Figures (c) and (d) show results for the VV 1-lep merged (left) and resolved (right) region.

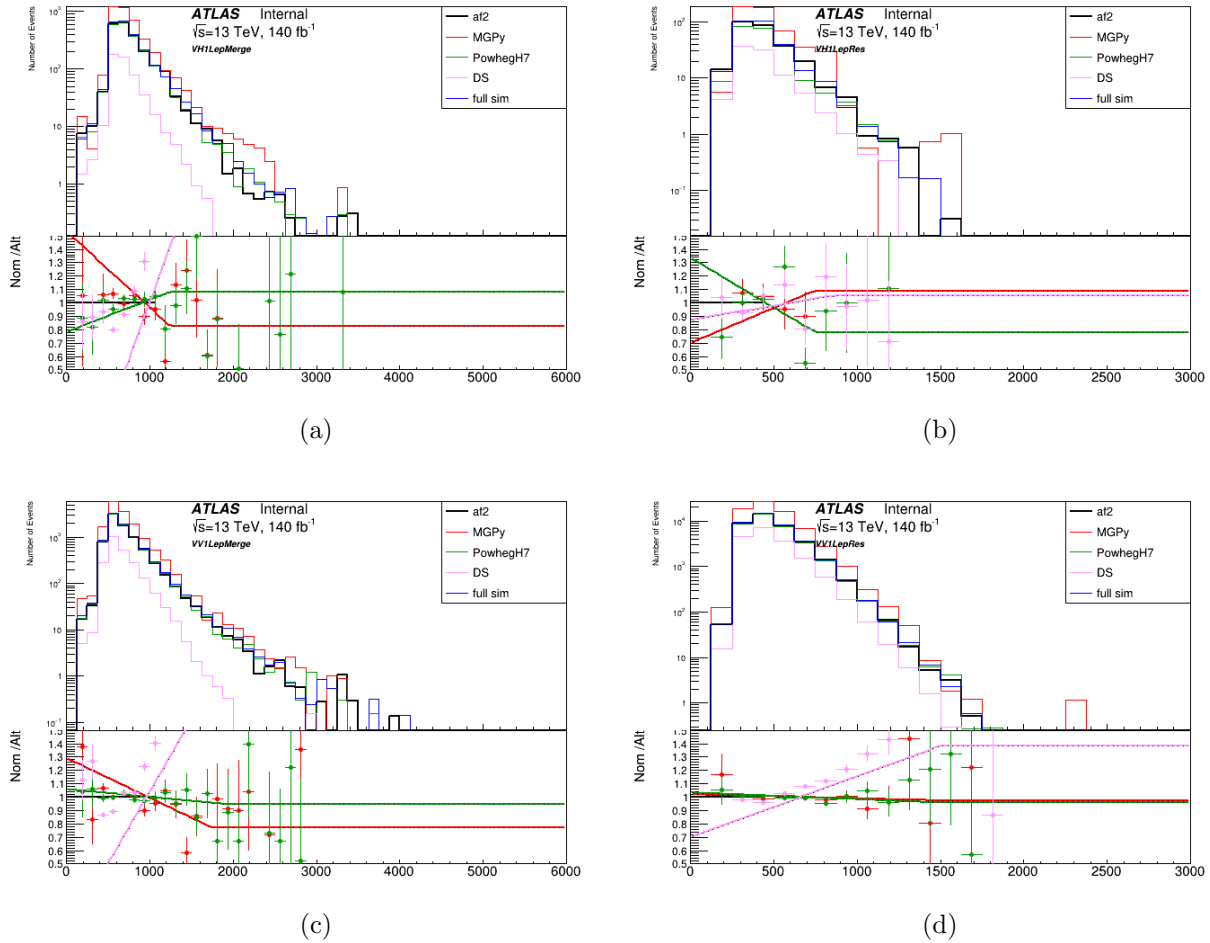


Figure 6.23: Comparisons of the single top AF2 sample with each systematic uncertainty in m_{VV} or m_{VH} for each TCR of the 1-lep channel. The bottom panel shows the normalized ratio (after all have been normalized to the integral of the nominal) of each systematic to the nominal AF2 sample after normalisation (or FULL SIM for DS), and a degree-1 polynomial fit is applied. Figures (a) and (b) show results for VH 1-lep in the merged (left) and resolved (right) region. Figures (c) and (d) show results for the VV 1-lep merged (left) and resolved (right) region.

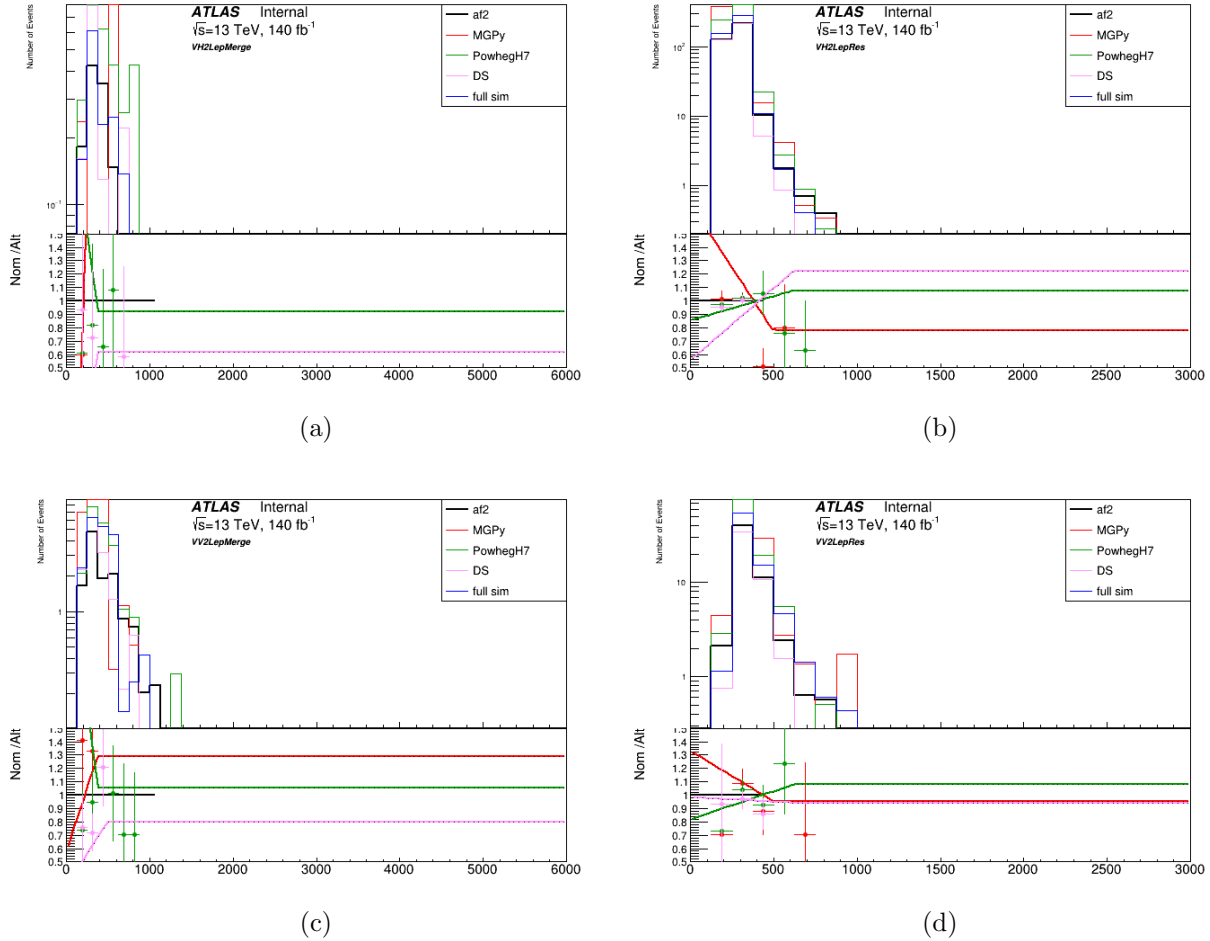


Figure 6.24: Comparisons of the single top AF2 sample with each systematic uncertainty in m_{VV} or m_{VH} for each SR of the 2-lep channel. The bottom panel shows the normalized ratio (after all have been normalized to the integral of the nominal) of each systematic to the nominal AF2 sample after normalisation (or FULL SIM for DS), and a degree-1 polynomial fit is applied. Figures (a) and (b) show results for VH 2-lep in the merged (left) and resolved (right) region. Figures (c) and (d) show results for the VV 2-lep merged (left) and resolved (right) region.

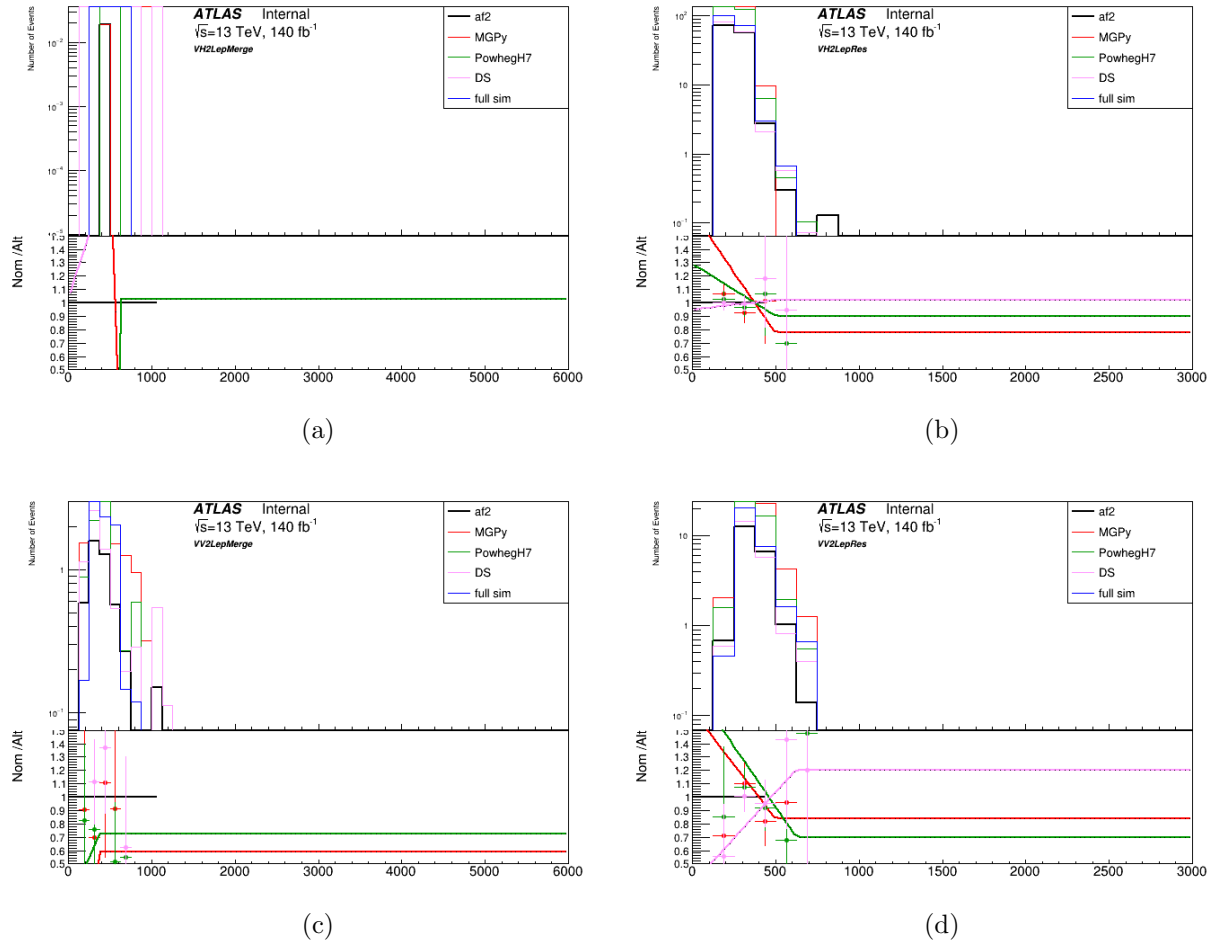


Figure 6.25: Comparisons of the single top AF2 sample with each systematic uncertainty in m_{VV} or m_{VH} for each MCR of the 2-lep channel. The bottom panel shows the normalized ratio (after all have been normalized to the integral of the nominal) of each systematic to the nominal AF2 sample after normalisation (or FULL SIM for DS), and a degree-1 polynomial fit is applied. Figures (a) and (b) show results for VH 2-lep in the merged (left) and resolved (right) region. Figures (c) and (d) show results for the VV 2-lep merged (left) and resolved (right) region.

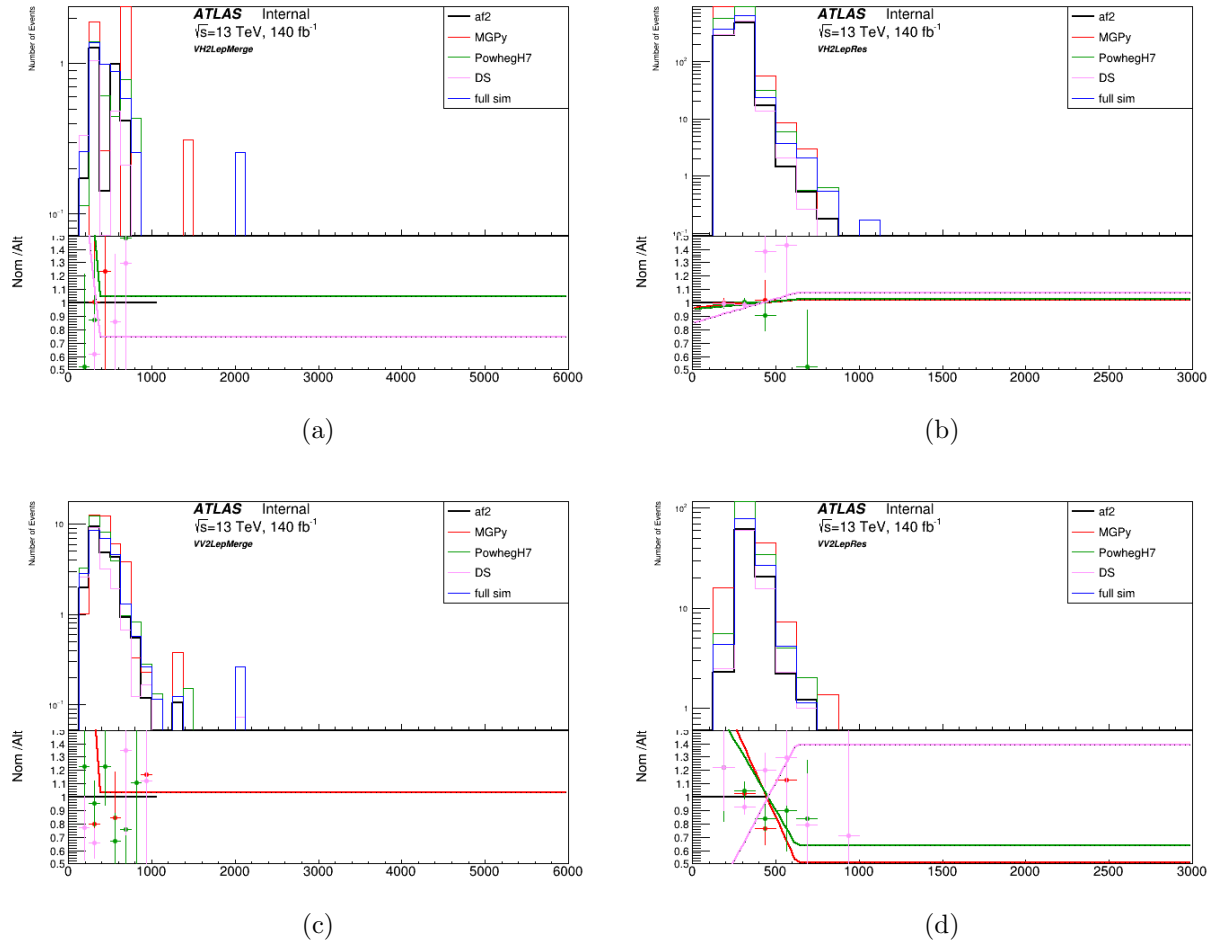


Figure 6.26: Comparisons of the single top AF2 sample with each systematic uncertainty in m_{VV} or m_{VH} for each TCR of the 2-lep channel. The bottom panel shows the normalized ratio (after all have been normalized to the integral of the nominal) of each systematic to the nominal AF2 sample after normalisation (or FULL SIM for DS), and a degree-1 polynomial fit is applied. Figures (a) and (b) show results for VH 2-lep in the merged (left) and resolved (right) region. Figures (c) and (d) show results for the VV 2-lep merged (left) and resolved (right) region.

6.6.2.2 $V + \text{jets}$ Modeling

The $V + \text{jets}$ modeling approach is similar to the $t\bar{t}$ method described above. The ratio of the invariant mass distributions of the different MC generator predictions with respect to the nominal generator are fit with a linear function. The variations to consider are

- Envelope of 6 variations of renormalization and factorization scale
- 100 NNPDF3.0nnlo variations, combined into 1 by adding in quadrature to reduce the number of nuisance parameters (following NNPDF recommendations)
- 2 α_s variations
- 2 nominal PDF set variations with respect to MMHT14 and CT14

6.6.2.3 Minor Background

The minor background contributions from SM VV , $t\bar{t}H$, and $t\bar{t}V$ processes are assessed directly from MC. For diboson processes, a 10% uncertainty of the cross-section is estimated [156, 157]. For $t\bar{t}H$ and $t\bar{t}V$, a variation of a 50% uncertainty is considered.

6.7 Statistical Interpretation

The statistical interpretation of the $VV+VH$ analysis follows the following format: first a likelihood model is built, then the profile-likelihood ratio is used to form a test statistic, and then finally that test statistic is used for hypothesis testing.

6.7.1 Binned Maximum Likelihood Fit

A binned profile⁴ maximum likelihood fit is applied to the observed data using the likelihood function $\mathcal{L}(\mu, \vec{\theta})$, where μ denotes the signal strength and $\vec{\theta}$ represents nuisance parameters for systematic and statistical uncertainties, assuming the analysis measures event counts in bins of an observable x with estimable signal and background yields. The parameter of interest (POI) is μ , the different values of μ correspond to the type of prediction: $\mu = 0$ for background only, and $\mu = 1$ for a signal plus background prediction. The likelihood can then be constructed as a product of Poisson probabilities to measure x_i events,

$$L(\mu) = \prod_i e^{-(\mu s_i + b_i)} \frac{(\mu s_i + b_i)^{x_i}}{x_i!} = \prod_i \text{Pois}(x_i | \mu s_i + b_i) \quad (6.8)$$

where i indicates the product over all the bins. s_i and b_i can be derived from template functions of the expected signal and background distributions, respectively

$$s_i = \int_{\text{bin } i} f_s(x) dx \quad b_i = \int_{\text{bin } i} f_b(x) dx \quad (6.9)$$

The inclusion of nuisance parameters (NP), θ_k , account for the systematic and statistical uncertainties arising from the various sources of uncertainties. The NP can be reflected in the template functions: $f_s(x, \vec{\theta})$ and $f_b(x, \vec{\theta})$, encoding the shape and normalization effects. The NP can also be constrained by adding an additional term to the likelihood: $f(\theta_k, \vec{\alpha}_k)$. This additional term represents the set of constraints on θ_k from the external measurements $\vec{\alpha}_k$. The likelihood function can now be written as

⁴In this context, “profiling” meant to reduce the multivariate function to a lower-dimension function (reducing the degrees of freedom in the fit), by maximizing over nuisance parameters at each fixed value of the parameter of interest (i.e. setting μ to 0 or 1).

$$L(\mu, \boldsymbol{\theta}) = \prod_i \text{Pois}(n_i | \mu s_i(\boldsymbol{\theta}) + b_i(\boldsymbol{\theta})) \prod_k f(\theta_k | \alpha_k) \quad (6.10)$$

6.7.2 Test Statistic

A test statistic, q_μ , is used to measure the compatibility of the background-only model (where $\mu = 0$) with the observed data, and is based on the profile likelihood ratio

$$\lambda(\mu) = \frac{L(\mu | \hat{\boldsymbol{\theta}}(\mu))}{L(\hat{\mu} | \hat{\boldsymbol{\theta}})} \quad (6.11)$$

Where $\hat{\boldsymbol{\theta}}$ and $\hat{\mu}$ are parameters which maximize the likelihood, and $\hat{\boldsymbol{\theta}}$ are NP values which maximize the likelihood for a given μ . This methodology relies on the Neyman-Pearson Lemma: the most powerful test at a fixed significance level uses the likelihood ratio; and using the profiled values of the nuisance parameters allows for this lemma to hold for in the case of this multi-dimensional likelihood.

From the likelihood ratio provided above, the test statistic can be constructed for two different types of hypothesis testing: limit settings (using signal plus background) or discovery (background only), shown in eq. (6.12) and eq. (6.13), respectively.

$$\tilde{q}_\mu = \begin{cases} -2 \ln \frac{L(\mu | \hat{\boldsymbol{\theta}}(\mu))}{L(0 | \hat{\boldsymbol{\theta}}(0))} & \hat{\mu} < 0, \\ -2 \ln \frac{L(\mu | \hat{\boldsymbol{\theta}}(\mu))}{L(\hat{\mu} | \hat{\boldsymbol{\theta}})} & 0 < \hat{\mu} < \mu, \\ 0 & \mu < \hat{\mu} \end{cases} \quad (6.12)$$

$$q_0 = \begin{cases} -2 \ln \frac{L(0 | \hat{\boldsymbol{\theta}}(\mu))}{L(\hat{\mu} | \hat{\boldsymbol{\theta}})} & \hat{\mu} > 0, \\ 0 & \hat{\mu} < 0 \end{cases} \quad (6.13)$$

where higher values of q_μ indicate a worse agreement, or compatibility, of the data with hypothesized signal model with signal strength μ . In the case where $\hat{\mu} < 0$, the best fit value should be for $\mu = 0$ since we are only searching for positive excesses (or positive fluctuations).

The level of agreement between the data and the null hypothesis ($\mu = 0$) can be measured with the p-value, defined as

$$p_0 = \int_{q_{0,\text{obs}}}^{\infty} f(q_0 | b) dq_0 \quad (6.14)$$

where the p-value measures the probability to observe a test statistic of that value *or more extreme*. In particle physics, the p-values are often converted to a signal significance, Z , defined as

$$Z = \phi^{-1}(1 - p) \quad (6.15)$$

where ϕ^{-1} is the inverse of the Gaussian cumulative distribution function. The motivation behind this Z-score is to take the p-value that was measured from this complicated model, and map it to a Gaussian distribution. Then the standard deviations of a Gaussian can be used to describe the (hopeful) discovery. Analysis can claim discovery if the background-only hypothesis is rejected with $Z = 5$ (corresponding to p-value of 2.87×10^{-7}).

Upper limits on model parameters, such as the signal strength μ or the mass of a new particle, can be set using the CL_s method [158]. This approach defines a signal as excluded

at a significance level α if:

$$CL_s = \frac{p_{s+b}}{1 - p_b} < \alpha \quad (6.16)$$

where p_{s+b} is the p-value under the signal-plus-background hypothesis and p_b is the p-value under the background-only hypothesis. The method reduces sensitivity to downward background fluctuations by incorporating the power of the test to reject the background-only hypothesis via the $1 - p_b$ term (also called CL_b). This ensures that signal models are not unjustly excluded in cases where the observed data lies below the expected background due to statistical variation, making the CL_s method a more conservative and robust approach; typically, at the 95% confidence level where $\alpha = 0.05$.

6.8 Results

This chapter presents the results of the search for heavy resonances decaying to pairs of Standard Model bosons in semileptonic final states, based on the full Run 2 dataset collected by the ATLAS detector, corresponding to an integrated luminosity of 140 fb^{-1} at a center-of-mass energy of $\sqrt{s} = 13 \text{ TeV}$. The analysis probes multiple final states arising from combinations of vector bosons (W, Z) and the Higgs boson (H), including WW, WZ, ZZ, WH, and ZH, across the 0-lepton, 1-lepton, and 2-lepton channels. A unified analysis strategy is employed, utilizing a consistent event selection and reconstruction framework built upon the new UFO jet definition and updated boosted object taggers. These improvements enhance the tagging performance for hadronically decaying bosons and top quarks, improving sensitivity to signals of interest.

The results are derived from simultaneous maximum-likelihood fits performed across

multiple signal and control regions. These fits incorporate data-driven background estimates, systematic uncertainties, and modeling corrections, including scale factors derived from a dedicated $t\bar{t}$ study. This chapter begins with a pre-fit validation of control regions to ensure reliable background modeling, followed by post-fit comparisons in both control and signal regions. The impact of systematic uncertainties is assessed through pull and ranking plots, and the final section presents the expected and observed upper limits on the cross-section of benchmark models, with comparisons to previous iterations of the search.

6.8.1 Pre-Fit Validation

Before performing the statistical fit, it is essential to validate the modeling of key background processes in the control regions using pre-fit distributions. These comparisons between observed data and MC predictions provide a baseline understanding of how well the input modeling describes the data prior to any adjustments from the fit. The control regions are enriched in dominant background processes, and are designed to constrain normalization and shape systematics of these components.

Figure 6.27 to Figure 6.32 show representative kinematic distributions, such as large-R jet kinematics, number of jets, MET, MET Significance, and mass, in the control regions in the 0-lepton channel (the 1-lepton and 2-lepton channels can be found in Appendix C). Figure 6.27 and Figure 6.28 shows the VH merged MCR in the 0/1-b-tagged region for the ggF and VBF production, respectively. Similarly Figure 6.29 and Figure 6.30 show the VV HP merged 0/1-b-tagged region for VV the ggF and VBF production, respectively. Finally Figure 6.31 and Figure 6.32 show the VH resolved 1-b-tagged region for both ggF and VBF productions. In general, the MC simulations reproduce the overall shapes of the distributions reasonably well, though some discrepancies in normalization and substructure observables are

observed. These deviations are addressed by the inclusion of dedicated nuisance parameters and normalization factors in the statistical model.

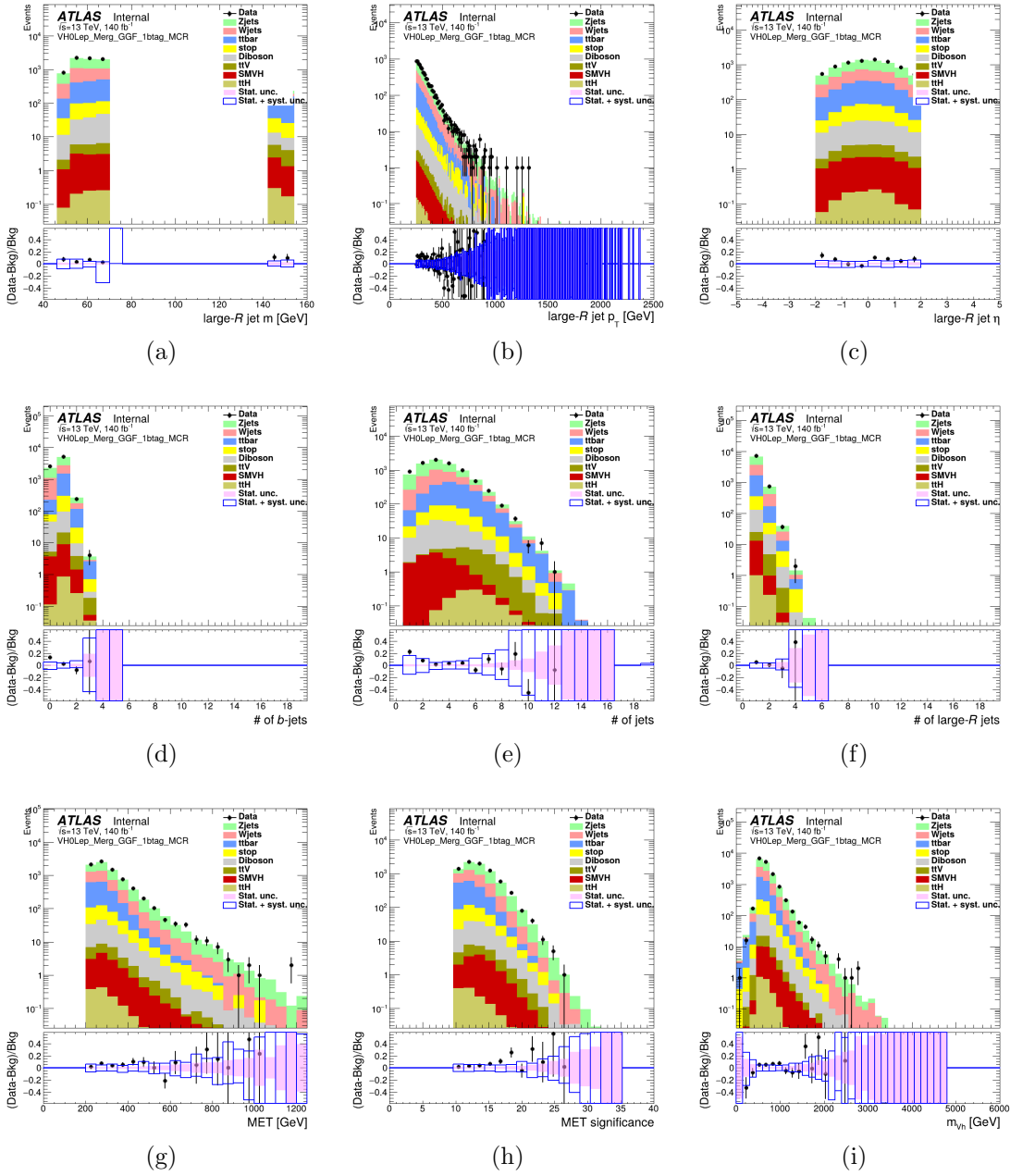


Figure 6.27: Comparisons of the observed data and the expected background distributions of various kinematic variables in the MCR of the 0-lepton channel for the VH merged region, 0/1 b-tagged, with ggF production. The bottom panes show the ratios of the observed data to the background predictions. The blue boxes represent the uncertainties in the total background predictions, combining statistical and systematic contributions.

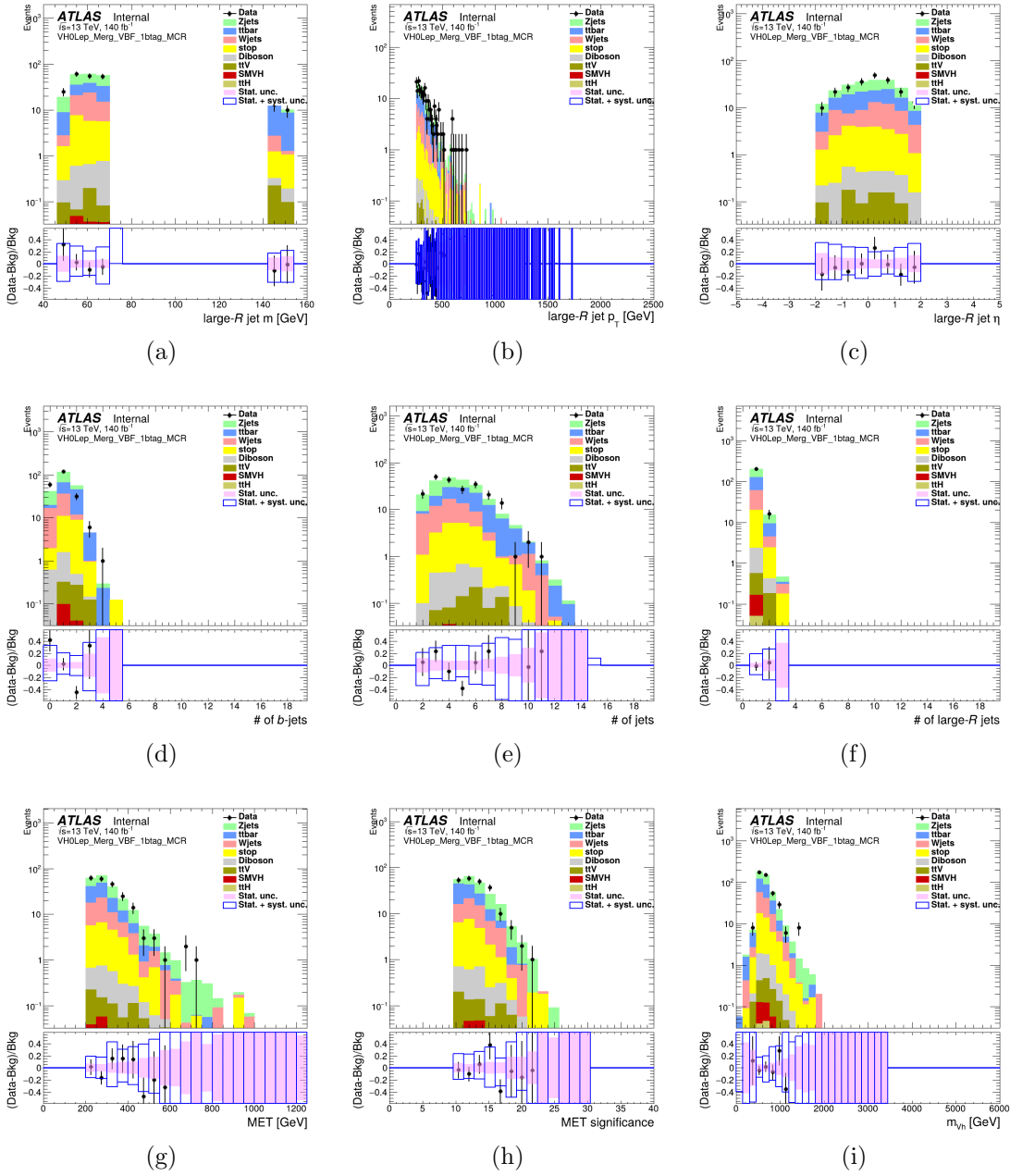


Figure 6.28: Comparisons of the observed data and the expected background distributions of various kinematic variables in the MCR of the 0-lepton channel for the VH merged region, 0/1 b-tagged, with VBF production. The bottom panes show the ratios of the observed data to the background predictions. The blue boxes represent the uncertainties in the total background predictions, combining statistical and systematic contributions.

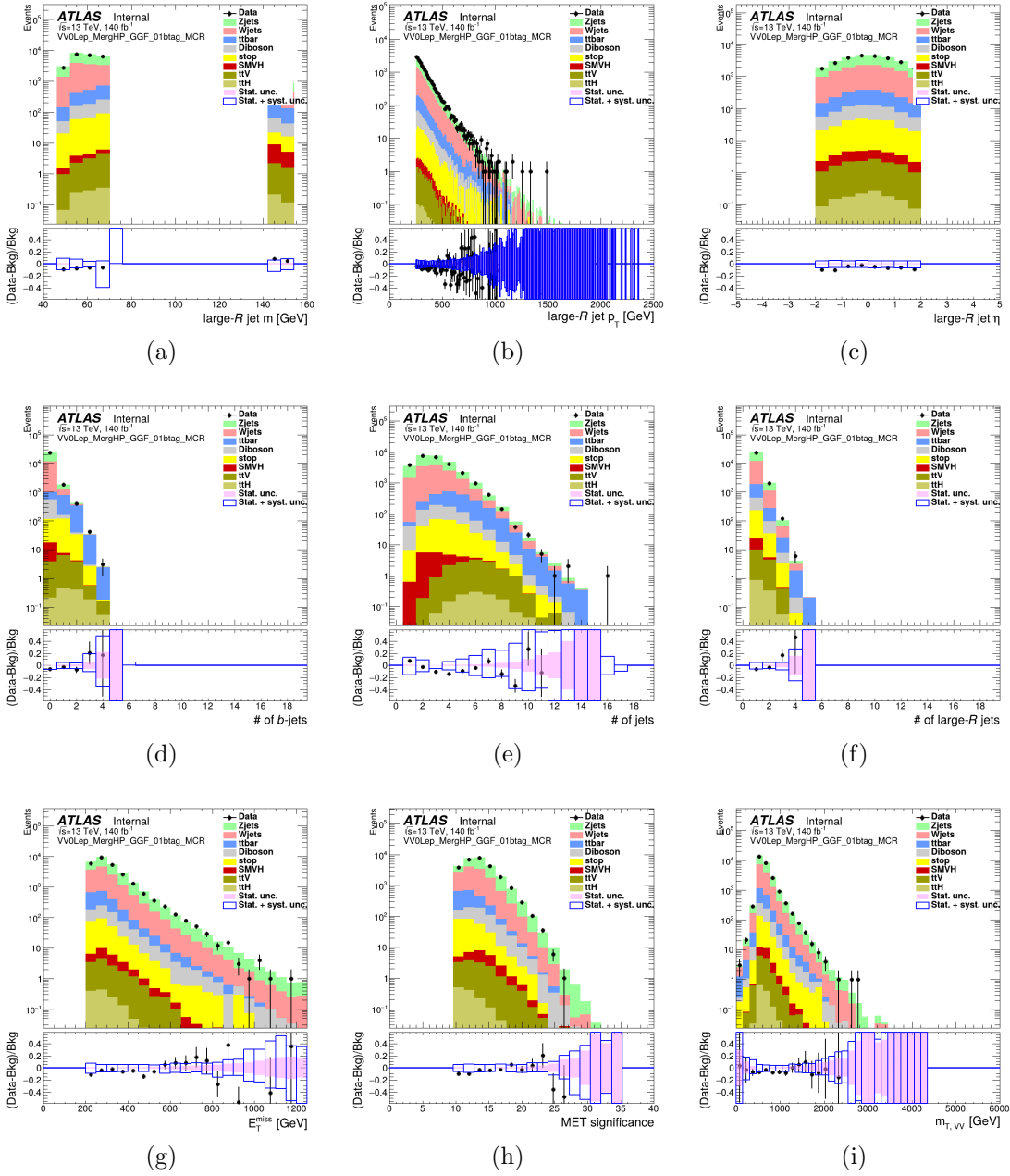


Figure 6.29: Comparisons of the observed data and the expected background distributions of various kinematic variables in the MCR of the 0-lepton channel for the VV merged HP region, 0/1 b-tagged, with ggF production. The bottom panes show the ratios of the observed data to the background predictions. The blue boxes represent the uncertainties in the total background predictions, combining statistical and systematic contributions.

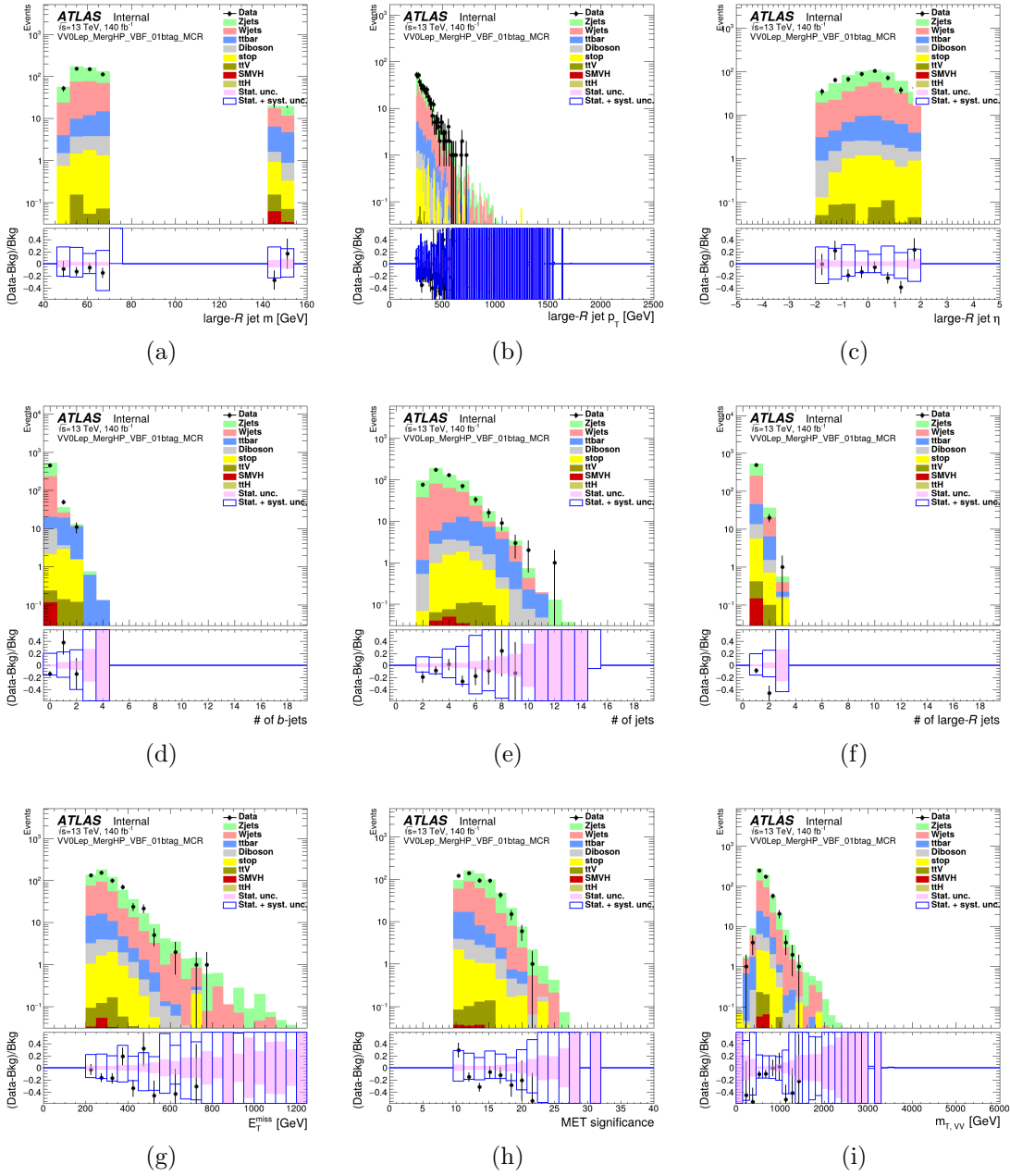


Figure 6.30: Comparisons of the observed data and the expected background distributions of various kinematic variables in the MCR of the 0-lepton channel for the VV merged HP region, 0/1 b-tagged, with VBF production. The bottom panes show the ratios of the observed data to the background predictions. The blue boxes represent the uncertainties in the total background predictions, combining statistical and systematic contributions.

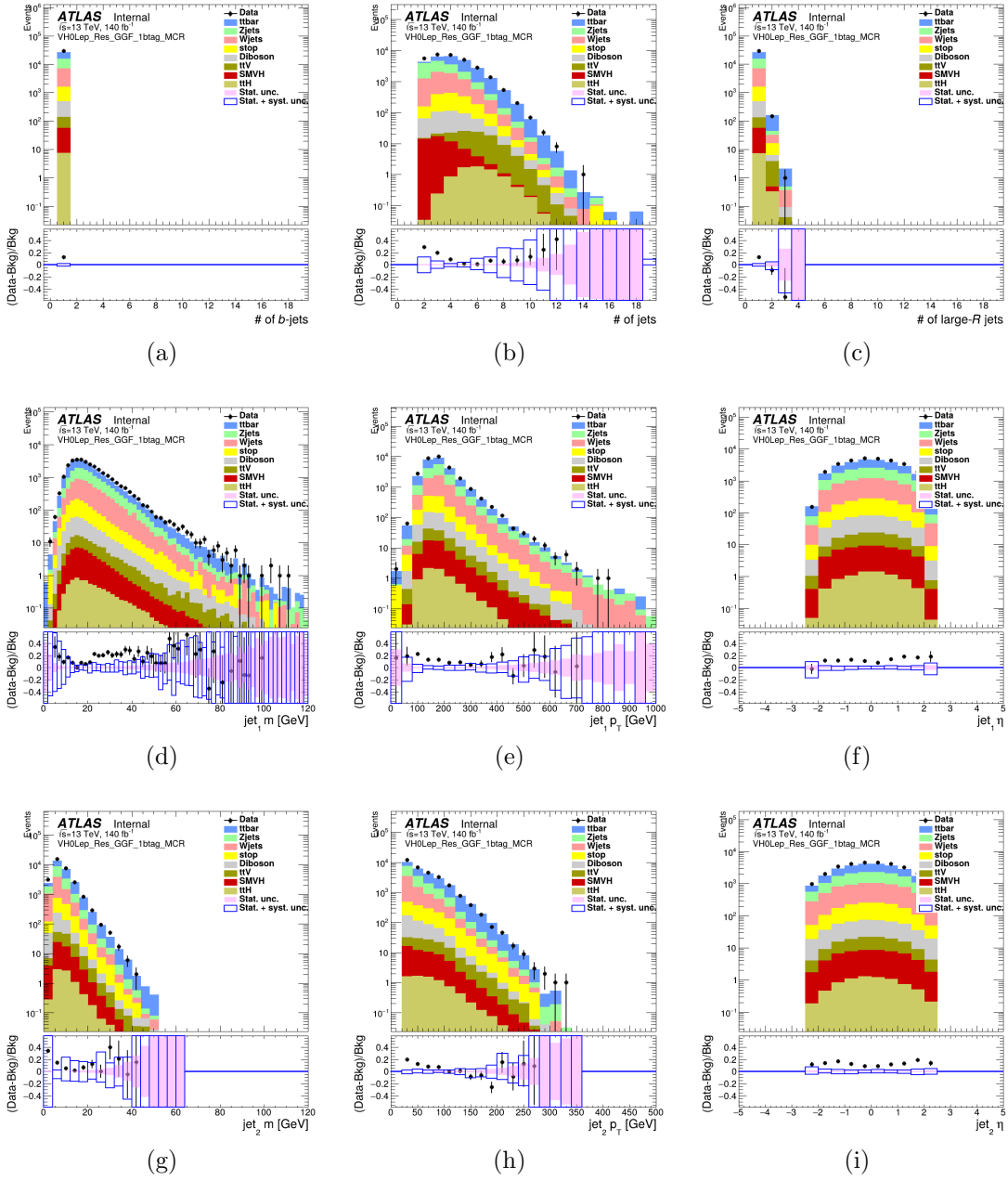


Figure 6.31: Comparisons of the observed data and the expected background distributions of various kinematic variables in the MCR of the 0-lepton channel for the VH resolved region, 0/1 b-tagged, with ggF production. The bottom panes show the ratios of the observed data to the background predictions. The blue boxes represent the uncertainties in the total background predictions, combining statistical and systematic contributions.

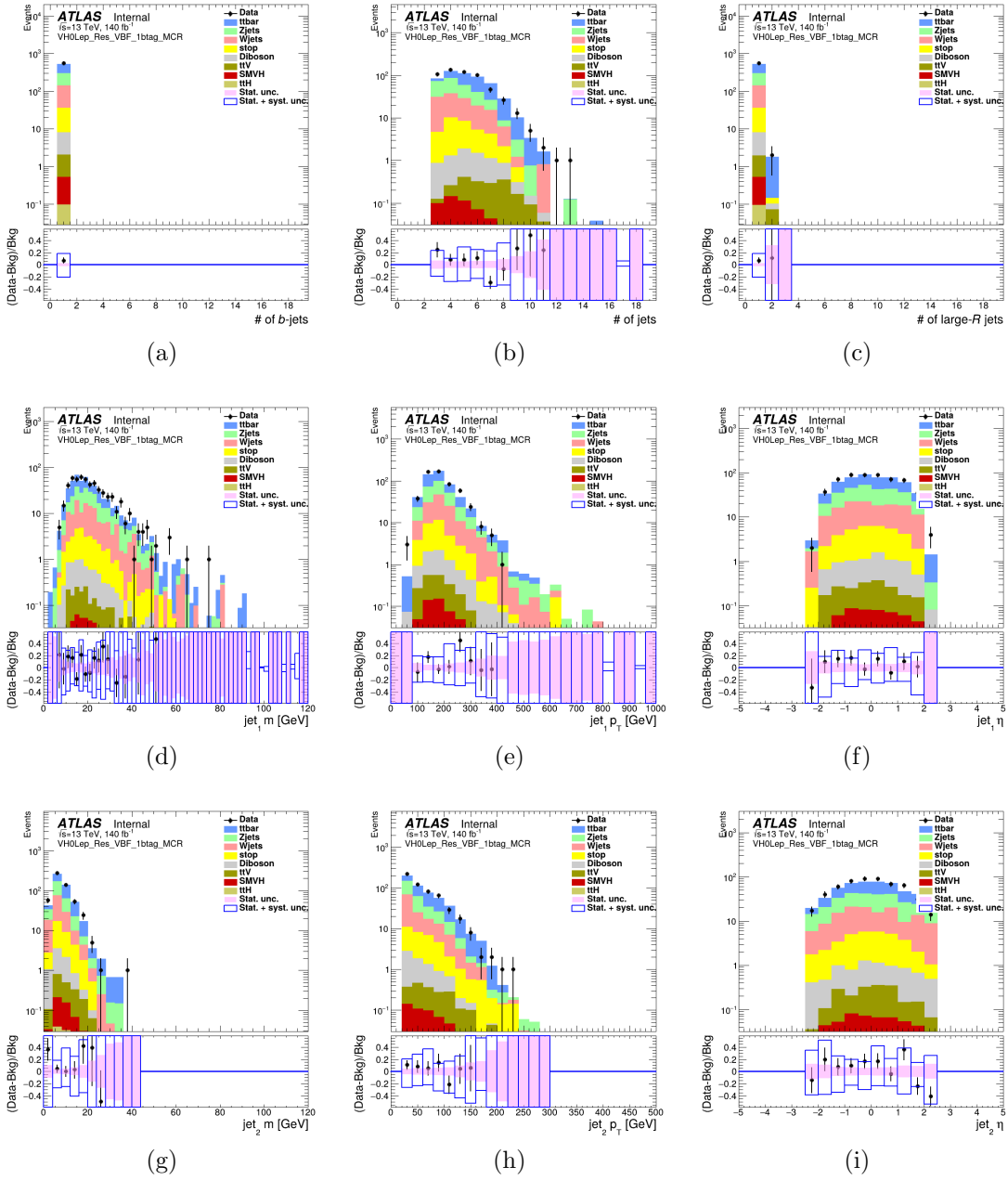


Figure 6.32: Comparisons of the observed data and the expected background distributions of various kinematic variables in the MCR of the 0-lepton channel for the VH resolved region, 0/1 b-tagged, with VBF production. The bottom panes show the ratios of the observed data to the background predictions. The blue boxes represent the uncertainties in the total background predictions, combining statistical and systematic contributions.

The pre-fit agreement in the control regions supports the robustness of the background modeling and motivates the use of these regions in the combined fit. Any observed mismodeling is propagated through systematic uncertainties and corrected during the fit procedure, as discussed in the subsequent sections. This pre-fit validation serves as a crucial cross-check, ensuring that the fit starts from a well-understood baseline and that any observed post-fit agreement is not artificially driven by poor initial modeling.

6.8.2 Post-Fit Validation

6.8.2.1 Control Regions

Figure 6.33 and Figure 6.34 show post-fit invariant mass distributions in the control regions in the 0-lepton channel using full Run-2 data (the 1-lepton and 2-lepton channels can be found in Appendix C). Stacked histograms represent the fitted background components: diboson, $t\bar{t}$, single-top, W+jets, and Z+jets. The black points indicate the observed data, with a hypothetical 3 TeV HVT W' signal overlaid for reference. However, even though the signal is overlaid, the control regions are designed to not have any signal present. The lower panel shows the ratio of data to the post-fit prediction, along with associated uncertainties, allowing for validation of the background modeling and sensitivity to potential signal excesses. In all cases, the fitted background components show good agreement with the observed data, validating the background modeling. The control regions, particularly those enriched in $t\bar{t}$ and V+jets, provide strong constraints on normalization and shape systematics. No significant discrepancies are observed post-fit, with differences remaining within combined statistical and systematic uncertainties.

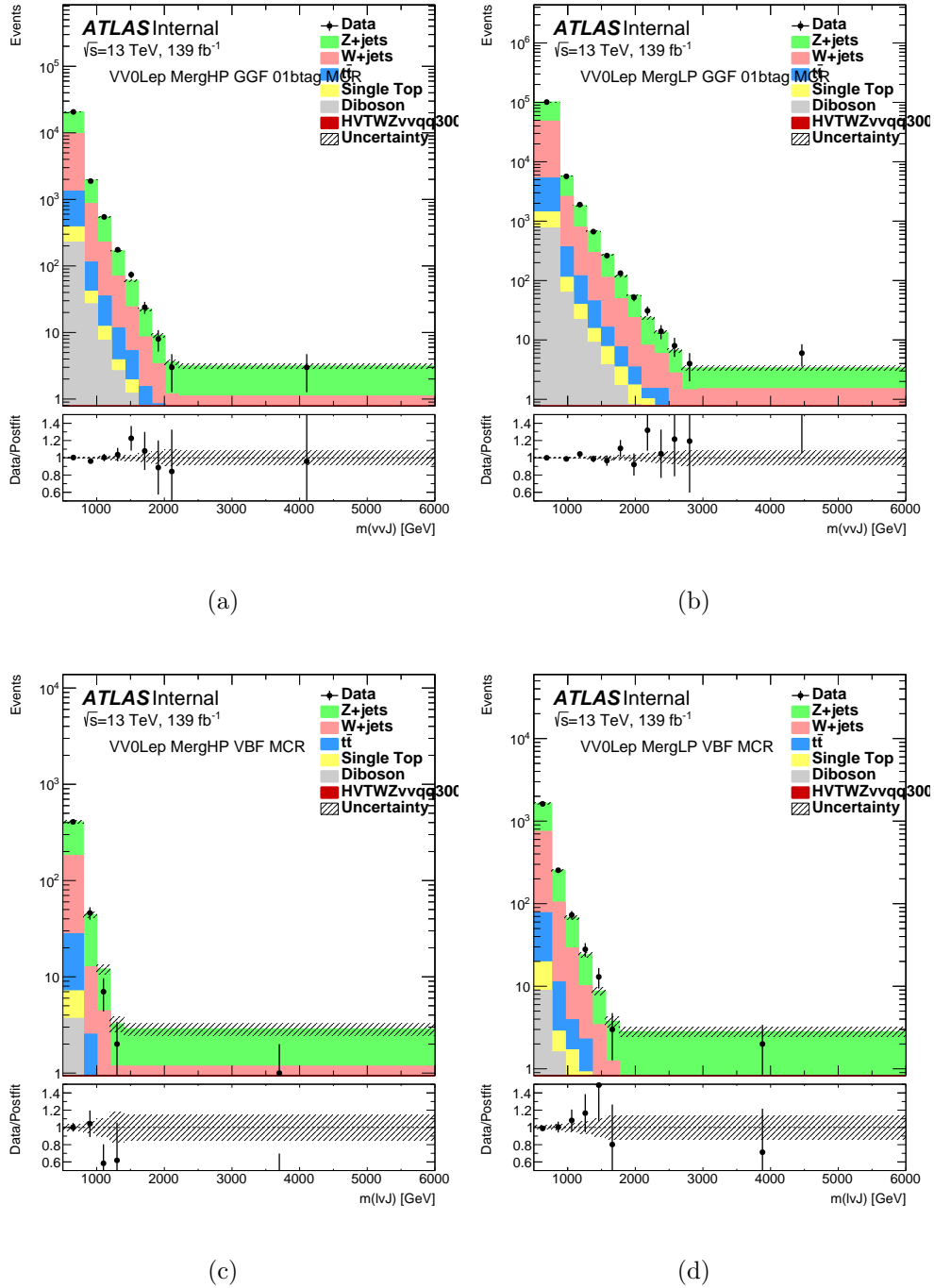


Figure 6.33: Post-fit invariant mass distributions in the WZ control regions of the VV 0-lepton channel, shown separately for the gluon-gluon fusion (ggF) and vector boson fusion (VBF) categories. Subfigures (a) and (b) correspond to the merged high-purity (HP) and low-purity (LP) ggF control regions and (c) and (d) show the corresponding merged HP and LP VBF control regions. The stacked histograms represent background predictions after the background-only fit, with data overlaid. The lower panels display the Data/Prediction ratio, with shaded bands indicating the total post-fit uncertainty, which includes both statistical and systematic components.

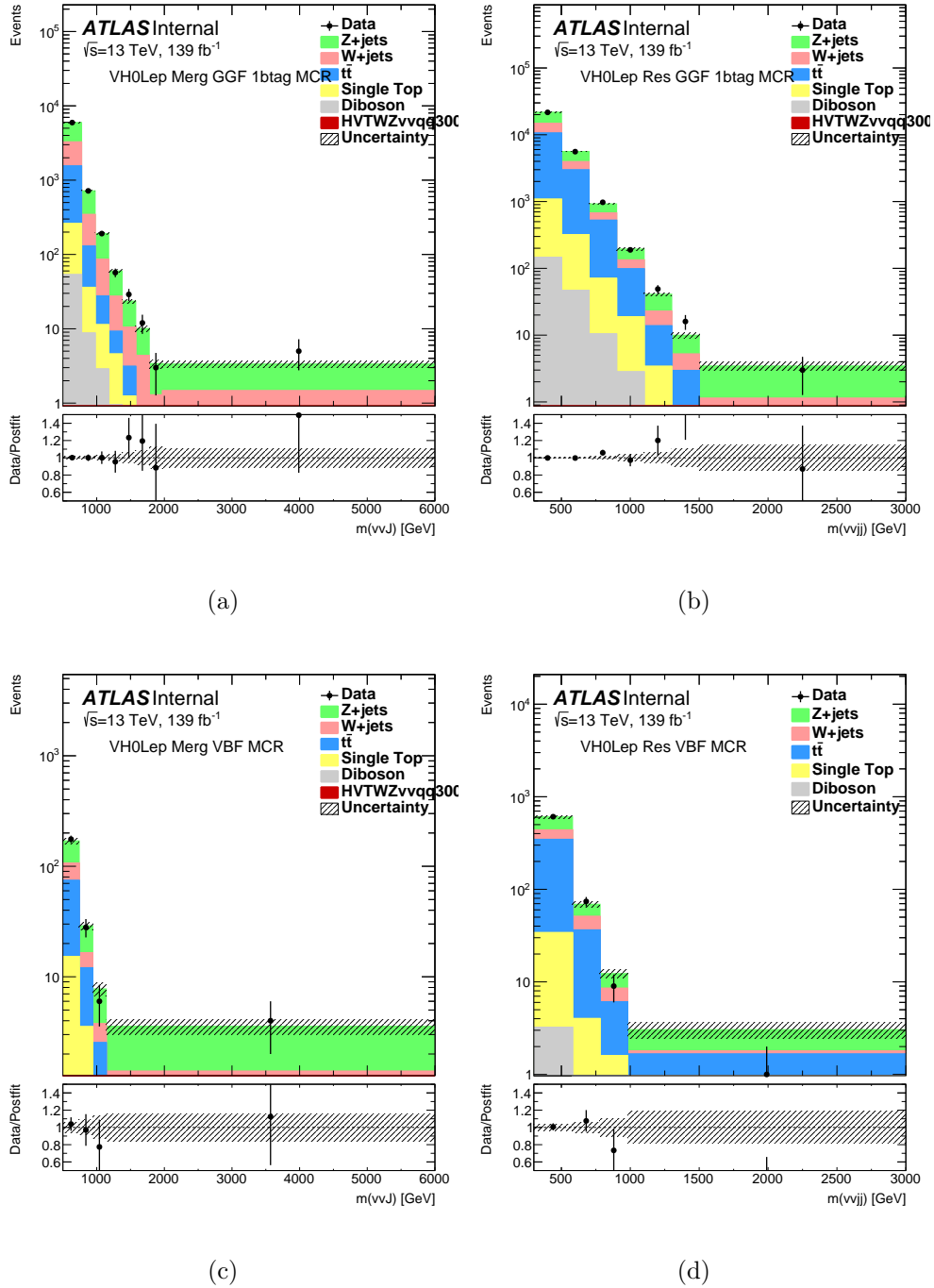


Figure 6.34: Post-fit invariant mass distributions in the WZ control regions of the VH 0-lepton channel, shown separately for the gluon-gluon fusion (ggF) and vector boson fusion (VBF) categories. Subfigures (a) and (b) correspond to the merged high-purity (HP) and low-purity (LP) ggF control regions and (c) and (d) show the corresponding merged HP and LP VBF control regions. The stacked histograms represent background predictions after the background-only fit, with data overlaid. The lower panels display the Data/Prediction ratio, with shaded bands indicating the total post-fit uncertainty, which includes both statistical and systematic components.

6.8.2.2 Signal Regions

Figure 6.35 to Figure 6.38 display a subset of the post-fit distributions of the main discriminating variable, the reconstructed diboson invariant mass, in the signal regions. The plots compare real data with the fitted background predictions and include representative regions from both the ggF and VBF production modes. Background components are stacked and normalized using the results of the background-only fit. The lower panels show the data-to-prediction ratio, with dashed bands representing the total post-fit uncertainty. Modest excesses are observed in the following set of post-fit distributions, with localized deviations from the background-only predictions appearing around a mass of approximately 2 TeV. Although these deviations do not achieve statistical significance, their consistency across multiple signal regions and production modes motivates further examination. These features will be revisited in the context of the exclusion limits presented in the following section.

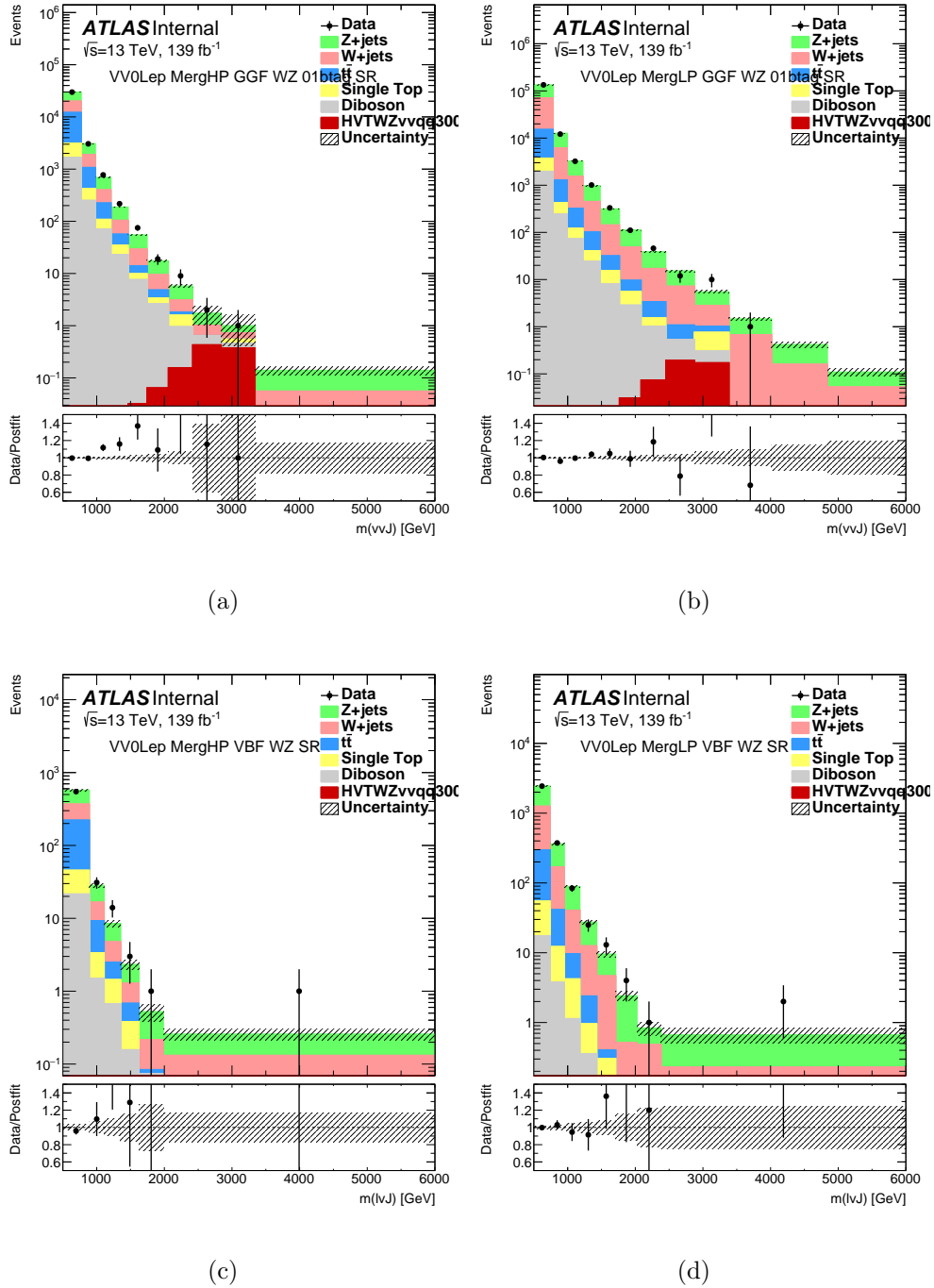


Figure 6.35: Post-fit invariant mass distributions in the WZ signal regions of the VV 0-lepton channel, categorized by production mode and purity. Subfigures (a) and (b) show the gluon-gluon fusion (ggF) merged high-purity (HP) and low-purity (LP) signal regions, and subfigures (c) and (d) display the vector boson fusion (VBF) HP and LP signal regions. Stacked histograms represent background predictions after the background-only fit to all WZ signal and control regions. Data points are overlaid, and the lower panels show the Data/Postfit ratio, with shaded bands indicating the total post-fit uncertainty, including both statistical and systematic components.

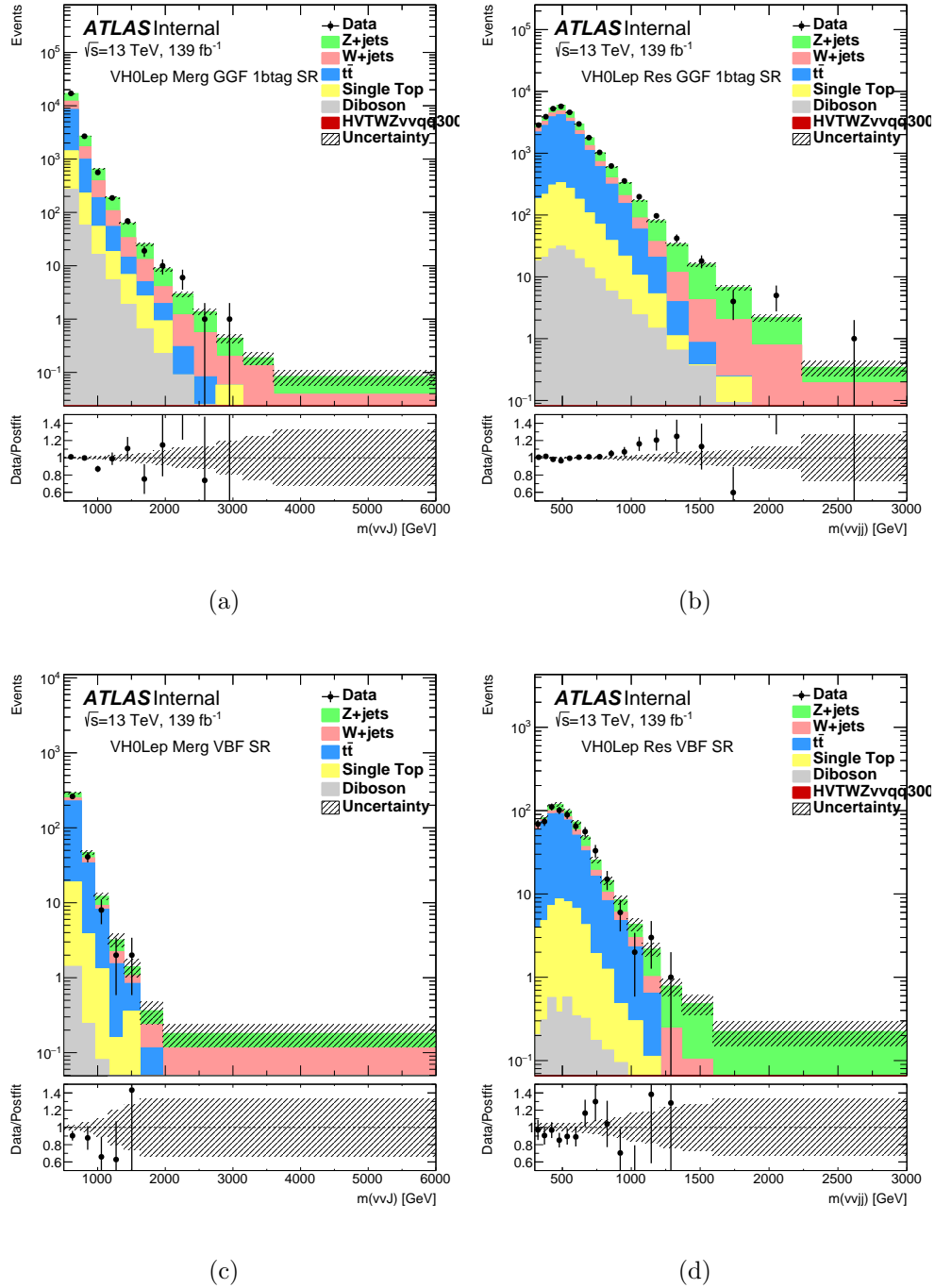


Figure 6.36: Post-fit invariant mass distributions in the WZ signal regions of the VH 0-lepton channel, categorized by production mode and purity. Subfigures (a) and (b) show the gluon-gluon fusion (ggF) merged high-purity (HP) and low-purity (LP) signal regions, and subfigures (c) and (d) display the vector boson fusion (VBF) HP and LP signal regions. Stacked histograms represent background predictions after the background-only fit to all WZ signal and control regions. Data points are overlaid, and the lower panels show the Data/Postfit ratio, with shaded bands indicating the total post-fit uncertainty, including both statistical and systematic components.

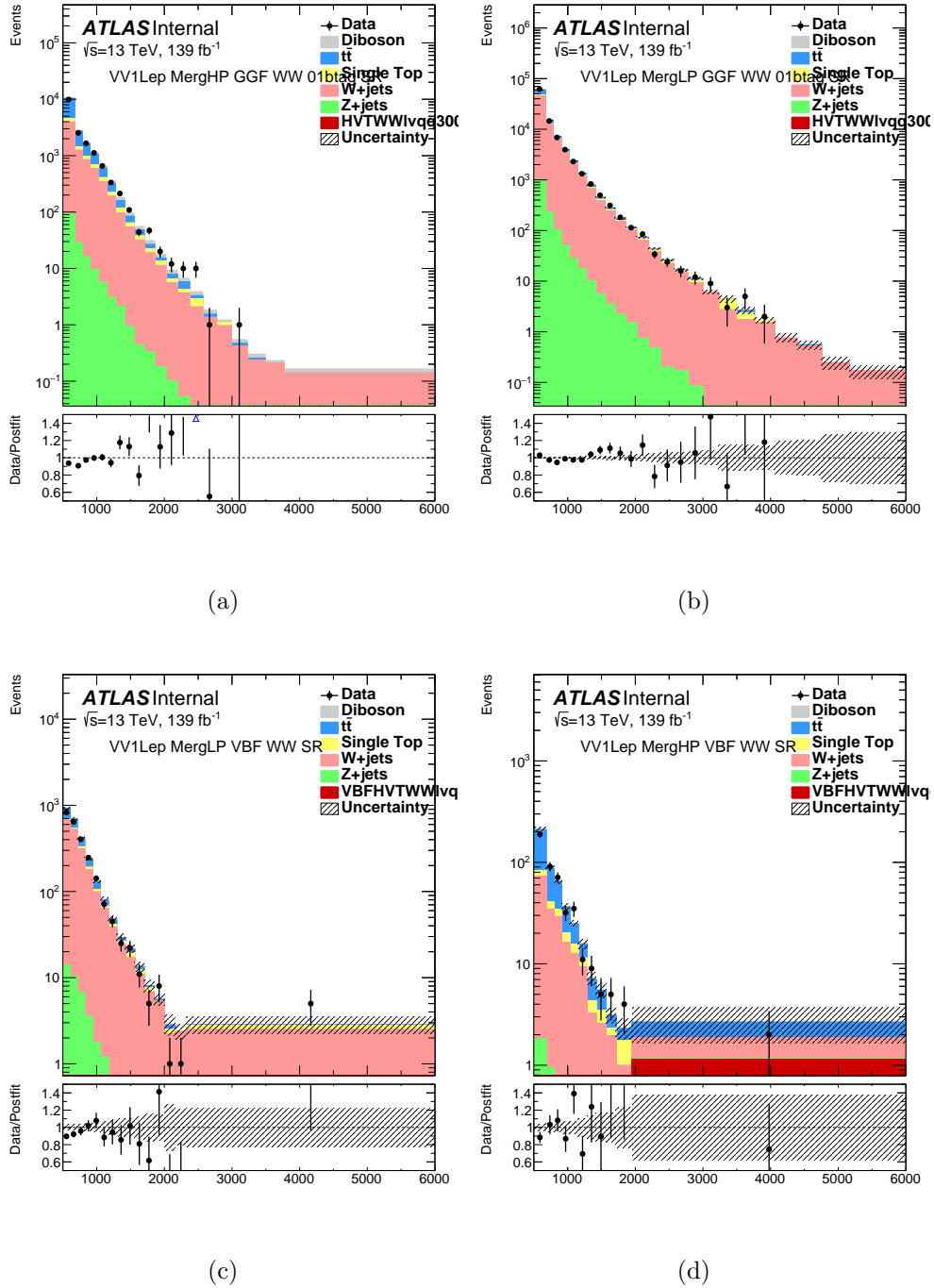


Figure 6.37: Post-fit invariant mass distributions in the WW signal regions of the VV 1-lepton channel, categorized by production mode and purity. Subfigures (a) and (b) show the gluon-gluon fusion (ggF) merged high-purity (HP) and low-purity (LP) signal regions, and subfigures (c) and (d) display the vector boson fusion (VBF) HP and LP signal regions. Stacked histograms represent background predictions after the background-only fit to all WZ signal and control regions. Data points are overlaid, and the lower panels show the Data/Postfit ratio, with shaded bands indicating the total post-fit uncertainty, including both statistical and systematic components.

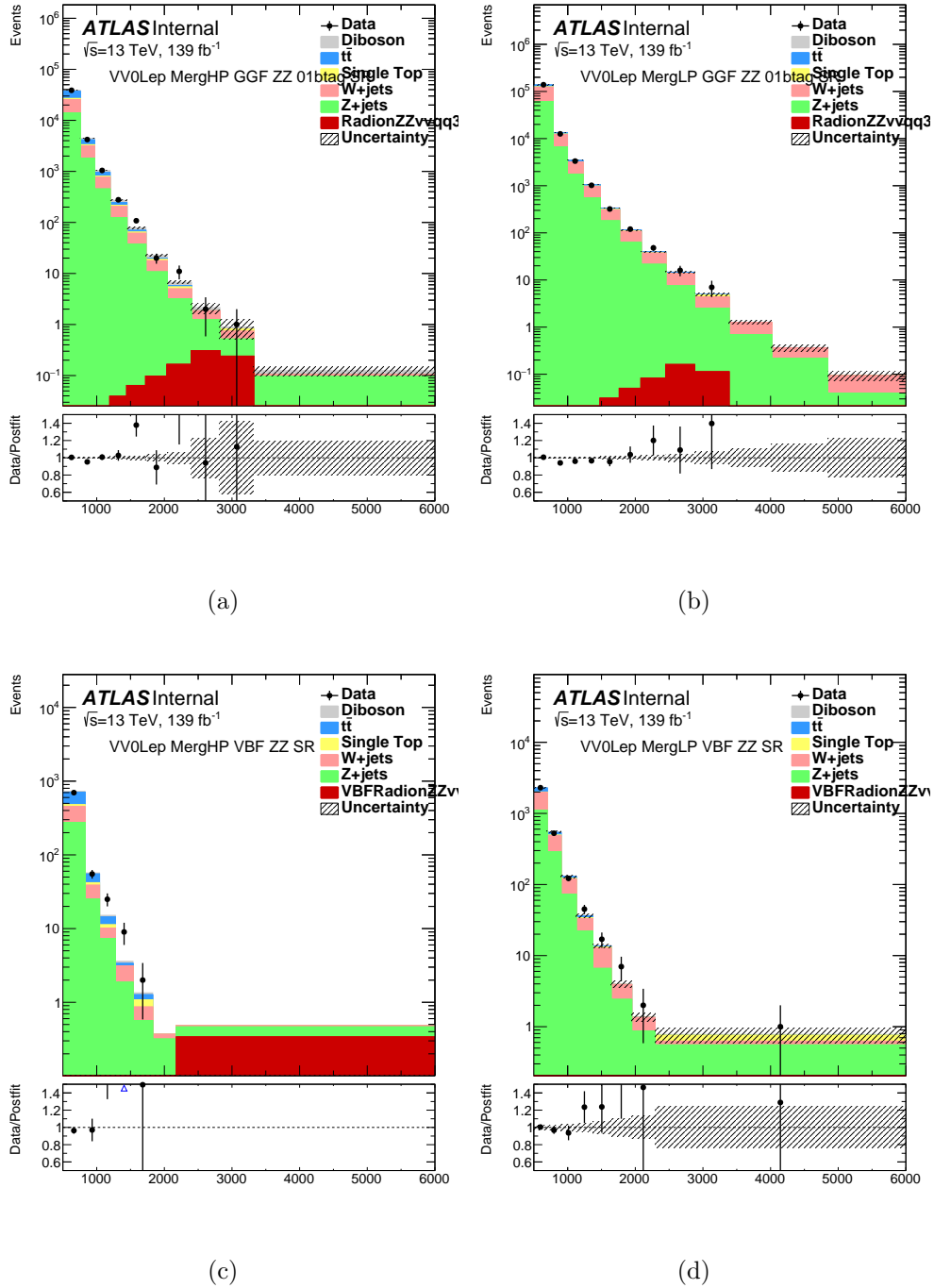


Figure 6.38: Post-fit invariant mass distributions in the ZZ signal regions of the VV 0-lepton channel, categorized by production mode and purity. Subfigures (a) and (b) show the gluon-gluon fusion (ggF) merged high-purity (HP) and low-purity (LP) signal regions, and subfigures (c) and (d) display the vector boson fusion (VBF) HP and LP signal regions. Stacked histograms represent background predictions after the background-only fit to all WZ signal and control regions. Data points are overlaid, and the lower panels show the Data/Postfit ratio, with shaded bands indicating the total post-fit uncertainty, including both statistical and systematic components.

6.8.3 Systematic Constraints

The impact of systematic uncertainties on the fit is summarized using nuisance parameter pull and ranking plots, as shown in Figure 6.39 to Figure 6.41 for HVT. These plots highlight the most constrained nuisance parameters and those with the largest effect on the signal strength. The most impactful uncertainties typically include the jet energy scale and resolution, as well as modeling uncertainties for $t\bar{t}$, V+jets, and multijet backgrounds. No unusually strong pulls or constraints are observed, though a few nuisance parameters show mild shifts consistent with known limitations in background modeling. Additional nuisance parameter plots are provided in Appendix C for reference.

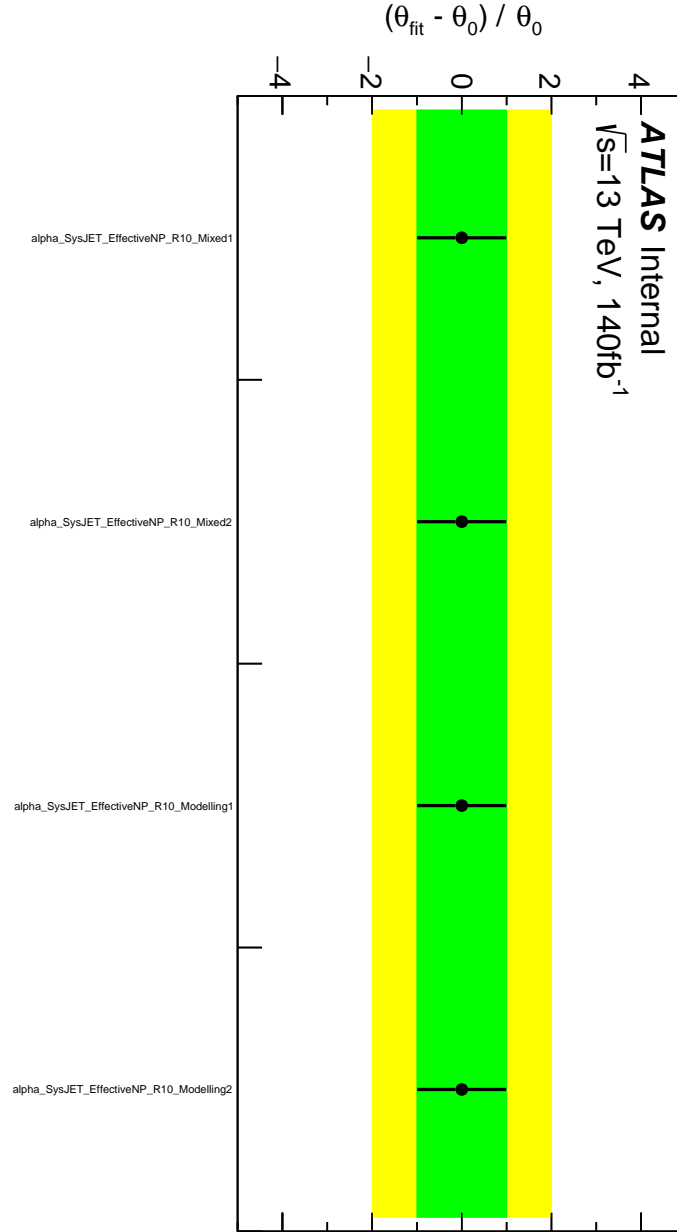


Figure 6.39: Post-fit pull values for a subset of nuisance parameters related to jet energy scale (JES) systematic uncertainties. The plot shows the deviation of the fitted nuisance parameters (θ_{fit}) from their pre-fit nominal values (θ_0), normalized to their pre-fit uncertainties. The green and yellow bands represent the 1σ and 2σ confidence intervals, respectively. All nuisance parameters shown remain well-constrained after the fit, with no significant deviations from the nominal values, indicating stable behavior of the JES uncertainties in the statistical model.

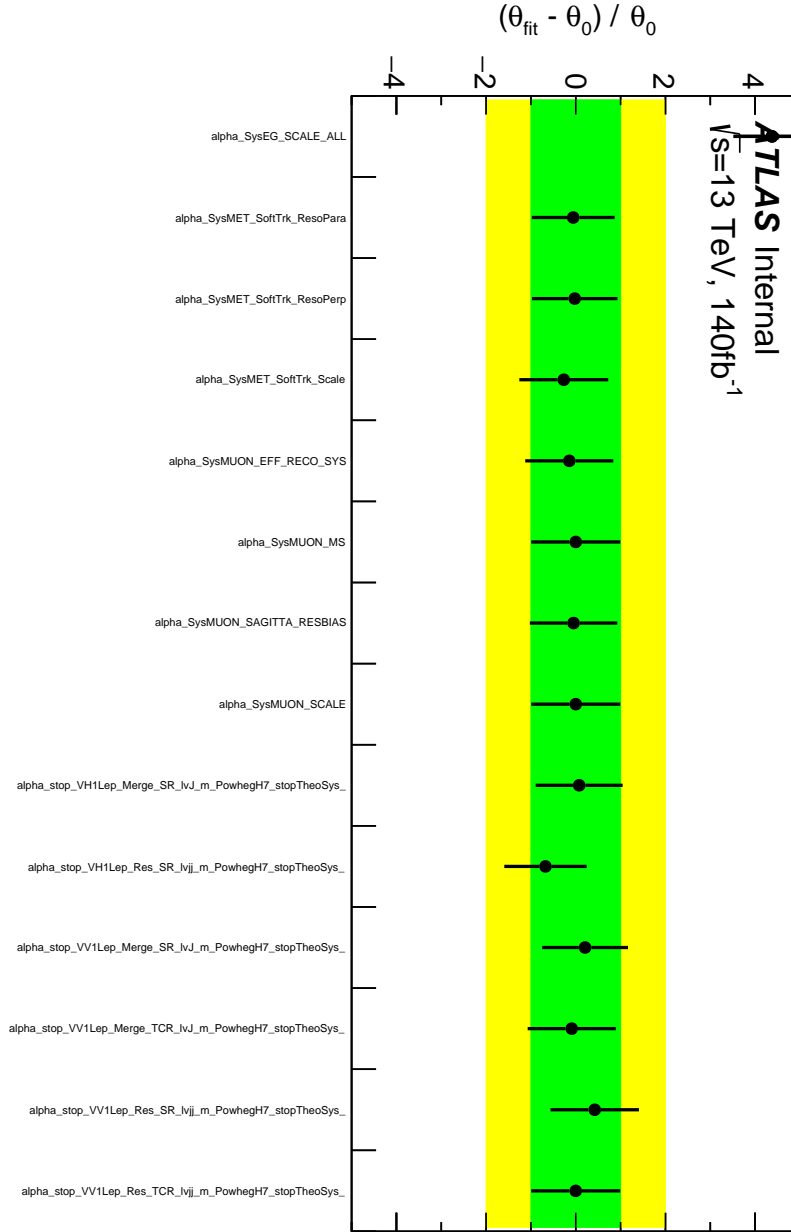


Figure 6.40: Post-fit pull distribution for a representative set of nuisance parameters related to theoretical modeling and detector systematic uncertainties. Each point shows the shift of the fitted nuisance parameter (θ_{fit}) from its nominal pre-fit value (θ_0), normalized by the pre-fit uncertainty. The green and yellow bands correspond to the 1σ and 2σ confidence intervals, respectively. All pulls remain within acceptable ranges, indicating no significant tensions between the data and the systematic uncertainty parameterizations, and validating the background modeling in the statistical interpretation.

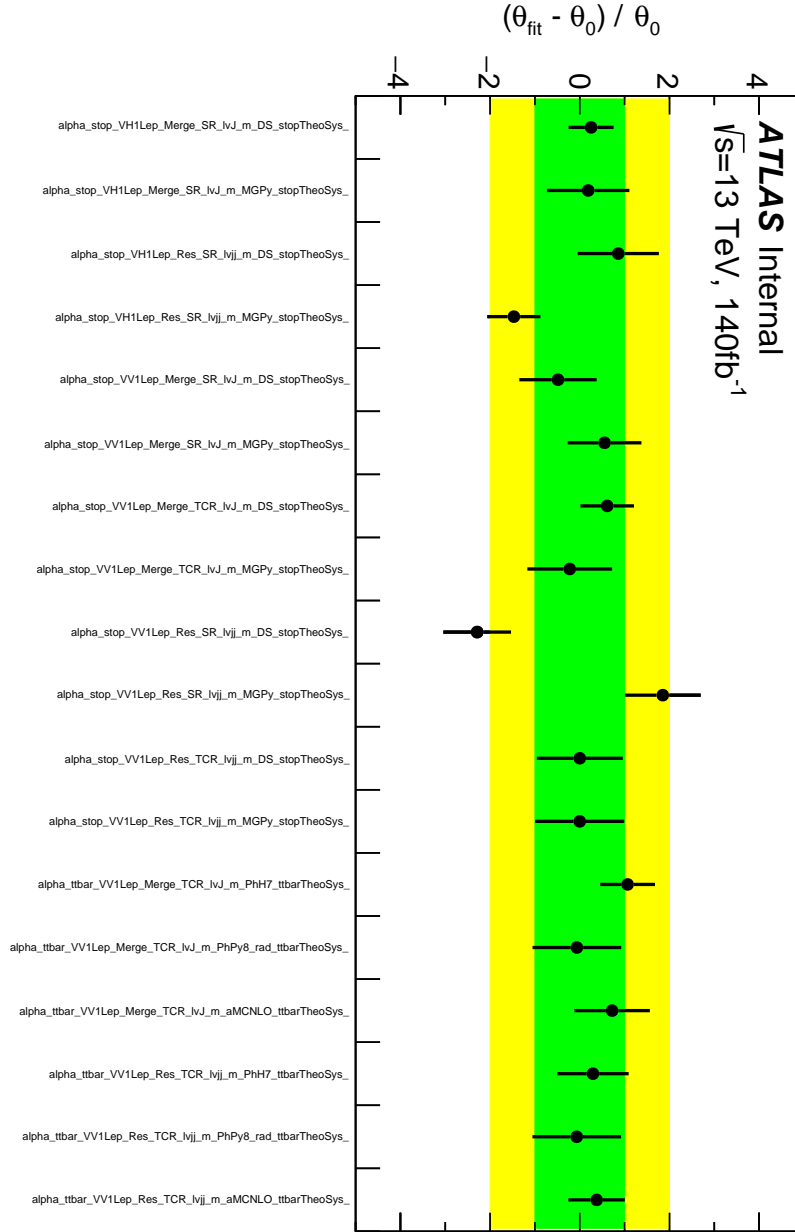


Figure 6.41: Post-fit pull distribution for a representative set of nuisance parameters related to $t\bar{t}$ and single-top modeling. Each point shows the shift of the fitted nuisance parameter (θ_{fit}) from its nominal pre-fit value (θ_0), normalized by the pre-fit uncertainty. The green and yellow bands correspond to the 1σ and 2σ confidence intervals, respectively. All pulls remain within acceptable ranges, indicating no significant tensions between the data and the systematic uncertainty parameterizations, and validating the background modeling in the statistical interpretation.

6.8.4 Exclusion Limits

Based on the post-fit distributions and systematic constraints, there is no strong indication of a significant signal-like excess above the background expectation, despite there being some localized small excesses. The observed data in all signal regions are fairly well described by the fitted background model, and therefore we proceed to set exclusion limits on the models under consideration.

The exclusion limits presented account for statistical uncertainties in the data and expected backgrounds, as well as the leading experimental systematic uncertainties affecting both signal and background predictions.

6.8.4.1 HVT $W' \rightarrow WZ$

Upper limits on the product of the production cross-section and branching ratio for an HVT W' decaying into W or Z bosons are derived from a simultaneous fit to all signal and control regions across the VV 0-lepton, 1-lepton, and 2-lepton channels. Figure 6.42 presents the expected 95% confidence level (CL) upper limits as a function of the W' mass for both the ggF and VBF production modes. In both (a) and (b) of Figure 6.42 there is a slight excess at 2 TeV. Looking back at the posifit plots, there were some excesses seen in Figure 6.35 (a) as well as (b). Additionally, we see excess in Figure 6.38 (c), even though it has a small number of events.

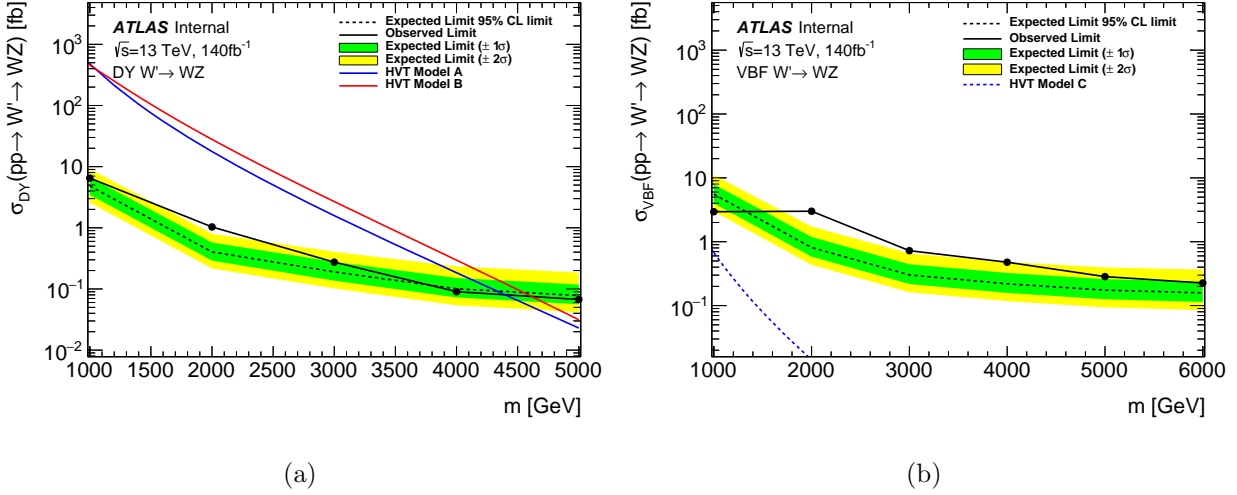


Figure 6.42: Expected 95% CL upper limits on $\sigma(pp \rightarrow W' \rightarrow WZ)$ as a function of the W' mass, using 140fb^{-1} of data at $\sqrt{s} = 13$ TeV. The dashed line shows the expected limit, with green and yellow bands representing $\pm 1\sigma$ and $\pm 2\sigma$ uncertainties. Results are interpreted in the context of the Heavy Vector Triplet (HVT) model via (a) DY production and (b) VBF production.

6.8.4.2 HVT $W' \rightarrow WH$

Upper limits on the product of the production cross-section and branching ratio for an HVT W' to WH decays are derived from a simultaneous fit to all signal and control regions across the VH 0-lepton and 1-lepton channels. Figure 6.43 presents the expected 95% confidence level (CL) upper limits as a function of the W' mass for both the ggF and VBF production modes. Interestingly, the small excess seen in VV is not corroborated here as the excess seen in VV does not appear in VH.

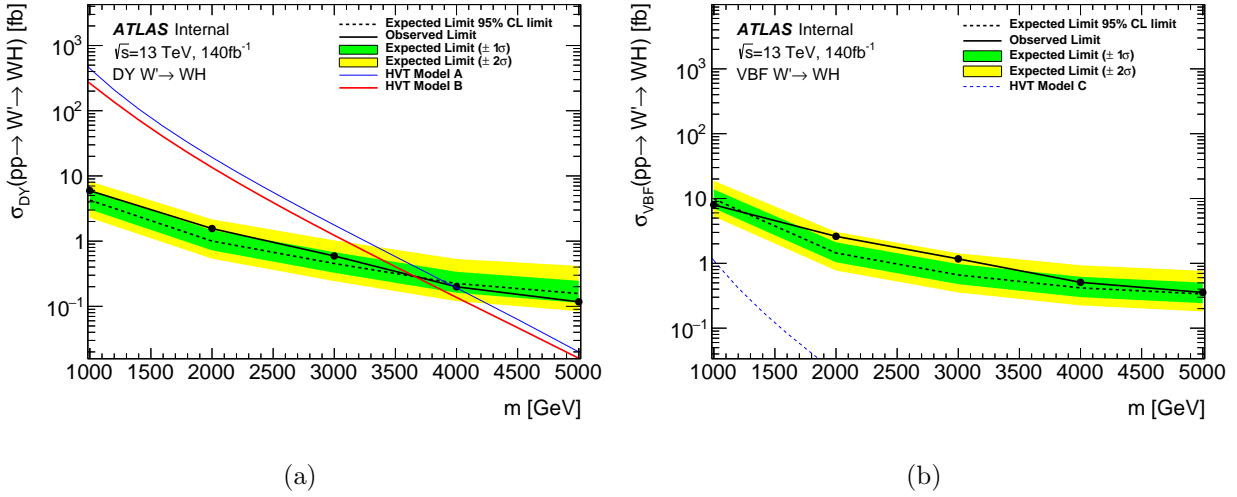


Figure 6.43: Expected 95% CL upper limits on $\sigma(pp \rightarrow W' \rightarrow WH)$ as a function of the W' mass, using 140 fb^{-1} of data at $\sqrt{s} = 13 \text{ TeV}$. The dashed line shows the expected limit, with green and yellow bands representing $\pm 1\sigma$ and $\pm 2\sigma$ uncertainties. Results are interpreted in the context of the Heavy Vector Triplet (HVT) model.

6.8.4.3 HVT $Z' \rightarrow WW$

Upper limits on the product of the production cross-section and branching ratio for an HVT Z' decaying into two W bosons are derived from a simultaneous fit to all signal and control regions across the VV 1-lepton channel. Figure 6.44 presents the expected 95% confidence level (CL) upper limits as a function of the Z' mass for both the ggF and VBF production modes.

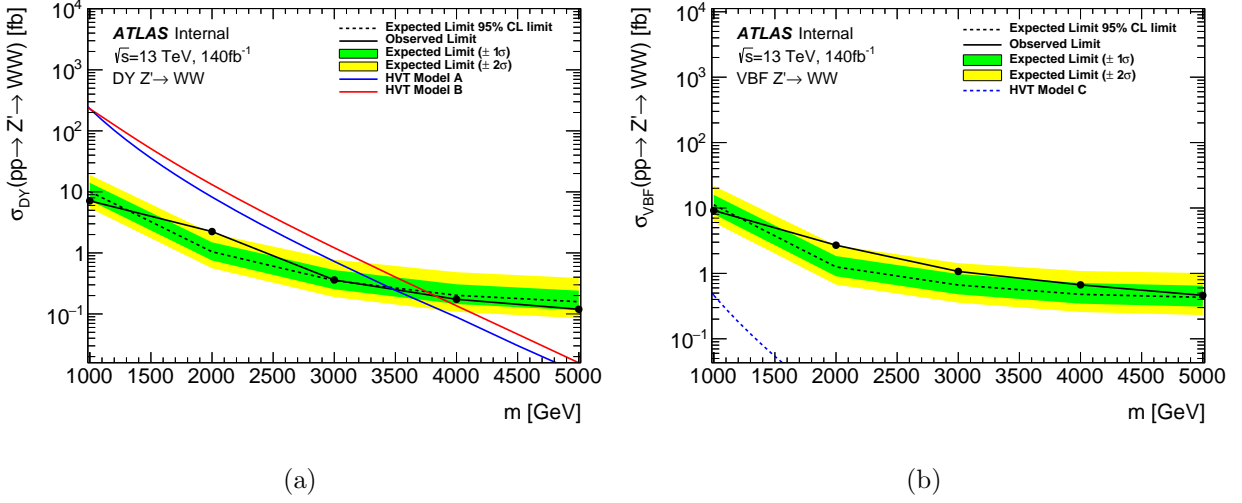


Figure 6.44: Expected 95% CL upper limits on $\sigma(pp \rightarrow Z' \rightarrow WW)$ as a function of the Z' mass, using 140 fb^{-1} of data at $\sqrt{s} = 13 \text{ TeV}$. The dashed line shows the expected limit, with green and yellow bands representing $\pm 1\sigma$ and $\pm 2\sigma$ uncertainties. Results are interpreted in the context of the Heavy Vector Triplet (HVT) model.

6.8.4.4 HVT $Z' \rightarrow ZH$

Upper limits on the product of the production cross-section and branching ratio for an HVT Z' to ZH decays are derived from a simultaneous fit to all signal and control regions across the VH 0-lepton and 1-lepton channels. Figure 6.45 presents the expected 95% confidence level (CL) upper limits as a function of the Z' mass for both the ggF and VBF production modes.

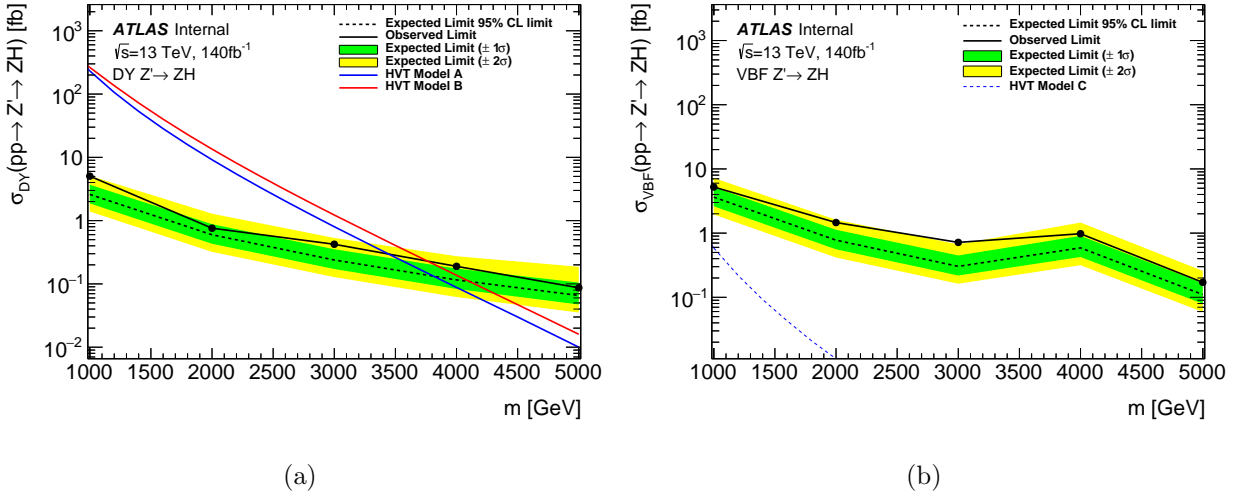


Figure 6.45: Expected 95% CL upper limits on $\sigma(pp \rightarrow Z' \rightarrow ZH)$ as a function of the Z' mass, using 140 fb^{-1} of data at $\sqrt{s} = 13 \text{ TeV}$. The dashed line shows the expected limit, with green and yellow bands representing $\pm 1\sigma$ and $\pm 2\sigma$ uncertainties. Results are interpreted in the context of the Heavy Vector Triplet (HVT) model.

6.8.4.5 HVT VV+VH Combination

Upper limits on the product of the production cross-section and branching ratio for HVT VV+VH decays are derived from a simultaneous fit to all signal and control regions. Figure 6.46 presents the expected 95% confidence level (CL) upper limits as a function of the invariant $VV + VH$ mass for the ggF production mode. The limit is set on a generic V' assuming the W' and Z' are degenerate in mass. All relevant experimental systematic uncertainties are correlated between the two analyses, as well as background normalization factors and modelling systematics. In the combination of VV+VH the excess in the VV has been slightly tempered by the lack of excess in VH (but a slight excess at 2 TeV is still seen).

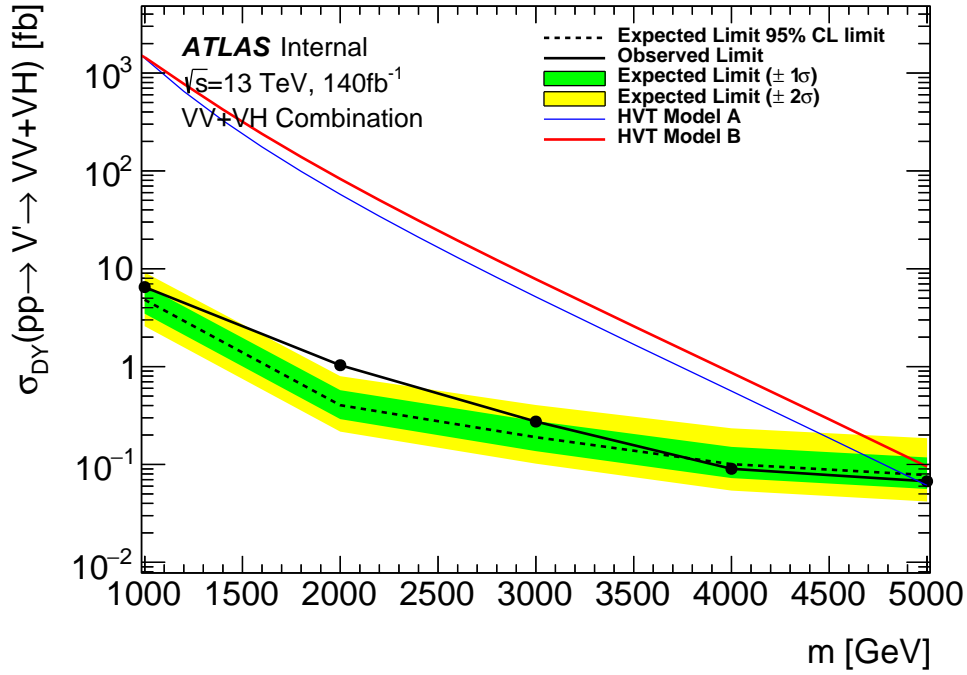


Figure 6.46: Expected 95% CL upper limits on $\sigma(VV+VH)$ as a function of the invariant $VV+VH$ mass, using 140 fb^{-1} of data at $\sqrt{s} = 13 \text{ TeV}$. The dashed line shows the expected limit, with green and yellow bands representing $\pm 1\sigma$ and $\pm 2\sigma$ uncertainties. Results are interpreted in the context of the Heavy Vector Triplet (HVT) model.

6.8.4.6 $G_{KK} \rightarrow \mathbf{WW} + \mathbf{ZZ}$

Upper limits on the product of the production cross-section and branching ratio for a RS Graviton are derived from a simultaneous WW and ZZ fit of all the signal and control region from the three leptonic final states. Figure 6.47 presents the expected 95% confidence level (CL) upper limits as a function of the Graviton mass for both the ggF and VBF production modes. In Figure 6.47 (a) there is a slight excess at 2 TeV. Looking back at the posifit plots, there were some excesses seen in Figure 6.37 (a).

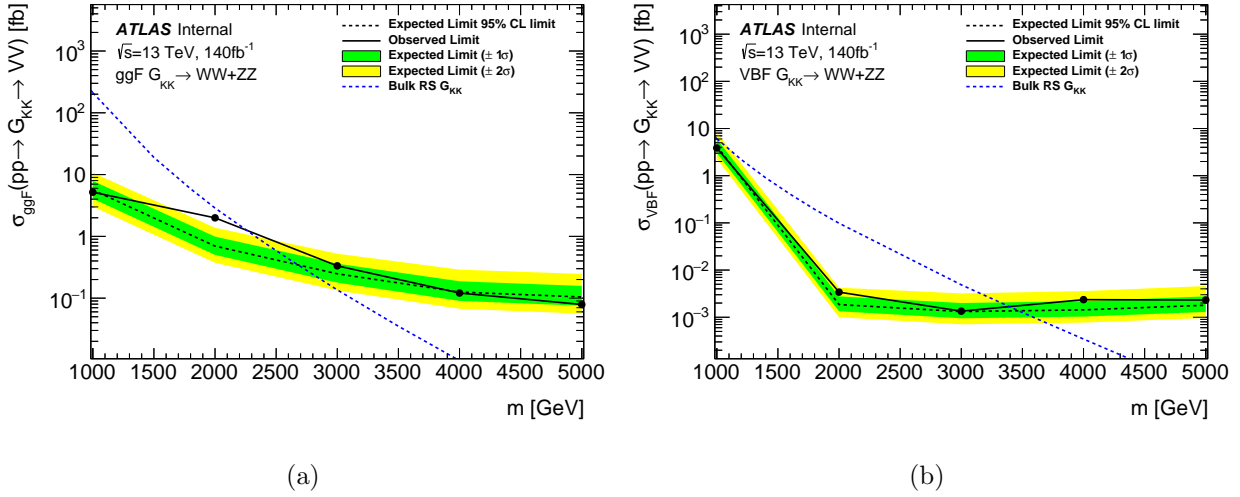


Figure 6.47: Expected 95% CL upper limits on $\sigma(pp \rightarrow G_{KK} \rightarrow WW + ZZ)$ as a function of the Graviton mass, using 140 fb^{-1} of data at $\sqrt{s} = 13 \text{ TeV}$. The dashed line shows the expected limit, with green and yellow bands representing $\pm 1\sigma$ and $\pm 2\sigma$ uncertainties. Results are interpreted in the context of the Bulk RS Graviton model via (a) ggF production and (b) VBF production.

6.8.4.7 $R \rightarrow WW + ZZ$

Upper limits on the product of the production cross-section and branching ratio for a RS Radion are derived from a simultaneous WW and ZZ fit of all the signal and control region from the three leptonic final states. Figure 6.48 presents the expected 95% confidence level (CL) upper limits as a function of the Radion mass for both the ggF and VBF production modes. In Figure 6.48 (a) there is a slight excess at 2 TeV. Looking back at the posifit plots, there were some excesses seen in Figure 6.38 but only around a 3σ -type excess.

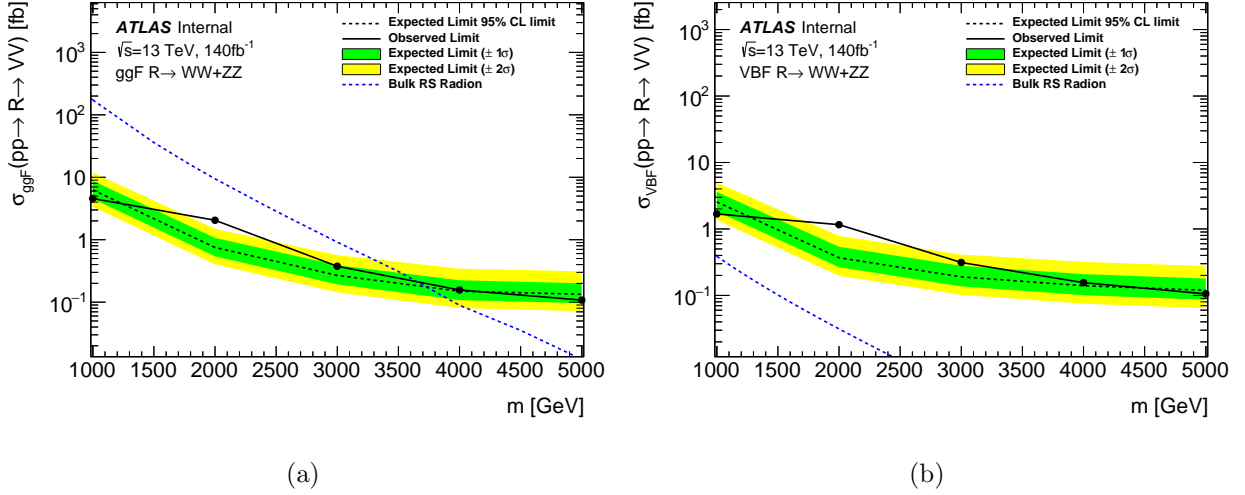


Figure 6.48: Expected 95% CL upper limits on $\sigma(pp \rightarrow R \rightarrow WW + ZZ)$ as a function of the Radion mass, using 140 fb^{-1} of data at $\sqrt{s} = 13 \text{ TeV}$. The dashed line shows the expected limit, with green and yellow bands representing $\pm 1\sigma$ and $\pm 2\sigma$ uncertainties. Results are interpreted in the context of the Bulk RS Radion model via (a) ggF production and (b) VBF production.

6.8.4.8 Summary

Table 6.3 summarizes the expected and observed 95% confidence level (CL) exclusion limits on the mass of heavy resonances for various theoretical models and production channels explored in this analysis. The HVT Models A, B, and C are evaluated across four decays modes (WZ, WH, WW, and ZH) and up to 12 total final states (accounting for 0/1/2-lepton channels). Among these, the most stringent observed limits are found in the HVTWZ channel with Model A, excluding resonance masses up to 4.5 TeV. In contrast, Model C consistently yields significantly worse exclusion limits, reflecting its reduced production cross section for VBF. The analysis also includes scalar resonances such as the Radion and RSG, assessed under both ggF and VBF productions. The VBF RSG is excluded up to 1.1 TeV, compared to 2.2 TeV for ggF. Similarly, the ggF Radion is excluded up to 3.7 TeV, while the VBF Radion exclusion reaches only 0.5 TeV, indicative of its suppressed cross section in

that production mode. Although no mass exclusion is achieved for the VBF W'/Z' signal hypotheses, the resulting cross-section limits still represent an improvement over previous searches and serve as an important benchmark for enhancing sensitivity in Run-3. These results extend the exclusion reach of previous ATLAS searches and place constraints on a wide array of benchmark BSM models.

Process	Model	Exp Limit (TeV)	Obs Limit (TeV)
$W' \rightarrow WZ$	HVT Model A	4.4	4.4
	HVT Model B	4.2	4.3
	HVT Model C	-	-
$W' \rightarrow WH$	HVT Model A	3.9	4.0
	HVT Model B	3.7	3.6
	HVT Model C	-	-
$Z' \rightarrow WW$	HVT Model A	3.5	3.5
	HVT Model B	3.8	3.9
	HVT Model C	-	-
$Z' \rightarrow ZH$	HVT Model A	3.8	3.4
	HVT Model B	4.2	3.8
	HVT Model C	-	-
$V' \rightarrow VV + VH$	HVT Model A	4.9	4.9
	HVT Model B	5.1	5.1
$G_{KK} \rightarrow WW + ZZ$	RSG	2.6	2.2
	VBF RSG	1.1	1.1
$R \rightarrow WW + ZZ$	Radion	3.5	3.4
	VBF Radion	-	-

Table 6.3: Expected and observed exclusion limits at 95% CL for various benchmark models and production modes.

6.8.5 Comparison of the limits

The cross-section upper limits obtained in this analysis are significantly more stringent than those reported in previous searches targeting the same final states and using the same dataset. As shown in the left panel of Figure 6.49, the limits for the HVT $W' \rightarrow WZ$ search is significantly improved compared to those in the VV (and later VH) search using the full Run-2

dataset but in the first round [135]. Similarly, the right panel shows that the limits for the HVT $Z' \rightarrow ZH$ search improve by approximately 20% relative to the results reported in [138]. These enhanced limits substantially extend the exclusion reach for heavy vector resonances, further constraining the HVT model parameter space and offering stronger guidance for future theoretical developments and experimental searches. The increase in sensitivity has come from many factors, such as the new UFO jet collection (providing a better jet resolution), selection optimization (such outlined in Subsection 6.5.3.1) as well as the MCT to cleanly orthogonalize the VV and VH channels. While this took a long time to achieve, these limits show great improvement and is a great point to start the Run-3 version of the analysis, with the machinery ready to go.

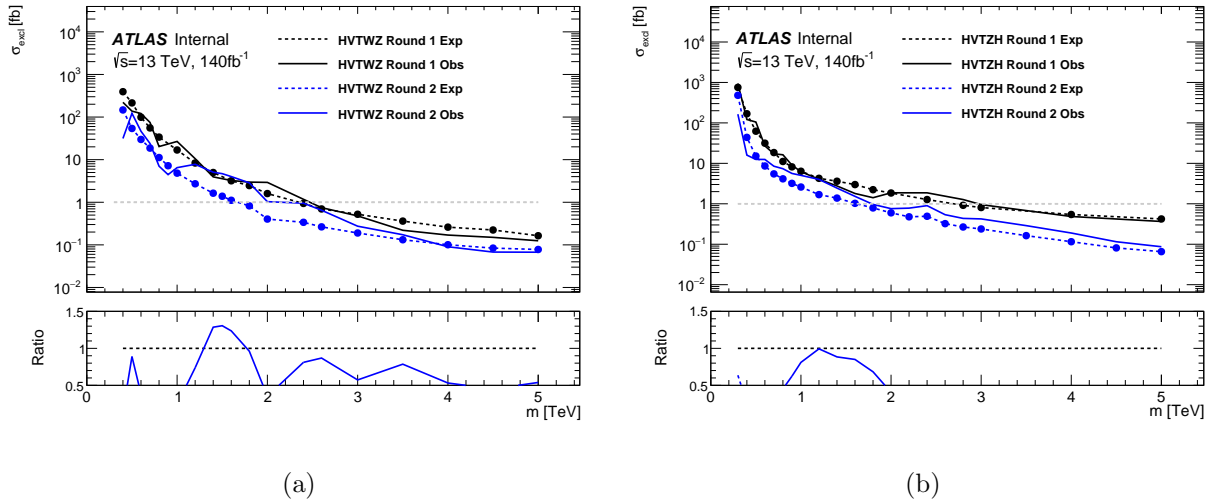


Figure 6.49: Expected 95% confidence level (CL) upper limits on the cross-section for HVT $W' \rightarrow WZ$ production (a) and HVT $Z' \rightarrow ZH$ production (b) as a function of the W' or Z' mass, using 140 fb^{-1} of data at $\sqrt{s} = 13 \text{ TeV}$. The plot compares the results from two rounds of ATLAS analyses: the previously published limits (black dashed line and markers), and updated limits (blue dashed line and markers) from the current analysis. The lower panel shows the ratio of the previous to current limits, indicating a consistent improvement in sensitivity across most of the mass range.

6.9 Summary

This chapter details a search for heavy resonances decaying to pairs of Standard Model bosons in semi-leptonic final states, using 140 fb^{-1} of proton-proton collision data collected by the ATLAS detector at $\sqrt{s} = 13 \text{ TeV}$ during LHC Run 2. The analysis strategy begins with an overview of the theoretical signal models, background processes, and data samples used in the search. Emphasis is placed on object reconstruction, including the adoption of the Unified Flow Object (UFO) jet definition for improved jet substructure resolution. Large-R jets, small-R jets, electrons, muons, tracks, and missing transverse energy are all reconstructed and calibrated with dedicated algorithms. Advanced tagging techniques such as flavor tagging, variable-radius track jets, and multi-class classifiers are applied to enhance the identification of boosted bosons and top quarks.

Event selection proceeds through preselection and channel-specific optimization in 0-, 1-, and 2-lepton final states, defining distinct signal and control regions for different production mechanisms (ggF and VBF) and decay topologies (WW, WZ, WH, ZH, ZZ). Systematic uncertainties are addressed, including experimental effects and modeling uncertainties for $t\bar{t}$, single-top, and V+jets backgrounds. These uncertainties are incorporated into a binned maximum likelihood fit, providing the statistical framework for testing the presence of a signal.

The results section presents both pre-fit validation in control regions and post-fit comparisons between data and Standard Model predictions. Kinematic distributions and signal discriminants are shown across all final states, with pull and impact plots illustrating the behavior of key nuisance parameters. No statistically significant excess over background expectations is observed. As such, 95% confidence-level upper limits are placed on the pro-

duction cross sections of hypothetical spin-1 and spin-2 resonances decaying to WW , WZ , WH , ZH , and ZZ . These limits significantly improve upon previous ATLAS results, enhancing the exclusion sensitivity and placing tighter constraints on parameter spaces in models such as the Heavy Vector Triplet and Randall-Sundrum models.

Chapter 7. Conclusion

This dissertation presents the research I conducted over six years at Michigan State University as part of the ATLAS Collaboration at CERN. As first discussed, the overarching theory of particle physics is introduced, including concepts of both the Standard Model as well as Beyond Standard Model theories. Then, an overview of the ATLAS detector and the various subcomponents therein are briefly described, leading into the process of event generation and reconstruction. Following that, boosted object identification techniques are discussed in detail, and the novel jet definition based on Unified Flow Objects (UFO) is introduced. The performance of the top-quark and W-boson jet taggers is studied in events of $t\bar{t}$ production in the semileptonic final state, and tagger efficiencies and scale factors are calculated. These scale factors are used for correcting discrepancies in tagging efficiency and background rejection between data and MC simulation. A relatively flat signal efficiency response across the jet p_T spectrum is observed for all taggers, with an uncertainty between data and MC prediction of about 10% for the DNN Top Tagger, 20-30% for the 3-Variable W-Tagger, and 15-30% for the ANN W-Tagger. Finally, this dissertation describes a search for heavy resonances decaying to pairs of SM bosons in semileptonic final states using 140 fb^{-1} of proton-proton collisions at a center-of-mass energy of $\sqrt{s} = 13$ TeV recorded by the ATLAS detector during Run 2 of the LHC at CERN.

Historically separate analyses, the two distinct searches $X \rightarrow VV$ and $X \rightarrow VH$ have been harmonized into one coherent analysis with the event selection reoptimized to a common criterion between the two searches, resulting in the new VV+VH semileptonic analysis. The main contributions of this work include the optimization of the 0-lepton channel, providing $t\bar{t}$ modeling uncertainties, and $t\bar{t}$ scale factors for UFO jets. Applying the new UFO jet

definition also brought improvement to the reconstruction of large-radius jets. With these changes, the overall analysis sensitivity is improved by at least 20% compared to the previous ATLAS searches in the same channels using the same dataset. Lastly, upper limits on the vector boson fusion production cross section of heavy resonances decaying to a W or Z boson and a Higgs boson is set by this round of the analysis for the first time.

BIBLIOGRAPHY

- [1] Merriam-Webster, “particle.” <https://www.merriam-webster.com/dictionary/particle>, 2025. Accessed: 2025-05-03.
- [2] J. J. Thomson, “Xl. cathode rays,” *The London, Edinburgh, and Dublin Philosophical Magazine and Journal of Science*, vol. 44, p. 293316, Oct. 1897.
- [3] E. Rutherford, “Lxxix. the scattering of α and β particles by matter and the structure of the atom,” *The London, Edinburgh, and Dublin Philosophical Magazine and Journal of Science*, vol. 21, p. 669688, May 1911.
- [4] J. Chadwick, “Possible existence of a neutron,” *Nature*, vol. 129, p. 312312, Feb. 1932.
- [5] J. D. Bjorken and E. A. Paschos, “Inelastic Electron Proton and gamma Proton Scattering, and the Structure of the Nucleon,” *Phys. Rev.*, vol. 185, pp. 1975–1982, 1969.
- [6] M. K. Gaillard, P. D. Grannis, and F. J. Sciulli, “The standard model of particle physics,” *Reviews of Modern Physics*, vol. 71, p. S96S111, Mar. 1999.
- [7] A. Collaboration, “Observation of a new particle in the search for the standard model higgs boson with the atlas detector at the lhc,” *Physics Letters B*, vol. 716, p. 129, Sept. 2012.
- [8] C. Collaboration, “Observation of a new boson at a mass of 125 gev with the cms experiment at the lhc,” *Physics Letters B*, vol. 716, p. 3061, Sept. 2012.
- [9] D. Griffiths, *Introduction to elementary particles*. 2008.
- [10] Wikipedia, “File:standard model of elementary particles.svg,” n.d. Accessed: 2025-01-08.
- [11] S. Biswas, “Fermi-dirac statistics,” 2015.
- [12] I. G. Kaplan, “Pauli exclusion principle and its theoretical foundation,” 2019.
- [13] P. Pessoa, “Bose-einstein statistics for a finite number of particles,” *Physical Review A*, vol. 104, Oct. 2021.
- [14] B. Diu, C. Cohen-Tannoudji, and F. Lalo, *Quantum Mechanics, Volume 3: Fermions, Bosons, Photons, Correlations, and Entanglement*. Weinheim, Germany: Wiley-VCH, 2007.
- [15] M. E. Peskin and D. V. Schroeder, *An Introduction to quantum field theory*. Reading, USA: Addison-Wesley, 1995.

- [16] M. D. Schwartz, *Quantum Field Theory and the Standard Model*. Cambridge University Press, 3 2014.
- [17] A. Zee, *Quantum field theory in a nutshell*. 2003.
- [18] C. N. Yang and R. L. Mills, “Conservation of isotopic spin and isotopic gauge invariance,” *Phys. Rev.*, vol. 96, pp. 191–195, Oct 1954.
- [19] E. Noether, “Invariant variation problems,” *Transport Theory and Statistical Physics*, vol. 1, pp. 186–207, Jan. 1971.
- [20] R. P. Feynman, “Space-time approach to quantum electrodynamics,” *Physical Review*, vol. 76, p. 769789, Sept. 1949.
- [21] G. Zweig, *An $SU(3)$ model for strong interaction symmetry and its breaking. Version 2*, pp. 22–101. 2 1964.
- [22] H. Fritzsch, M. Gell-Mann, and H. Leutwyler, “Advantages of the Color Octet Gluon Picture,” *Phys. Lett. B*, vol. 47, pp. 365–368, 1973.
- [23] G. Rajasekaran, “Fermi and the theory of weak interactions,” *Resonance*, vol. 19, p. 1844, Jan. 2014.
- [24] A. Salam, “Weak and Electromagnetic Interactions,” *Conf. Proc. C*, vol. 680519, pp. 367–377, 1968.
- [25] F. Englert and R. Brout, “Broken symmetry and the mass of gauge vector mesons,” *Phys. Rev. Lett.*, vol. 13, pp. 321–323, Aug 1964.
- [26] P. W. Higgs, “Broken symmetries and the masses of gauge bosons,” *Phys. Rev. Lett.*, vol. 13, pp. 508–509, Oct 1964.
- [27] G. S. Guralnik, C. R. Hagen, and T. W. B. Kibble, “Global conservation laws and massless particles,” *Phys. Rev. Lett.*, vol. 13, pp. 585–587, Nov 1964.
- [28] P. W. Higgs, “Spontaneous symmetry breakdown without massless bosons,” *Phys. Rev.*, vol. 145, pp. 1156–1163, May 1966.
- [29] J. L. Rosner, “The Cabibbo-Kobayashi-Maskawa matrix,” pp. 91–049, 9 1991.
- [30] A. Azatov and J. Galloway, “Electroweak Symmetry Breaking and the Higgs Boson: Confronting Theories at Colliders,” *Int. J. Mod. Phys. A*, vol. 28, p. 1330004, 2013.
- [31] C. Amsler, M. Doser, M. Antonelli, D. M. Asner, K. S. Babu, H. Baer, H. R. Band, R. M. Barnett, E. Bergren, J. Beringer, G. Bernardi, W. Bertl, H. Bichsel, O. Biebel,

- P. Bloch, E. Blucher, S. Blusk, R. N. Cahn, M. Carena, C. Caso, A. Ceccucci, D. Chakraborty, M.-C. Chen, R. S. Chivukula, G. Cowan, O. Dahl, G. D’Ambrosio, T. Damour, A. de Gouvea, T. DeGrand, B. Dobrescu, M. Drees, D. A. Edwards, S. Eidelman, V. D. Elvira, J. Erler, V. V. Ezhela, J. L. Feng, W. Fetscher, B. D. Fields, B. Foster, T. K. Gaiser, L. Garren, H.-J. Gerber, G. Gerbier, T. Gherghetta, G. F. Giudice, M. Goodman, C. Grab, A. V. Gritsan, J.-F. Grivaz, D. E. Groom, M. Grnewald, A. Gurtu, T. Gutsche, H. E. Haber, K. Hagiwara, C. Hagmann, K. G. Hayes, J. J. Hernandez-Rey, K. Hikasa, I. Hinchliffe, A. Hcker, J. Huston, P. Igo-Kemenes, J. D. Jackson, K. F. Johnson, T. Junk, D. Karlen, B. Kayser, D. Kirkby, S. R. Klein, I. G. Knowles, C. Kolda, R. V. Kowalewski, P. Kreitz, B. Krusche, Y. V. Kuyanov, Y. Kwon, O. Lahav, P. Langacker, A. Liddle, Z. Ligeti, C.-J. Lin, T. M. Liss, L. Littenberg, J. C. Liu, K. S. Lugovsky, S. B. Lugovsky, H. Mahlke, M. L. Mangano, T. Mannel, A. V. Manohar, W. J. Marciano, A. D. Martin, A. Masoni, D. Milstead, R. Miquel, K. Mnig, H. Murayama, K. Nakamura, M. Narain, P. Nason, S. Navas, P. Nevski, Y. Nir, K. A. Olive, L. Pape, C. Patrignani, J. A. Peacock, A. Piepke, G. Punzi, A. Quadt, S. Raby, G. Raffelt, B. N. Ratcliff, B. Renk, P. Richardson, S. Roesler, S. Rolli, A. Romaniouk, L. J. Rosenberg, J. L. Rosner, C. T. Sachrajda, Y. Sakai, S. Sarkar, F. Sauli, O. Schneider, D. Scott, W. G. Seligman, M. H. Shaevitz, T. Sjstrand, J. G. Smith, G. F. Smoot, S. Spanier, H. Spieler, A. Stahl, T. Stanev, S. L. Stone, T. Sumiyoshi, M. Tanabashi, J. Terning, M. Titov, N. P. Tkachenko, N. A. Trnqvist, D. Tovey, G. H. Trilling, T. G. Trippe, G. Valencia, K. van Bibber, M. G. Vincter, P. Vogel, D. R. Ward, T. Watari, B. R. Webber, G. Weiglein, J. D. Wells, M. Whalley, A. Wheeler, C. G. Wohl, L. Wolfenstein, J. Womersley, C. L. Woody, R. L. Workman, A. Yamamoto, W.-M. Yao, O. V. Zenin, J. Zhang, R.-Y. Zhu, P. A. Zyla, G. Harper, V. S. Lugovsky, and P. Schaffner, “Review of particle physics,” *Physics Letters B*, vol. 667, no. 1-5, pp. 1–6, 2008.
- [32] G. Bhattacharyya, “Hierarchy problem and BSM physics,” *Pramana*, vol. 89, no. 4, p. 53, 2017.
- [33] G. Bertone and D. Hooper, “History of dark matter,” *Reviews of Modern Physics*, vol. 90, Oct. 2018.
- [34] A. I. Lonappan, S. Kumar, Ruchika, B. R. Dinda, and A. A. Sen, “Bayesian evidences for dark energy models in light of current observational data,” *Physical Review D*, vol. 97, Feb. 2018.
- [35] U. of Cambridge, “Planck captures portrait of the young universe, revealing earliest light.” <https://www.cam.ac.uk/research/news/planck-captures-portrait-of-the-young-universe-revealing-earliest-light>, 2013. Accessed: 2025-05-17.
- [36] B. A. Robson, “The Matter-antimatter Asymmetry Problem,” in *International Conference on Cosmology, Gravitational Waves and Particles*, pp. 154–162, 2018.

- [37] D. Pappadopulo, A. Thamm, R. Torre, and A. Wulzer, “Heavy Vector Triplets: Bridging Theory and Data,” *JHEP*, vol. 09, p. 060, 2014.
- [38] D. Alves, “Simplified Models for LHC New Physics Searches,” *J. Phys. G*, vol. 39, p. 105005, 2012.
- [39] L. Randall and R. Sundrum, “Large mass hierarchy from a small extra dimension,” *Physical Review Letters*, vol. 83, p. 33703373, Oct. 1999.
- [40] L. Randall and R. Sundrum, “An alternative to compactification,” *Physical Review Letters*, vol. 83, p. 46904693, Dec. 1999.
- [41] J. Cook, “Consciousness, the paranormal and higher dimensions.” <https://cosmology.com/ConsciousTime105.html>, 2005. Cosmology.com, accessed 2025-06-29.
- [42] K. Agashe, H. Davoudiasl, G. Perez, and A. Soni, “Warped gravitons at the cern lhc and beyond,” *Physical Review D*, vol. 76, 8 2007.
- [43] N. ArkaniHamed, S. Dimopoulos, and G. Dvali, “The hierarchy problem and new dimensions at a millimeter,” *Physics Letters B*, vol. 429, p. 263272, June 1998.
- [44] A. Carvalho, “Gravity particles from warped extra dimensions, predictions for lhc,” 2018.
- [45] CERN, “The History of CERN: Early beginnings.” <https://timeline.web.cern.ch/early-beginnings>, 2024. [Accessed 11-01-2024].
- [46] CERN Users Office, “Evolution of the Number of CERN Users.” <https://usersoffice.web.cern.ch/sites/default/files/statistics/Evolution%20of%20the%20number%20of%20CERN%20Users.pdf>. [Accessed 01-08-2025].
- [47] CERN, “CERN Annual report 2023,” tech. rep., CERN, Geneva, 2024.
- [48] CERN, “Facts and Figures about the LHC.” <https://home.cern/resources/faqs/facts-and-figures-about-lhc>, 2024. [Accessed 01-08-2025].
- [49] A. Lopes and M. L. Perrey, “FAQ-LHC The guide.” 2022.
- [50] R. Alemany-Fernandez, E. Bravin, L. Drosdal, A. Gorzawski, V. Kain, M. Lamont, A. Macpherson, G. Papotti, M. Pojer, L. Ponce, S. Redaelli, G. Roy, M. Solfaroli Camillocci, W. Venturini, and J. Wenninger, “Operation and Configuration of the LHC in Run 1,” 2013.
- [51] CERN, “Long Shutdown 1.” <https://home.web.cern.ch/tags/long-shutdown-1#:~:text=In%20early%202013%20the%20CERN,higher%20energy%20of%2013%20TeV.> [Accessed 01-08-2025].

- [52] R. Steerenberg, M. Albert, R. Alemany-Fernndez, T. Argyropoulos, E. Bravin, G. Crockford, J.-C. Dumont, K. Fuchsberger, R. Giachino, M. Giovannozzi, G.-H. Hemelsoet, W. Hfle, D. Jacquet, M. Lamont, E. Mtral, D. Nisbet, G. Papotti, M. Pojer, L. Ponce, S. Redaelli, B. Salvachua, M. Schaumann, M. Solfaroli Camillocci, R. Suykerbuyk, G. Trad, J. Uythoven, S. Uznanski, D. Walsh, J. Wenninger, and M. Zerlauth, “Operation and performance of the CERN Large Hadron Collider during proton Run 2,” p. MOPMP031, 2019.
- [53] CERN, “The LHC and the Long Shutdown 2.” https://indico.cern.ch/event/315665/contributions/1690164/attachments/605824/833763/LHC_LS2_paper_rev_final.pdf. [Accessed 01-08-2025].
- [54] CERN, “Run 3 at the LHC: A New Era of High-Energy Physics.” <https://home.cern/press/2022/run-3>, 2022. [Accessed 01-08-2025].
- [55] CERN, “New Schedule for CERN’s Accelerators.” <https://home.cern/news/news/accelerators/new-schedule-cerns-accelerators>. [Accessed 01-08-2025].
- [56] E. Lopienska, “The CERN accelerator complex, layout in 2022. Complexe des acclra-teurs du CERN en janvier 2022,” 2022. General Photo.
- [57] D. Boussard and T. P. R. Linnecar, “The LHC Superconducting RF System,” tech. rep., CERN, Geneva, 1999.
- [58] LHC: Taking a Closer Look, “RF Cavities.” https://www.lhc-closer.es/taking_a_closer_look_at_lhc/0.rf_cavities. [Accessed 01-08-2025].
- [59] A. Collaboration., *ATLAS detector and physics performance: Technical Design Report, 1*. Technical design report. ATLAS, Geneva: CERN, 1999.
- [60] T. A. Collaboration, “The atlas experiment at the cern large hadron collider,” *Journal of Instrumentation*, vol. 3, p. S08003, aug 2008.
- [61] CMS, *CMS Physics: Technical Design Report Volume 1: Detector Performance and Software*. Technical design report. CMS, Geneva: CERN, 2006. There is an error on cover due to a technical problem for some items.
- [62] A. Collaboration, “ALICE Electromagnetic Calorimeter Technical Design Report,” tech. rep., 2008.
- [63] LHCb, “The LHCb Detector at the LHC,” *JINST*, vol. 3, p. S08005, 2008. Also published by CERN Geneva in 2010.
- [64] W. Herr and B. Muratori, “Concept of luminosity,” 2006.

- [65] ATLAS Collaboration, “Luminosity Public Results Run 2.” <https://twiki.cern.ch/twiki/bin/view/AtlasPublic/LuminosityPublicResultsRun2>, 2018. [Accessed 01-08-2025].
- [66] N. Garelli, “Performance of the ATLAS Detector in Run-2,” *EPJ Web Conf.*, vol. 164, p. 01021, 2017.
- [67] R. Reed, “The upgrade of the atlas tile calorimeter readout electronics for phase ii,” *Journal of Physics Conference Series 1742-6588*, vol. 623, 12 2014.
- [68] *ATLAS magnet system: Technical Design Report, 1*. Technical design report. ATLAS, Geneva: CERN, 1997.
- [69] *ATLAS inner detector: Technical Design Report, 1*. Technical design report. ATLAS, Geneva: CERN, 1997.
- [70] Christophe Ochando, “Physics of Electromagnetic Showers.” <https://indico.cern.ch/event/782305/contributions/3256087/>, 2019. [Accessed 01-08-2025].
- [71] Silvia Masciocchi, “Hadronic Calorimeters.” <https://www.physi.uni-heidelberg.de/~sma/teaching/ParticleDetectors2/sma.HadronicCalorimeters.pdf>, 2017. [Accessed 01-08-2025].
- [72] *ATLAS calorimeter performance: Technical Design Report*. Technical design report. ATLAS, Geneva: CERN, 1996.
- [73] *ATLAS muon spectrometer: Technical Design Report*. Technical design report. ATLAS, Geneva: CERN, 1997.
- [74] *ATLAS level-1 trigger: Technical Design Report*. Technical design report. ATLAS, Geneva: CERN, 1998.
- [75] “The Grid: A system of tiers,” 2012.
- [76] e. a. Agostinelli, S., “Geant4a simulation toolkit,” *Nuclear Instruments and Methods in Physics Research Section A: Accelerators, Spectrometers, Detectors and Associated Equipment*, vol. 506, p. 250303, July 2003.
- [77] C. Ay, A. Buckley, J. Butterworth, J. Ferland, I. Hinchliffe, O. Jinnouchi, J. Katzy, B. Kersevan, E. Lobodzinska, J. Monk, Z. Qin, V. Savinov, and J. Schumacher, “Monte carlo generators in atlas software,” *Journal of Physics: Conference Series*, vol. 219, p. 032001, Apr. 2010.
- [78] T. Sjstrand, S. Ask, J. R. Christiansen, R. Corke, N. Desai, P. Ilten, S. Mrenna, S. Prestel, C. O. Rasmussen, and P. Z. Skands, “An introduction to pythia 8.2,” *Computer Physics Communications*, vol. 191, p. 159177, June 2015.

- [79] G. Marchesini, B. Webber, G. Abbiendi, I. Knowles, M. Seymour, and L. Stanco, “HERWIG version 5.9,” tech. rep., CERN, Geneva, 1996.
- [80] T. Jeo, M. Klasen, and A. Neuwirth, “Prompt photon production with two jets in powheg,” 2024.
- [81] T. Gleisberg, S. Hche, F. Krauss, M. Schnherr, S. Schumann, F. Siegert, and J. Winter, “Event generation with sherpa 1.1,” *Journal of High Energy Physics*, vol. 2009, p. 007007, Feb. 2009.
- [82] J. Alwall, M. Herquet, F. Maltoni, O. Mattelaer, and T. Stelzer, “Madgraph 5: going beyond,” *Journal of High Energy Physics*, vol. 2011, June 2011.
- [83] S. Dulat, T.-J. Hou, J. Gao, M. Guzzi, J. Huston, P. Nadolsky, J. Pumplin, C. Schmidt, D. Stump, and C.-P. Yuan, “New parton distribution functions from a global analysis of quantum chromodynamics,” *Physical Review D*, vol. 93, Feb. 2016.
- [84] T. N. Collaboration, R. D. Ball, A. Barontini, A. Candido, S. Carrazza, J. Cruz-Martinez, L. D. Debbio, S. Forte, T. Giani, F. Hekhorn, Z. Kassabov, N. Laurenti, G. Magni, E. R. Nocera, T. R. Rabemananjara, J. Rojo, C. Schwan, R. Stegeman, and M. Ubiali, “The path to n³lo parton distributions,” 2024.
- [85] A. D. Martin, W. J. Stirling, R. S. Thorne, and G. Watt, “Parton distributions for the lhc,” *The European Physical Journal C*, vol. 63, p. 189285, July 2009.
- [86] L. A. Harland-Lang, A. D. Martin, P. Motylinski, and R. S. Thorne, “Parton distributions in the lhc era: Mmht 2014 pdfs,” *The European Physical Journal C*, vol. 75, May 2015.
- [87] J. Allison, “Geant4 developments and applications,” *IEEE Trans. Nucl. Sci.*, vol. 53, p. 270, 2006.
- [88] T. S. Virdee, “Physics requirements for the design of the atlas and cms experiments at the large hadron collider,” *Philosophical Transactions of the Royal Society A: Mathematical, Physical and Engineering Sciences*, vol. 370, p. 876891, Feb. 2012.
- [89] W. Lukas, “Fast Simulation for ATLAS: Atlfast-II and ISF,” tech. rep., CERN, Geneva, 2012.
- [90] Z. Marshall, “Simulation of pile-up in the atlas experiment,” *Journal of Physics: Conference Series*, vol. 513, p. 022024, June 2014.
- [91] “Constituent-level pile-up mitigation techniques in ATLAS,” tech. rep., CERN, Geneva, 2017. All figures including auxiliary figures are available

at <https://atlas.web.cern.ch/Atlas/GROUPS/PHYSICS/CONFNOTES/ATLAS-CONF-2017-065>.

- [92] J. Adelman, L. Ancu, A. Annovi, J. Baines, D. Britzger, W. Ehrenfeld, P. Giannetti, C. Luongo, C. Pandini, S. Schmitt, G. Stewart, L. Tompkins, A. Vaniachine, and G. Volpi, “Atlas ftk challenge: Simulation of a billion-fold hardware parallelism,” *Procedia Computer Science*, vol. 66, pp. 540–545, 12 2015.
- [93] F. Meloni, “Track and vertex reconstruction in the ATLAS experiment,” tech. rep., CERN, Geneva, 2012.
- [94] T. Cornelissen, M. Elsing, I. Gavrilenko, W. Liebig, E. Moyse, and A. Salzburger, “The new atlas track reconstruction (newt),” *Journal of Physics: Conference Series*, vol. 119, p. 032014, July 2008.
- [95] R. Fruhwirth, “Application of Kalman filtering to track and vertex fitting,” *Nucl. Instrum. Meth. A*, vol. 262, pp. 444–450, 1987.
- [96] G. Borissov, D. W. Casper, K. Grimm, S. Pagan Griso, L. E. Pedersen, K. Prokofiev, M. S. Rudolph, and A. M. Wharton, “ATLAS strategy for primary vertex reconstruction during Run-2 of the LHC,” Tech. Rep. 7, CERN, Geneva, 2015.
- [97] “Characterization of Interaction-Point Beam Parameters Using the pp Event-Vertex Distribution Reconstructed in the ATLAS Detector at the LHC,” tech. rep., CERN, Geneva, 2010. All figures including auxiliary figures are available at <https://atlas.web.cern.ch/Atlas/GROUPS/PHYSICS/CONFNOTES/ATLAS-CONF-2010-027>.
- [98] W. Lampl, S. Laplace, D. Lelas, P. Loch, H. Ma, S. Menke, S. Rajagopalan, D. Rousseau, S. Snyder, and G. Unal, “Calorimeter Clustering Algorithms: Description and Performance,” tech. rep., CERN, Geneva, 2008. All figures including auxiliary figures are available at <https://atlas.web.cern.ch/Atlas/GROUPS/PHYSICS/PUBNOTES/ATL-LARG-PUB-2008-002>.
- [99] A. Collaboration, “Electron and photon efficiencies in LHC Run 2 with the ATLAS experiment,” *JHEP*, vol. 2405, p. 162, 2024.
- [100] A. Collaboration, “Muon reconstruction performance of the atlas detector in proton-proton collision data at $\sqrt{s} = 13\text{TeV}$,” *The European Physical Journal C*, vol. 76, May 2016.

- [101] A. Schwartzman, “Jet tutorial.” https://indico.cern.ch/event/429853/contributions/1907847/attachments/926770/1311913/Jet_Tutorial.pdf, 2015. ATLAS Induction Day, CERN, 2015.
- [102] M. Cacciari, G. P. Salam, and G. Soyez, “The anti-ktjet clustering algorithm,” *Journal of High Energy Physics*, vol. 2008, p. 063063, Apr. 2008.
- [103] A. Collaboration, “Jet reconstruction and performance using particle flow with the atlas detector,” *The European Physical Journal C*, vol. 77, July 2017.
- [104] “Improving jet substructure performance in ATLAS using Track-CaloClusters,” tech. rep., CERN, Geneva, 2017. All figures including auxiliary figures are available at <https://atlas.web.cern.ch/Atlas/GROUPS/PHYSICS/PUBNOTES/ATL-PHYS-PUB-2017-015>.
- [105] “Optimisation of large-radius jet reconstruction for the ATLAS detector in 13 TeV proton-proton collisions,” tech. rep., CERN, Geneva, 2020. All figures including auxiliary figures are available at <https://atlas.web.cern.ch/Atlas/GROUPS/PHYSICS/CONFNOTES/ATLAS-CONF-2020-021>.
- [106] P. Berta, M. Spousta, D. W. Miller, and R. Leitner, “Particle-level pileup subtraction for jets and jet shapes,” *Journal of High Energy Physics*, vol. 2014, June 2014.
- [107] M. Cacciari, G. P. Salam, and G. Soyez, “Softkiller, a particle-level pileup removal method,” *The European Physical Journal C*, vol. 75, Feb. 2015.
- [108] A. J. Larkoski, S. Marzani, G. Soyez, and J. Thaler, “Soft drop,” *Journal of High Energy Physics*, vol. 2014, May 2014.
- [109] “Expected performance of missing transverse momentum reconstruction for the ATLAS detector at $\sqrt{s} = 13$ TeV,” tech. rep., CERN, Geneva, 2015. All figures including auxiliary figures are available at <https://atlas.web.cern.ch/Atlas/GROUPS/PHYSICS/PUBNOTES/ATL-PHYS-PUB-2015-023>.
- [110] M. Borodin, K. De, J. E. Garca Navarro, D. Golubkov, A. Klimentov, T. Maeno, and A. Vaniachine, “Scaling up ATLAS production system for the LHC Run 2 and beyond: project ProdSys2,” Tech. Rep. 6, CERN, Geneva, 2015.
- [111] *ATLAS Computing: technical design report*. Technical design report. ATLAS, Geneva: CERN, 2005.

- [112] P. Van Gemmeren, A. S. Mete, M. J. Nowak, J. Catmore, J. C. Burzynski, N. E. Krumnack, and L. A. Heinrich, “Framework for custom event sample augmentations for ATLAS analysis data,” tech. rep., CERN, Geneva, 2024.
- [113] J. Schaarschmidt, J. Catmore, J. Elmsheuser, L. A. Heinrich, N. E. Krumnack, A. S. Mete, and N. Ozturk, “PHYSLITE - A new reduced common data format for ATLAS,” tech. rep., CERN, Geneva, 2023.
- [114] K. Koneke and (for the ATLAS Collaboration), “Distributing and storing data efficiently by means of special datasets in the atlas collaboration,” *Journal of Physics: Conference Series*, vol. 331, p. 032018, dec 2011.
- [115] R. Brun, F. Rademakers, P. Canal, A. Naumann, O. Couet, L. Moneta, V. Vassilev, S. Linev, D. Piparo, G. GANIS, B. Bellenot, E. Guiraud, G. Amadio, Wverkerke, P. Mato, TimurP, Matev Tadel, Wlav, E. Tejedor, J. Blomer, A. Gheata, S. Hageboeck, S. Roiser, Marsupial, S. Wunsch, O. Shadura, Anirudha Bose, CristinaCristescu, X. Valls, and R. Iseman, “root-project/root: v6.18/02,” 2019.
- [116] “Identification of hadronically-decaying top quarks using UFO jets with ATLAS in Run 2,” tech. rep., CERN, Geneva, 2021. All figures including auxiliary figures are available at <https://atlas.web.cern.ch/Atlas/GROUPS/PHYSICS/PUBNOTES/ATL-PHYS-PUB-2021-028>.
- [117] S. Marzani, G. Soyez, and M. Spannowsky, *Looking Inside Jets: An Introduction to Jet Substructure and Boosted-object Phenomenology*. Springer International Publishing, 2019.
- [118] C. F. Berger, T. Kcs, and G. Sterman, “Event shapeenergy flow correlations,” *Physical Review D*, vol. 68, July 2003.
- [119] A. Collaboration, “Measurement of k t splitting scales in w events at $\sqrt{s} = 7$ TeV with the atlas detector,” *The European Physical Journal C*, vol. 73, May 2013.
- [120] A. J. Larkoski, G. P. Salam, and J. Thaler, “Energy correlation functions for jet substructure,” *Journal of High Energy Physics*, vol. 2013, June 2013.
- [121] A. Collaboration, “Atlas measurements of the properties of jets for boosted particle searches,” *Physical Review D*, vol. 86, Oct. 2012.
- [122] L. Spiller, “Modification of fox-wolfram moments for hadron colliders,” *Journal of High Energy Physics*, vol. 2016, Mar. 2016.
- [123] J. Thaler and L.-T. Wang, “Strategies to identify boosted tops,” *Journal of High Energy Physics*, vol. 2008, p. 092092, July 2008.

- [124] C. Chen, “New approach to identifying boosted hadronically decaying particles using jet substructure in its center-of-mass frame,” *Physical Review D*, vol. 85, Feb. 2012.
- [125] “Boosted hadronic vector boson and top quark tagging with ATLAS using Run 2 data,” tech. rep., CERN, Geneva, 2020. All figures including auxiliary figures are available at <https://atlas.web.cern.ch/Atlas/GROUPS/PHYSICS/PUBNOTES/ATL-PHYS-PUB-2020-017>.
- [126] M. Das-Gupta and G. P. Salam, “Event shapes in e+e- annihilation and deep inelastic scattering,” *J. Phys. G*, vol. 30, p. 143, 2004.
- [127] L. G. Almeida, S. J. Lee, G. Perez, I. Sung, and J. Virzi, “Top quark jets at the lhc,” *Phys. Rev. D*, vol. 79, p. 074012, Apr 2009.
- [128] A. Collaboration, “Atlas measurements of the properties of jets for boosted particle searches,” *Phys. Rev. D*, vol. 86, p. 072006, Oct 2012.
- [129] C. Chen, “New approach to identifying boosted hadronically decaying particles using jet substructure in its center-of-mass frame,” *Phys. Rev. D*, vol. 85, p. 034007, Feb 2012.
- [130] J. Thaler and L.-T. Wang, “Strategies to identify boosted tops,” *Journal of High Energy Physics*, vol. 2008, p. 092, jul 2008.
- [131] S. Catani, Y. L. Dokshitzer, M. H. Seymour, and B. R. Webber, “Longitudinally-invariant k_{\perp} -clustering algorithms for hadron-hadron collisions,” *Nucl. Phys. B*, vol. 406, pp. 187–224, 1993.
- [132] G. Cowan, *Statistical data analysis*. Oxford university press, 1998.
- [133] A. Collaboration, “Search for ww/wz resonance production in qq final states in pp collisions at $\sqrt{s} = 13$ tev with the atlas detector,” *Journal of High Energy Physics*, vol. 2018, Mar. 2018.
- [134] A. Collaboration, “Searches for heavy zz and zw resonances in the qq and qq final states in pp collisions at $\sqrt{s} = 13$ tev with the atlas detector,” *Journal of High Energy Physics*, vol. 2018, Mar. 2018.
- [135] A. Collaboration, “Search for heavy diboson resonances in semileptonic final states in pp collisions at $\sqrt{s} = 13$ tev with the atlas detector,” *The European Physical Journal C*, vol. 80, Dec. 2020.
- [136] A. Collaboration, “Search for new resonances decaying to a w or z boson and a higgs boson in the +bb, bb, and bb channels with pp collisions at $\sqrt{s} = 13$ tev with the atlas detector,” *Physics Letters B*, vol. 765, p. 3252, Feb. 2017.

- [137] A. Collaboration, “Search for heavy resonances decaying into a w or z boson and a higgs boson in final states with leptons and b-jets in 36 fb1 of $\sqrt{s} = 13$ tev pp collisions with the atlas detector,” *Journal of High Energy Physics*, vol. 2018, Mar. 2018.
- [138] A. Collaboration, “Search for heavy resonances decaying into a z or w boson and a higgs boson in final states with leptons and b-jets in 139 fb1 of pp collisions at $\sqrt{s} = 13$ tev with the atlas detector,” *Journal of High Energy Physics*, vol. 2023, June 2023.
- [139] C. Collaboration, “Search for heavy resonances decaying to ww, wz, or wh boson pairs in a final state consisting of a lepton and a large-radius jet in proton-proton collisions at $\sqrt{s} = 13$ tev,” *Physical Review D*, vol. 105, Feb. 2022.
- [140] C. Collaboration, “Search for a heavy vector resonance decaying to a z boson and a higgs boson in proton-proton collisions at $\sqrt{s} = 13$ tev,” *The European Physical Journal C*, vol. 81, Aug. 2021.
- [141] D. Pappadopulo, A. Thamm, R. Torre, and A. Wulzer, “Heavy vector triplets: bridging theory and data,” *Journal of High Energy Physics*, vol. 2014, 9 2014.
- [142] W. D. Goldberger and M. B. Wise, “Modulus stabilization with bulk fields,” *Physical Review Letters*, vol. 83, pp. 4922–4925, 12 1999.
- [143] W. D. Goldberger and M. B. Wise, “Phenomenology of a stabilized modulus,” *Physics Letters B*, vol. 475, pp. 275 – 279, 3 2000.
- [144] A. Alloul, N. D. Christensen, C. Degrande, C. Duhr, and B. Fuks, “Feynrules 2.0 a complete toolbox for tree-level phenomenology,” *Computer Physics Communications*, vol. 185, pp. 2250–2300, 8 2014.
- [145] A. Collaboration, “Optimisation of large-radius jet reconstruction for the atlas detector in 13 tev proton-proton collisions,” *The European Physical Journal C*, vol. 81, Apr. 2021.
- [146] A. Collaboration, “Luminosity determination in pp collisions at
- $$\sqrt{s} = 13$$
- tev using the atlas detector at the lhc,” *The European Physical Journal C*, vol. 83, Oct. 2023.
- [147] A. Collaboration, “Measurement of the inelastic proton-proton cross section at
- $$\sqrt{s} = 13$$
- tev with the atlas detector at the lhc,” *Physical Review Letters*, vol. 117, Oct. 2016.

- [148] A. Collaboration, “Electron and photon performance measurements with the atlas detector using the 20152017 lh proton-proton collision data,” *Journal of Instrumentation*, vol. 14, p. P12006P12006, Dec. 2019.
- [149] “Electron and photon reconstruction and performance in ATLAS using a dynamical, topological cell clustering-based approach,” tech. rep., CERN, Geneva, 2017. All figures including auxiliary figures are available at <https://atlas.web.cern.ch/Atlas/GROUPS/PHYSICS/PUBNOTES/ATL-PHYS-PUB-2017-022>.
- [150] A. Collaboration, “Performance of missing transverse momentum reconstruction with the atlas detector using proton-proton collisions at
- $$\sqrt{s} = 13 \text{ TeV}$$
- = 13 tev,” *The European Physical Journal C*, vol. 78, Nov. 2018.
- [151] A. Collaboration, “Jet energy scale measurements and their systematic uncertainties in proton-proton collisions at $\sqrt{s} = 13$ tev with the atlas detector,” *Physical Review D*, vol. 96, Oct. 2017.
- [152] A. Collaboration, “In situ calibration of large-radius jet energy and mass in $\sqrt{s} = 13$ tev proton-proton collisions with the atlas detector,” *The European Physical Journal C*, vol. 79, Feb. 2019.
- [153] A. Collaboration, “Atlas b-jet identification performance and efficiency measurement with
- $$t\bar{t}$$
- events in pp collisions at
- $$\sqrt{s} = 13$$
- tev,” *The European Physical Journal C*, vol. 79, Nov. 2019.
- [154] “Measurement of b -tagging Efficiency of c -jets in $t\bar{t}$ Events Using a Likelihood Approach with the ATLAS Detector,” tech. rep., CERN, Geneva, 2018. All figures including auxiliary figures are available at <https://atlas.web.cern.ch/Atlas/GROUPS/PHYSICS/CONFNOTES/ATLAS-CONF-2018-001>.
- [155] “Calibration of light-flavour b -jet mistagging rates using ATLAS proton-proton collision data at $\sqrt{s} = 13$ TeV,” tech. rep., CERN, Geneva, 2018. All figures including auxiliary figures are available at <https://atlas.web.cern.ch/Atlas/GROUPS/PHYSICS/CONFNOTES/ATLAS-CONF-2018-006>.

- [156] J. M. Campbell, R. K. Ellis, and C. Williams, “Vector boson pair production at the lhc,” *Journal of High Energy Physics*, vol. 2011, July 2011.
- [157] T. Gleisberg, S. Höche, F. Krauss, M. Schönherr, S. Schumann, F. Siegert, and J. Winter, “Event generation with sherpa 1.1,” *Journal of High Energy Physics*, vol. 2009, p. 007007, Feb. 2009.
- [158] A. L. Read, “Presentation of search results: theclstechnique,” *Journal of Physics G: Nuclear and Particle Physics*, vol. 28, p. 26932704, Sept. 2002.

APPENDIX A. $t\bar{t}$ SF tables

ANN Results

Signal efficiency as a function of leading large-R jet p_t for the ANN W-tagger is shown in Figure A.1 for the 60%, 70%, and 90% WPs. Figure A.2 show the nominal SF values for the ANN W-tagger along with the total statistical uncertainty and total statistical plus systematic uncertainties.

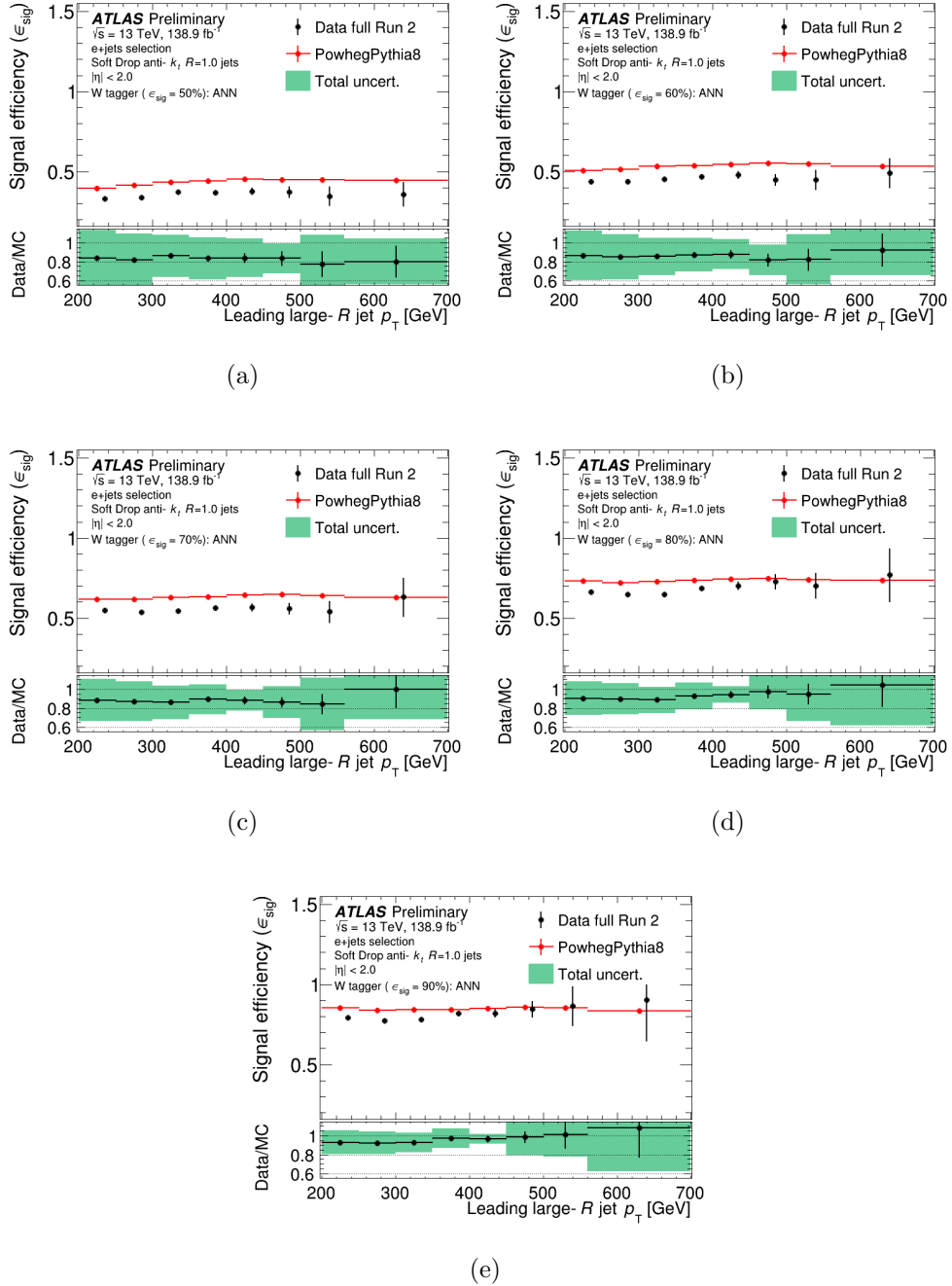


Figure A.1: Signal efficiency and data-to-MC scale factors for the ANN W-tagger as a function of the leading large- R jet transverse momentum (p_T) in $t\bar{t}$ events in the semileptonic final state. Each subplot corresponds to a different ANN tagging working point: (a) 50%, (b) 60%, (c) 70%, (d) 80%, and (e) 90%, defined by the expected signal efficiency on simulated events. The green bands represent the total systematic and statistical uncertainty. The bottom panel of each plot shows the ratio of data to simulation (Data/MC).

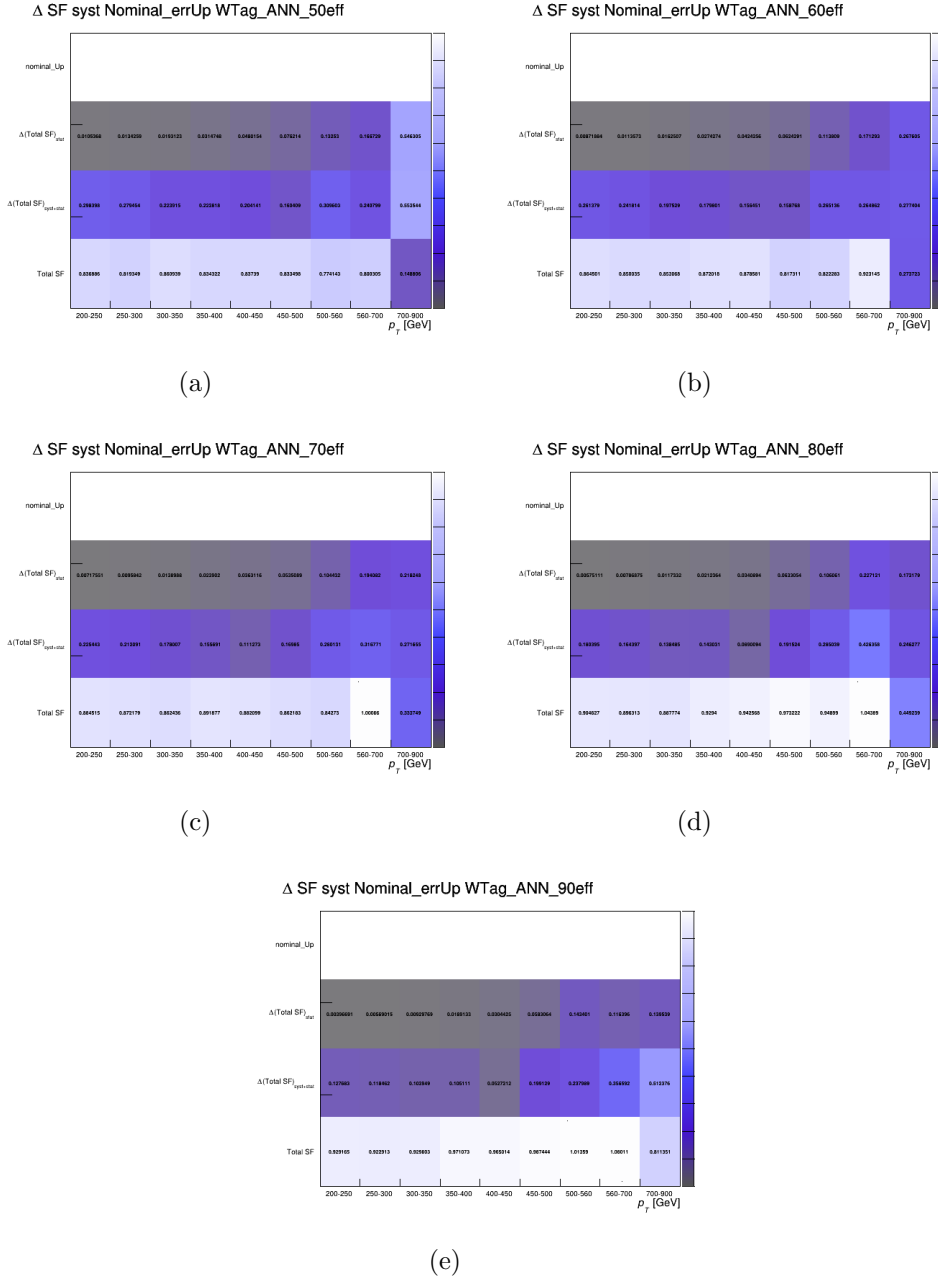


Figure A.2: Nominal SF values and systematic uncertainties on the W-tagger scale factors for the ANN-based tagger across various signal efficiency working points: (a) 50%, (b) 60%, (c) 70%, (d) 80%, and (e) 90%. Each heatmap shows the upward variation of the scale factor due to combined systematic effects, binned in leading large-R jet transverse momentum (p_T) and lepton channel (electron or muon).

APPENDIX B. Previous Cuts for VV+VH

Historically, VV and VH were separate analyses. This analysis combines the efforts of both VV+VH into one joint analysis. During optimization of the 0-lepton channel, cuts applied in both VV+VH were considered, combined, and reduced. The cuts applied when VV and VH were considered separate analyses are presented in Table B.1 for VV and Table B.2 for VH.

Selection	SR		CR	
	HP	LP	HP	LP
Number of Loose leptons	0			
E_T^{miss}	> 250 GeV			
p_T^{miss}	> 50 GeV			
$\min(\Delta\Phi(E_T^{miss}, \text{small-R jets}))$	> 0.4			
$\Delta\Phi(E_T^{miss}, p_T^{miss})$	< 1			
Number of large-R jets	≥ 1 large-R jets			
D_2 cut	pass	fail	pass	fail
W/Z mass window cut	pass	pass	$m_J > 50$ GeV, fail mass window cut	
Numb. of associated VR track jets b -tagged	For $Z \rightarrow J$: ≤ 1 ($= 2$) for untagged (tagged) category			

Table B.1: A summary of signal region selection requirements used in the previous iteration of the VV resonance search. These regions are split into VBF and ggF(DY) categories.

Variable	Resolved	Merged
Common selection		
Number of jets	≥ 2 small- R jets (0, 2-lep.) 2 or 3 $R = 0.4$ jets (1-lep.)	≥ 1 large- R jet ≥ 2 VR track jets (matched to leading $R = 1.0$ jet) ^{‡‡}
Leading jet p_T [GeV]	> 45	> 250
m_h [GeV]	110–140 (0,1-lep.), 100–145 (2-lep.)	75–145
0-lepton selection		
E_T^{miss} [GeV]	> 150	> 200
H_T [GeV]	> 150 (120 [*])	–
$\Delta\phi_{bb}$	$< 7\pi/9$	–
p_T^{miss} [GeV]		> 60
$\Delta\phi(\vec{E}_T^{miss}, \vec{p}_T^{miss})$		$< \pi/2$
$\Delta\phi(\vec{E}_T^{miss}, H)$		$> 2\pi/3$
$\min[\Delta\phi(E_T^{miss}, R = 0.4\text{jet})]$		$> \pi/9$ (2 or 3 jets), $> \pi/6$ (≥ 4 jets)
$N_{\tau\text{had}}$		0 ^{**}
MET Significance		$\begin{cases} > 9 & \text{if } m_{Vh} < 240, \\ > 6.6 + 0.01 \cdot m_{Vh} & \text{if } 240 < m_{Vh} < 700, \\ > 13.6 & \text{if } m_{Vh} > 700, \end{cases}$
1-lepton selection		
Leading lepton p_T [GeV]	> 27	> 27
E_T^{miss} [GeV]	> 40 (80 [†])	> 100
$p_{T,W}$ [GeV]	$> \max[150, 710 - (3.3 \times 10^5 \text{ GeV})/m_{Vh}]$	$> \max[150, 394 \cdot \ln(m_{Vh}/(1 \text{ GeV})) - 2350]$
$m_{T,W}$ [GeV]		≥ 300
2-lepton selection		
Leading lepton p_T [GeV]	> 27	> 27
Sub-leading lepton p_T [GeV]	> 20	> 25
$E_T^{miss}/\sqrt{H_T}$ [$\sqrt{\text{GeV}}$]		$< 1.15 + 8 \times 10^{-3} \cdot m_{Vh}/(1 \text{ GeV})$
$p_{T,\ell\ell}$ [GeV]		$> 20 + 9 \cdot \sqrt{m_{Vh}/(1 \text{ GeV})} - 320$ ^{††}
$m_{\ell\ell}$ [GeV]		$[\max[40 \text{ GeV}, 87 - 0.030 \cdot m_{Vh}/(1 \text{ GeV})], 97 + 0.013 \cdot m_{Vh}/(1 \text{ GeV})]$

Table B.2: A summary of the signal region selection requirements used in the previous iteration of the VH resonance search. These regions are split into merged and resolved categories.

APPENDIX C. Data/MC Plots

This section shows the MC to data agreement of various kinematic variables in a subset of the regions explored in the analysis for the 1-lepton and 2-lepton channels.

C.0.1 Modelling in 1-lepton Control regions

C.0.2 Modelling in 2-lepton Control regions

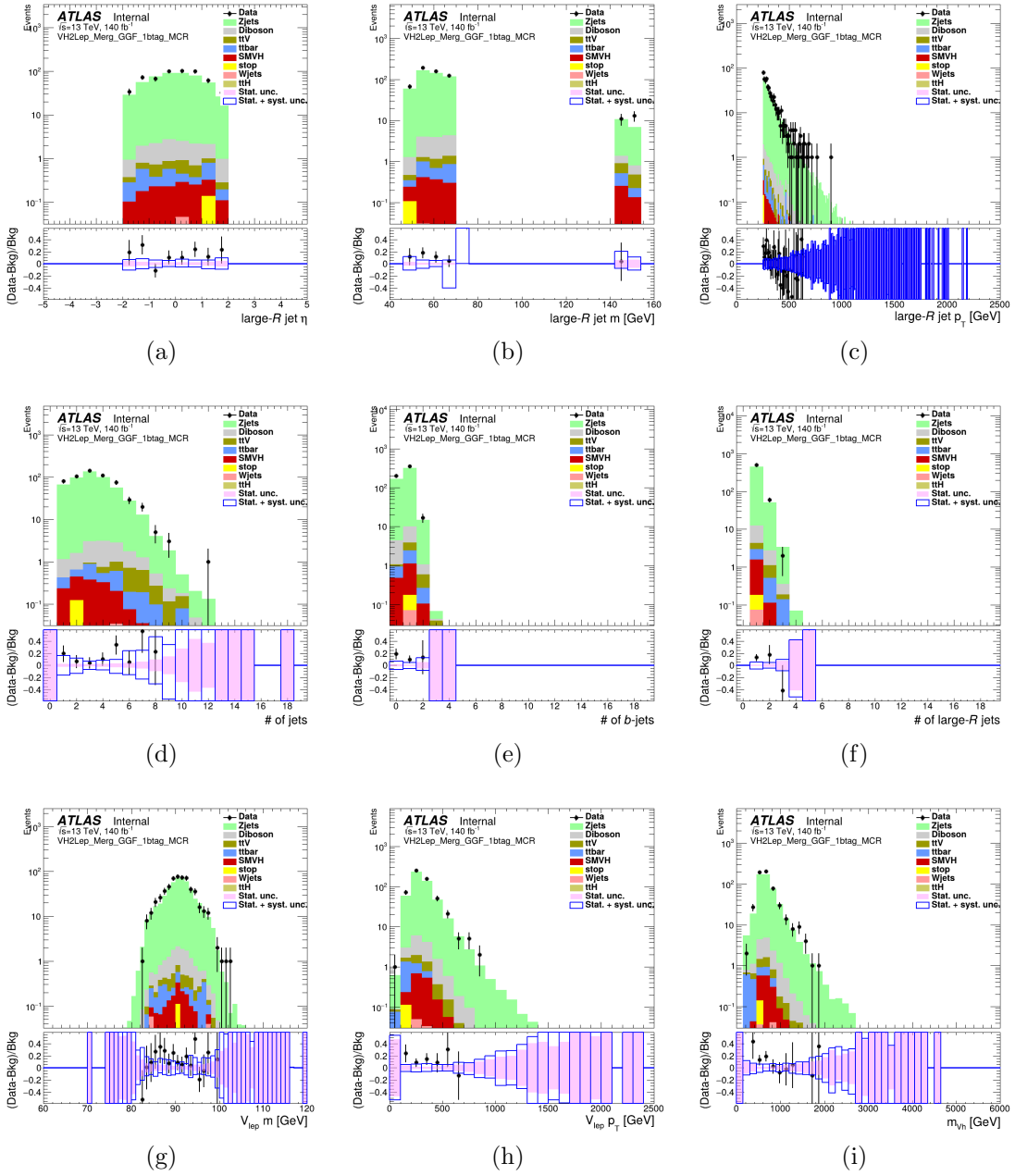


Figure C.1: Comparisons of the observed data and the expected background distributions of various kinematic variables in the MCR of the 2-lepton channel for the VH merged region, 0/1 b-tagged, with ggF production. The bottom panes show the ratios of the observed data to the background predictions. The blue boxes represent the uncertainties in the total background predictions, combining statistical and systematic contributions.

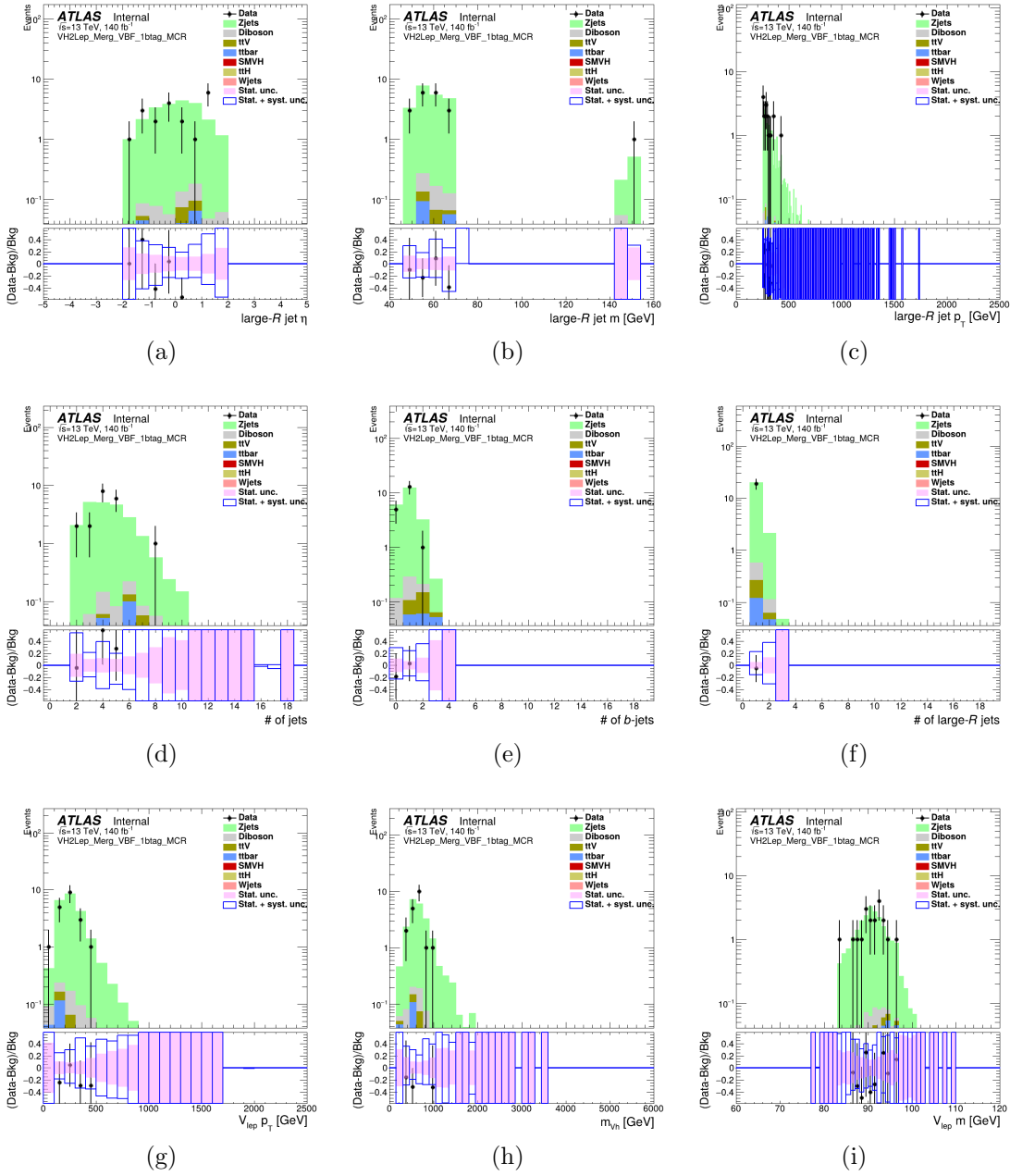


Figure C.2: Comparisons of the observed data and the expected background distributions of various kinematic variables in the MCR of the 2-lepton channel for the VH merged region, 0/1 b-tagged, with VBF production. The bottom panes show the ratios of the observed data to the background predictions. The blue boxes represent the uncertainties in the total background predictions, combining statistical and systematic contributions.

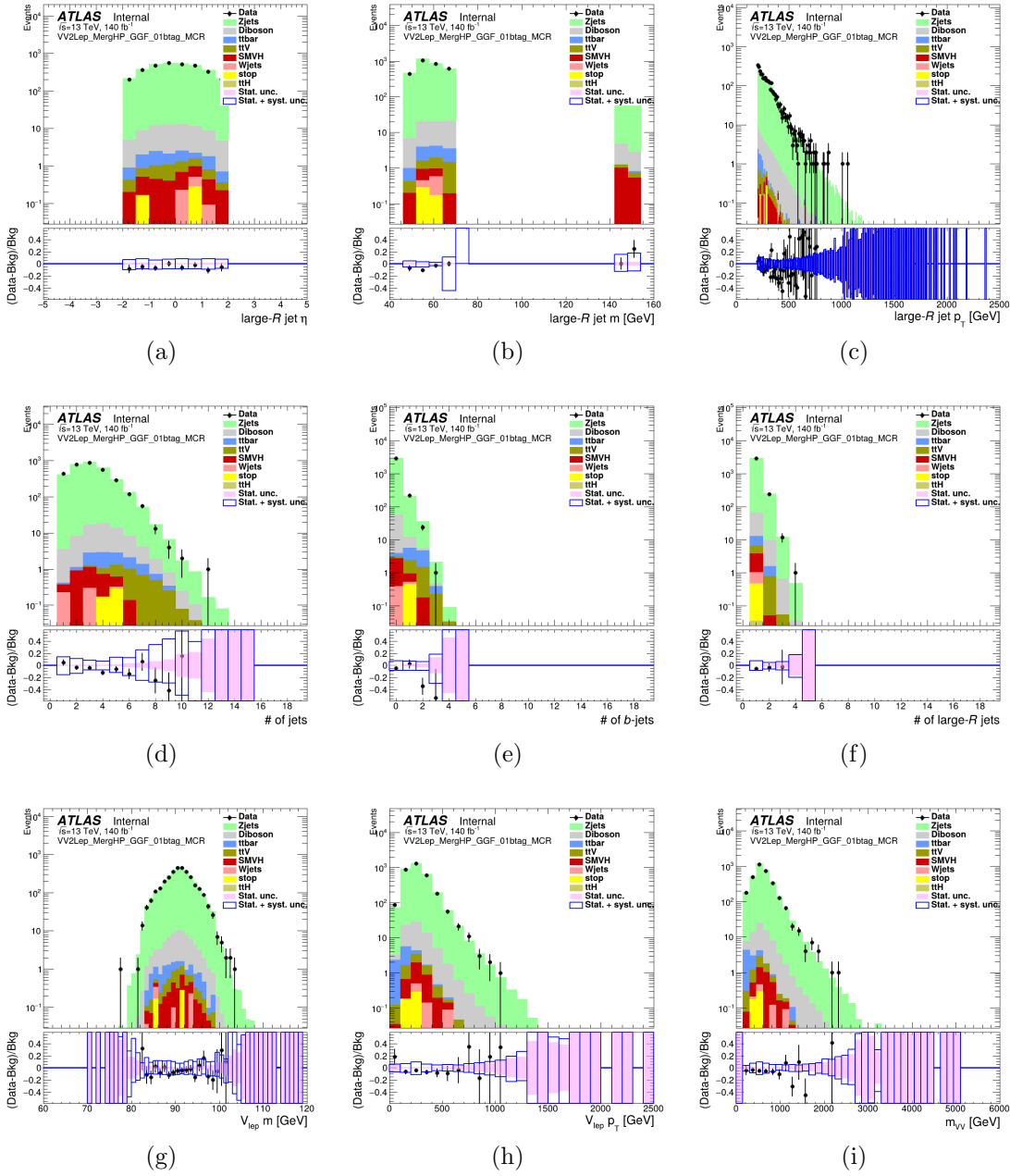


Figure C.3: Comparisons of the observed data and the expected background distributions of various kinematic variables in the MCR of the 2-lepton channel for the VV merged HP region, 0/1 b-tagged, with ggF production. The bottom panes show the ratios of the observed data to the background predictions. The blue boxes represent the uncertainties in the total background predictions, combining statistical and systematic contributions.

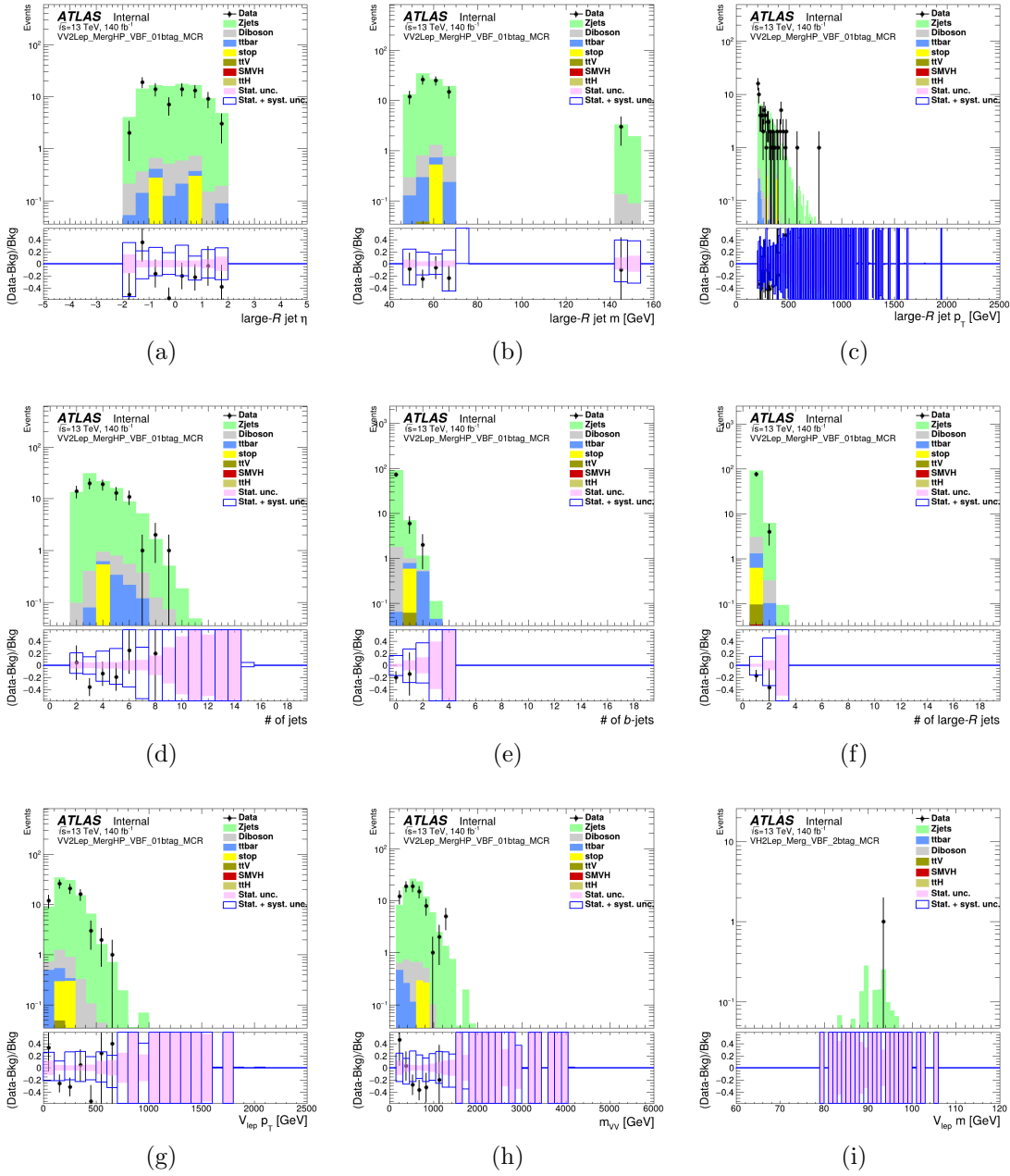


Figure C.4: Comparisons of the observed data and the expected background distributions of various kinematic variables in the MCR of the 2-lepton channel for the VV merged HP region, 0/1 b-tagged, with VBF production. The bottom panes show the ratios of the observed data to the background predictions. The blue boxes represent the uncertainties in the total background predictions, combining statistical and systematic contributions.

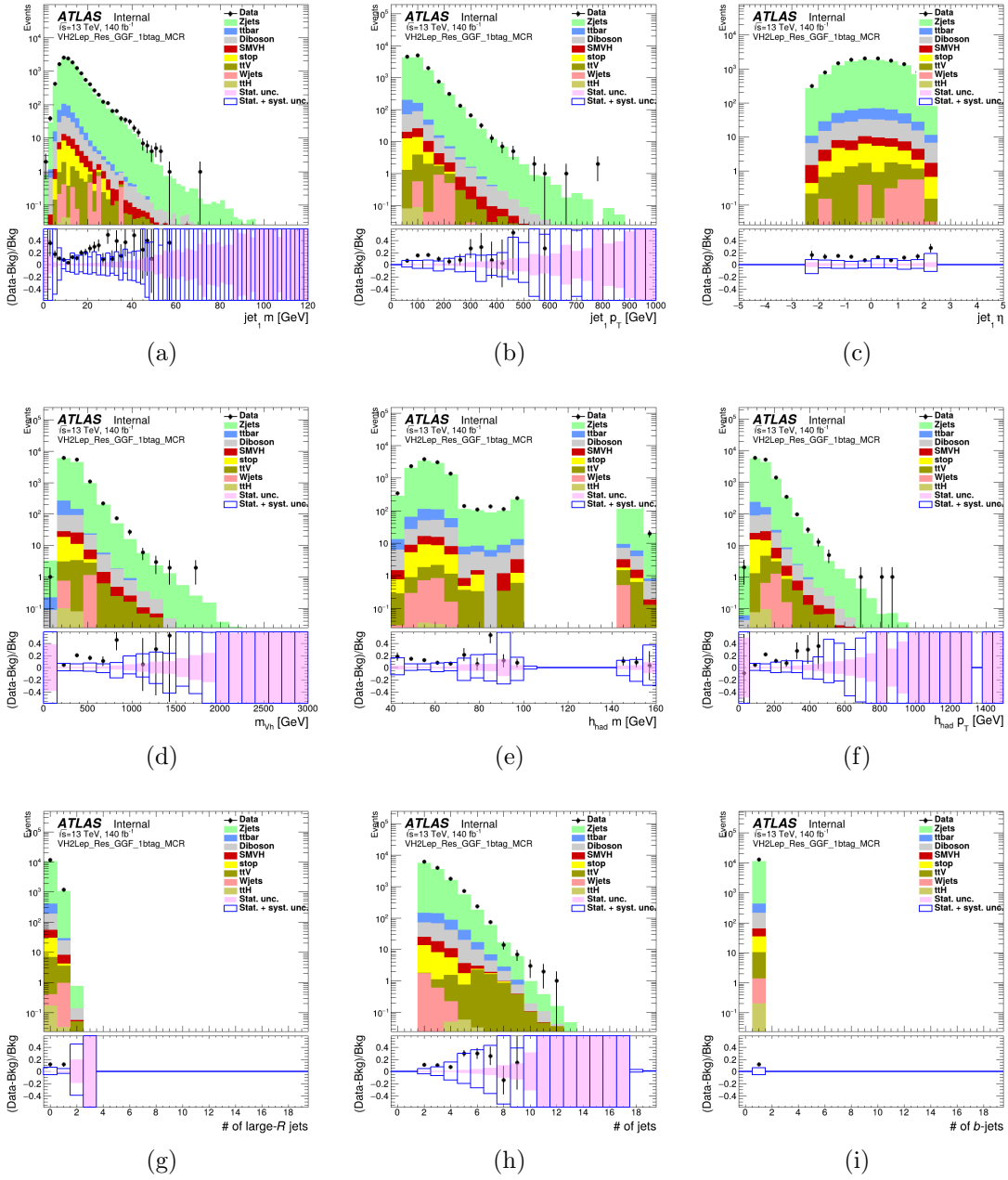


Figure C.5: Comparisons of the observed data and the expected background distributions of various kinematic variables in the MCR of the 2-lepton channel for the VH resolved region, 0/1 b-tagged, with ggF production. The bottom panes show the ratios of the observed data to the background predictions. The blue boxes represent the uncertainties in the total background predictions, combining statistical and systematic contributions.

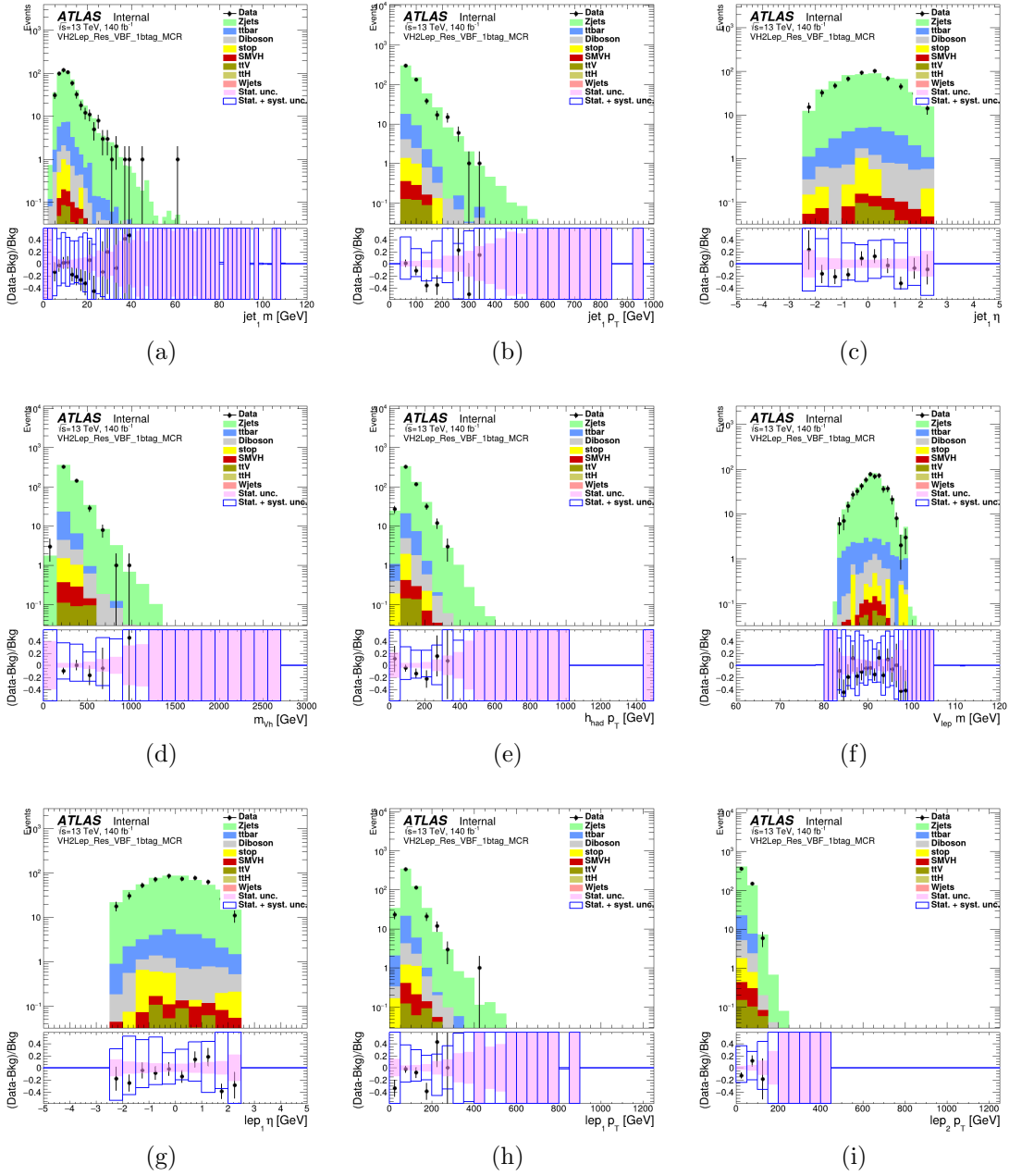


Figure C.6: Comparisons of the observed data and the expected background distributions of various kinematic variables in the MCR of the 2-lepton channel for the VH resolved region, 0/1 b-tagged, with VBF production. The bottom panes show the ratios of the observed data to the background predictions. The blue boxes represent the uncertainties in the total background predictions, combining statistical and systematic contributions.

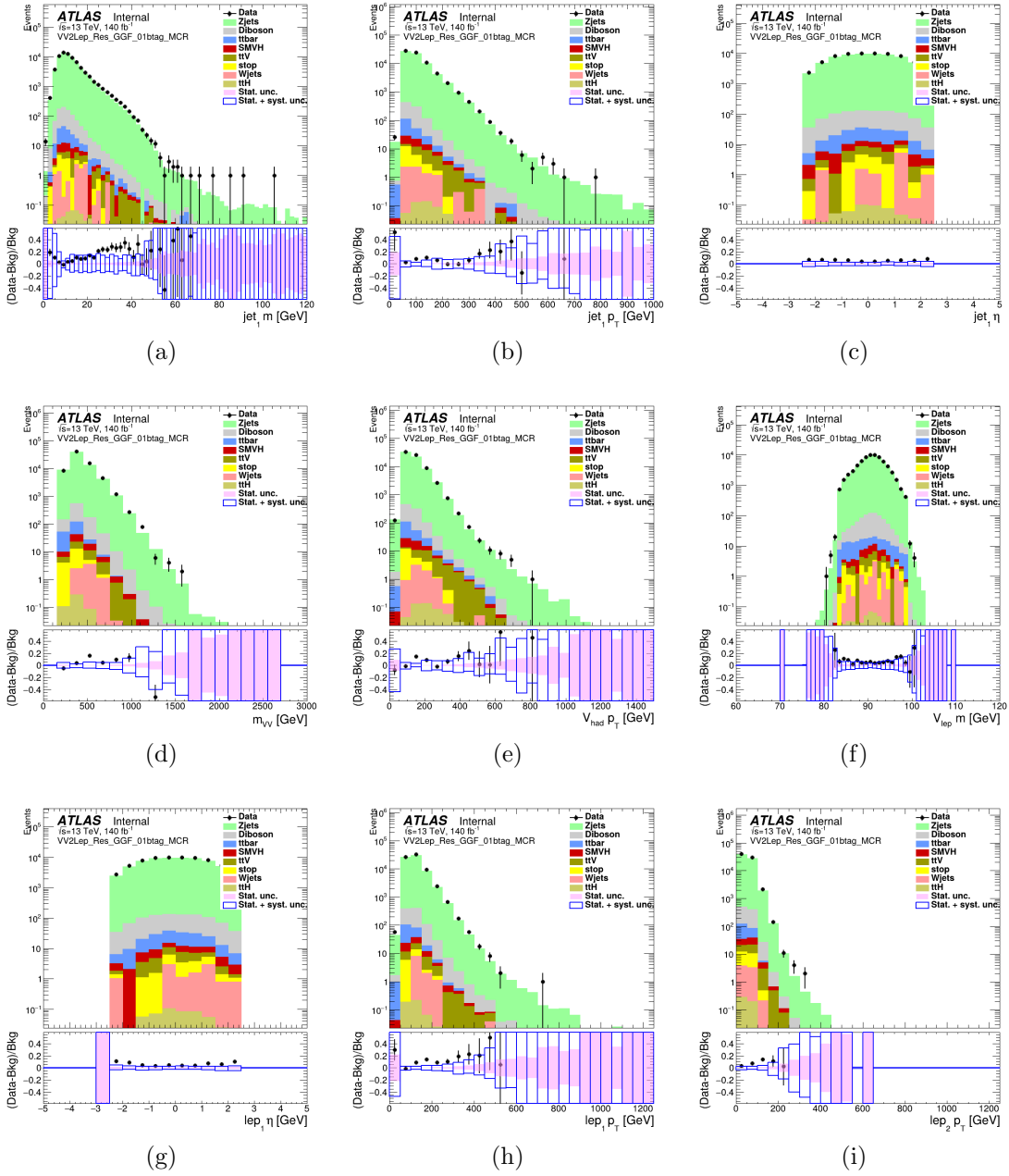


Figure C.7: Comparisons of the observed data and the expected background distributions of various kinematic variables in the MCR of the 2-lepton channel for the VV resolved region, 0/1 b-tagged, with ggF production. The bottom panes show the ratios of the observed data to the background predictions. The blue boxes represent the uncertainties in the total background predictions, combining statistical and systematic contributions.

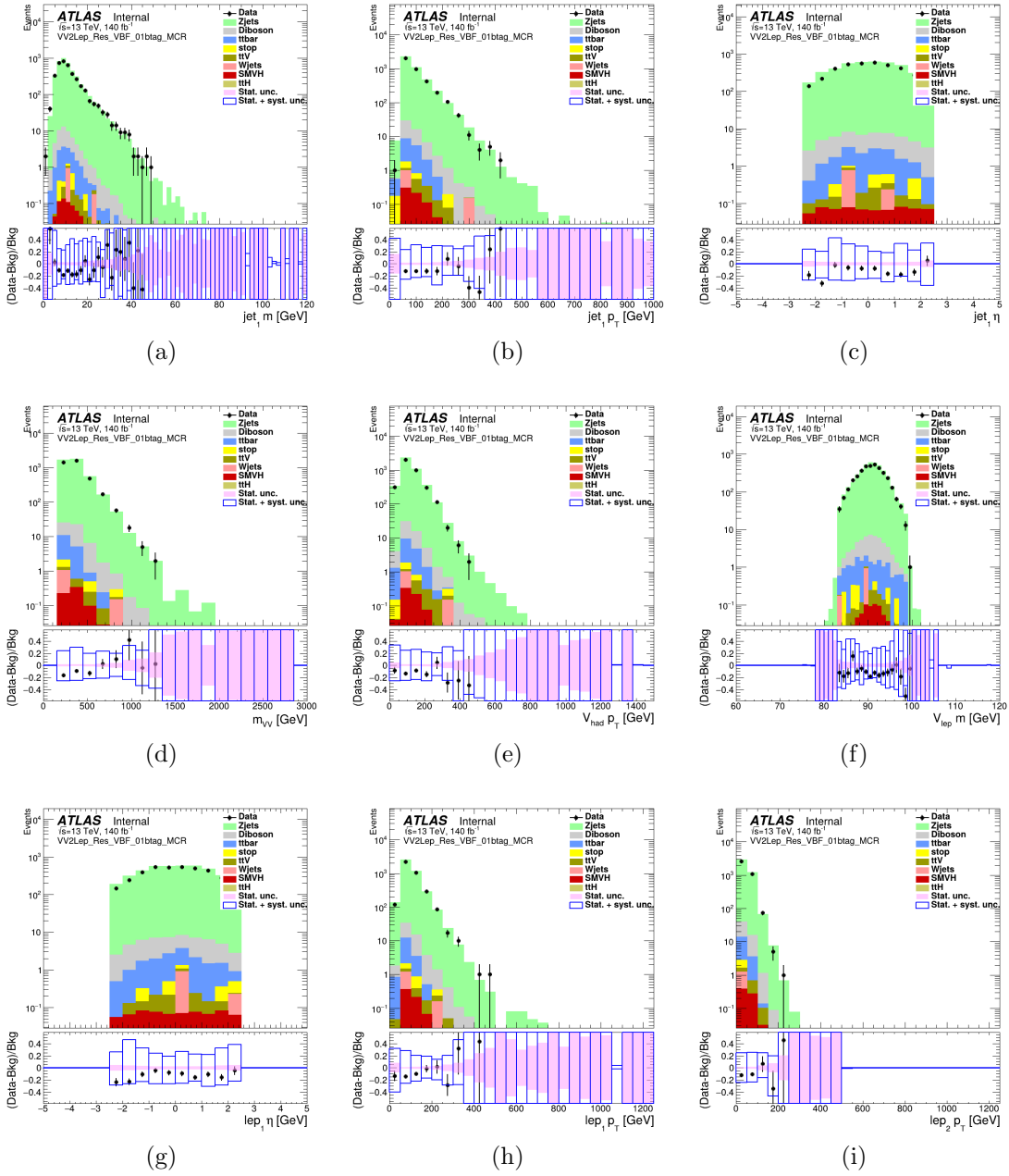


Figure C.8: Comparisons of the observed data and the expected background distributions of various kinematic variables in the MCR of the 2-lepton channel for the VV resolved region, 0/1 b-tagged, with VBF production. The bottom panes show the ratios of the observed data to the background predictions. The blue boxes represent the uncertainties in the total background predictions, combining statistical and systematic contributions.

C.0.3 Post-Fit Validation in Control Regions for 1-Lepton and 2-Lepton Channels

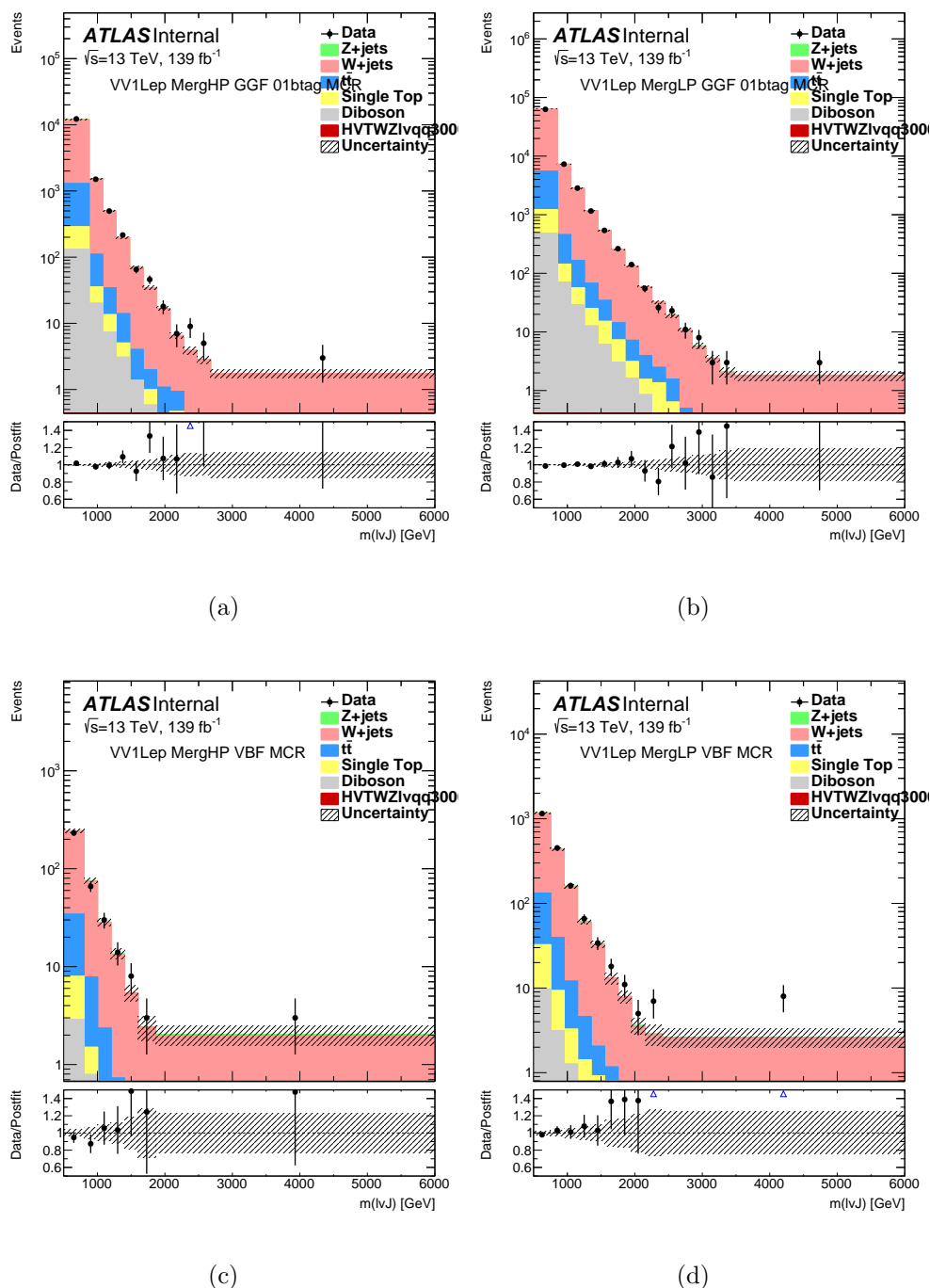


Figure C.9: Post-fit invariant mass distributions in the WZ signal regions of the VV 1-lepton channel, categorized by production mode and purity. Subfigures (a) and (b) show the ggF merged high-purity (HP) and low-purity (LP) MCR regions, and subfigures (c) and (d) display the VBF HP and LP MCR regions. Stacked histograms represent background predictions after the background-only fit to all WZ signal and control regions. Data points are overlaid, and the lower panels show the Data/Postfit ratio, with shaded bands indicating the total post-fit uncertainty, including both statistical and systematic components.

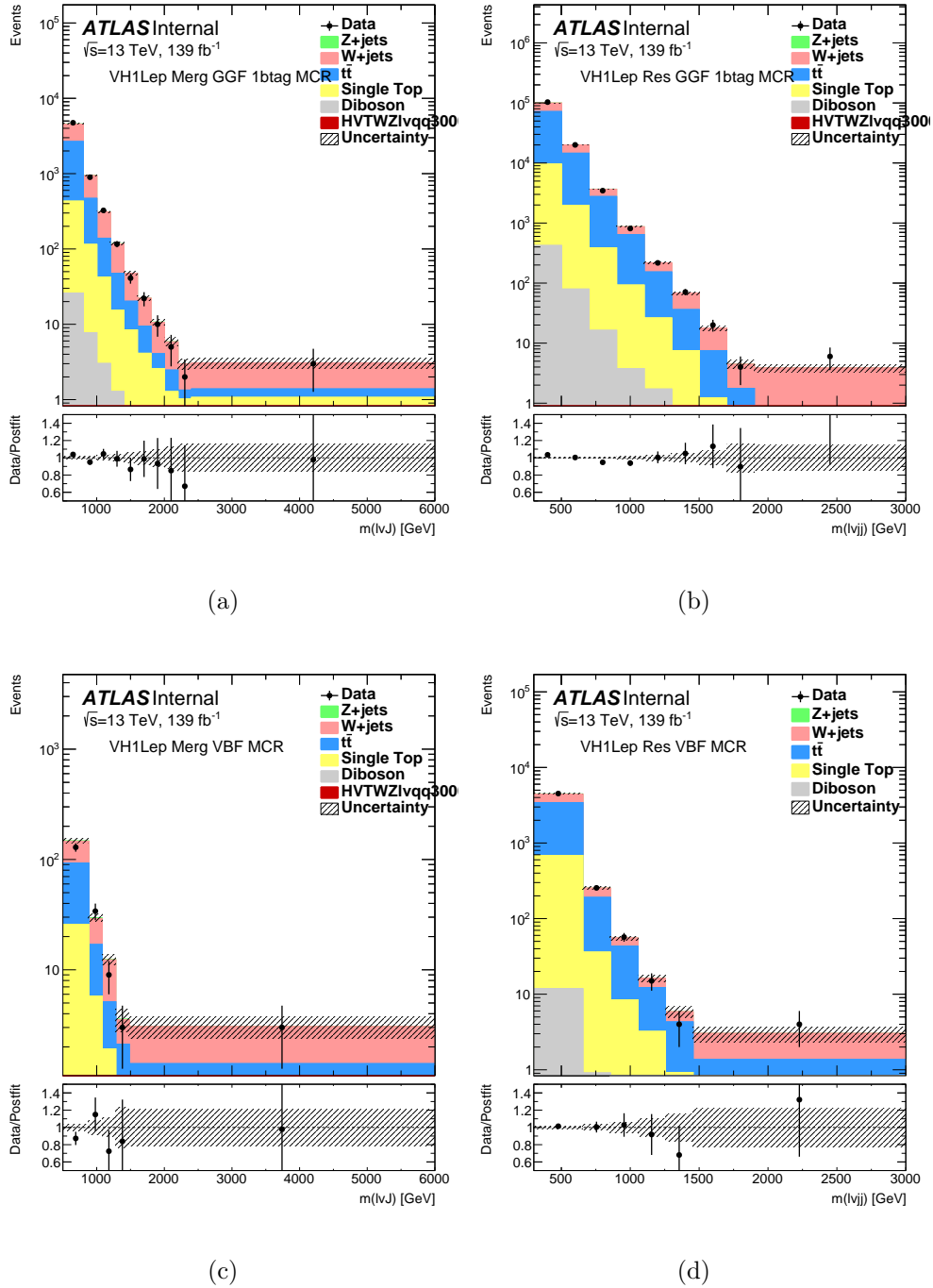


Figure C.10: Post-fit invariant mass distributions in the WZ signal regions of the VH 1-lepton channel, categorized by production mode and purity. Subfigures (a) and (b) show the ggF merged high-purity (HP) and low-purity (LP) MCR regions, and subfigures (c) and (d) display the VBF HP and LP MCR regions. Stacked histograms represent background predictions after the background-only fit to all WZ signal and control regions. Data points are overlaid, and the lower panels show the Data/Postfit ratio, with shaded bands indicating the total post-fit uncertainty, including both statistical and systematic components.

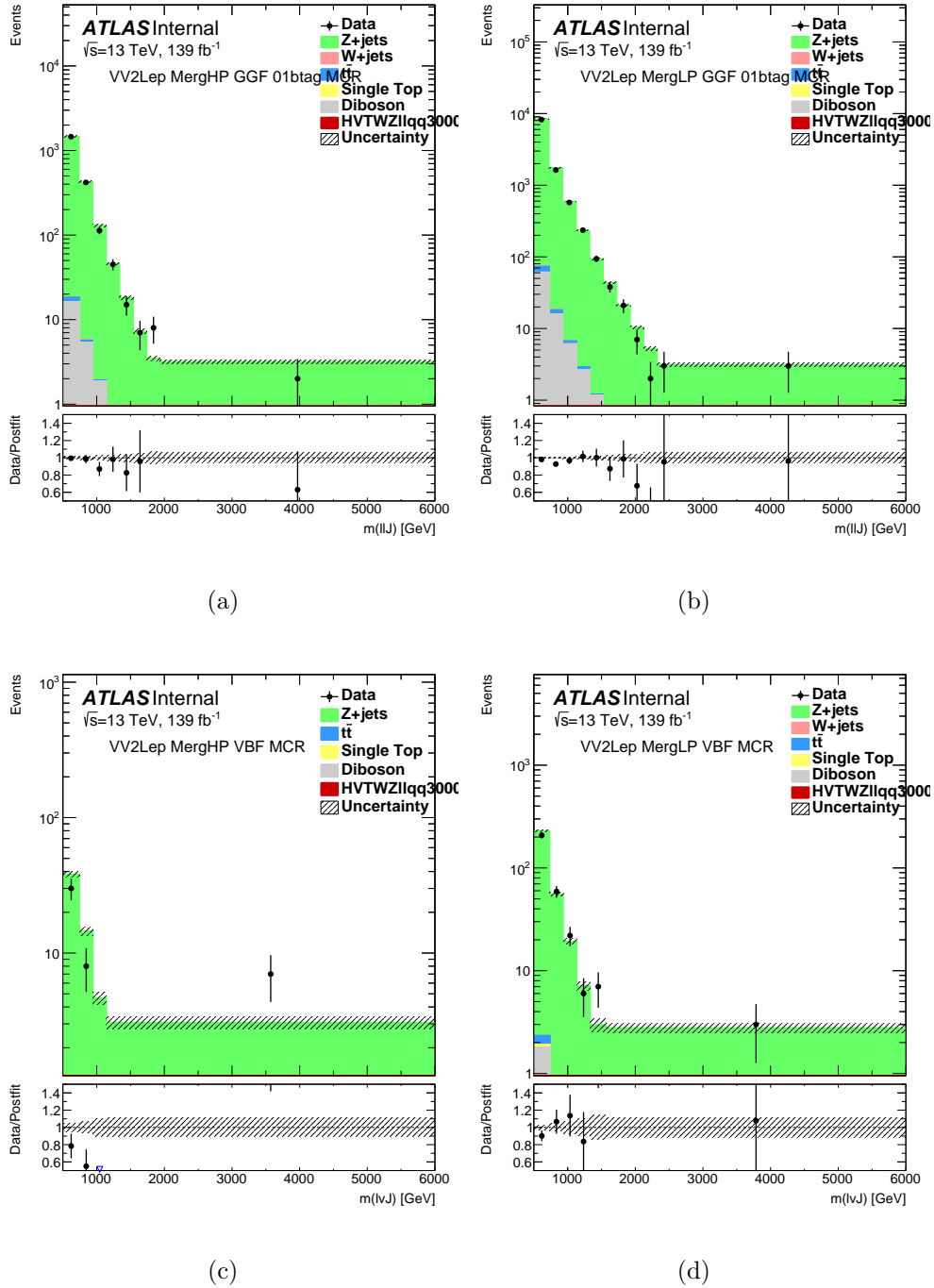


Figure C.11: Post-fit invariant mass distributions in the WZ signal regions of the VV 2-lepton channel, categorized by production mode and purity. Subfigures (a) and (b) show the ggF merged high-purity (HP) and low-purity (LP) MCR regions, and subfigures (c) and (d) display the VBF HP and LP MCR regions. Stacked histograms represent background predictions after the background-only fit to all WZ signal and control regions. Data points are overlaid, and the lower panels show the Data/Postfit ratio, with shaded bands indicating the total post-fit uncertainty, including both statistical and systematic components.

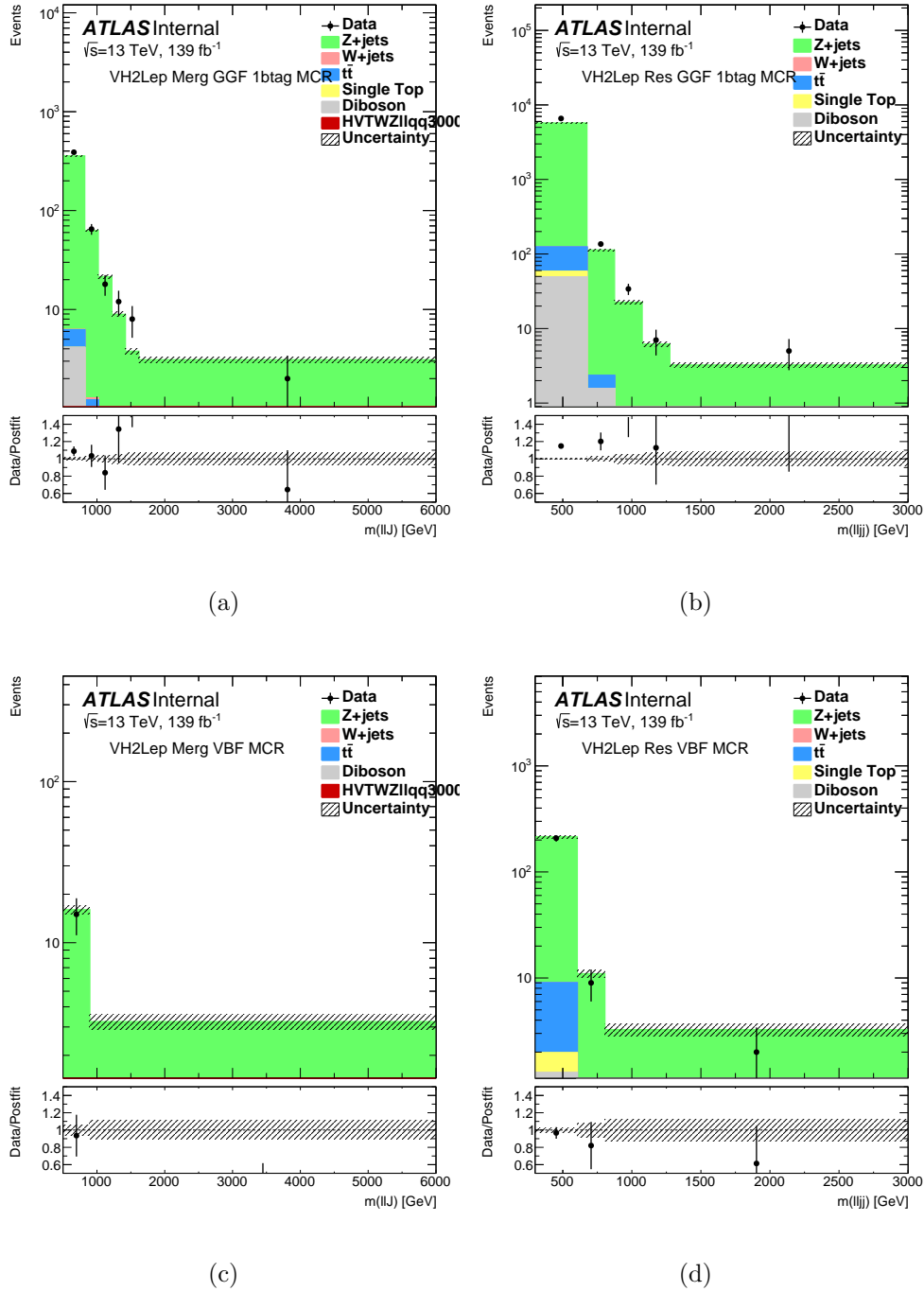


Figure C.12: Post-fit invariant mass distributions in the WZ signal regions of the VH 2-lepton channel, categorized by production mode and purity. Subfigures (a) and (b) show the ggF merged high-purity (HP) and low-purity (LP) MCR regions, and subfigures (c) and (d) display the VBF HP and LP MCR regions. Stacked histograms represent background predictions after the background-only fit to all WZ signal and control regions. Data points are overlaid, and the lower panels show the Data/Postfit ratio, with shaded bands indicating the total post-fit uncertainty, including both statistical and systematic components.

C.0.4 Post-Fit Validation in Signal Regions for 1-Lepton and 2-Lepton Channels

C.0.4.1 HVT $W' \rightarrow WZ$

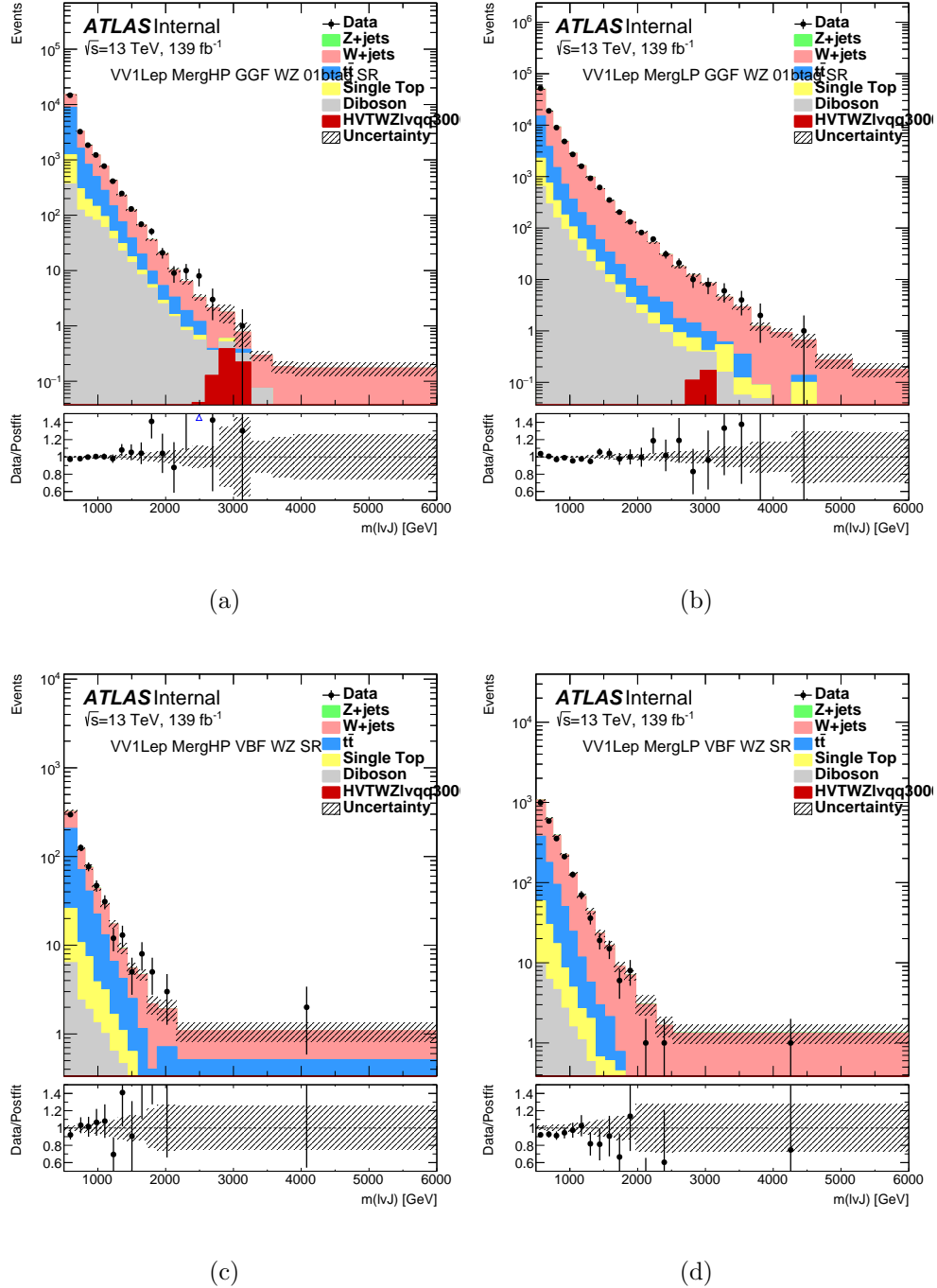


Figure C.13: Post-fit invariant mass distributions in the WZ signal regions of the VV 1-lepton channel, categorized by production mode and purity. Subfigures (a) and (b) show the ggF merged high-purity (HP) and low-purity (LP) signal regions, and subfigures (c) and (d) display the VBF HP and LP signal regions. Stacked histograms represent background predictions after the background-only fit to all WZ signal and control regions. Data points are overlaid, and the lower panels show the Data/Postfit ratio, with shaded bands indicating the total post-fit uncertainty, including both statistical and systematic components.

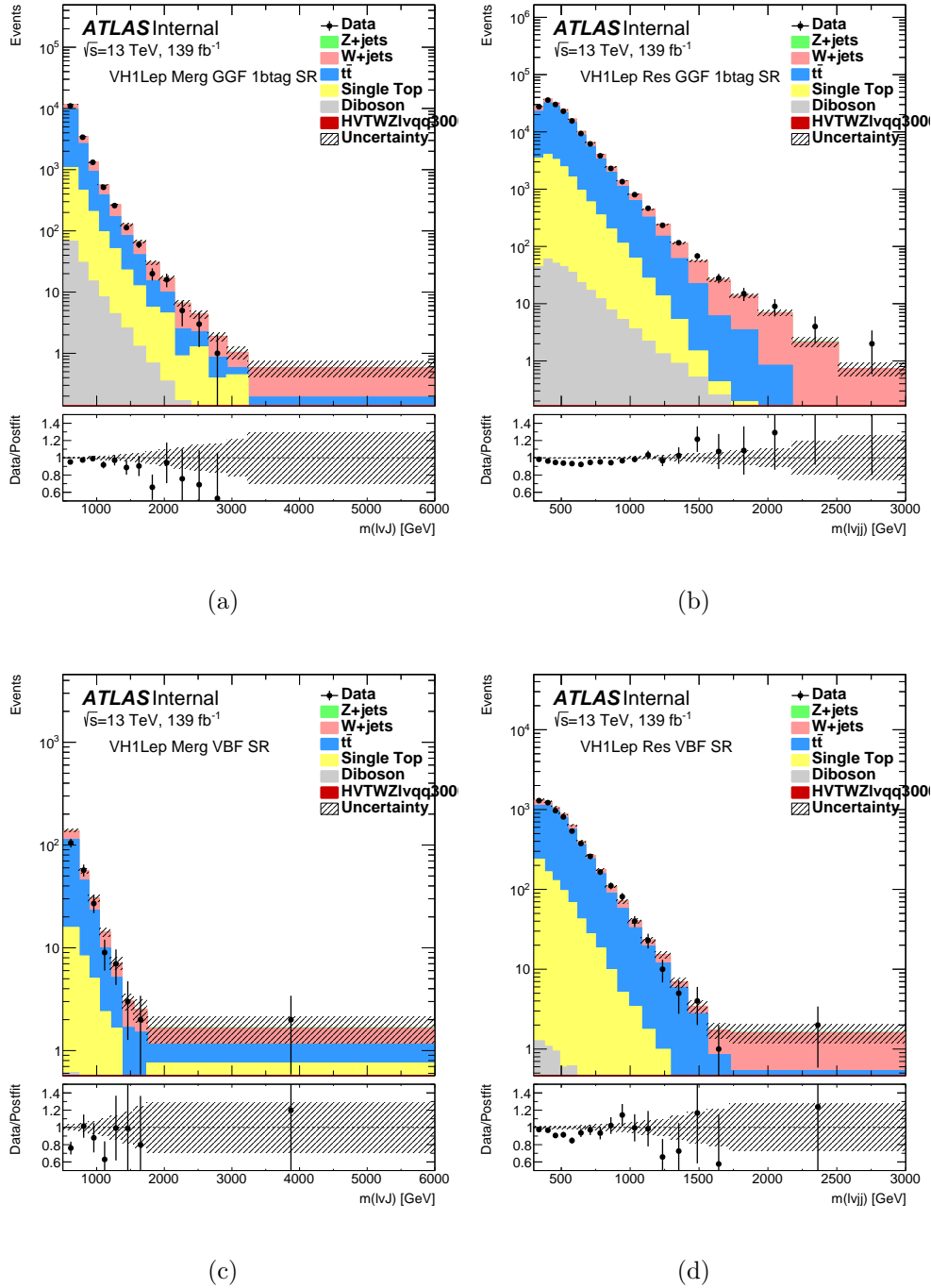


Figure C.14: Post-fit invariant mass distributions in the WZ signal regions of the VH 1-lepton channel, categorized by production mode and purity. Subfigures (a) and (b) show the ggF merged high-purity (HP) and low-purity (LP) signal regions, and subfigures (c) and (d) display the VBF HP and LP signal regions. Stacked histograms represent background predictions after the background-only fit to all WZ signal and control regions. Data points are overlaid, and the lower panels show the Data/Postfit ratio, with shaded bands indicating the total post-fit uncertainty, including both statistical and systematic components.

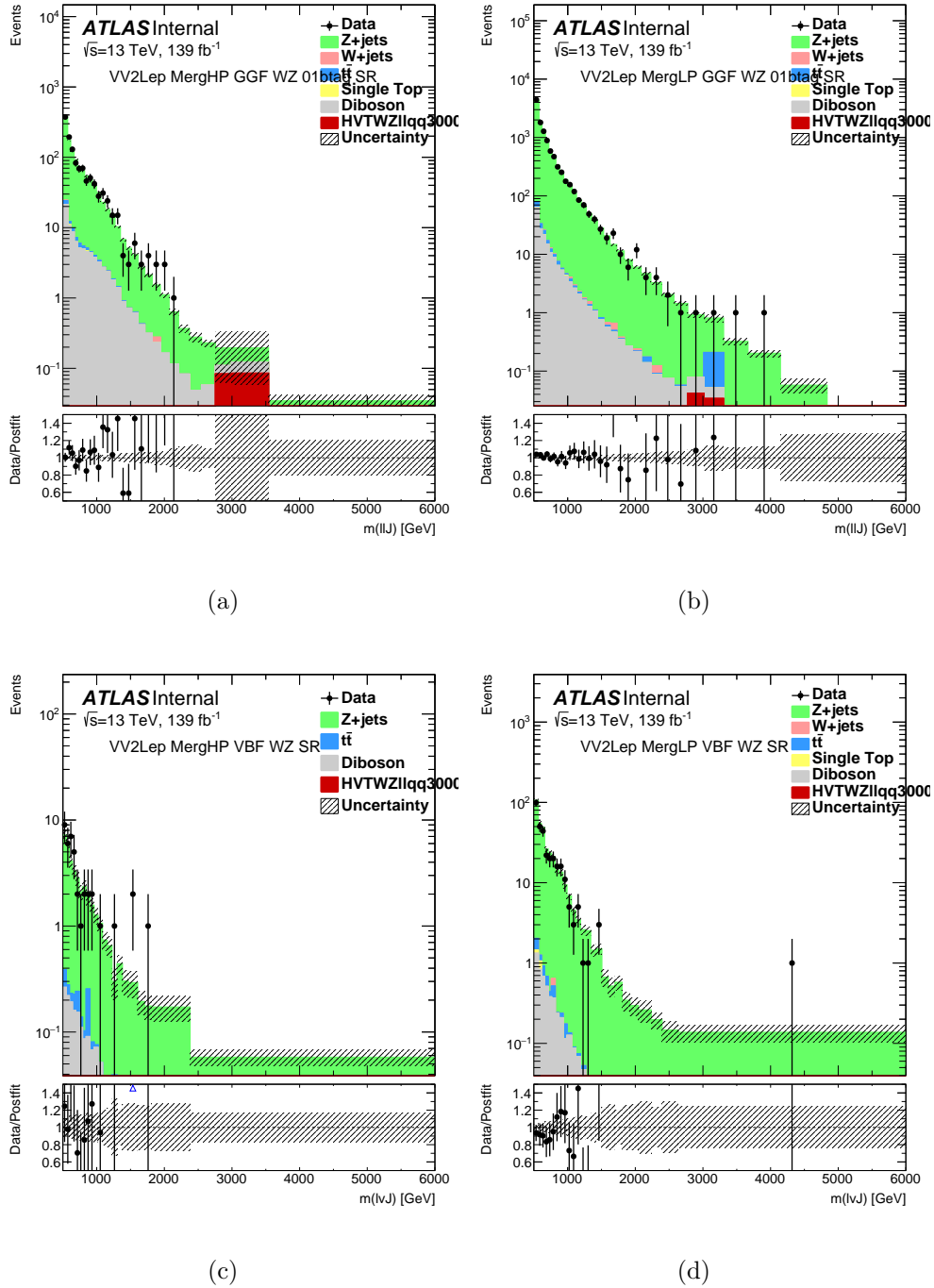


Figure C.15: Post-fit invariant mass distributions in the WZ signal regions of the VV 2-lepton channel, categorized by production mode and purity. Subfigures (a) and (b) show the ggF merged high-purity (HP) and low-purity (LP) signal regions, and subfigures (c) and (d) display the VBF HP and LP signal regions. Stacked histograms represent background predictions after the background-only fit to all WZ signal and control regions. Data points are overlaid, and the lower panels show the Data/Postfit ratio, with shaded bands indicating the total post-fit uncertainty, including both statistical and systematic components.

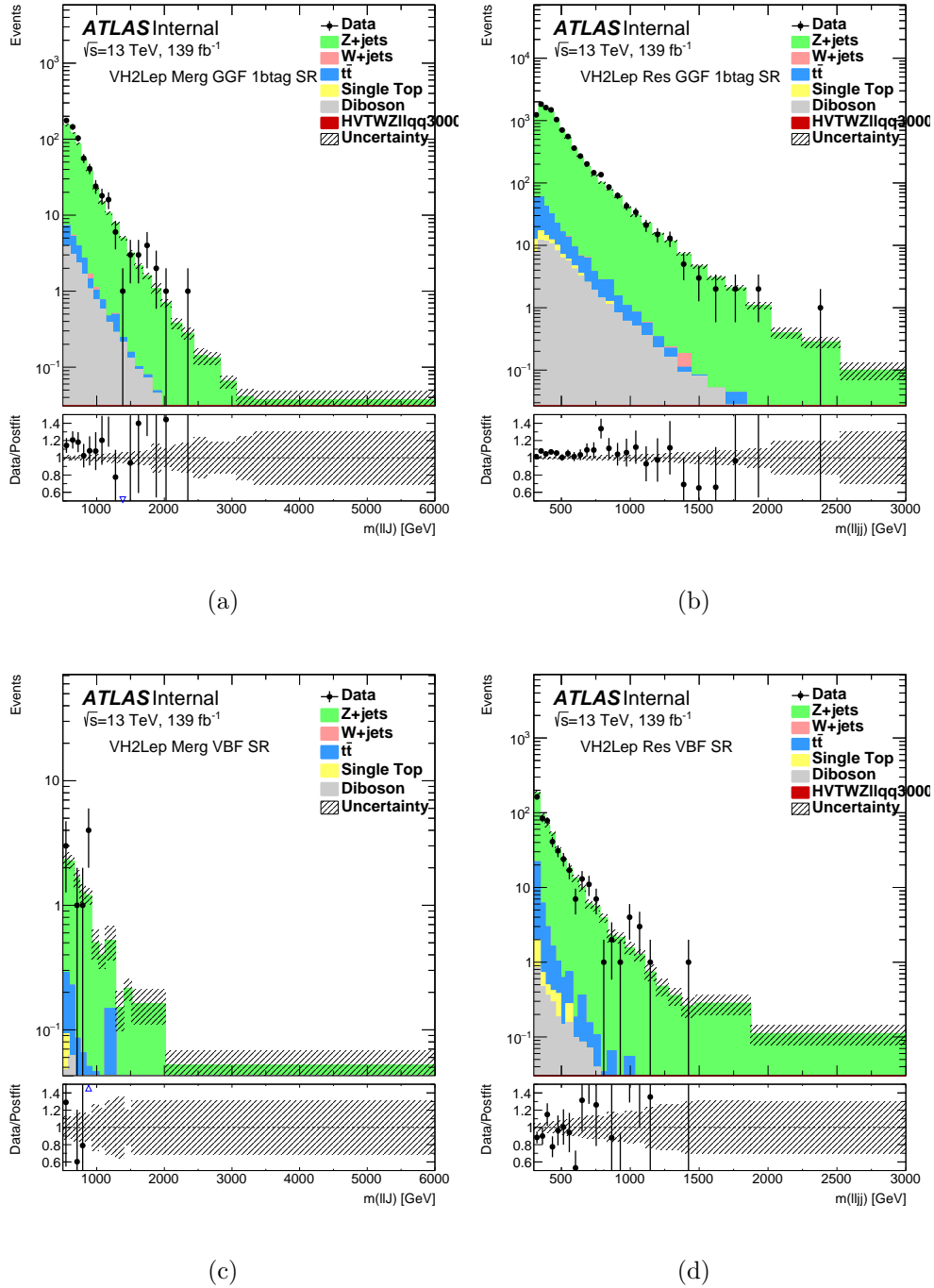


Figure C.16: Post-fit invariant mass distributions in the WZ signal regions of the VH 2-lepton channel, categorized by production mode and purity. Subfigures (a) and (b) show the ggF merged high-purity (HP) and low-purity (LP) signal regions, and subfigures (c) and (d) display the VBF HP and LP signal regions. Stacked histograms represent background predictions after the background-only fit to all WZ signal and control regions. Data points are overlaid, and the lower panels show the Data/Postfit ratio, with shaded bands indicating the total post-fit uncertainty, including both statistical and systematic components.

C.0.5 More Systematic Constraints

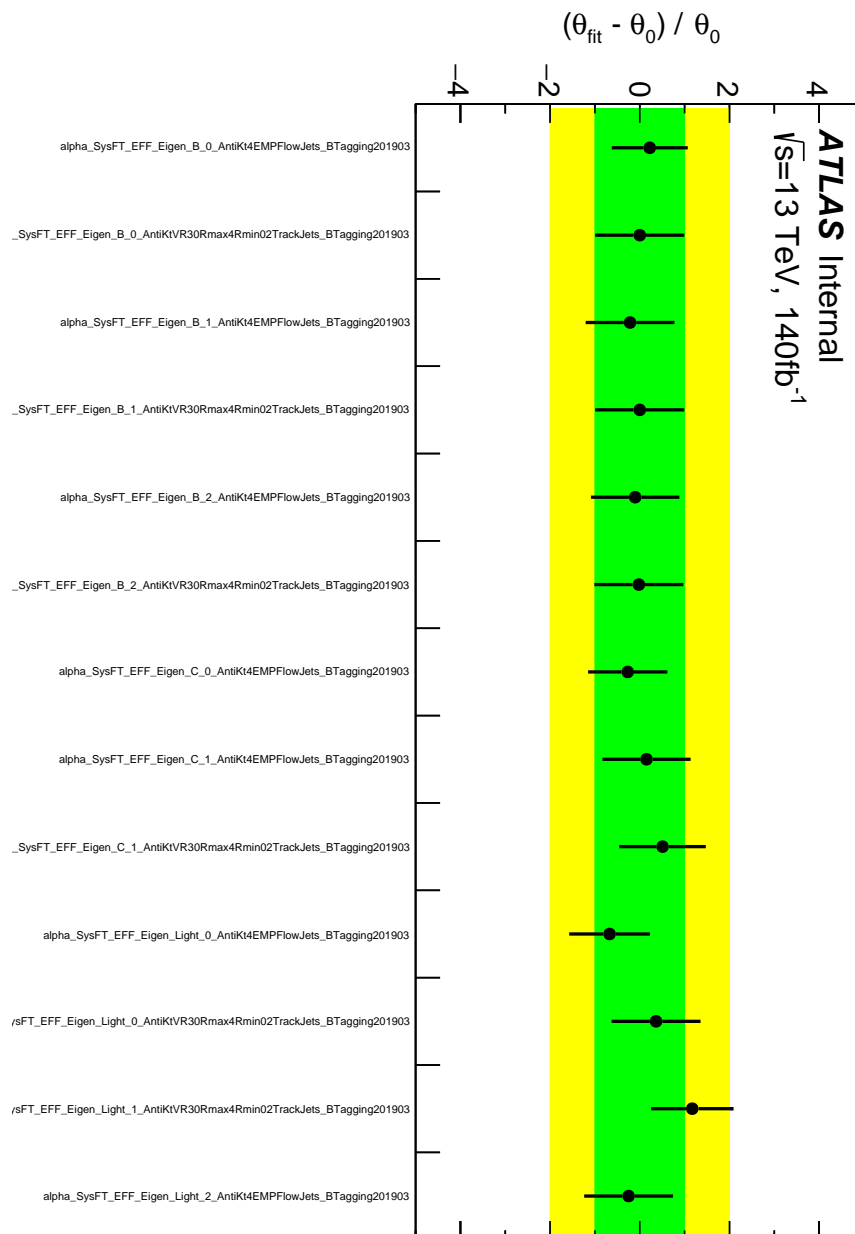


Figure C.17: Post-fit pull distribution for a representative set of nuisance parameters related to b-jet systematic uncertainties. Each point shows the shift of the fitted nuisance parameter (θ_{fit}) from its nominal pre-fit value (θ_0), normalized by the pre-fit uncertainty. The green and yellow bands correspond to the 1σ and 2σ confidence intervals, respectively. All pulls remain within acceptable ranges, indicating no significant tensions between the data and the systematic uncertainty parameterizations, and validating the background modeling in the statistical interpretation.

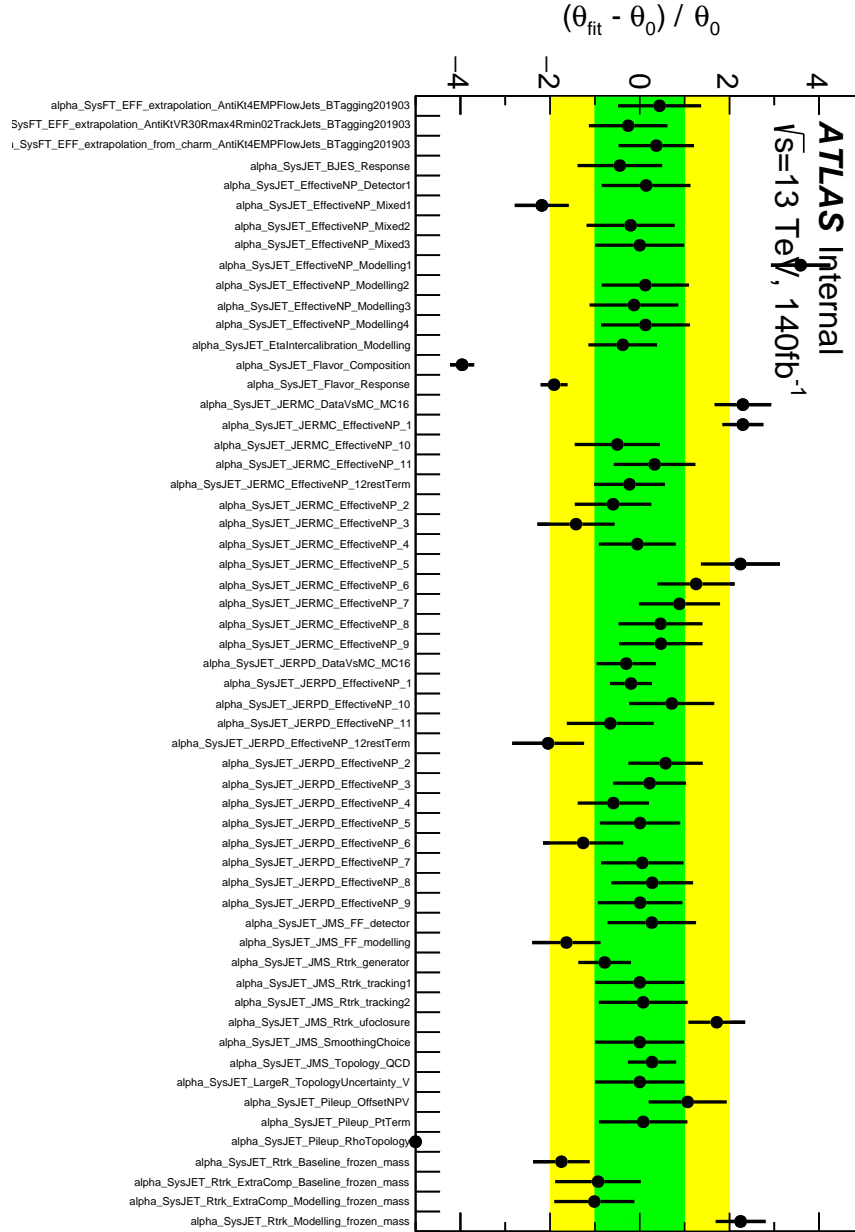


Figure C.18: Post-fit pull distribution for a representative set of nuisance parameters related to jet systematic uncertainties. Each point shows the shift of the fitted nuisance parameter (θ_{fit}) from its nominal pre-fit value (θ_0), normalized by the pre-fit uncertainty. The green and yellow bands correspond to the 1σ and 2σ confidence intervals, respectively. Some pulls extend beyond the expected range, indicating notable tensions between the data and certain systematic uncertainty parameterizations. These deviations suggest potential mismodeling or underestimated uncertainties in specific components of the background model.

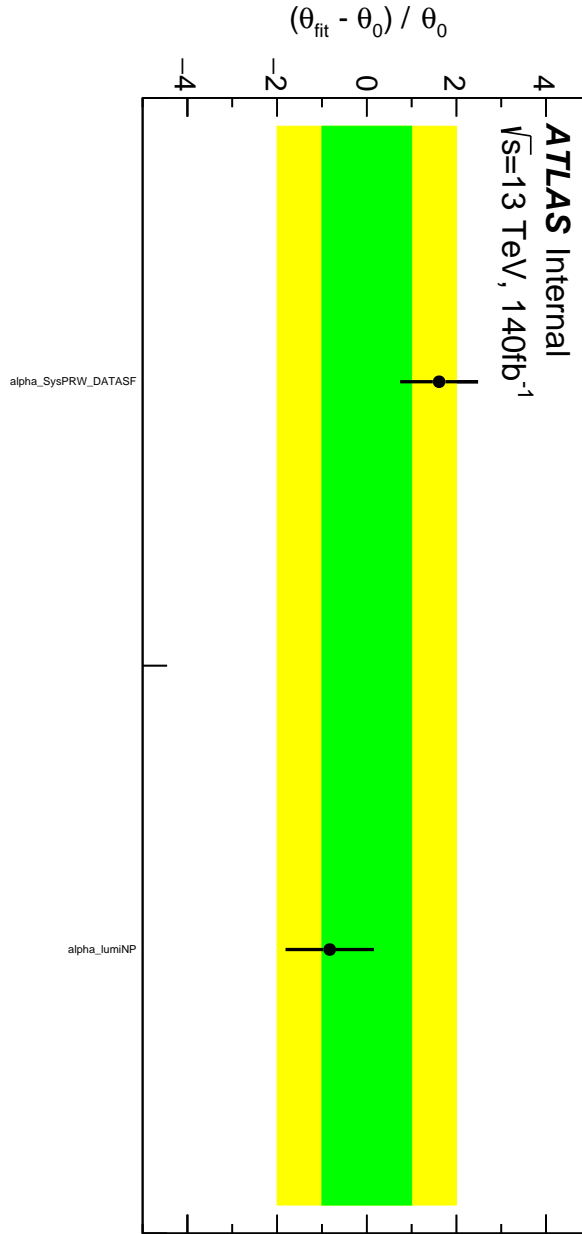


Figure C.19: Post-fit pull distribution for data SF and luminosity uncertainties. Each point shows the shift of the fitted nuisance parameter (θ_{fit}) from its nominal pre-fit value (θ_0), normalized by the pre-fit uncertainty. The green and yellow bands correspond to the 1σ and 2σ confidence intervals, respectively. Both pulls remain within acceptable ranges, indicating no significant tensions between the data and the systematic uncertainty parameterizations, and validating the background modeling in the statistical interpretation.

